Innovative design of rare earth nickelates as cathodes for solid oxide fuel cells

Rakesh Sharma

Communauté
UNIVERSITÉ Grenoble Alpes

THÈSE

Pour obtenir le grade de

DOCTEUR DE LA COMMUNAUTÉ UNIVERSITÉ GRENOBLE ALPES

Spécialité : **Matériaux, Mécanique, Génie Civil, Electrochimie**
Arrêté ministériel : 25 mai 2016

Présentée par

Rakesh Kumar SHARMA

Thèse dirigée par **Elisabeth DJURADO** et
codirigée par **Jean-Marc BASSAT** et **Mónica BURRIEL**

préparée au sein du **Laboratoire d'Electrochimie et de Physico-chimie des Matériaux et des Interfaces (LEPMI)**
dans **l'École Doctorale Ingénierie – Matériaux, Mécanique, Environnement, Energétique, Procédés, Production**

Conception innovante de cathodes à base de nickelates de terres rares pour piles à combustible à oxyde électrolyte solide

Thèse soutenue publiquement le **24 Novembre 2016**,
devant le jury composé de :

M. Werner PAULUS
Professeur, Institut Charles Gerhardt, Université de Montpellier, Président
Mme Rose-Noëlle VANNIER
Professeur, Ecole Nationale Supérieure de Chimie, Lille, Rapporteur
M. Pierre-Marie GEFFROY
Chargé de recherche, CNRS, SPCTS Limoges, Rapporteur
Mme Mónica BURRIEL
Chargée de recherche, CNRS, LMGP, Co-encadrant
M. Jean-Marc BASSAT
Directeur de recherche, CNRS, ICMCB, Bordeaux, Co-directeur
Mme Elisabeth DJURADO
Professeur, Grenoble INP, Directeur

Acknowledgement

At the time when I have just finished my entire PhD work, I am sitting in front of my laptop and looking back the whole three years in Grenoble. I cannot find exact words to express how I appreciate and cherish this wonderful life. This thesis is the result of 3 years of work whereby I have been accompanied and supported by many people. I have now the opportunity to express my sincere gratitude for all of them.

First of all, I would like to thank Prof. Jean-Claude Leprêtre, Director of LEPMI, to welcome me in the laboratory to prepare my PhD thesis.

I am deeply indebted to my guides Prof. Elisabeth Djurado (LEPMI, Grenoble), Dr. Jean-Marc Bassat (ICMCB, Bordeaux) and Dr. Monica Burriel (LMGP, Grenoble) for their constant motivation, guidance and ideas, who gave me the opportunity to complete this research work. I would like to express my gratitude for their enormous support and encouragement to make this PhD work an invaluable learning experience for me.

First and foremost, I would especially like to express my sincere gratitude to my guide. Prof. Elisabeth Djurado again, for giving me the opportunity to work in her laboratory and group for all these years as well as for her patient guide and tutor in the whole research work. Without your support and input this thesis would not have been completed so fast. I would like to thank as well for taking care of every administrative and financial matters and also for her kindness in everyday life. During these years I have known to her as sympatic and principle centered person. Her overly enthusiasm and integral view on research and her mission for providing only high-quality work and not less has made a deep impression on me. I owe her lots of gratitude for having me shown this way of research. I also appreciate that she let me fly around the France to present our work at many conferences. Thank you that you took care of the work and also that you were always helping me in Grenoble. It is my honor to be your student. MERCI!

I would like to express my deepest appreciation to my co-guide, Dr. Jean-Marc Bassat again for your guidance, help and encouragement. I thank you for your consistent trust and support during my thesis work. Whenever I got stuck with my research, he was always available to provide kind help with lots of encouragement and inspiration. This gave me a lot of strength and motivation during my PhD life. I also thank you to give me an opportunity to work at ICMCB, Bordeaux and allow me to have a hand on experience on TGA, screen-

printing, compositional analysis by ICP-MS and FULLPROF refinement. Thank you for all suggestions, ideas and discussions without which the completion of this work would not be possible.

I would like to thank again my co-guide, Dr. Monica Burriel for your guidance, support and unselfish transfer of her knowledge, which enlightened the path where I looked for solutions and made this thesis possible. Your valuable inputs and suggestions shaped me both as a professional and independent individual. Thank you for your helpful comments and discussion.

I would like to thank to Prof. Laurent Dessemond (LEPMI-IES) for suggestions and the interesting conversations and the great help in analysis and discussion on electrochemical behavior of the oxygen electrode, impedance spectroscopy and many other things. I would like to say thanks to Prof. Elisabeth Siebert for ideas and conversations on impedance spectroscopy and aging study under polarization. Thanks to Prof. Abdelkader Hammou for his help and motivation and Prof. Saïd Obbade for his help in FULLPROF refinement. I would also like to thank Dr. Samuel Georges and Cécile Rossignol for their kind support.

I also like to thank Vincent Martin for teaching me TGA and helping to solve technical issues. In addition, I also want to acknowledge Claude Roux for helping me in EIS set up and measurement. I owe a huge gratitude to researchers and technicians of platform M2E for their continuous support throughout my graduate studies. Especially, I want to thank Marlu César Steil and Etienne Omnès-Sabardak for their initial and immense contribution in sorting out the problem related with CGO pellet fabrication. I also thank Sandrine for sharing her knowledge on screen printing and showing me the way to prepare inks properly.

I am also indebted to Encinas Thierry and Stephane Coindeau for spending time with me in measurement and discussion of XRD. I also thank Joëlle Calabro for preparing my samples for FEG-SEM, Rachel Martin and Frédéric Charlot CMTC (Consortium des Moyens Technologiques Communs) in Grenoble for carrying out FEG-SEM observations.

I would like to extend my sincere thanks to Dr. Guillaume Constantin, Dr. Moustafa Sanad and Dr. Cheah Seng Kian, for their help, support and encouragement. I would like to extend my sincere thanks to my friends Özden Celikbilek, Philippe Dumaz, Hana El Khal, Zeinab El Moussawi, Olesia Danyliv, Marie Lachal and Nicolas Bailly. The friendship I developed here is an unforgettable memory. They gave me great support and encouragement for my research and life.

I would like to thank all my jury members, and particularly Prof. Rose-Noëlle VANNIER (Ecole Nationale Supérieure de Chimie, Lille) and Dr. Pierre-Marie GEFFROY (SPCTS, Limoges) as reviewers and Prof. Werner PAULUS **(**Institut Charles Gerhardt, Université de Montpellier) for their valuable time in reading and commenting my work.

Special thanks to the "Ministère de l'Enseignement Supérieur et de la Recherche" for providing a Fellowship for my PhD education at Grenoble INP.

Finally, I would like to add special thanks to my dear family members. It has been 3 years since I left India to pursue my PhD degree at Grenoble INP, University Grenoble Alpes. Your unconditional love, endless support and encouragement made me go through my PhD life, which is full of ups and downs. Special thanks to my mother Nagina Sharma and brother Dr. Rajesh Sharma who provided tremendous helps during these three years. I definitely owe a lot to them. Thank you for always being there. I would like to thank all whose direct and indirect support helped me completing my thesis in time. At last but not at least, thank God almighty for all his blessing.

Rakesh Kumar Sharma
Saint Martin d'Hères,
November, 2016

Abstract (EN)

Layered Ruddlesden-Popper type (RP) oxides are promising cathodes for solid oxide fuel cells operating at intermediate temperature (~500 - 700 °C). This thesis is focused on the synthesis of mixed ionic-electronic conducting (MIEC) materials such as pure $La_{2-x}Pr_xNiO_{4+\delta}$, $0 \leq x \leq 2$, higher order $La_{n+1}Ni_nO_{3n+1}$ (n= 2 and 3) RP phases and composites adding $Ce_{0.9}Gd_{0.1}O_{2-\delta}$ (CGO) component. An innovative microstructure and architecture of these electrodes were successfully prepared using electrostatic spray deposition (ESD) and screen-printing (SP) processes. These materials were evaluated through structural, compositional, oxygen non-stoichiometry and microstructural characterizations using X-ray diffraction, energy-dispersive X-ray spectroscopy, thermogravimetric analysis and scanning electron microscopy. The electrochemical properties and chemical stability of these oxygen electrodes are discussed according to the architectural design and composition using electrochemical impedance spectroscopy (EIS) and X-ray diffraction, respectively. Finally, a single SOFC based on $LaPrNiO_{4+\delta}$ cathode has been measured.

Keywords: Solid Oxide Fuel cell (SOFC), Mixed Ionic and Electronic Conductor (MIEC), Cathode, Nickelates, $Ce_{0.9}Gd_{0.1}O_{2-\delta}$ (CGO), Coral-type microstructure, Architectural design, Interfaces, Chemical stability, Electrostatic Spray Deposition (ESD), Screen-Printing (SP), Electrochemical Impedance Spectroscopy (EIS).

Abstract (FR)

Des oxydes appartenant à la famille structurale Ruddlesden-Popper (RP) sont des matériaux de cathode prometteurs des piles à combustible à oxyde électrolyte solide (SOFC) fonctionnant à température intermédiaire (~ 500-700 °C). L'objectif de cette thèse est l'élaboration de conducteurs ioniques et électroniques, mixtes (MIEC) tels que la solution solide, $La_{2-x}Pr_xNiO_{4+\delta}$, $0 \leq x \leq 2$, des phases RP de formule $La_{n+1}Ni_nO_{3n+1}$ (n= 2 and 3) et les composites associant les matériaux précédents à la cérine gadoliniée, $Ce_{0.9}Gd_{0.1}O_{2-\delta}$ (CGO). Une microstructure et une architecture innovantes de ces électrodes ont été obtenues avec succès en utilisant l'atomisation électrostatique (ESD) et la sérigraphie (SP). La structure, la composition, la non-stoechiométrie en oxygène et la microstructure de ces matériaux ont été caractérisées par diffraction des rayons X, par spectroscopie des rayons X à dispersion d'énergie, par analyse thermogravimétrique et par microscopie électronique à balayage. Les propriétés électrochimiques et la stabilité chimique de ces électrodes à oxygène ont été discutées en fonction de leur architecture et de la composition en utilisant la spectroscopie d'impédance électrochimique (SIE) et la diffraction des rayons X, respectivement. Enfin, une cellule complète SOFC intégrant la cathode $LaPrNiO_{4+\delta}$ a été mesurée.

Mots Clés: Pile à combustible à oxyde électrolyte solide (SOFC), Conducteur mixte ionique et électronique (MIEC), Cathode, Nickélates, $Ce_{0.9}Gd_{0.1}O_{2-\delta}$ (CGO), Microstructure de type corail, Design architectural, Interfaces, Stabilité chimique, Atomisation électrostatique (ESD), Sérigraphie (SP), Spectroscopie d'impédance électrochimique (EIS).

Table of Contents

Introduction

Energy is critical for the development as well as for the socio-economic activities of any modern society. Indeed, the growth based on energy fuels economic is of paramount concern for all countries. However, the current power generation economy is mainly dependent on the fossil fuels availability. Thus such economy is not sustainable because fossil fuels are not a renewable energy source. Moreover, energy consumption increases with the continuous increase of population whose living standards are improved, leading to a larger global demand of energy [1, 2].

On one hand fossil fuels are diminishing because of the existence of finite resources (oil, coal and natural gas) [4]. On the other hand, the world energy demand has risen by approximately 50% from the year 1980 [4, 5]. Therefore, with the present level of usage, fossil energy resources created over several hundred million years will be finished within just some generations. This will certainly be problematic for all countries in the future. Along with the rise in energy demand, dependence on fossil fuels also leads to high carbon emissions resulting in climate change problems. Additionally, such emissions significantly degrade the air quality all over the world [6]. Such health and climate impacts are unacceptable. Drastic natural catastrophes such as floods, droughts, heat waves, hurricanes, even earthquakes and tsunamis have occurred in the past decades as the consequence of climate change [5].

Moreover, the abundance of oil has led to negligence in the research on alternative energy topics during the 20^{th} century. Therefore, renewable energy sources and the development of new technologies, such as fuel cells, are crucial for enhancing the quality of life for individuals and societies [7].

A fuel cell is an electrochemical device that directly converts fuel (chemical) energy into electrical energy in a highly clean and efficient way. Fuel cells can be used for co-generation of heat and electricity for household or industrial applications [8] or even in portable applications [9]. Cars powered by fuel cells already exist and show satisfactory performance [10]. Therefore fuel cells possess great potential to influence significantly the global energy economy based on fossil energy to a cleaner and more sustainable one. Among the different type of fuel cells, solid oxide fuel cells (SOFCs) [11] are promising devices since they present the most efficient and cost-effective utilization of a wide multiplicity of fuels such as hydrocarbons, coal gas and gasified biomass [12]. SOFC devices exist as prototypes because there are still issues related to the storage and distribution of hydrogen [13], the high costs and the technological immaturity of the high temperature technology

[14]. However predictions show that fuel cells could dominate the transportation market, but only after the years 2030-2040 [15].

Motivations and objectives of this work

The operating temperature of SOFCs is very high (~1000 °C). As a consequence there are many issues such as high operation costs, durability etc. which could be resolved by lowering the operation temperature. Hence, working at intermediate temperatures (IT), *i.e.* at 700 °C or below, would greatly decrease operation and fabrication expenses associated with interconnect materials, while improving the overall lifetime of solid oxide fuel cells, labeled and referred as IT-SOFCs for this intermediate temperature range [16]. However, lowering the operating temperature down to 500-700 °C leads to many challenges. One of them is to develop cathode materials with sufficiently high electrocatalytic activity for oxygen reduction. Intensive research has thus been carried out to explore alternative electrodes and in particular new cathode materials are sought in order to achieve superior and stable electrochemical performance [17]. In this context, the first member of the layered Ruddelsden-Popper ($Ln_{n+1}Ni_nO_{3n+1}$) series, $Ln_2NiO_{4+\delta}$ (Ln = La, and Pr) with hyperstoichiometric oxygen, as well as higher-order RP phases (n >1), have recently attracted significant attention as promising alternatives to conventional oxygen deficient perovskites for use as promising IT-SOFCs cathode materials [18-21]. Earlier studies demonstrated that $Pr_2NiO_{4+\delta}$ materials show very good electrochemical properties in comparison to $La_2NiO_{4+\delta}$ [18]. In addition, the long-term stability of $Pr_2NiO_{4+\delta}$ was evaluated by Vibhu et al. [18], who found that $Pr_2NiO_{4+\delta}$ is not chemically stable even at 600 °C for 30 days. On the other hand $La_2NiO_{4+\delta}$ is very much stable even at 700 °C for 30 days but displays poor electrochemical performance. Thus, neither of them is ideally suited for practical utilization of IT-SOFCs but their combination could be. Moreover, the higher order RP phases, $La_3Ni_2O_{7+\delta}$ (n=2) and $La_4Ni_3O_{10-\delta}$ (n=3), could be of interest for their use as SOFC cathodes because of their superior electrical conductivity, and good chemical stability at intermediate temperatures (500-700 °C) [21]. Moreover, for a given composition the electrochemical properties strongly depend upon the microstructure of the cathode. In this context, electrostatic spray deposition (ESD) technique (annex A) seems to be one of the most promising fabrication techniques since various microstructures can be obtained by varying some key process parameters, as mentioned in Marinha's PhD thesis, dedicated to the preparation, microstructural and

electrochemical characterization of $La_{0.6}Sr_{0.4}Co_{0.2}Fe_{0.8}O_{3-\delta}$ (LSCF) cathodes on gadolina-doped ceria (CGO) [22].

The major goal of this PhD work is to elaborate new oxygen electrode materials for IT-SOFC applications based on new materials, such as $La_{2-x}Pr_xNiO_{4+\delta}$, $La_{n+1}Ni_nO_{3n+1}$ (n=2 and 3), CGO + $Ln_2NiO_{4+\delta}$ (Ln = La and Pr) and CGO + $La_{n+1}Ni_nO_{3n+1}$ (n=2 and 3) composite films, with a special emphasis on the optimization of the microstructure, architecture and composition of the oxygen electrode to improve electrochemical electrode properties. All the cathode materials were deposited on CGO substrates, either by ESD, by screen printing or by both techniques, in order to optimize the microstructure and architecture. The particular objectives are:

- to coat original porous "coral" $La_2NiO_{4+\delta}$ films on CGO substrates using the electrostatic spray deposition (ESD) process; to optimize the corresponding microstructure and the architectural design by varying the ESD process parameters in order to improve the percolation of $La_2NiO_{4+\delta}$ grains and their interface with the CGO electrolyte and study their electrochemical properties for IT-SOFC cathode applications;
- to study the influence of the Pr content on the microstructure, electrochemical properties and chemical stability of $La_{2-x}Pr_xNiO_{4+\delta}$; evaluate the electrochemical properties of architecturally designed $La_{2-x}Pr_xNiO_{4+\delta}$ cathodes by using the ESD combined with screen-printing (SP) deposition technique; study their chemical stability and compatibility with CGO substrate under OCV and polarization; to prepare and to characterize complete cells based on the composition showing the best compromise between chemical stability and electrochemical properties;
- to study the effect of the ESD process parameters on the microstructure of $La_4Ni_3O_{10-\delta}$ and evaluate the electrochemical response as a function of microstructure;
- to increase the number of electrochemical reaction sites close to the electrolyte improving the contact between the $Ln_2NiO_{4+\delta}$ (Ln = La, Pr) cathode and CGO the electrolyte, using $Ln_2NiO_{4+\delta}$ /CGO composite layers located on top of the electrolyte and evaluate the functional role of the CGO + $Ln_2NiO_{4+\delta}$ (Ln = La, Pr) composite on the electrochemical performance;

- to synthesize powder corresponding to the higher members (n=2 and 3) of the Ruddelsden Popper series $La_{n+1}Ni_nO_{3n+1\pm\delta}$; investigate their electrochemical properties and their composites formed with CGO under the SOFC operation conditions.

Outline of the thesis

This thesis work presents the deposition, characterization, microstructure optimization, architectural design and electrochemical properties of layered RP-type materials, particularly $La_{2-x}Pr_xNiO_{4+\delta}$, $La_3Ni_2O_{7+\delta}$, $La_4Ni_3O_{10-\delta}$ and the composites that these oxides form with a CGO electrolyte. Electrostatic spray deposition and screen-printing techniques have been used to prepare the cathodes. The organization of the manuscript is as follows:

Chapter 1 presents a literature survey on SOFC with a focus on nickelate-based cathodes.

Chapter 2 describes the synthesis and characterization of $La_2NiO_{4+\delta}$ films. The effect of the ESD process parameters has been presented in detail. Finally, the electrochemical properties of architecturally designed cathodes have been described.

Chapter 3 presents the architecturally designed $La_{2-x}Pr_xNiO_{4+\delta}$ films with the final objective to find the best compromise between the electrochemical properties and the chemical stability. $La_{2-x}Pr_xNiO_{4+\delta}$ films have been prepared by ESD using the parameters optimized in chapter 2, and have been further characterized by XRD, SEM. In addition, the electrochemical properties of architecturally designed cathodes have been studied by impedance spectroscopy. The preparation and characterization of the full cell based on the composition showing the best compromise are also presented in the chapter 3.

Chapter 4 is focused on the effect of the ESD parameters on the microstructure of the $La_4Ni_3O_{10-\delta}$ films. The microstructure strongly depends upon the ESD parameters. The electrochemical properties of $La_4Ni_3O_{10-\delta}$ films with different microstructures have also been described. They are microstructurally dependent.

Chapter 5 describes the preparation and the structural, microstructural and electrochemical characterizations of various composite compositions with the aim to improve the electrochemical properties of $Ln_2NiO_{4+\delta}$ (Ln = La, Pr) and $La_{n+1}Ni_nO_{3n+1}$ (n=2 and 3) based cathodes. The first part of this chapter is devoted to $La_2NiO_{4+\delta}$ and $Pr_2NiO_{4+\delta}$ electrodes on CGO with the fabrication of a composite interface in between the electrode and CGO

electrolyte in order to improve the chemical contact between $Ln_2NiO_{4+\delta}$ and CGO. The second part of chapter 5 also details the synthesis and characterizations of $La_3Ni_2O_{7+\delta}$ and $La_4Ni_3O_{10-\delta}$ materials whose powders have been prepared by auto-combustion. The oxygen non-stoichiometry and thermal expansion coefficients have been calculated by TGA and dilatometry, respectively. The electrochemical properties of $La_3Ni_2O_{7+\delta}$ and $La_4Ni_3O_{10-\delta}$ based cathodes prepared by screen-printing have been evaluated in a separate section. In order to further improve the electrochemical properties, CGO + $La_3Ni_2O_{7+\delta}$ and CGO + $La_4Ni_3O_{10-\delta}$ composite cathodes have been prepared by screen-printing and characterized by XRD, SEM and impedance spectroscopy measurements.

Some conclusions are given in the last part and some perspectives are proposed to reinforce the current results.

References:

[1] N. Tanaka, World Energy Outlook, N. Tanaka, Editor (2009) p. 58.
[2] B. Dudley, BP Energy Outlook 2030, BP plc. (2011) p. 8.
[3] A. Züttel, A. Remhof, A. Borgschulte, O. Friedrichs, Philosophical Transactions of the Royal Society of London A: Mathematical, Physical and Engineering Science 368, 1923 (2010) 3329-3342.
[4] N. Tanaka, World Energy Outlook, N. Tanaka Editor (2009) p. 74-75.
[5] A.B. Stambouli, E. Traversa, *Renewable and Sustainable Energy Reviews*, 6 (2002) 433-455.
[6] J. Dignon, *Atmospheric Environment. Part A. General Topics*, 26 (1992) 1157-1163.
[7] N.S. Lewis, D.G. Nocera, *Proceedings of the National Academy of Sciences*, 103 (2006) 15729-15735.
[8] A. Osman, R. Ries, *International Journal of Life Cycle Assessment*, 12 (2007) 308- 316.
[9] *News: Toshiba, Hitachi DMFCs feature in prototype audio players, cell phones*. *Fuel Cells Bulletin*, 11 (2005). p. 8.
[10] *The Honda FCX fuel cell vehicles.* AutoTechnology, (2007) p. 59-63.
[11] D. Marinha, L. Dessemond, E. Djurado, *Curr. Inorg. Chem.*, 3 (2013) 2–22.
[12] Z. L. Zhan, S. A. Barnett, *Science*, 308 (2005) 844 847.
[13] A. Züttel, *Materials Today*, 6 (2003) 24-33.
[14] R.K. Dixon, *Mitigation and Adaptation Strategies for Global Change*, 12 (2007) 325-341.
[15] W. McDowall, M. Eames, *Energy policy*, 34 (2006) 1236-1250.
[16] J. S. Herring, J. Obrien, C. Stoots, G. Hawkes, J. Hartvigsen, and M. Shahnam, *Int. J. Hydrogen Energy*, 32 (2007) 440–450.
[17] T. Horita, Y. Katsuhiko, S. Natsuko, Y. Harumi, A. Weber, E. Ivers-Tiffée, *Electrochim. Acta*, 46 (2001) 1837-1845.

[18] V. Vibhu, A. Rougier, C. Nicollet, A. Flura, J.-C. Grenier, J.-M. Bassat, *Solid State Ionics*, 278 (2015) 32–37.
[19] S. Takahashi, S. Nishimoto, M. Matsuda, M. Miyake, *Journal of the American Ceramic Society*, 93 (2010) 2329–2333.
[20] G. Amow, S. J. Skinner, *Journal of Solid State Electrochemistry*, 10 (2006) 538-546.
[21] G. Amow, I. J. Davidson, S. J. Skinner, *Solid State Ionics*, 177 (2006) 1205–1210.
[22] D. Marinha, PhD Thesis, Grenoble INP, 2010.

Chapter 1

Literature survey

A fuel cell is a device that directly converts the chemical energy of a fuel into electrical energy. A great advantage of this system is a higher conversion efficiency compared to conventional thermo-mechanical methods. The elementary fuel cell is composed of an electrolyte, a cathode and an anode. Gaseous fuels are fed continuously to the anode and an oxidant gas is fed continuously to the cathode. There are several types of fuel cells as shown in **Fig. 1**, generally classified by the chemical characteristics of the electrolyte which is a pure ionic conductor.

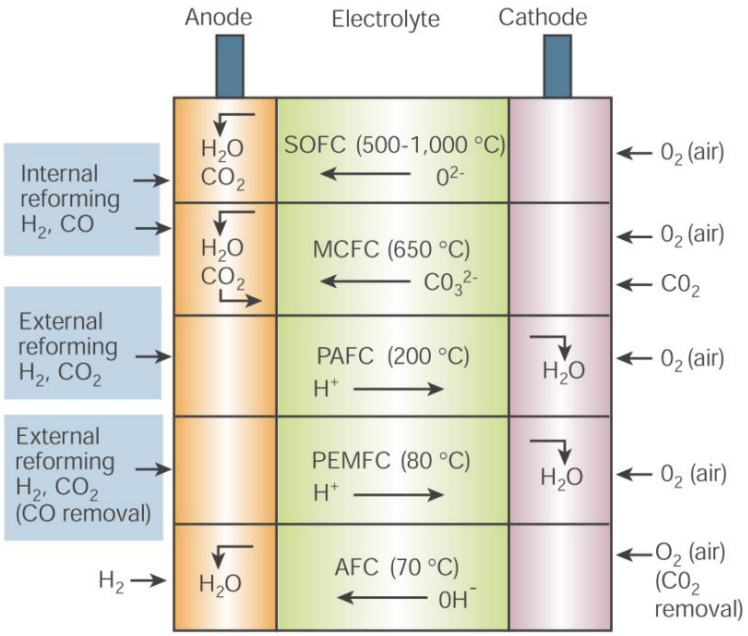

Fig. 1 Different types of fuel cells with their working temperature range [1].

1. Solid Oxide Fuel Cell (SOFC)

Solid oxide fuel cell (SOFC) is a device which operates at high temperature (~1000 ^oC). Unlike low temperature fuel cells, it can run without previous reforming with various fuels such as natural gas, bio-gas, and methanol [2]. SOFCs are composed of solid-state oxide materials. Different configurations are possible such as planar button cells, flat-plate cells, tubular cells or rolled tubes. **Fig. 2** shows a schematic diagram of a planar cell, which is the most usual configuration. At the cathode side exposed to air, electrons dissociate and reduce adsorbed gaseous oxygen, thus forming oxygen anions. These anions diffuse through the electrolyte and oxidize the fuel at the anode side, forming steam or carbon dioxide and electrons. Electrons then flew in an external circuit towards the cathode. They can be used for

running electric devices. Chemical reactions involved in a SOFC are summarized as following:

At the cathode, the formation of oxygen anion by reduction of the oxygen gas:

$$^1/_2O_2 + 2e^- \rightarrow O^{2-} \quad (1.1)$$

At the anode, the oxidation of the fuel:

$$H_2 + O^{2-} \rightarrow H_2O + 2e^- \quad (1.2)$$

The complete cell reactions are:

$$^1/_2O_2 + H_2 \rightarrow H_2O \quad (1.3)$$

The Gibbs free energy change ΔG per mole of reactions (1.3) can be directly transformed into electric energy by the SOFC.

$$\Delta G = -zF \cdot E \quad (1.4)$$

where F (96485 C) is the Faraday constant, *E* the cell voltage and *z* the number of charges involved in the reaction (z =2).

The electromotive force E_r, or the reversible voltage, is described by Nernst equation:

$$E_r = E^0 + \frac{RT}{2F} \ln\left(\frac{p_{H_2} p_{O_2}^{1/2}}{p_{H_2O}}\right) \quad (1.5)$$

where: E^0: Standard potential, V,

R: gas constant, 8.31, J mol^{-1} K^{-1},

T: temperature, K,

p_{H_2}, p_{H_2O}, p_{O_2}: respective partial pressures of hydrogen, water and oxygen gases, bar. The real energy, E, is lower than E_r. The difference is due to ohmic voltage losses in the cell components and their interfaces, and to electrodes polarization. The total polarization consists of cathode (η_c), anode (η_a) and electrolyte (IR) over-potentials. The final E of the cell is described as the following:

$$E = E_r - IR - \eta_c - \eta_a \quad (1.6)$$

Although SOFCs have demonstrated excellent efficiency, fuel flexibility and clean emission, yet they are not widely used for power generation because of the problems of long-term stability and high production cost [4]. Both problems are related to the high operation temperatures (approximately 800-1000ºC) of SOFC systems. Moreover the high temperatures also limit the choice of materials: degradation phenomena due to chemical reactions and

cationic inter-diffusion, which restrict the lifetime of a SOFC. To overcome these issues, current research is focused on lowering the operating temperature to the intermediate-temperature range (500-700 ^{o}C) while retaining a high efficiency and solving the significantly restrictions for the applications of intermediate temperature SOFCs (IT-SOFC) such as material cost, long-term stability and longevity [1, 5, 6].

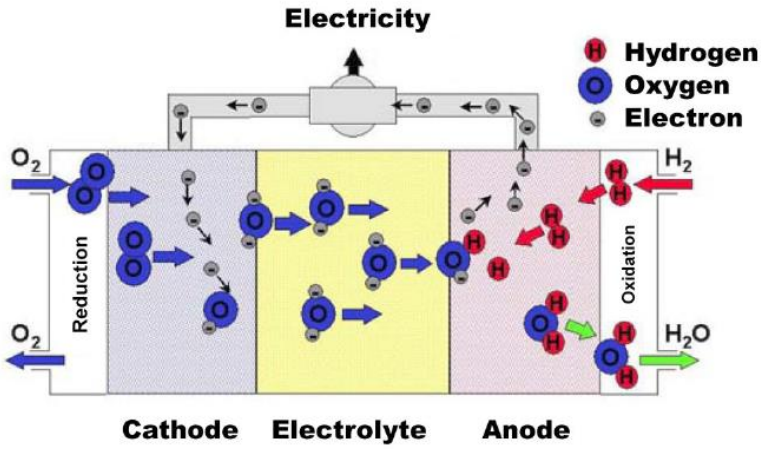

Fig. 2 Schematic diagram of transport and reaction mechanisms in a solid oxide fuel cell [3].

To optimize the performance of the cells, seeking suitable anode, electrolyte and cathode materials is therefore a critical task for the development of IT SOFCs. The requirements of each component and their current development will be briefly described as follows.

1.1. Electrolyte

There are several requirements for an ideal electrolyte to be used in IT-SOFC such as high oxygen ionic conductivity (typically above 1×10^{-2} S cm^{-1} at the operating temperature) combined with very low electronic conductivity (electronic insulating materials are required), fully-dense microstructure, good thermal and chemical stability towards both electrode materials along with a good thermal expansion coefficient (TEC) [7]. Different possible electrolyte materials are summarized in **Fig. 3** [8]. Among the various electrolytes, yttria stabilized zirconia (8YSZ), 8 mol. % Y_2O_3 doped ZrO_2, is the most widely used electrolyte in SOFCs [9-11]. 8YSZ has sufficient mechanical properties and excellent chemical stability over a wide range of temperatures and oxygen partial pressures (10^{-22} < P_{O_2} (atm) < 0.2). Other dopants such as CaO, MgO, Sc_2O_3 and Yb_2O_3 have been also used to stabilize the cubic structure of ZrO_2 [11-12].

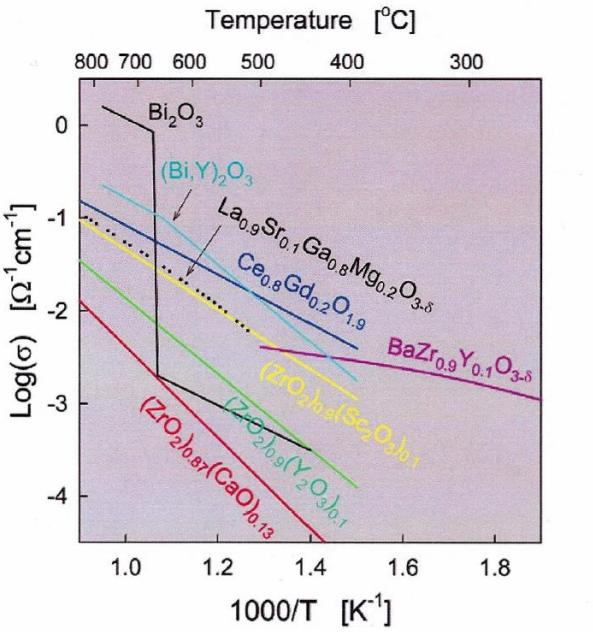

Fig. 3 Conductivity versus temperature of chosen solid electrolytes used in SOFC [8].

The doping reaction is shown in the equation below using Kröger-Vink notation where the trivalent Y^{3+} cation substitutes the Zr^{4+} ion, resulting in oxygen vacancies (eq.1.7), which amount depends on the nature of dopants and on the substitution level [11-12].

$$Y_2O_3 \overset{ZrO_2}{\Longleftrightarrow} 2Y'_{Zr} + V_O^{\cdot\cdot} + 3O_O^x \qquad (1.7)$$

Badwal et al. [13] have shown that the ionic conductivity of YSZ is increased when the mol. % of Y_2O_3 is increased. The maximum ionic conductivity of 0.1 S cm^{-1} at 1000 °C and 0.03 S cm^{-1} at 800 °C is achieved for a dopant value of 8 – 10 % mol. % Y_2O_3 [14] after which the ionic conductivity severely drops. A too high dopant concentration leads to a phenomenon of association in between punctual defects, reducing their mobility and consequently diminishing the ionic conductivity [15]. As can be seen in **Fig. 4**, the nature of the dopant must also be considered. Indeed it has been shown that when the dopant ionic radius has a close size mismatch to the ionic radius of the host, a larger ionic conductivity has been observed [16]. On the other hand, a larger mismatch leads to stresses lattice which can destabilize the crystalline structure leading to a phase transition. For a doping rate of about 3 mol% Y_2O_3 in ZrO_2 (3TZP, Tetragonal Zirconia Polycrystalline), the thermomechanical properties are improved [17] with respect to 8YSZ, but the ionic conductivity is lower. Nevertheless, 8YSZ has the disadvantage of chemically reacting at high temperature with several cathode materials such as $La_{1-x}Sr_xFeO_{3-\delta}$ (LSF), $La_{1-x}Sr_xCr_{1-y}Mn_yO_{3-\delta}$ (LSCM), Ba_{1-}

$_xSr_xCo_{1-y}Fe_yO_{3-\delta}$ (BSCF), $La_{1-x}Sr_xCoO_{3-\delta}$ (LSC), $La_{1-x}Sr_xCo_{1-y}Fe_yO_{3-\delta}$ (LSCF) and $LaNi_{1-x}Fe_xO_{3-\delta}$ (LNF). As the consequence of such reactivity, the formation of insulating phases such as $SrZrO_3$ (perovskite) and $La_2Zr_2O_7$ (pyrochlore type) has been often reported at the electrode/electrolyte interface [18-22]. This leads to a substantial degradation in performance during operation because of larger reactivity over time at the operating temperature [23-26].

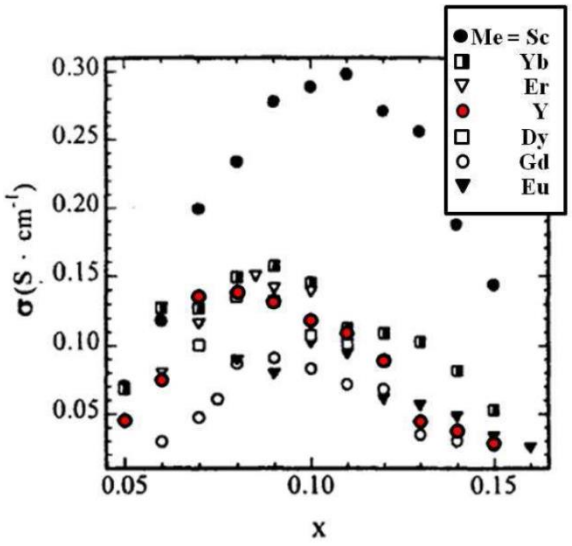

Fig. 4 Variations in ionic conductivity at 1000°C of $(ZrO_2)_{1-x}(Me_2O_3)_x$ (Me = metal) with different Me content [14].

The next promising material for electrolyte application is doped-ceria. Ceria crystallizes into a fluorite structure type. Common doping cations are Gd or Sm with molar percentage of 10 – 30 %. The doping reaction is similar to zirconia doping, in that Ce^{4+} cations are substituted by trivalent cations (eq. 1.7). As a result, oxygen vacancies are formed which enlarge the O^{2-} concentration. Sm doped ceria shows the highest ionic conductivity (**Fig. 5**). However, substitution with gadolinium is the most preferred one because of the high cost and low availability of Sm. Moreover, a substituting level of 10 mol. % (CGO10: $Ce_{0.9}Gd_{0.1}O_{1.95}$) shows a larger ionic conduction than 20 mol. % doping (CGO20: $Ce_{0.8}Gd_{0.2}O_{1.9}$) [27, 28]. However, both CGO10 and CGO20 are considered for the application. The advantage of CGO10 is a higher oxygen ion conductivity compared to 8YSZ (2×10^{-2} S.cm^{-1} for CGO and 8×10^{-3} S.cm^{-1} for 8YSZ at 650 °C) [27, 30, 31]. In this case the substituted ceria can replace YSZ as electrolyte for IT-SOFC. Unlike YSZ, CGO is more chemically stable with the typical electrode materials, LSM, LSC, LSF, LSCF, LNF [32-36], except some possible strontium and lanthanum diffusion as reported by Izuki et al. [37].

Nevertheless, the major drawback of CGO electrolyte in SOFC is that it must not be used at temperatures above 600 °C due to the reduction of Ce^{4+} ions to Ce^{3+} observed under fuel rich conditions (reducing atmosphere) at higher temperature [28, 38-40]. This mixed valence Ce^{4+}/Ce^{3+} creates electronic mobility and hence n-type electronic conductivity, leading to short circuit in SOFC cell. There are some other candidates for electrolytes such as Mg doped-lanthanum strontium gallate, $La_{0.9}Sr_{0.1}Ga_{0.8}Mg_{0.2}O_{3-\delta}$ (LSGM), as shown in **Fig. 3** [41, 42]. LSGM presents higher oxygen-ion conductivity in comparison to YSZ and can efficiently work at lower temperatures (650 – 800 °C). These materials have however not been yet largely developed. A comprehensive review, published by Goodenough [43] with regard to oxygen ion electrolytes is recommended, and for the most recent development of electrolyte materials for IT-SOFCs the reader can refer to references [44, 45].

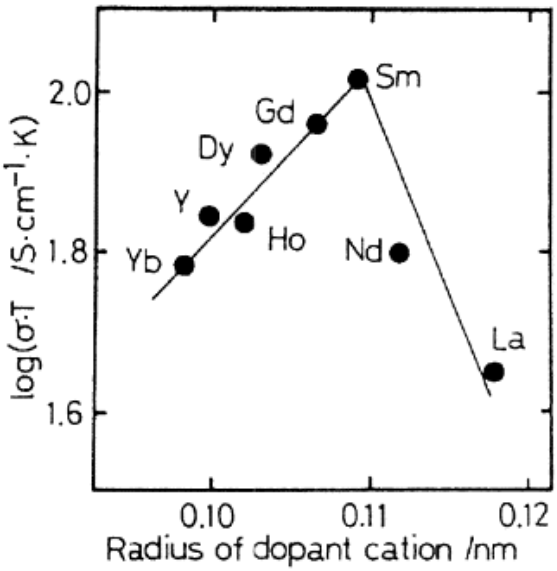

Fig. 5 Evolution of the ionic conductivity of ceria (20 mol. %) at 800 °C for different trivalent dopants [29].

1.2. Anode

Anode should conduct ions and electrons and must be permeable to gas. Ni/YSZ cermet (ceramic-metal composite) is the most common anode in SOFCs [46], showing no chemical reaction with typical electrolyte materials, i.e. YSZ and CGO. About 30 vol. % Ni is required to create effective electronic paths inside the cermet material. Oxidation of hydrogen molecules at anode begins with chemisorption and dissociation processes at the electrode surface [47], therefore the catalytic activity of the anode is very important. Ni/YSZ cermet not only possesses excellent catalytic properties for fuel oxidation but also highly porous

structures to facilitate the mass transport of reactant and product gas, and appropriate thermal expansion coefficient (TEC) with the common electrolytes. However, Ni/YSZ-based anode has some drawbacks; for example, sulphur poisoning and carbon deposition are observed when using natural gas as fuel due to the cracking of methane. Nickel metal is not only chosen because of its cost effectiveness but also because it can be easily produced by co-sintering NiO and YSZ, followed by in-situ reduction of the nickel oxide. Other metals that may be used are copper, cobalt and noble metals. Copper could also be considered as a replacement for nickel [48, 49], but has a higher propensity for carbon deposition and sulphur poisoning at lower temperature. Other materials are currently being investigated as potential replacements for the Ni/YSZ combination. Developments regarding anode materials have been extensively addressed in details in a review article [46].

1.3. Cathode

SOFC cathodes must fulfill several criteria [5, 50] such as i) high catalytic activity for reduction of molecular oxygen to be dissociated into charged atoms (O^{2-}), which will be incorporated into electrolyte, ii) high electronic conductivity for transferring electrons from the current collector to the reaction area (in general > 100 S cm^{-1} at the operating temperature) [51, 52], iii) sufficient ionic conductivity (even if it will be at least four orders of magnitude lower that the electronic one) iv) chemical compatibility with electrolyte and interconnect materials, v) good thermal and chemical stability in air, vi) sufficient durability when operating at high temperature and temperature cycling [53].

Cathode materials can be classified in three different types: pure electronic conductor, composite cathode mixing a pure electronic phase and a pure ionic one (such as CGO or YSZ), and single phase mixed ionic and electronic conductor (so-called MIEC).

With a pure electronic conductor as cathode, the oxygen reduction reaction (ORR) occurs at the cathode/electrolyte/gas phase boundary, known as TPB (Triple Phase Boundary), as shown in **Fig. 6(a)**. For such type of cathode, the microstructure plays an important role in improving the performance because an optimized microstructure will maximize the TPB sites number and shape; i.e. will extend the active regions for ORR. In particular, the porosity has to be sufficient through the cathode to bring oxygen molecules in contact with the electrolyte. (La, Sr)MnO_3 (LSM), which is a well-known pure electronic conducting cathode, has been widely used as a cathode in various SOFC designs [51] because it shows good stability under oxidizing atmospheres, high (p-type) electronic conductivity and

close TEC with conventional YSZ-based electrolytes. LSM was during long time the classical SOFCs cathode material, in case of high operating temperature (900-1000 °C) since ionic conductivity of the cathode material is not mandatory at such high temperature. As the consequence of high operating temperature, this material reacts with the conventional YSZ electrolyte leading to the formation of $La_2Zr_2O_7$ insulating phase [35].

Second type of cathode is a composite, mixing a pure electronic phase (LSM) and an ionic phase (YSZ). In this case, there are more possible reaction routes than in purely metallic electrodes [54] because the reduction of oxygen occurs not only at TPB but also at the boundary between the two phases provided porosity is sufficient, as shown in **Fig. 6(b)**.

Third type of cathode uses MIEC-type oxides. Contrarily to pure electronic electrodes, such cathodes permit the extension (delocalization) of the ORR area over part of the surface of the cathode materials, as shown in **Fig. 6(c)**. It means that ORR can occur all over the grains, if they are in contact with air. As a consequence, a significant improvement of the cell performance is expected at a lower operating temperature.

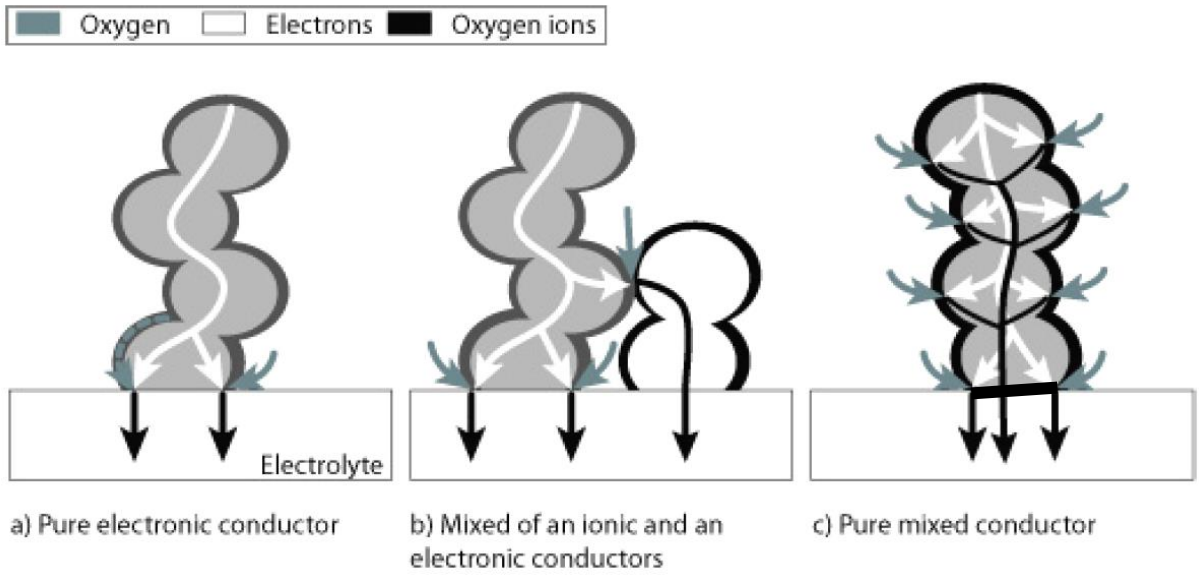

Fig. 6 Reaction routes for the oxygen reduction reaction: (a) in a pure electronic conductor (b), in a composite (electronic plus ionic conductors) and (c) in a single-phased MIEC.

A wide range of perovskite-based cathodes have been extensively investigated in the past [6, 9, 44, 45, 52, 55-57] and have been found to be appropriate for cathode operation. Nevertheless, each of them has several drawbacks. For instance, $La_{1-x}Sr_xCoO_{3-\delta}$ (LSC) material possesses superior transport and good catalytic properties with respect to the oxygen

reduction reaction [58-60] and is considered as a reference material. However, it has a high TEC which makes it difficult to be used in combination with conventional electrolytes such as YSZ and CGO. In order to address the drawback of LSC, partial substitution of iron for cobalt produces $La_{1-x}Sr_xCo_{1-y}Fe_yO_{3-\delta}$ (LSCF), which exhibits good ionic and acceptable electronic conductivity, catalytic activity, and even lower TEC [55, 56, 61-64]. Another disadvantage of these materials is that they easily form insulating phases such as $La_2Zr_2O_7$ and $SrCoO_3$ at the interface with YSZ electrolyte, which further degrade the performance of the cell.

In addition to perovskite-type cathode materials, there are a number of promising cathode materials such as layered double perovskite (e.g. $GdBaCoO_{5+\delta}$ and $PrBaCoO_{5+\delta}$) and perovskite-related Ruddlesden-Popper (RP) phases (e.g. $Ln_2NiO_{4+\delta}$, Ln = La, Pr and Nd and $La_{n+1}Ni_nO_{3n+1}$, n = 2 and 3). All these oxide materials have exhibited promising performance as MIECs [9, 44, 45, 65, 66]. For all three types of cathodes, the effect of the microstructure and of the composition of the cathode is very important in order to improve the efficiency of the SOFC. A detailed review on current development and properties related to nickelate based RP-phase materials associated with this work is given in the following section.

2. $Ln_{n+1}Ni_nO_{3n+1}$ -type materials: state of the art

Nickelates belonging to the Ruddlesden-Popper (RP) series have recently attracted much attention as promising cathode materials for the next generation of IT- SOFCs [67-69]. RP phases adopt general formula $A_{n+1}M_nO_{3n+1}$ (typically n = 1, 2 and 3, A = rare earth, M = metal) [70]. The layered crystal structure of the RP phases, $(AO)(AMO_3)_n$, is illustrated in **Fig. 7**. It consists of n consecutive $(AMO_3)_n$ perovskite layers, alternating with one AO rock-salt layer along the crystallographic c-axis. The well-known perovskite (AMO_3) and K_2NiF_4-type structure correspond to n = ∞ and n = l, respectively. The A and M site cations are typically comprised of rare/alkaline earth metals (La, Pr, Nd) and transition metals (Ni, Co, Cu), respectively. Such layered MIECs display diverse defect chemistry, allowing non-stoichiometric defect structures (oxygen hypo- and hyper-stoichiometry, which can also be defined as oxygen deficiency and excess, respectively) due to their oxygen content through tailoring A- and M-site. This feature makes these oxides very attractive for the fine-tuning of their electrical and electrochemical properties [68, 69, 71-81]. For the case of oxygen hyper-stoichiometry, particularly, the excess oxygen occupies interstitial sites within the AO rock-salt layers.

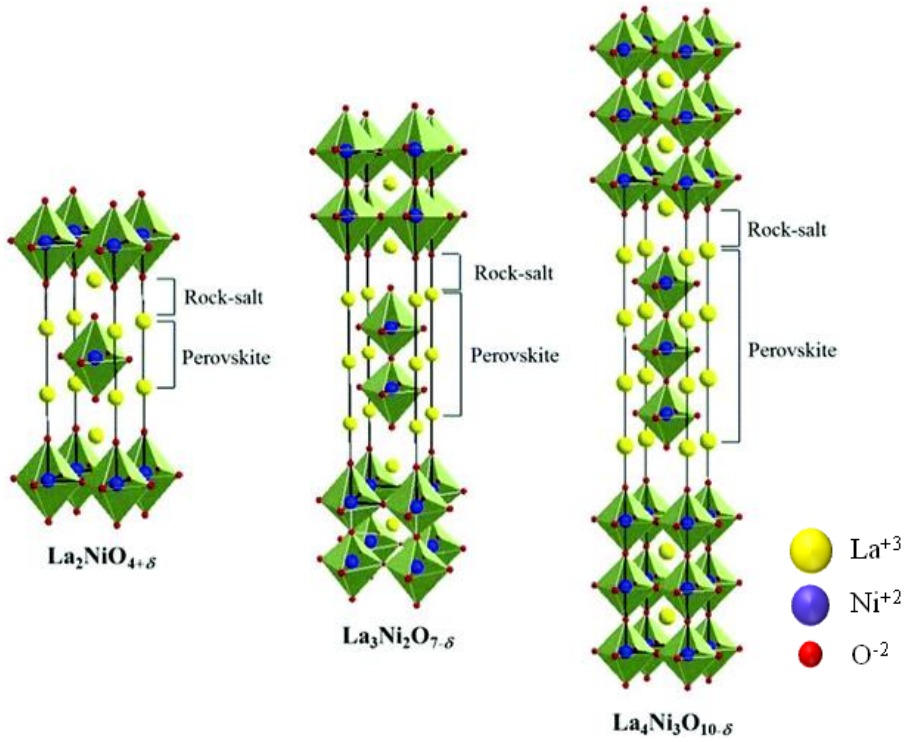

Fig. 7 Schematic crystal structures of the n = 1, 2 and 3 members of the Ruddlesden–Popper (RP) type $A_{n+1}M_nO_{3n+1}$. The unit cell of each structure is presented by a black rectangle [82].

2.1. K_2NiF_4-type materials ($Ln_2NiO_{4+\delta}$, Ln = La, Pr and Nd)

In earlier studies, the $Ln_2NiO_{4+\delta}$ (Ln = La, Pr and Nd) materials have been extensively studied for their application as a SOFC cathode [45, 82-85]. They have been widely synthesized by various techniques such as conventional ceramic processes (solid state and sol-gel methods) [65, 68, 69, 86-88], pulsed laser deposition (PLD) [89-91], metallorganic chemical vapor deposition [72, 92, 93]. As mentioned above, the crystal structure of $Ln_2NiO_{4+\delta}$ is consisted of a $LnNiO_3$ perovskite block intergrown with LnO rock-salt blocks, as shown in **Fig. 7** and **Fig. 8** (for $La_2NiO_{4+\delta}$). In general, two different crystallographic structures: tetragonal and orthorhombic (including different space groups in the latter case), have been reported in literature. Phase transitions between the two structures were evidenced in a whole range of temperature for $La_2NiO_{4+\delta}$ [94, 95]. A low temperature transition occurs at ~80 K from a low temperature tetragonal (LTT) phase (*$P4_2/ncm$* space group) to a low temperature orthorhombic (LTO) one (*Bmab* or *Fmmm* space group) [96-98]. With increasing temperature up to ~ 423 K, the LTO phase transforms to a high temperature tetragonal (HTT) one (*I4/mmm* space group) [95]. Similar phase transition has been also reported for $Pr_2NiO_{4+\delta}$ and $Nd_2NiO_{4+\delta}$ [99-101]. These transition temperatures are highly dependent on the oxygen

stoichiometry of the material [94, 95]. It has been well established that $Ln_2NiO_{4+\delta}$ (Ln = La, Pr and Nd) materials with K_2NiF_4 structure exhibit a large range of oxygen over-stoichiometry [100, 102-104], and the additional oxygens are mainly responsible of the high ionic conductivity [66, 85]. This is also dependent upon the size of rare-earth ion as well as the synthesis method for a given composition [105, 106]. In general, oxygen non-stoichiometry "δ" is determined by iodometric titration and / or thermo-gravimetric analysis under an atmosphere partially or completely reductive. **Table 1** shows the "δ" for $Ln_2NiO_{4+\delta}$ compounds, prepared by different methods.

Table 1. Non-stoichiometry "δ" in $Ln_2MO_{4+\delta}$ compounds

δ (20 °C)	Preparation	Method of determination	References
$La_2NiO_{4+\delta}$			
0.12 and 0.22 0.22 and 0.23	sol-gel	TGA iodometry	[86, 88]
0.17	sol-gel	TGA	[95]
0.15-0.19	sol-gel	iodometry	[107, 108]
0.12	solid state reaction	iodometry	[109]
0.11	crystallization melting zone	TGA	[110]
0.14	sol-gel	iodometry	[111]
$Pr_2NiO_{4+\delta}$			
0.21		iodometry	[85]
$Nd_2NiO_{4+\delta}$			
0.25		iodometry	[104]

2.1.1. Oxygen diffusion and ionic conductivity

The rate of oxygen reduction decreases with decreasing the SOFC operating temperature. The ion conduction (and the O^{2-} ions transfer at the interface cathode electrolyte) must be improved in order to optimize the performance. The ionically conductive O^{2-} is linked to the presence of structural defects which may be of two types: i) oxygen vacancy, as in the perovskites sub-stoichiometric oxygen or ii) interstitial oxygen associated with over-stoichiometric oxygen, in the oxides as K_2NiF_4 type.

The oxygen diffusion (D*) and surface exchange (k*) coefficients of these nickelates are among the highest values available in the literature, especially at intermediate temperatures (about one order of magnitude larger than that of conventional perovskites in an intermediate temperature range, 600 < T (°C) < 800). **Table 2** shows oxygen diffusion (D*) and surface exchange coefficients (k*) at 700 °C obtained by different researchers. The diffusion coefficients (D*) of the materials $A_2NiO_{4+\delta}$ are higher than those of perovskites. The ionic conductivity of these materials is directly related to the D* value, hence the ionic conductivity is the highest for $Pr_2NiO_{4+\delta}$ [107]. The favoured mechanism is probably of intersticialcy type, involving both apical and interstitial oxygens [112, 113], as shown in **Fig. 8**. Compared to the perovskite materials, these materials exhibit strong anisotropic ionic transport properties [81, 111, 114].

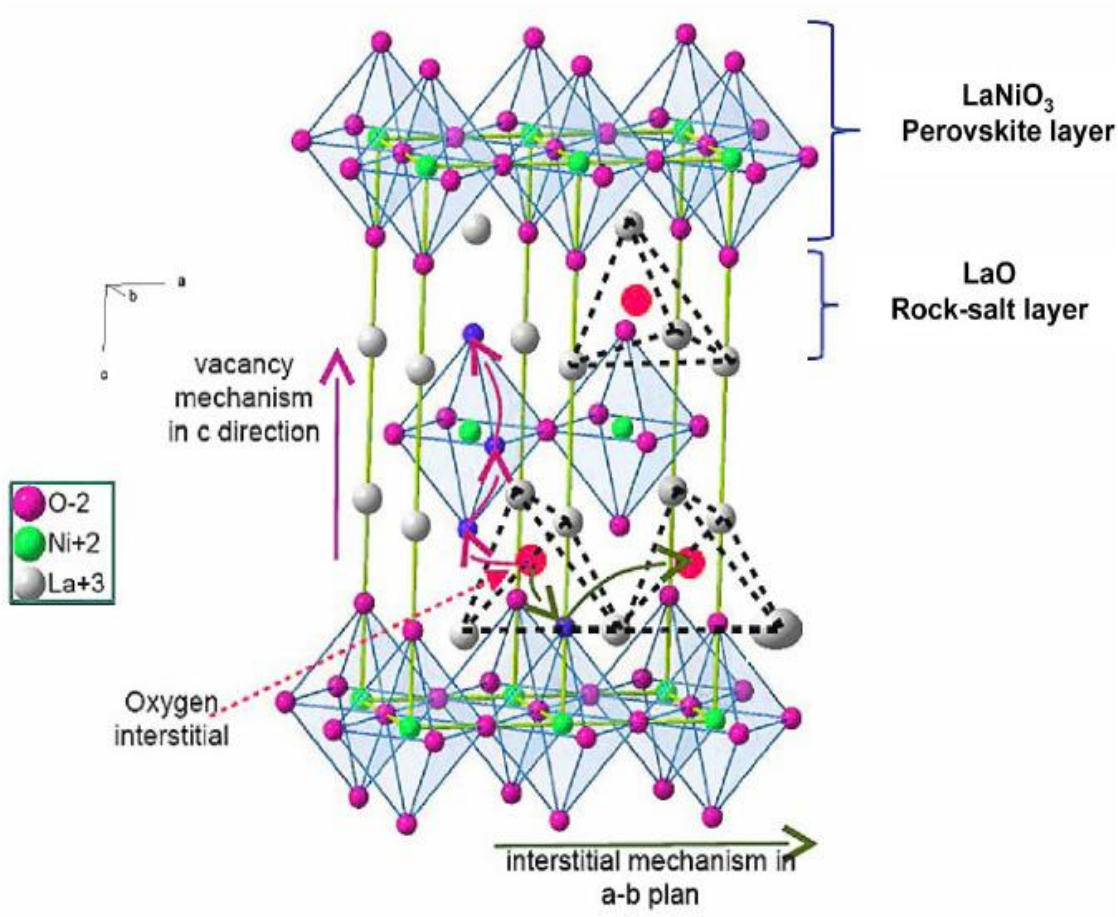

Fig. 8 Schematic illustration of the $La_2NiO_{4+\delta}$ structure showing the vacancy and interstitialcy ionic transport directions. $LaNiO_3$ perovskite and LaO rock-salt layers are indicated [115].

The corresponding *k** values at 700 °C are 1.6×10^{-7}, 1×10^{-6} and 3×10^{-7} $cm.s^{-1}$ for $La_2NiO_{4+\delta}$, $Pr_2NiO_{4+\delta}$ and $Nd_2NiO_{4+\delta}$ respectively [85]. The surface exchange coefficient "k*" of $La_2NiO_{4+\delta}$, is improved when the nickel is substituted with cobalt. Recently, Vibhu et al.

have studied the thermal variation of the oxygen diffusion coefficients, D*, and surface exchange coefficients, k*, in $La_{2-x}Pr_xNiO_{4+\delta}$ (x = 0.0, 0.5, 1.0, 1.5 and 2.0) as shown in **Fig. 9** [65]. The value of D* increases with increasing Pr content. The D* values of mixed phases (x = 0.5, 1.0 and 1.5) are in the range of those reported for $Pr_2NiO_{4+\delta}$ (2.5×10^{-8} cm^2 s^{-1}) and $La_2NiO_{4+\delta}$ (1.5×10^{-8} cm^2 s^{-1}) at 600 °C [85]. As a comparison, the D* values for LSCF are much smaller than the ones of the nickelates (**Fig. 9a**) [85]. Regarding the k* values (**Fig. 9b**), except at 500 °C, they are slightly higher at high temperature than those reported for $La_2NiO_{4+\delta}$ and $Pr_2NiO_{4+\delta}$ [85].

Table 2. D*and k* coefficients of $Ln_2NiO_{4+\delta}$ materials (determined at 700 ºC).

Composition	D* (cm^2 s^{-1})	k* (cm s^{-1})	Reference
$La_2NiO_{4+\delta}$	3.20 x10^{-8}	1.60 x10^{-7}	[116]
$La_2NiO_{4+\delta}$	5.50 x10^{-8}	2.00 x10^{-6}	[117]
$La_2NiO_{4+\delta}$	7.00 x10^{-8}	2.30 x10^{-6}	[118]
$La_2Ni_{0.75}Cu_{0.25}O_{4+\delta}$	4.00 x10^{-8}	1.50 x10^{-6}	[118]
$La_2NiO_{4+\delta}$	3.40 x10^{-8}	1.75 x10^{-7}	[119]
La_2 $Ni_{0.5}Cu_{0.5}O_{4+\delta}$	7.50 x10^{-8}	5.00 x10^{-7}	[120]
$La_2Ni_{0.25}Cu_{0.75}O_{4+\delta}$	2.00 x10^{-8}	1.50 x10^{-7}	[118]
$La_2Ni_{0.9}Co_{0.1}O_{4+\delta}$	2.50 x 10^{-8}	1.60 x10^{-6}	[116]
$La_2Ni_{0.8}Co_{0.2}O_{4+\delta}$	4.00 x 10^{-8}	7.90 x10^{-7}	[116]
$La_2Ni_{0.5}Co_{0.5}O_{4+\delta}$	8.00 x10^{-8}	1.30 x10^{-6}	[116]
$Nd_2NiO_{4+\delta}$	5.00 x10^{-8}	3.00 x10^{-7}	[121]
$Pr_2NiO_{4+\delta}$	9.00 x10^{-8}	1.00 x10^{-6}	[107]

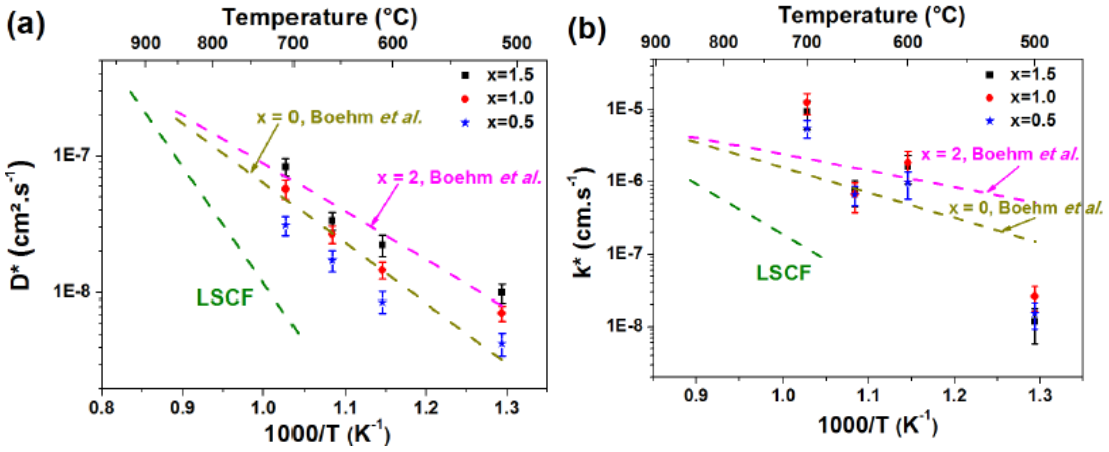

Fig. 9 Thermal variation of (a) the diffusion coefficient D* and (b) the surface exchange coefficient k* for $La_{2-x}Pr_xNiO_{4+\delta}$ (x = 0.5, 1 and 1.5) [65]. The values of D* for x = 0, 2 and LSCF are from reference [85]. The error bars represent the deviation from the average value of the coefficients determined using three different measurements.

2.1.2. Electronic Conductivity

The total electrical conductivity of oxides, measured in air, comprises an electronic contribution and a very much lower ionic contribution. The electrical conductivity of $Ln_2NiO_{4+\delta}$ is characterized by a semiconductor-type electronic conductivity, which occurs via hopping of p-type charge carriers between mixed-valence nickel cations [122-125]. A maximum in conductivity is observed between 600 and 700 K, above which a smooth apparent change from semiconducting to a metallic-like behavior is observed [123, 126, 127]. Bassat et al. [123] presented convincing evidence for various La deficient $La_{2-x}NiO_{4\pm\delta}$ phases that the increase in resistivity with increasing temperature, previously attributed to a metal-insulator transition at T > 600 K, is actually due to oxygen loss and the associated decrease in the number of charge carriers (Ni^{3+}). The maximum reported conductivity values for polycrystalline bulk ceramics, films (maximum ≈ 80 S/cm) [68, 105, 122-128], and on single crystal samples along the a-b plane (maximum ≈ 200 S/cm) [124, 129] are acceptable for using such materials as SOFC cathodes.

E. Boehm et al have shown the conductivity variation *vs.* temperature for $Ln_2NiO_{4+\delta}$ (Ln = La, Nd and Pr) compounds, as shown in **Fig. 10** [85]. Note that the electrical conductivity of praseodymium nickelate (Pr) is greater than those of the corresponding neodymium (Nd) and lanthanum (La) one in the whole temperature range. In the same figure, it is evidenced that the conductivity of the compounds in the $Nd_{2-x}NiO_{4+\delta}$ series (x = 0, 0.05, 0.10) at 700 ° C varies within a relatively wide range on the order of 35 to 100 S cm^{-1}.

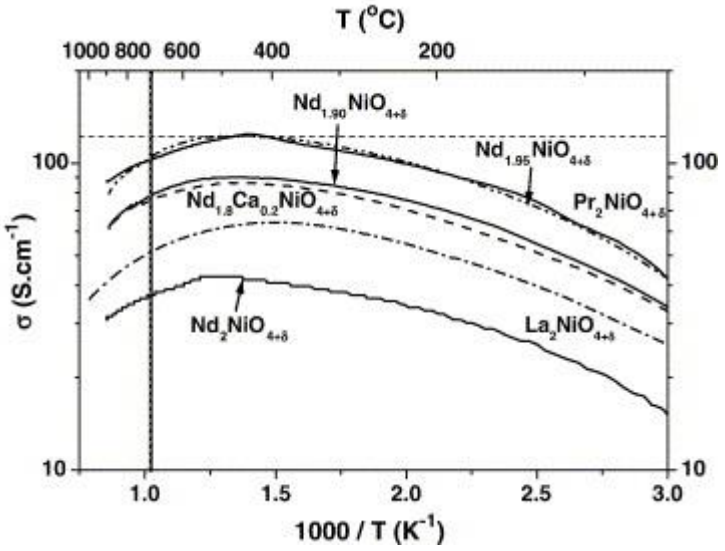

Fig. 10 Electrical conductivity as a function of temperature for $Ln_2MO_{4+\delta}$ [85].

Moreover, the variation of the total electrical conductivity vs. 1000/T under air for $La_{2-x}Pr_xNiO_{4+\delta}$ compounds was recently reported by Vibhu et al. (**Fig. 11**) [65].

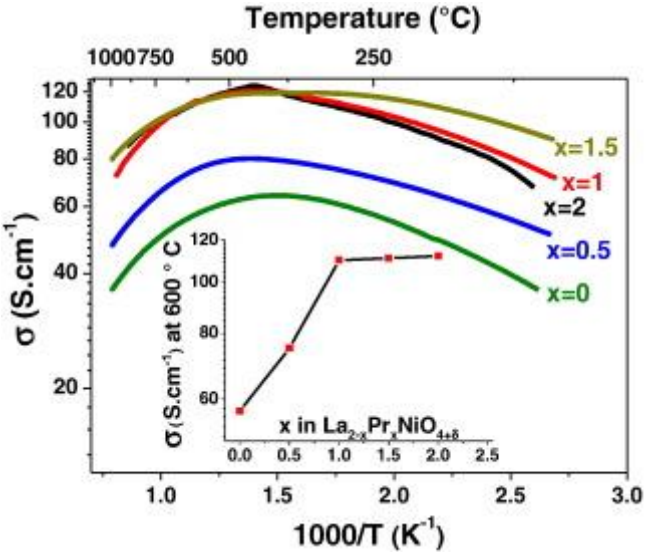

Fig. 11 Thermal variation of the electrical conductivity measured under air for $La_{2-x}Pr_xNiO_{4+\delta}$ [65].

The mixed nickelates also present a semi-conducting behavior for T < 600 °C, with a maximum of conductivity observed in the 400–600 °C range. A small addition of Pr in $La_2NiO_{4+\delta}$ (x = 0.5) leads to a moderate increase of the conductivity (from 50 to 70 S cm^{-1} at 600 °C). However, for x = 1, 1.5 or 2, (i.e. high praseodymium contents), the conductivity

increases more largely reaching a value close to 110 S cm^{-1} at 600 °C for the three compositions (inset in **Fig. 11**).

2.1.3. Current development on $Ln_2NiO_{4+\delta}$ (Ln = La and Pr) for SOFC application

Therefore, on basis of these above specific features (ionic and electronic transport), $Ln_2NiO_{4+\delta}$ has gained a large interest as cathode material for SOFC during the last few years. **Fig. 12** shows the Arrhenius plots of R_{pol} for $Ln_2NiO_{4+\delta}$ (Ln = La, Pr and Nd) based electrodes included in a symmetrical cell ($Ln_2NiO_{4+\delta}$ / YSZ / $Ln_2NiO_{4+\delta}$) [130]. The R_{pol} values are measured by electrochemical impedance spectroscopy and defined as:

$$R_{pol} = R_{electrode} \times S/2 \quad (1.8)$$

where $R_{electrode}$ is measured from the difference between the value of the low frequency and high intercept of the electrode characteristic on the real axis and S is the electrode surface area.

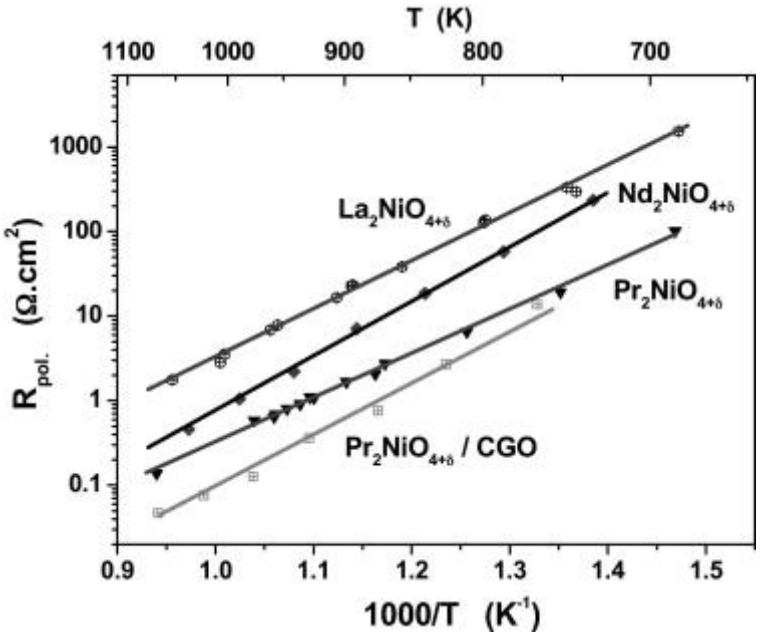

Fig. 12 Arrhenius plots of R_{pol} for $Ln_2NiO_{4+\delta}$ (Ln = La, Nd and Pr) cathodes in symmetrical cells (electrode/YSZ/electrode) [130].

Pr phase exhibits the smallest polarization R_{pol} resistances. The quite poor electrochemical performance of $La_2NiO_{4+\delta}$ deposited on YSZ electrolyte and heated at high temperature is partly due to the formation of the insulating pyrochlore-type oxide $La_2Zr_2O_7$ [131]. An addition of a ceria layer as a diffusion barrier is beneficial as shown in **Fig. 12**. The variations of the measured polarization resistance, R_p, for $La_{2-x}Pr_xNiO_{4+\delta}$ electrodes at different

temperatures and as a function of x are shown in **Fig. 13** [65]. The electrochemical performance is notably improved irrespective of the temperature of measurement when La is substituted by Pr. For instance, an R_{pol} value of 0.93 Ω cm^2 is achieved at 600 °C for $La_2NiO_{4+\delta}$ while after substitution of La by Pr, the R_{pol} values decrease down to 0.37, 0.29, 0.23 and 0.15 Ω cm^2 for $La_{1.5}Pr_{0.5}NiO_{4+\delta}$, $LaPrNiO_{4+\delta}$, $La_{0.5}Pr_{1.5}NiO_{4+\delta}$ and $Pr_2NiO_{4+\delta}$, respectively (**Fig. 13**).

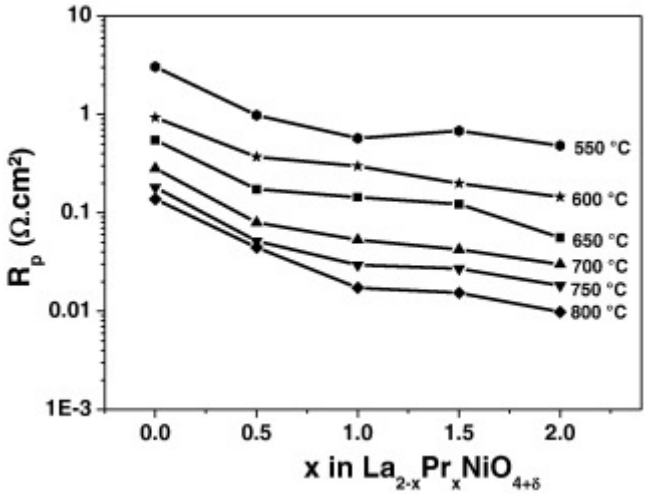

Fig. 13 Composition dependence of the polarization resistance, R_p, for $La_{2-x}Pr_xNiO_{4+\delta}$ phases in the 550 °C to 800 °C temperature range [65].

Recently, the preparation of composite SOFC cathodes via the infiltration of a MIEC oxide in an ionic conductor backbone leads to increase the electrochemical performance significantly [132, 133]. C. Nicollet et al. have prepared composite cathodes of $La_2NiO_{4+\delta}$ infiltrated into a Gd-doped ceria backbone itself deposited on CGO electrolyte, followed by adding a screen-printed layer of $LaNi_{06}Fe_{0.4}O_{3-\delta}$ current collecting. They have reported polarization resistance values down to 0.15 Ω cm^2 at 600 °C [132]. They have also prepared $Pr_2NiO_{4+\delta}$ infiltrated into a Gd-doped ceria backbone deposited on 90 µm thick YSZ electrolyte followed by the screen-printing of $LaNi_{06}Fe_{0.4}O_{3-\delta}$ current collecting layer. The polarization resistance falls down to 0.075 Ω cm^2 at 600 °C [133].

2.1.4. Chemical compatibility and stability

Cathode materials must show both good chemical stability and compatibility with the electrolyte (YSZ, CGO, LSGM) to be used as IT-SOFC air electrode. First, the thermal expansion coefficients (TEC) of the cathode materials must be close to that of electrolyte, to

ensure thermomechanical compatibility at the electrode / electrolyte interface at the required temperature during the SOFC operation. The TECs of K_2NiF_4-type materials are close to the ones of the most commonly used electrolytes, as given in **Tables 3** and **4**, respectively.

Table 3. TEC values of some nickelates with K_2NiF_4 structure

Cathode materials	Temperature range (ºC)	TEC values (10^{-6} K^{-1})	Reference
$La_2NiO_{4+\delta}$	20-1000	13.0	107
$La_2NiO_{4+\delta}$	75-900	13.8	69
$Pr_2NiO_{4+\delta}$	20-1000	13.6	107

Table 4. Mean TEC values of some solid electrolytes

Electrolyte materials	Temperature range (ºC)	TEC values (10^{-6} K^{-1})	Reference
YSZ	600-1000	10.5-10.8	108-134
CGO	600-1000	12.2	107
LSGM	600-1000	10.1	107

As a second requirement the cathode materials must not react with the electrolyte over the desired operating period of time and temperature range. Presence of secondary phases may lower the performance of the cell by affecting the conduction in particular at the cathode / electrolyte interface. Several authors have studied the compatibility of $Ln_2NiO_{4+\delta}$ (Ln = La, Pr and Nd) compounds with electrolytes such as with 8YSZ and CGO. For instance, a mixture of $La_2NiO_{4+\delta}$ and YSZ powder in the weight ratio 1/1, gives secondary phases like pyrochlore, $La_2Zr_2O_7$ and perovskite, $LaNiO_3$, after the heat treatment of 5 days at 800 ºC. The same mixture treated at lower temperature (≤ 700 ºC) for the same duration has not shown the formation of any secondary phases [107]. Chemical stability of $Ln_2NiO_{4+\delta}$ in air and under different partial pressures of oxygen was studied at several temperatures [135]. Decomposition of $La_2NiO_{4+\delta}$ in La_2O_3 and Ni at high temperature (T > 900 ºC) in a reducing atmosphere or under very low oxygen partial pressures has been reported in literature [136-138]. $La_2NiO_{4+\delta}$ remains stable under the operating conditions of the cathode, T ≤ 700 °C and

$p_{O_2} \geq 0.2$ atm. Recently, Vibhu et al. have studied the stability of $La_{2-x}Pr_xNiO_{4+\delta}$ (x = 0, 0.5, 1 and 2) [139]. They have reported the high thermal stability of La-rich phases ($x = 0$ and $x = 0.5$). No additional XRD peaks were observed. On the contrary, from $x = 1$ to $x = 2$, the XRD patterns of the aged $La_{2-x}Pr_xNiO_{4+\delta}$ samples show the appearance of new peaks attributed to the (La, Pr)$NiO_{3-\delta}$, (La, Pr)$_4Ni_3O_{10+\delta}$ and Pr_6O_{11} phases, of which amount depends on both the Pr content as well as the ageing temperature. At 600 °C, a complete decomposition of pure $Pr_2NiO_{4+\delta}$ into $PrNiO_{3-\delta}$ and Pr_6O_{11} was observed. Whereas at 700 °C and 800 °C, the higher order Ruddlesden-Popper $Pr_4Ni_3O_{10+\delta}$ phase was also observed.

2.2. Higher order RP phases $La_{n+1}Ni_nO_{3n+1}$ (n =2 and 3)

Higher order RP phases, $La_3Ni_2O_{7+\delta}$ (n = 2) and $La_4Ni_3O_{10-\delta}$ (n = 3), have also attracted some attention for their possible use as SOFC cathode because of their superior electrical conductivity and good long-term stability in intermediate temperature range. For example, $La_3Ni_2O_{7+\delta}$ and $La_4Ni_3O_{10-\delta}$ have shown long-term thermal stability at 850 °C for 2 weeks in air contrary to $La_2NiO_{4+\delta}$ [69]. However, higher order RP phases, in particular, $La_3Ni_2O_{7+\delta}$ and $La_4Ni_3O_{10-\delta}$, are difficult to synthesize as pure phases because of the requirement of prolonged heating and reheating procedures at quite low temperatures [69, 76]. Such compounds can easily loose or gain oxygen [71, 72, 76] as well as form mixed intergrowths between the different terms [72, 140-142]. As consequence, this leads to difficulty in synthesize them with high purity. Hence, they are very sensitive to temperature and oxygen partial pressure as already reported by Zinkevich's and Bannikov's groups [133, 134, 143]. However, various techniques have been used to synthesize the higher order RP phases such as: single-step heat treatment of nano-sized metal hydroxide co-crystallites [144], spray pyrolysis [145] and pulsed injection metal-organic chemical vapour deposition (PI-MOCVD) [146]. Obtaining dense bulk samples higher order RP phases is also challenging.

Normally, for a standard ceramic preparation, the as-prepared $La_3Ni_2O_{7+\delta}$ and $La_4Ni_3O_{10-\delta}$ samples exhibit the oxygen content of 6.93-6.95 and 9.78-9.83, respectively [69, 136]. The structures of both materials, $La_3Ni_2O_{7+\delta}$ and $La_4Ni_3O_{10-\delta}$, generally are considered in tetragonal or orthorhombic symmetries [72, 76]. The structure of $La_3Ni_2O_{7+\delta}$ was found to vary with a wide range of oxygen stoichiometry (δ = 0, -0.08, -0.16 and -0.65) from orthorhombic (*Fmmm*) to tetragonal structure (*I4/mmm*) [76, 143]. For example, $La_3Ni_2O_{6.92}$ is reported in the *Fmmm* space group, but the phase with $\delta = 0.35$ is tetragonal *I4*/mmm [143].

A wide range of oxygen stoichiometry from 9.78 to 10.12 had been also reported for $La_4Ni_3O_{10-\delta}$ (n =3) by Carvalho *et al.* [147] for samples prepared under various oxidation and reduction processes. It is noticeable that for the high RP terms, $La_3Ni_2O_{7+\delta}$ (n = 2) and $La_4Ni_3O_{10-\delta}$ (n = 3) are usually considered as predominantly oxygen-deficient compounds (dominant by oxygen vacancies) rather than oxygen-excess ones (by interstitial, compared to $La_2NiO_{4+\delta}$ (n = 1) [69, 82]. The oxidation states of Ni for the oxygen stoichiometric compounds can be represented as $La_2(Ni^{2+})_1O_4$, $La_3(Ni^{2+})_1(Ni^{3+})_1O_7$, and $La_4(Ni^{2+})_1(Ni^{3+})_2O_{10}$ [143]. It means that the nickel average oxidation state in $La_2NiO_{4+\delta}$ is predominantly Ni^{2+}, then it increases with increasing n value from Ni^{2+} to Ni^{3+}. This variation of the average nickel oxidation state can be significantly influenced by oxygen content, and as a consequence, can presumably modify the physical properties.

2.2.1. Current development in higher Order RP phases for SOFC application

In higher order $La_{n+1}Ni_nO_{3n+1}$ (n= 2 and 3) RP phases, charge transport occurs via both holes and electrons whereas for n = ∞, only electrons are responsible of the electronic conduction [148]. Electronic transport in $La_{n+1}Ni_nO_{3n+1}$ depends to a large extent on the number of perovskite blocks (n) and gradually vary from a semiconducting to a metallic behavior upon increasing n [72, 73, 141,148].

Electrochemical properties of these materials have been studied by some researchers in symmetrical cells on various different electrolytes. For example, Amow *et al.* studied the symmetrical cells of these materials deposited on LSGM electrolyte. The polarization resistance (R_p) decreases with increasing n values and $La_4Ni_3O_{10-\delta}$ ($\delta = 0.22$) shows the lowest R_p value (~1 Ω cm^2) at 800 °C. However, it is still much higher than the desired value of 0.15 Ω cm^2 expected by Steele and Heinzel [1]. Nevertheless, the electrode performance of the higher order RP-phase $La_{n+1}Ni_nO_{3n+1}$ (n = 2 and 3) could be probably improved by further optimizing their microstructure.

More recently, further studies on the electrode performance of the series of RP phase have been performed. For instance, properties of the electrode/electrolyte/electrode cells with $La_3Ni_2O_{7+\delta}$ deposited on a samarium-oxide-doped ceria $Ce_{0.8}Sm_{0.2}O_{2-\delta}$ (SDC) + 2% Co as electrolyte has been studied by Pérez-Coll*et al.* [77] in the 700-900 °C temperature range: The corresponding R_p value is lower than that of a $La_2NiO_{4+\delta}$ electrode. Furthermore, Takahashi *et al*. [67] investigated the single fuel cell (Ni–SDC (anode) / SDC (electrolyte) / $La_{n+1}Ni_nO_{3n+1}$ (cathode)) performance for the n = 1, 2 and 3 members of RP-phase lanthanum nickel oxides at 500-700 °C. The authors noticed that the overpotential losses decreased with increasing n

value whereas electrical conductivity increases with increasing n, which is in good accordance with the results reported by Amow *et al*. [69]. $La_4Ni_3O_{10-\delta}$ exhibited better cathode properties than those of the lower members at 700 °C. Maximum power density of 10.2, 36.5, and 88.2 mW cm^{-2} at 500, 600 and 700 °C has been found, respectively. In comparison to conventional perovskite cathodes, the power density values are still relatively low. The results indicate that the performance of $La_3Ni_2O_{7+\delta}$ and $La_4Ni_3O_{10-\delta}$ electrodes is improved over $La_2NiO_{4+\delta}$. Lou *et al*. [149] investigated $La_3Ni_2O_{7+\delta}$ /YSZ cathode and found a promising R_p value of 0.39 Ω cm^2 at 750 °C. They have also reported that a single cell of NiO-YSZ//YSZ// $La_3Ni_2O_{7+\delta}$ had a maximum power density of 848 mW cm^{-2} at 750 °C.

A few recent studies have also been reported for RP based composite-type cathodes. Yoo *et al*. have studied the $La_{n+1}Ni_nO_{3n+1}$ (n = 1, 2 and 3)-YSZ composites prepared by infiltrating $La_{n+1}Ni_nO_{3n+1}$ (n = 1, 2 and 3) into YSZ scaffolds [82]. They have reported an increasing cathode performance with increasing n number, and therefore, it seems that $La_4Ni_3O_{10-\delta}$-YSZ is a promising composite cathode for IT-SOFC. Most recently, Woolley and Skinner [150] studied a series of novel $La_2NiO_{4+\delta}/La_4Ni_3O_{10-\delta}$ composites cathodes deposited on LSGM electrolyte with the objective of utilizing the complementary properties of each: high ionic conductivity of $La_2NiO_{4+\delta}$ and high electronic conductivity of $La_4Ni_3O_{10-\delta}$. They have reported that a 50:50 wt. % $La_2NiO_{4+\delta}$: $La_4Ni_3O_{10-\delta}$ mix gives the best R_p of 0.62 Ω cm^2 at 700 °C. They further studied the functionally graded composite based on $La_2NiO_{4+\delta}$ and $La_4Ni_3O_{10-\delta}$. They have reported further improvement in the R_p, 0.52 Ω cm^2 at 700°C for cathode consisting of compact $La_2NiO_{4+\delta}$ layer followed by porous 50:50 wt.% $La_2NiO_{4+\delta}$: $La_4Ni_3O_{10-\delta}$ further followed by denser layer of $La_4Ni_3O_{10-\delta}$ on LSGM electrolyte.

Based on the data reported in literature, microstructure, interface and architectural design of electrode are crucial on the control of the electrochemical performance. Optimization of such microstructural parameters for cathodes based on layered Ruddlesden-Popper (RP) type materials such as $La_{2-x}Pr_xNiO_{4+\delta}$, $0 \leq x \leq 2$ and $La_{n+1}Ni_nO_{3n+1}$ (n=2 and 3) as well as their composites with CGO, is a real challenge and it is the main theme of this PhD work.

References:

[1] B. C. H. Steele, A. Heinzel, *Nature*, 414 (2001) 345-352.
[2] M.V. Twigg, Catalyst Handbook, Wolfe Publishing Ltd., 2en edition, (1989).
[3] A. Weber, "Transport and reaction mechanism in a SOFC". Available from: http://www.iam.kit.edu/wet/english/mitarbeiter-sofc.php.
[4] E. D. Wachsman, K. T. Lee, *Science*, 334 (2011) 935-939.
[5] D. J. L. Brett, A. Atkinson, N. P. Brandon, S. J. Skinner, *Chem. Soc. Rev.*, 37 (2008) 1568-1578.
[6] N.P. Brandon, S.J. Skinner, B.C.H. Steele, *Annual Review of Materials Research*, 33 (2003) 183-213.
[7] S.B. Adler, *Chemical Reviews*, 104 (2004) 4791-4843.
[8] S. M. Haile, *Acta Mater.*, 51 (2003)5981–6000.
[9] A. J. Jacobson, *Chem. Mater.*, *22* (2010) 660–674.
[10] N. Q. Minh, T. Takahashi, Science and Technology of Ceramic Fuel Cells, *Elsevier Science Oxford*, UK, 1995.
[11] S. C. Singhal, *Solid State Ionics*, 152–153 (2002) 405–410.
[13] S. P. S. Badwal, *Solid State Ionics*, 52 (1992) 23–32.
[12] W. Tinglian, L. Xiaofei, K. Chukun, W. Weppner, *Solid State Ionics*, 18-19 (1986) 715–719.
[14] O. Yamamoto, Y. Arachi, H. Sakai, Y. Takeda, N. Imanishi, Y. Mizutani, M. Kawai, Y. Nakamura, *Ionics*, 4 (1998)403–408.
[15] J. W. Fergus, *J. Power Sources*, 162 (2006) 30–40.
[16] J. A. Kilner, *Solid State Ionics*, 6 (1982) 237–252.
[17] M. Morales, J. J. Roa, X. G. Capdevila, M. Segarra, S. Pinol, *Acta Materialia*, 58 (2010) 2504–2509.
[18] S. P. S. Badwal, *Solid State Ionics*, 143 (2001) 39–46.
[19] Z. Duan, M. Yang, A. Yan, Z. Hou, Y. Dong, Y. Chong, M. Cheng, W. Yang, *Journal of Power Sources*, 160 (2006) 57–64.
[20] G. C. Kostogloudis, G. Tsiniarakis, C. Ftikos, *Solid State Ionics*, 135 (2000) 529–535.
[21] J. M. A. van Roosmalen, E. H. P. Cordfunke, *Solid State Ionics*, 52 (1992) 303–312.
[22] A. M. Hernandez, L. Mogni, A. Caneiro, *International Journal of Hydrogen Energy*, 35 (2010) 6031–6036.
[23] C. Brugnoni, U. Ducati, M. Scagliotti, *Solid State Ionics*, 76 (1995) 177–182.
[24] G. Chiodelli, M. Scagliotti, *Solid State Ionics*, 73 (1994) 265–271.
[25] H. Y. Lee, S. M. Oh, *Solid State Ionics*, 90 (1996) 133–140.
[26] A. Mitterdorfer, L. J. Gauckler, *Solid State Ionics*, 111 (1998) 185–218.
[27] B. C. H. Steele, *Solid State Ionics*, 129 (2000) 95–110.
[28] B. C. H. Steele, *Solid State Ionics*, 129 (2000) 95–110.
[29] M. Mogensen, N. M. Sammes, G. A. Tompsett, *Solid State Ionics*, 129 (2000) 63–94.
[30] D. Pérez-Coll, P. Núñez, J. R. Frade, and J. C. C. Abrantes, *Electrochim. Acta*, 48 (2003) 1551–1557.
[31] M. Han, X. Tang, H. Yin, and S. Peng, *J. Power Sources*, 165 (2007) 757–763.
[32] V. Dusastre, J. A. Kilner, *Solid State Ionics*, 126 (1999) 163–174.
[33] L. Qiu, T. Ichikawa, A. Hirano, N. Imanishi, Y. Takeda, *Solid State Ionics*, 158 (2003) 55–65.
[34] J. M. Ralph, C. Rossignol, R. Kumar, *Journal of the Electrochemical Society*, 150 (2003) A1518–A1522.

[35] J. M. Ralph, A. C. Schoeler, M. Krumpelt, *Journal of Materials Science*, 36 (2001) 1161–1172.
[36] D. Waller, J. A. Lane, J. A. Kilner, B. C. H. Steele, *Solid State Ionics*, 86-88 (1996) 767–772.
[37] M. Izuki, M. E. Brito, K. Yamaji, H. Kishimoto, D. H. Cho, T. Shimonosono, T. Horita, H. Yokokawa, *Journal of Power Sources*, 196 (2011) 7232–7236.
[38] E. Ivers-Tiffe, A. Weber, D. Herbstritt, *Journal of the European Ceramic Society*, 21 (2001) 1805–1811.
[39] S. P. S. Badwal, F. T. Ciacchi, J. Drennan, *Solid State Ionics*, 121 (1999) 253–262.
[40] H. Inaba, H. Tagawa, *Solid State Ionics*, 83 (1996) 1–16.
[41] T. Takeyama, N. Takahashi, T. Nakamura, S. Itoh, *Surface Coating Technology*, 16 (2006) 4797-4801.
[42] I. Taniguchi, R.C. Van Landschoot, J. Shoonmann, *Solid State Ionics*, 160 (2003) 119-123.
[43] J.B. Goodenough, Proceedings of the Royal Society of London. Series A, Mathematical and Physical Sciences, 393 (1984), 215-234.
[44] A. Orera, P. R. Slater, New Chemical Systems for Solid Oxide Fuel Cells, *Chem. Mater.*, *22* (2010) 675–690.
[45] A. Aguadero, L. Fawcett, S. Taub, R. Woolley, K.T., Wu, N. Xu, J.A. Kilner, S.J. Skinner, *Jouranl of Materials Science*, 47 (2012) 3925-3948.
[46] S.P. Jiang, S.H. Chan, *Journal of Materials Science*, 39 (2004) 4405-4439.
[47] J.B. Goodenough, Y.-H. Huang, *Journal of Power Sources*, 173 (2007) 1-10.
[48] H. Kim, C. Lu, W. L. Worrell, J. M. Vohs, R. J. Gorte, *Journal of the Electrochemical Society*, 149 (3) (2002) A247–A250.
[49] X. F. Ye, S. R. Wang, J. Zhou, F. R. Zeng, H. W. Nie, T. L. Wen, *Journal of Power Sources*, 195 (2010) 7264–7267.
[50] O'Hayre, R. et al., Fuel cell fundamentals, 2nd ed. 2009.
[51] T. Kawada, Perovskite Oxide for Cathode of SOFCs, in Perovskite Oxide for Solid Oxide Fuel Cells, T. Ishihara, Editor. 2009, Springer. 147-166.
[52] C. Sun, R. Hui, J. Roller, *J. Solid State Electrochem*, 14(2009) 1125-1144.
[53] J. Fleig, H.L. Tuller, J. Maier, *Solid State Ionics*, 174 (2004) 261-270.
[54] A. Weber, E. Ivers-Tiffe, *Journal of Power Sources*, 127 (2004) 273-283.
[55] S. J. Skinner, *International Journal of Inorganic Materials*, 3 (2001) 113–121.
[56] S. J. Skinner, J. A. Kilner, *Materials Today*, 6 (2003) 30-37.
[57] S. Y. Istomin, E. V. Antipov, *Russian Chemical Reviews*, 82 (2013) p.686.
[58] S. R. Sehlin, H. U. Anderson, D. M. Sparlin, *Solid State Ionics*, 78 (1995) 235–243.
[59] A. N. Petrov, O. F. Kononchuk, A. V. Andreev, V. A. Cherepanov, P. Kofstad, *Solid State Ionics*, 80 (1995) 189–199.
[60] A. V. Berenov, A. Atkinson, J. A. Kilner, E. Bucher, W. Sitte, *Solid State Ionics*, 181 (2010) 819–826.
[61] H. Abe, K. Murata, T. Fukui, W.J. Moon, K. Kaneko, M. Naito, *Fuel Cells Bulletin*, 3 (2006) 12-15.
[62] A. Petric, P. Huang, F. Tietz, *Solid State Ionics*, 135 (2000) 719–725.
[63] S. -I. Hashimoto, Y. Fukuda, M. Kuhn, K. Sato, K. Yashiro, J. Mizusaki, *Solid State Ionics*, 181 (2010) 1713–1719.
[64] S. Carter, A. Selcuk, R. J. Chater, J. Kajda, J. A. Kilner, B. C. H Steele, *Solid State Ionics*, 53-56 (1992) 597–605.
[65] V. Vibhu, A. Rougier, C. Nicollet, A. Flura, J.-C. Grenier, J.-M. Bassat, *Solid State Ionics*, 278 (2015) 32–37.

[66] A. Tarancón, M. Burriel, J. Santiso, S. J. Skinner, J. A. Kilner, *J. Mater. Chem.*, 20 (2010) 3799-3813.
[67] S. Takahashi, S. Nishimoto, M. Matsuda, M. Miyake, *Journal of the American Ceramic Society*, 93 (2010) 2329-2333.
[68] G. Amow, S. J. Skinner, *Journal of Solid State Electrochemistry*, 10 (2006) 538-546.
[69] G. Amow, I. J. Davidson, S. J. Skinner, *Solid State Ionics*, 177 (2006) 1205-1210.
[70] G. Kim, S. Wang, A. J. Jacobson, C. L. Chen, *Solid State Ionics*, 177 (2006), 1461-1467.
[71] M. Greenblatt, *Current Opinion in Solid State and Materials Science*, 2 (1997) 174-83.
[72] Z. Zhang, M. Greenblatt, *Journal of Solid State Chemistry*, 117 (1995) 236-246.
[73] M. Greenblatt, Z. Zhang, M. H. Whangbo, *Synthetic Metals*, 85 (1997) 1451-1452.
[74] Y. Kobayashi, S. Taniguchi, M. Kasai, M. Sato, T. Nishioka, M. Kontani, *Journal of the Physical Society of Japan*, 65 (1996), 3978-3982.
[75] S. Taniguchi, T. Nishikawa, Y. Yasui, Y. Kobayashi, J. Takeda, S. I. Shamoto, M. Sato, *Journal of the Physical Society of Japan*, 64 (1995), 1644-1650.
[76] Z. Zhang, M. Greenblatt, J. B. Goodenough, *Journal of Solid State Chemistry*, 108 (1994) 402-409.
[77] D. Pérez-Coll, A. Aguadero, M. J. Escudero, L. Daza, *Journal of Power Sources*, 192 (2009) 2-13.
[78] M. D. Carvalho, M. M. Cruz, A. Wattiaux, J. M. Bassat, F. M. A. Costa, M. Godinho, *Journal of Applied Physics*, 88 (2000) 544-549.
[79] S. A. Nedilko, V. A. Kulichenko, A. G. Dziazko, E. G. Zenkovich, *Journal of Alloys and Compounds*, 367 (2004) 251-254.
[80] Z. Zhang, M. Greenblatt, *Journal of Solid State Chemistry*, 111.1 (1994) 141-146.
[81] J.M. Bassat, M. Burriel, O. Wahyudi, R. Castaing, M. Ceretti, P. Veber, I. Weill, A. Villesuzanne, J.C. Grenier, W. Paulus, J.A. Kilner, *The Journal of Physical Chemistry C*, 117 (2013) 26466-26472.
[82] S. Yoo, S. Choi, J. Shin, M. Liu, G. Kim, *RSC Advances*, 2 (2012) 4648-4655.
[83] V. V. Kharton, A. P. Viskup, E. N. Naumovkh, F. M. B. Marques, *Journal of Materials Chemistry*, 9 (1999) 2623–2629.
[84] S. J. Skinner, J. A. Kilner, *Solid State Ionics*, 135 (2000) 709–712.
[85] E. Boehm, J. -M. Bassat, P. Dordor, F. Mauvy, J. -C. Grenier, P. Stevens, *Solid State Ionics*, 176 (2005) 2717–2725.
[86] M. L. Fontaine, C. Laberty-Robert, M. Verelst, J. Pielaszeck, P. Lenormand, F. Ansart, P. Tailhades, *Materials Research Bulletin, 41* (2006) 1747-1753.
[87] M.L. Fontaine, C. Laberty-Robert, A. Barnabé, F. Ansart, P. Tailhades, *Ceramics International*, 30 (2004) 2087-98.
[88] M.L. Fontaine, C. Laberty-Robert, F. Ansart, P. Tailhades, *Journal of Solid State Chemistry*, 177 (2004) 1471-1479.
[89] A. Podpirka, V. Balakrishnan, S. Ramanathan, *Journal of Materials Research*, 28 (2013) 1420-1431.
[90] D. Telesca, B. O. Wells, B. Sinkovic, *Surface Science 606*, 9 (2012) 865-871.
[91] G. T. Kim, S. Wang, A.J. Jacobson, Z. Yuan, C. Chen, *Journal of Materials Chemistry*, 17 (2007) 1316-20.
[92] G. Garcia, M. Burriel, N. Bonanos, J. Santiso, *Journal of the Electrochemical Society*, 155 (2008) 28-32.
[93] V. Faucheux, S. Pignard, M. Audier, *Journal of Crystal Growth*, 275 (2005) 947-951.
[94] M. Hücker, K. Chung, M. Chand, T. Vogt, J. M. Tranquada, D. J. Buttrey, *Physical Review B*, 70 (2004) 064105.
[95] S. J. Skinner, *Solid State Sciences 5*, 3 (2003) 419-426.

[96] W. Paulus, A. Cousson, G. Dhalenne, J. Berthon, A. Revcolevschi, S. Hosoya, W. Treutmann, G. Heger, R. Le Toquin, *Solid State Sciences 4*, 5 (2002) 565-573.
[97] G. Burns, F. H. Dacol, D. E. Rice, D. J. Buttrey, M. K. Crawford, *Physical Review B*, 42 (1990) 10777.
[98] J. Rodriguez-Carvajal, M. T. Fernandez-Diaz, J. L. Martinez, *Journal of Physics: Condensed Matter* 3.19 (1991) 3215.
[99] C. Allançon, A. Gonthier-Vassal, J. M. Bassat, J. P. Loup, P. Odier, *Solid State Ion*, 74 (1994) 239–248.
[100] C. Allançon, J. Rodriguez-Carvajal, M. T. Fernandez-Diaz, P. Odier, J. M. Bassat, J. P. Loup, J. L. Martinez, *Zeitschrift fur Physik B-Condensed Matter*, 100 (1996) 85–90.
[101] K. Ishikawa, K. Metoki, H. Miyamoto, *J. Solid State Chem.*, 182 (2009) 2096–2103.
[102] P. Odier, J. M. Bassat, J. C. Rifflet, J. P. Loup, *Solid State Communications*, 85 (1993) 561–564.
[103] C. Allançon, P. Odier, J. M. Bassat, J. P. Loup, *Journal of Solid State Chemistry*, 131 (1997) 167–172.
[104] M. T. Fernandez-Diaz, J. L. Martinez, J. Rodriguez-Carvajal, *Solid State Ionics*, 63-65 (1993) 902–906.
[105] A. Aguadero, J. A. Alonso, M. J. Martínez-Lope, M. T. Fernández-Díaz, M. J. Escudero, L. Daza, *J. Mater. Chem.***,** 16 (2006) 3402-3408.
[106] A. Demourgues, A. Wattiaux, J. C. Grenier, M. Pouchard, J. L. Soubeyroux, J. M. Dance, P. Hagenmuller, *Journal of Solid State Chemistry*, 105 (1993) 458-468.
[107] E. Boehm, PhD Thesis University of Bordeaux I, France (2002).
[108] C. Li, T. Hu, H. Zhang, Y. Chen, J. Jin, N. Yang, *Journal of Membrane Science*, 226 (2003) 1-7.
[109] E. Iguchi, H. Satoh, H. Nakatsugawa, F. Munakata, *Physica B: Condensed Matter*, 270 (1999) 332-340.
[110] N. Poirot, P. Odier, P. Simon, F. Gervais, *Solid State Sciences*, 5 (2003) 735-739.
[111] J.M. Bassat, P. Odier, A. Villesuzanne, C. Marin, M. Pouchard, *Solid State Ionics***,** (2004) 341–347.
[112] M. Yashima, M. Enoki, T. Wakita, R. Ali, Y. Matsushita, F. Izumi, T. Ishihara, *Journal of the American Chemical Society*, 130 (2008) 2762–2763.
[113] L. Minervini, R. W. Grimes, J. A. Kilner, K. E. Sickafus, *Journal of Materials Chemistry*, 10 (2000) 2349–2354.
[114] M. Burriel, H. Téllez, R.J. Chater, R. Castaing, P. Veber, M. Zaghrioui, T. Ishihara, J.A. Kilner, J.M. Bassat, *The Journal of Physical Chemistry C*, 120 (2016)17927-38.
[115] M.A. Dragan, PhD Thesis, RWTH Aachen, Germany (2006) .
[116] J.A Kilner, C.K.M Shaw, *Solid State Ionics***,** 154 (2002) 523–527.
[117] M.L. Fontaine, PhD Thesis University of Toulouse III, France (2004).
[118] E. Boehm, J. M. Bassat, M. C. Steil, P. Dordor, F. Mauvy, J. C. Grenier, *Solid State Sciences*, 5 (2003) 973-981.
[119] S.J Skinner, J.A Kilner, *Solid State Ionics*, 135 (2000) 709–712.
[120] F. Mauvy, J.M. Bassat, E. Boehm, P. Dordor, J.C. Grenier, J.P. Loup, *Journal of the European Ceramic Society*, 24 (2004) 1265-1269.
[121] F. Mauvy, J.M. Bassat, E. Boehm, J.P. Manaud, P. Dordor, J.C. Grenier, *Solid State Ionics*, 158 (2003) 17-28.
[122] M. Sayer, P. Odier, *Journal of Solid State Chemistry***,** 67 (1987) 26–36.
[123] J.M. Bassat, J. P. Loup, P. Odier, *J. Phys.: Condens. Matter*, 6 1994) 8285.
[124] C.N.R. Rao, D.J. Buttrey, N. Otsuka, P. Ganguly, H.R. Harrison, C.J. Sandberg, J.M. Honig, *Journal of Solid State Chemistry***,** 51 (1984) 266–269.

[125] J.M. Bassat, F. Gervais, P. Odier, J.P. Loup, *Materials Science and Engineering: B*, 3 (1989) 507–514.
[126] H. Tamura, A. Hayashi, Y. Ueda, *Physica C: Superconductivity*, 216 (1993) 83-88.
[127] K. Ishikawa, W. Shibata, K. Watanabe, T. Isonaga, M. Hashimoto, Y. Suzuki, *Journal of Solid State Chemistry*, 131 (1997) 275–281.
[128] V. Vashook, S.P Tolochko, I.I Yushkevich, L.V Makhnach, I.F Kononyuk, H Altenburg, J Hauck, H Ullmann, *Solid State Ionics*, 110 (1998) 245–253.
[129] K. Dembinski, J. M. Bassat, J. P. Coutures, P. Odier, *Journal of Materials Science Letters*, 6 (1987) 1365-1367.
[130] C. Ferchaud, J.C. Grenier, Y. Zhang-Steenwinkel, M.M. Van Tuel, F.P. Van Berkel, J.M. Bassat, *Journal of Power Sources*, 196 (2011) 1872–1879.
[131] A. Aguadero, J.A. Alonso, M.J. Escudero, L. Daza, *Solid State Ionics*, 179 (2008) 393–400.
[132] C. Nicollet, A. Flura, V. Vibhu, A. Rougier, J.M. Bassat, J.C Grenier, *Journal of Power Sources*, 294 (2015) 473-482.
[133] C. Nicollet, A. Flura, V. Vibhu, S. Fourcade, A. Rougier, J.M. Bassat, J.C Grenier, *Journal of Solid State Electrochemistry*, (2016) 1-8.
[134] S. Zha, Y. Zhang, M. Liu, *Solid State Ionics*, 176 (2005) 25-31.
[135] A. Flura, S. Dru, C. Nicollet, V. Vibhu, S. Fourcade, E. Lebraud, A. Rougier, J.M. Bassat, J.C. Grenier, *Journal of Solid State Chemistry*, 228 (2015)189-98.
[136] D.O. Bannikov, V.A. Cherepanov, *Journal of Solid State Chemistry*, 179 (2006) 2721-2727.
[137] M. Zinkevich, F. Aldinger, *Journal of Alloys and Compounds*, 375 (2004) 147-161.
[138] V.A. Cherepanov et al., *Russian Journal of Physical Chemistry*, 57 (1983) 521-524.
[139] V. Vibhu, J.M. Bassat, A. Flura, C. Nicollet, J.C. Grenier, A. Rougier, *ECS Transactions*, 68 (2015) 825-835.
[140] C. N. R. Rao, A. K. Ganguli, R. Nagarajan, *Pramana*, 32 (1989) L177-L179.
[141] R. M. Ram, L. Ganapathi, P. Ganguly, C. N. R. Rao, *Journal of Solid State Chemistry*, 63 (1986) 139-147.
[142] J. Drennan, C. P. Tavares, B. C. H. Steele, *Materials Research Bulletin*, 17 (1982) 621-626.
[143] M. Zinkevich, N. Solak, H. Nitsche, M., Ahrens, F. Aldinger, *Journal of Alloys and Compounds*, 438 (2007) 92-99.
[144] X. Weng, P. Boldrin, I. Abrahams, S.J. Skinner, S. Kellici, J.A. Darr, *Journal of Solid State Chemistry*, 181 (2008) 1123-1132.
[145] T. Ryll, P. Reibisch, L. Schlagenhauf, A. Bieberle-Huetter, M. Döbeli, J.L. Rupp, L.J. Gauckler, *Journal of the European Ceramic Society*, 32 (2012) 1701-1709.
[146] M. Burriel, G. Garcia, M.D. Rossell, A. Figueras, G. Van Tendeloo, J. Santiso, *Chemistry of Materials*, 19 (2007) 4056-4062.
[147] M.D. Carvalho, A. Wattiaux, J. M. Bassat, J. C. Grenier, M. Pouchard, M. I. da Silva Pereira, F. M. A. Costa, *Journal of Solid State Electrochemistry*, 7 (2003) 700-705.
[148] K. Sreedhar, M. McElfresh, D. Perry, D. Kim, P. Metcalf, J.M. Honig, *Journal of Solid State Chemistry*, 110 (1994) 208–215.
[149] Z. Lou, J. Peng, N. Dai, J. Qiao, Y. Yan, Z. Wang, J. Wang. K. Sun, *Electrochemistry Communications*, 22 (2012) 97-100.
[150] R.J. Woolley, S.J. Skinner, *Journal of Power Sources*, 243 (2013) 790-795.

Chapter 2

An innovative architectural design to enhance the electrochemical performance of $La_2NiO_{4+\delta}$ cathodes for solid oxide fuel cell applications

R. K.Sharma, M. Burriel, L. Dessemond, V. Martin, J.-M. Bassat and E. Djurado, *Journal of Power Sources*, 2016, 316, 17-28.
DOI: http://dx.doi.org/10.1016/j.jpowsour.2016.03.067

An innovative architectural design to enhance the electrochemical performance of $La_2NiO_{4+\delta}$ cathodes for solid oxide fuel cell applications

Rakesh K. Sharma[a, b, c], Mónica Burriel[d, e], Laurent Dessemond[a, b], Vincent Martin[a, b], Jean-Marc Bassat[c], Elisabeth Djurado[*, a, b,]

[a] Univ. Grenoble Alpes, LEPMI, 1130 rue de la Piscine, BP 75, 38402 St Martin d'Hères Cedex, France
[b] CNRS. LEPMI, F-38000 Grenoble, France
[c] CNRS, Université Bordeaux, Institut de Chimie de la Matière Condensée de Bordeaux, 87 Av. du Dr Schweitzer, 33608 PESSAC Cedex (France)
[d]Catalonia Institute for Energy Research (IREC), Department of Advanced Materials for Energy, Jardins de les Dones de Negre 1, 2nd floor, 09930-Sant Adri*á* del Bes*ò*s, Barcelona, Spain
[e] Univ. Grenoble Alpes, CNRS, LMGP, F-38000 Grenoble, France

**Corresponding author:* Elisabeth Djurado
E-mail: elisabeth.djurado@lepmi.grenoble-inp.fr, Tel: +33-476826684; Fax: +33-476826777

Abstract

An architectural design of the cathode microstructure based on combining electrostatic spray deposition (ESD) and screen-printing (SP) techniques has demonstrated to be an innovative strategy to enhance the electrochemical properties of $La_2NiO_{4+\delta}$ (LNO) as oxygen electrode on $Ce_{0.9}Gd_{0.1}O_{2-\delta}$ (CGO) electrolyte for solid oxide fuel cells. For this purpose, the influence of the ESD process parameters on the microstructure has been systematically investigated. Electrochemical performances of four selected cathode microstructures are investigated: (i) 3-D coral nanocrystalline (average particle size ~ 100 nm) LNO film grown by ESD; (ii) 3-D coral nanocrystalline film (average particle size ~ 150 nm) grown by ESD with a continuous nanometric dense interface; (iii) porous screen-printed LNO film (average particle size ~ 400 nm); and (iv) 3-D coral nanocrystalline film (average particle size ~ 150 nm) with a continuous nanometric dense interface prepared by ESD topped by a LNO current collector prepared by SP. A significant reduction in the polarization resistance (R_{pol}) is obtained (0.08 Ω.cm² at 700 °C) for 3-D coral topped by the SP layer. Moreover LNO is found to be stable and compatible with CGO up to 800 °C for only 10 days duration in air, making it potentially suitable for SOFCs cathode application.

Keywords:

$La_2NiO_{4+\delta}$, electrostatic spray deposition, SOFC cathode, electrochemical impedance spectroscopy

1. Introduction

Solid Oxide Fuel Cells (SOFCs) have drawn much attention [1-4] because they convert chemical energy into electrical energy efficiently in eco-friendly way. The degradation problems at temperatures higher than 800 °C due to a number of different processes, such as reaction between different phases, delamination and surface segregation, have become one of the main issues in their widespread commercialization. This initiated the development of intermediate temperature SOFCs (IT-SOFCs) operating at 500-700 °C, as the requirements for material selection such as thermal and chemical compatibilities are not as stringent in this temperature range in comparison to SOFCs working at higher temperatures. However, finding a suitable cathode for IT-SOFC is critical and challenging. In this context, rare earth nickelates with chemical formula $Ln_2NiO_{4+\delta}$ (Ln: La, Nd, Pr), with K_2NiF_4-type structure, the so called Ruddlesden-Popper phases (with n = 1), are promising cathode materials for IT-SOFCs, as they exhibit excellent mixed ionic and electronic conducting properties [5-8], high oxygen exchange coefficients and similar thermal expansion coefficient (TEC) to $Zr_xY_{1-x}O_{(x+3)/2}$ and $Ce_xGd_{1-x}O_{(x+3)/2}$ electrolytes[9-12]. For example for $La_2NiO_{4+\delta}$ the values of the oxygen exchange coefficient, TEC and conductivity are of 2.3 $x10^{-6}$ cm s^{-1} (700°C) [13], 13.8 x 10^{-6} K^{-1} (75 – 900 °C) [14] and 70 Scm^{-1} (700 °C), respectively [6]. In general, the electrochemical properties of the LNO cathode have been characterized through the polarization resistance (R_{pol}). Various efforts have been made to reduce the R_{pol} value. For example, Sayers [15] reported a decrease in the R_{pol} value from 7.4 to 1.0 Ω cm^2 at 700 °C for the cathode which consisted of a compact LNO layer (1-2 μm thick) on a dense CGO electrolyte, topped by a 12 μm thick porous screen-printed LNO layer (particles in the range of 1-2 μm). This work proved that the insertion of a thin compact LNO layer enhances the oxygen transfer to the electrolyte. Typically an improved electrode/electrolyte contact and a better connectivity between grains are the result of a higher sintering temperature. But at the same time the surface area of the electrode material decreases. Hildenbrand et al. showed that the insertion of a dense base-layer improves the LNO electrode footprint, lowers the sintering temperature and enlarges the Triple Phase Boundary (TPB) region [16]. A polarization resistance as low as 0.42 Ω cm^2 has been reported at 700 °C by Philippeau for screen-printed LNO electrode on CGO electrolyte obtained from fine LNO powders (0.5 μm in diameter) [17]. In addition, Vibhu [18] has recently reported the lowest R_{pol} (0.3 Ω cm^2 at 700 °C) for

this class of materials for a 20 μm thick screen-printed LNO (starting from powders of 0.6 μm average particle size) on YSZ (yttria stabilized zirconia).

In SOFC operation, the ORR is likely to occur in the vicinity of TPB points. The microstructure of the cathode is therefore crucial to enhance the electrode performance by enabling the access of oxygen and improving the electronic and ionic percolation, as well as expanding the number of TPB sites by increasing the total cathode surface area. SOFC electrodes are particularly sensitive to microstructural properties such as porosity, surface area; particle size, percolation path and tortuosity. Various deposition techniques such as radiofrequency magnetron sputtering [19], chemical vapor deposition [20-22], microwave plasma coating [23] and electrostatic spray deposition (ESD) [24-26] have been used for the deposition of the cathodes. Among these techniques, ESD has several advantages such as a simple set-up, low cost, the use of non-toxic precursors, high deposition efficiency, direct deposition under ambient atmosphere and easy control of surface morphology of the deposited layers. A wide range of microstructures can be obtained by just varying few key process parameters [27].

This paper reports, for the first time, the effects of several ESD deposition parameters on the final microstructure of $La_2NiO_{4+\delta}$ deposited on gadolinium-doped ceria (CGO) substrates in order to obtain an optimized cathode with enhanced ORR and charge transfer from the electrode to the electrolyte. The ESD parameters studied include the deposition time, the nozzle-to-substrate distance, the substrate temperature, the flow rate of the precursor solution and the solvents used. The polarization resistance of $La_2NiO_{4+\delta}$ electrodes with different optimal microstructures prepared on $Ce_{0.9}Gd_{0.1}O_{2-\delta}$ (CGO) by ESD and screen-printing (SP) have been investigated in air by electrochemical impedance spectroscopy (EIS) from 450-750 °C on symmetrical cells. In addition, the chemical stability of LNO and its chemical reactivity with CGO have been also studied after heat treatments of 10 days duration in air at 700, 800 and 1100 °C.

2. Experimental Section

2.1. Films preparation

$La_2NiO_{4+\delta}$ electrodes have been prepared by two different methods: Electrostatic Spray Deposition (ESD) and screen-printing (SP). For the films prepared by ESD, stoichiometric amounts of nickel nitrate hexahydrate [$Ni(NO_3)_2 \cdot 6H_2O$, 99.9%, Aldrich] and

lanthanum nitrate hexahydrate [$La(NO_3)_3$ $6H_2O$, 99.9%, Alfa Aesar] were dissolved into a 30 mL solution of ethanol (EtOH, CH_3CH_2OH, >99.9%, VWR Chemicals) or a mixture of ethanol-distilled water (EtOH: H_2O, 1:2 and 2:1) under vigorous stirring over 0.5 h. The ratio of La^{3+} and Ni^{2+} concentrations was fixed to 2. The total concentration of metal ions was 0.02 M. Citric acid [$C_6H_8O_7$, 99.9%, Alfa Aesar] acting as a chelating agent was added in excess into each solution and kept at room temperature with constant stirring over 1 h. LNO films were deposited on $Ce_{0.9}Gd_{0.1}O_{2-\delta}$ (CGO) substrates (19.6 mm in diameter, 1.2 mm thick) by ESD under ambient atmosphere using a vertical set-up configuration [27, 28]. The ESD technique is a method for coating films based on the principle of electrostatic atomization. A positive high voltage is applied to the stainless steel nozzle from which positively charged droplets are then generated and directed to the grounded substrate. It is basically a simple three-step process. The first step consists in the creation of an aerosol from the precursor solution at the needle tip by applying a high dc voltage between the tip and the substrate. The second step is the transportation of the aerosol from the needle to the surface of the substrate in the electric field. The third and last step is the formation of the coating due to the impact of the droplets on the substrate. The last two steps play a major role on the microstructure of the coating since the droplet size has to be well controlled versus the ESD process parameters.

The ESD process parameters used in this work for all coatings are given in **Table 1**. First, in order to evaluate the growth rate, the deposition time was increased from 1.33 to 6.67 h. Next, the influence of the nozzle-to-substrate distance on LNO microstructure was evaluated between 20 and 50 mm. In addition, the substrate temperature was varied between 300 and 450 °C. A syringe pump (KDS scientific) was used to control the flow rate of the precursor solution in the range from 0.5 to 1.5 mL/h. Finally, the effect of solvents (pure EtOH, EtOH: H_2O (1:2, 2:1) was also evaluated. During the ESD deposition, the voltage was fixed to approximately 8.5, 10-11 and 14 kV for the solution with EtOH, EtOH: H2O (2:1) and EtOH: H_2O (1:2), respectively. The prepared films were subsequently calcined at 950 °C in air for 6 h. For the electrodes prepared by screen-printing, LNO powder (for the ink preparation) was synthesized by auto-combustion (at 150 °C) using the same precursor solution as for the ESD process (in pure EtOH) and was then sintered at 950 °C for 6h in air. For the screen-printing, LNO ink was prepared by mixing the LNO powder into a solvent with a commercial dispersant (terpineol) and binder (ethylcellulose). Two CGO/LNO half cells were prepared: one which was consisted of symmetrically screen-printed LNO on both sides of the CGO electrolyte and another one based on symmetrically screen-printed LNO on

the LNO cathode functional layer (CFL) prepared by ESD. After the screen-printing step, the samples were sintered at 1050 °C for 2 h in air followed by a sintering of 1100 °C for 0.5 h in air.

Table 1. ESD process parameters

Parameter varied	Substrate temperature [°C]	Deposition time [h]	Flow rate [$mL.h^{-1}$]	Nozzle-to-substrate distance [mm]	Nature of solvent(s)
Deposition time	300	1.33 2.17 4.00 6.67	1.0	30	EtOH
Nozzle-to-substrate distance	300	1.33	1.0	20 30 50	EtOH
Substrate temperature	300 400 450	1.00	1.0	30	EtOH
Flow rate	300	2.00	0.5 1.0 1.5	30	EtOH
Nature of solvent(s)	300	1.33	1.0	30	EtOH EtOH:H2O, 2:1 EtOH:H2O, 1:2
ESD coatings for electrochemistry	350	3.00	1.5	50	EtOH EtOH:H2O, 1:2

2.2. Characterization

The crystal structure was determined by X-ray diffraction (XRD, Philips X'Pert-MPD system, Cu Kα radiation, λ =1.54056 Å) for 2θ in the range from 20° to 60° at a scanning rate of 0.017° per second. The phase identification was carried out using International Centre for Diffraction data (ICDD). The positions of the X-ray diffraction peaks as well as the cell parameters were obtained by refinement using Fullprof software [29]. Scanning electron microscopy (ZEISS Ultra 55) instrument with field emission gun (FEG) and energy-dispersive X-ray spectroscopy (EDX) analyzer were used for morphology evaluation of the film surfaces and cross-sections, the determination of particle size, and the composition analysis, respectively. The symmetrical cells were analyzed by impedance spectroscopy between 500 and 700 °C in air with PARSTAT 302N, in the frequency range from 0.05 Hz to 100 kHz. Measurements were performed with an ac signal amplitude of 0.02 V at open circuit

potential (OCP), using Au grids (Heraeus, 1024 meshes.cm^{-2}, woven from 0.06 mm dia. wire) as current collectors. The data were fitted with equivalent circuits using the ZView® software (Scribner Associates) to study separately the different electrode contributions involved in the ORR.

3. Results and discussion

3.1. Microstructural control of $La_2NiO_{4+\delta}$ coating by ESD

Crystallization of pure $La_2NiO_{4+\delta}$ was obtained after calcination at 950 °C for 6 h in air for all the as-deposited films prepared by ESD, as shown by X-ray diffraction (**Fig. 1**). All diffraction peaks matched well those of the $La_2NiO_{4.16}$ phase (ICDD # 01-074-9394) and the $Ce_{0.9}Gd_{0.1}O_{2-\delta}$ substrate (ICDD # 04-013-6577). The LNO phase was indexed to an orthorhombic unit cell with the Fmmm space group (No 69) and the obtained cell parameters of a = 5.454(8) Å, b = 5.461(8) Å and c = 12.690(6) Å are in a well agreement with literature data [18].

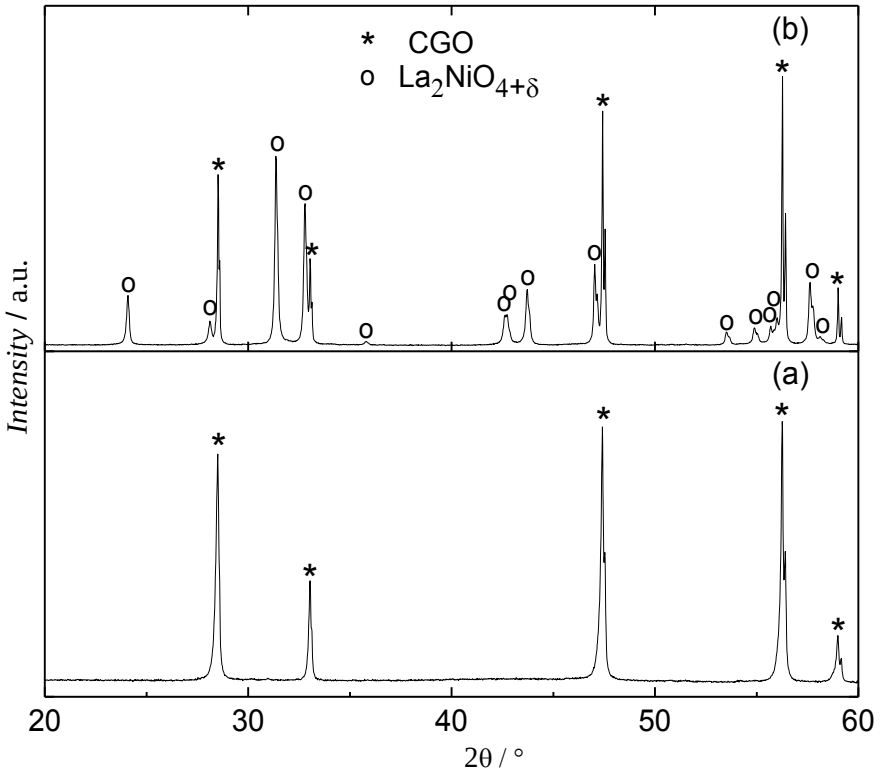

Fig. 1 Typical XRD patterns of a LNO film deposited by ESD on a CGO substrate: (a) as-deposited, (b) calcined at 950 °C for 6 h in air.

EDX quantitative analysis confirms the presence of La, Ni and O elements in the film with a La/Ni ratio of 2.09 ± 0.05, as expected from the starting precursor solution composition (**Fig. S1**).

In order to qualitatively optimize the electrode microstructure, including the particle size along with the particle connectivity and the electrolyte-electrode interface contact, with the aim of designing an improved cathode architecture that enhances the electrochemical performance, the influence of the ESD deposition parameters (deposition time, nozzle-to-substrate distance, substrate temperature, flow rate of the precursor solution and nature of the solvents) have been investigated in detail.

3.1.1. Influence of the deposition time

To assess the evolution of the morphology, LNO films with deposition times of 1.33, 2.17, 4 and 6.67 h were prepared. The substrate temperature, nozzle-to-substrate distance and flow rate were fixed to 300 °C, 30 mm and 1.0 $mL.h^{-1}$, respectively (**Table 1**). Pure ethanol was used as solvent in the precursor solution. The surface morphology of these films after calcination at 950 °C for 6 h in air is shown in **Fig. 2a-2d**. By increasing the deposition time, a larger area coverage as well as better connected particles are obtained; these results are in good agreement with previous studies on other oxide films [30]. By increasing the deposition time, the sintering rate increases without affecting the initial morphology, as shown in the large magnification micrographs in **Fig. S2**. The particle diameter, obtained from SEM micrographs (**Fig. S2**) was of approximately 100 nm in average whatever the deposition time. Consequently the particle connectivity through the LNO grains in the layer is improved. No crust or hollow particles have been detected when ethanol is used as the solvent. This suggests that the evaporation of ethanol and the precipitation of the solutes proceed homogeneously in each droplet. From the cross-section of the film deposited for 6.67 h (**Fig. 2e**) a uniform open tree-like 3-D microstructure, referred to as "coral-type", can be observed. The average thickness was measured and its variation with the deposition time is shown in **Fig. 2f**. As previously reported [31], the observed non-linear growth is caused by a time-dependent morphological evolution of the ESD coatings. The coral microstructure originates from the preferential landing and agglomeration of droplets when impacting the hot substrate. Under the strong electrostatic field, induced charges exist on the surface of the grounded substrate, with a sign opposite to that of the droplets and the nozzle.

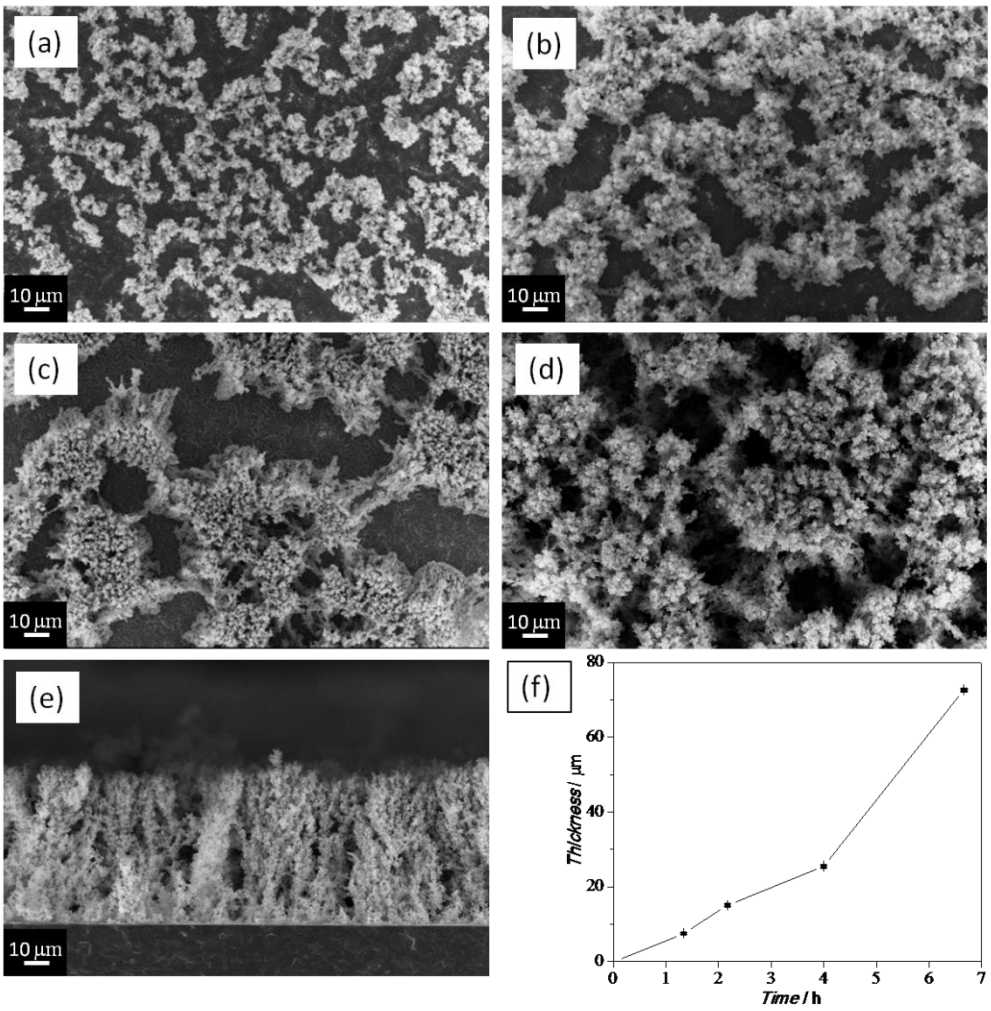

Fig. 2 SEM micrographs of the calcined LNO films (950 °C for 6 h) deposited by ESD at T = 300 °C using EtOH, a distance nozzle to substrate of 30 mm and a flow rate of 1.0 $mL.h^{-1}$ after a deposition time of: (a) 1.33 h (surface), (b) 2.17 h (surface), (c) 4 h (surface), (d) 6.67 h (surface), (e) 6.67 h (cross section) ; (f) LNO growth rate, error bars range from 0.2 to 0.4 µm.

The droplet charge distribution is generally not uniform but depends on the position relative to the nozzle and, in particular, on the local curvature of the surface. The charge concentrates more at the places where the curvature is greater, making the electric field the strongest there. Therefore, when a charged droplet approaches the surface, it will be attracted more towards these more curved areas. It is only the case if there is a negative curvature. This is referred to as "preferential landing". It becomes more pronounced at higher temperatures, at larger distances or for longer deposition times because the smaller the particles are, the easier they are diverted. This action usually causes agglomeration of the particles and then the formation of a coral like microstructure, resulting in a drastic increase of the thickness as soon as enough

agglomerates are deposited after ~ 4 h deposition. This well-known phenomenon in ESD technique has been already mentioned by Chen et al. [32], Taniguchi et al. [25], Marinha et al. [27, 28], Neagu et al. [30], Lintanf et al. [31].

3.1.2. Influence of the nozzle-to-substrate distance

To study the influence of the nozzle-to-substrate distance on the morphology of the layer, LNO films were deposited at distances of 20, 30 and 50 mm. The solution flow rate, substrate temperature and deposition time remained constant at 1.0 $mL.h^{-1}$, 300 °C and 1.33 h, respectively (**Table 1**) using pure ethanol (EtOH) as solvent. The resulting micrographs are shown in **Fig. 3a-3c**.

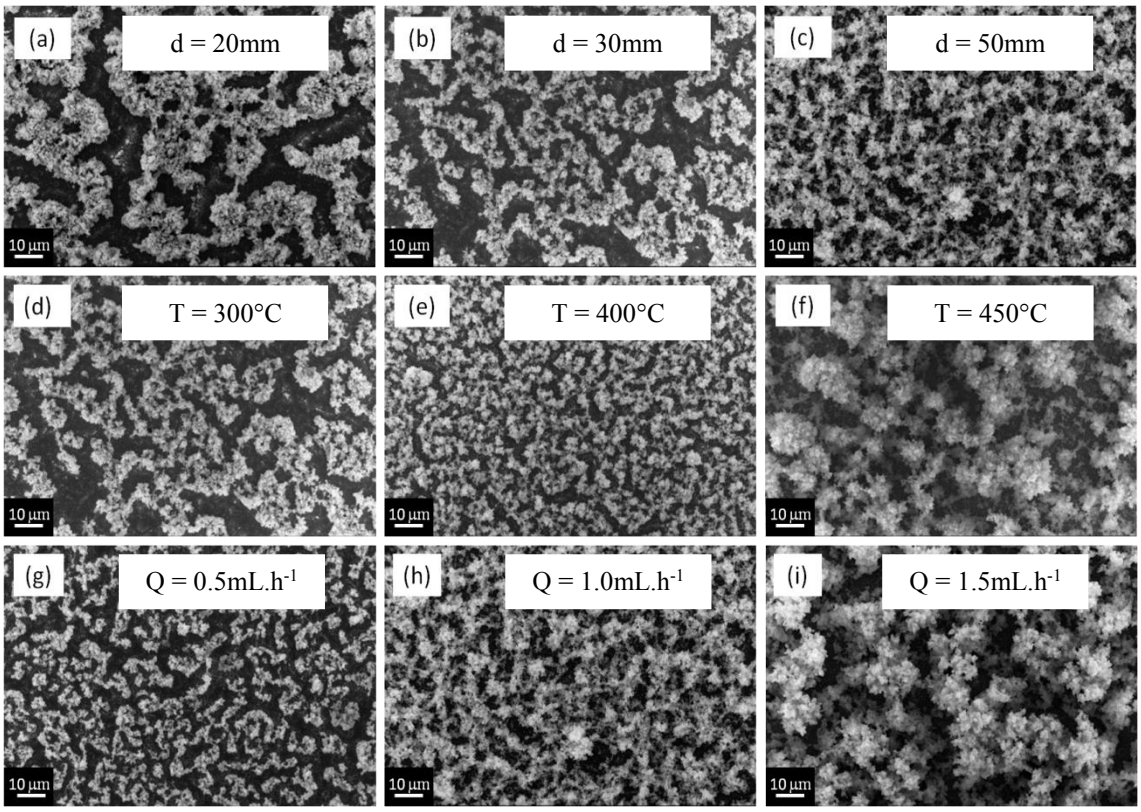

Fig. 3 SEM surface microstructures of the calcined LNO films (950 °C for 6 h) using pure EtOH and coated at a nozzle-to-substrate distance of (a) 20 mm (b) 30 mm and (c) 50 mm and at fixed flow rate 1.0 $mL.h^{-1}$, substrate temperature T = 300 °C and deposition time 1.33 h; –at a substrate temperature of (d) 300 °C (e) 400 °C (f) 450 °C and at fixed flow rate 1.0 $mL.h^{-1}$, nozzle to substrate distance 30 mm and deposition time 1 h; –and at a flow rate of (g) 0.5 $mL.h^{-1}$ (h) 1.0 $mL.h^{-1}$ and (i) 1.5 $mL.h^{-1}$, and at fixed substrate temperature T = 300 °C, nozzle to substrate distance 30 mm and deposition time 2 h.

The deposited films are composed by a network of interconnected round-shaped particles that have successively agglomerated on the substrate, creating a porous layer with an homogeneous microstructure over large areas. By increasing the nozzle-to-substrate distance, drier and smaller droplets reach the substrate due to the increase in the droplet flight time from nozzle-to-substrate. As a consequence a larger solvent evaporation is taking place. Drier droplets lead to the deposition of smaller particles, decreasing from 400 to 150 nm with better packing, as well as an increase in the film density as previously reported by Marinha et al. for LSCF cathodes [27]. This can be observed in **Fig. 3c** for the film deposited at the largest distance (50 mm) and in the surface micrographs at high magnification (**Fig. S3a-S3c)**. In all three cases, the microstructure can be described as a porous network of LNO particles, with internal submicron-sized pores.

3.1.3. Influence of the substrate temperature

Fig. 3d-3f show the morphological evolution of the films deposited at different temperatures (300, 400 and 450 °C). The nozzle-to-substrate distance, solution flow rate and deposition time were fixed to 30 mm, 1.0 $mL.h^{-1}$ and 1 h, respectively and pure EtOH was used as solvent (**Table 1**). At the deposition temperature of 300 °C (**Fig. 3d**), the evaporation of the droplets before landing is incomplete, giving rise to wet droplets. When they reach the substrate, the droplets spread rapidly, evaporate and boil at the same time creating strains which lead to voids between the particles. Due to the temperature gradient, the evaporation rate of the droplets during the flight between the nozzle and the substrate increases by increasing the substrate temperature. At 400 °C (**Fig. 3e**), a larger area coverage is obtained with the presence of discrete agglomerates of smaller particles. The temperature increase from 400 to 450 °C led to the formation of rapidly dried particles. At 450 ºC a complete solvent evaporation is expected to occur during the flight. The particle agglomeration results from the preferential landing of fine and charged aerosol droplets and the lack of wetting on the substrate, as previously observed by Chen et al. [32] Solidified finer particles accumulate more easily at the preferred landing sites and form large agglomerates (**Fig. 3f**). This leads to the formation of branched structures resembling corals, in good agreement with results obtained by Princivalle et al. [33] and Marinha et al. [27] Using larger magnification (**Fig. S3d-S3f**), a decrease in particle size (from 100 to 80 nm) as the temperature increases and the formation of the tree branches at 450 °C can be observed. The fast evaporation of ethanol

occurring when the droplets impact the substrate at a high flow rate proceeds simultaneously to the precipitation of the solutes which form hollow aggregates.

3.1.4. Influence of the flow rate

The influence of the flow rate was studied by varying its value from 0.5 to 1.5 $mL.h^{-1}$ using pure EtOH as solvent and keeping the other parameters constant: nozzle-to-substrate distance, deposition time and substrate temperature of 30 mm, 2 h and 300 °C, respectively (**Table 1**). According to the Gañan-Calvo's relationship [34], specified in Equation (1),

$$d \sim \left(\frac{\rho \varepsilon_0 Q^3}{\gamma K} \right)^{1/6} \qquad \text{Equation (1)}$$

which correlates the droplet size, d, to the density ρ, the vacuum permeability ε_0, the flow rate Q, the surface tension γ and the electrical conductivity of the solution K; the droplet size mainly varies with the flow rate and less strongly with the conductivity and surface tension of the solution. The increase in flow rate from 0.5 to 1.5 $mL.h^{-1}$is expected to lead to the generation of larger droplets and, consequently, larger particles. In this set of data, it is not observed from **Fig. 3g-3i** and **Fig. S3g-S3i** since both substrate temperature and nozzle-to-substrate distances values are quite low and thus favor the formation of large droplets. In the process of electrohydrodynamic atomization in the cone-jet mode, the shape of a liquid droplet is transformed by electrical forces into a conical shape. However, it is worth to notice that an addition of citric acid, at mM concentration, which behaves like a surface-active agent, leads to a decrease of the surface tension of the aqueous solutions from 0.072 to 0.065 $N\ m^{-1}$ [35]. In these conditions, radial electric forces will surpass the surface tension during the droplets formation at the top of the needle [36]. These larger electric forces should mainly control the break-up of the liquid cone-jet into much smaller droplets. Thus modified properties at the solution/air interface due to citric acid addition are essential for the smaller droplets formation. In these conditions, flow rate is not affecting the particle size for a given substrate temperature and nozzle-to-substrate distance**.** Since the surface where the droplets impact becomes rough, a reticulated microstructure can be observed evolving towards a larger agglomeration of particles (**Fig. S3i**). Hollow aggregates can also be detected, particularly at high flow rates. This can be explained by a fast evaporation of ethanol and precipitation of the solutes which proceed simultaneously. As shown in **Fig. 3g-3i**, the droplets covered the surface more readily.

3.1.5. Influence of the nature of the solvent

The microstructural features of the LNO films deposited by ESD also depend on the physico-chemical properties of the precursor solution and particularly on the nature of the solvents. In this study, three solutions based on EtOH and H_2O were tested fixing the other ESD parameters: T = 300 °C, deposition time 1.33 h, nozzle to substrate distance 30 mm and flow rate1.0 $mL.h^{-1}$ (**Table 1**). According to Equation 1, the droplet size also depends upon the conductivity and the surface tension of the precursors' solution [35]. So when changing the solvent from ethanol to the ethanol:water (1:2) mixture, the solution conductivity (of concentration 0.02 M) and surface tension increase from 3.1 x 10^{-4} to 2.5 x 10^{-3} S cm^{-1} (values measured with a CDRV 62 conductimeter) and from 0.022 to 0.073 N m^{-1}, respectively [37]. In these conditions a decrease in the droplet size is expected. In agreement with equation (1), the droplet size was roughly estimated to be reduced by less than a factor 2 when water is added. Moreover, as the boiling point of H_2O (100 °C) is larger than that of EtOH (78 °C), a lower droplet evaporation rate is expected and consequently larger droplets can be present. Thus, two competitive processes controlling the droplet size occur when the H_2O content in EtOH is increased. From an experimental point of view, we observe the presence of less porous coatings, as shown in **Fig. 4c** and **Fig. 4e** in comparison to **Fig. 4a**. This denser microstructure is the result of predominant smaller droplets which are more packed when 33 vol. % of H_2O is added (**Fig. 4c**) in comparison to pure EtOH (**Fig. 4a**). When the H_2O content is increased up to 67 vol. % (**Fig. 4e**), the droplets will contain more water. So, when they impact the hot substrate, stresses occur during the fast drying process leading to the formation of cracks and larger voids (**Fig. 4e**) than when only 33 vol. % H_2O is used (**Fig. 4c**). Regarding the cross-sections (**Fig. 4b**, **Fig. 4d** and **Fig. 4f**), for solutions with higher water percentages, a 3-D coral microstructure can be observed like porous trees originated from the water drying. Such modification of the coating microstructure is strongly dependent on the solvent composition. These 3-D coral type microstructures differ qualitatively from each other in terms of percolation path inside the electrode and in the quality of the contact at the LNO /CGO interface. For example with pure ethanol, a discontinuous interface between the cathode and the electrolyte is always observed (inset of **Fig. 4b**) irrespective of the ESD conditions, whereas a continuous and adherent interface was obtained for both coatings starting with water addition in the precursors' solution (inset of **Fig. 4d and Fig. 4f**).

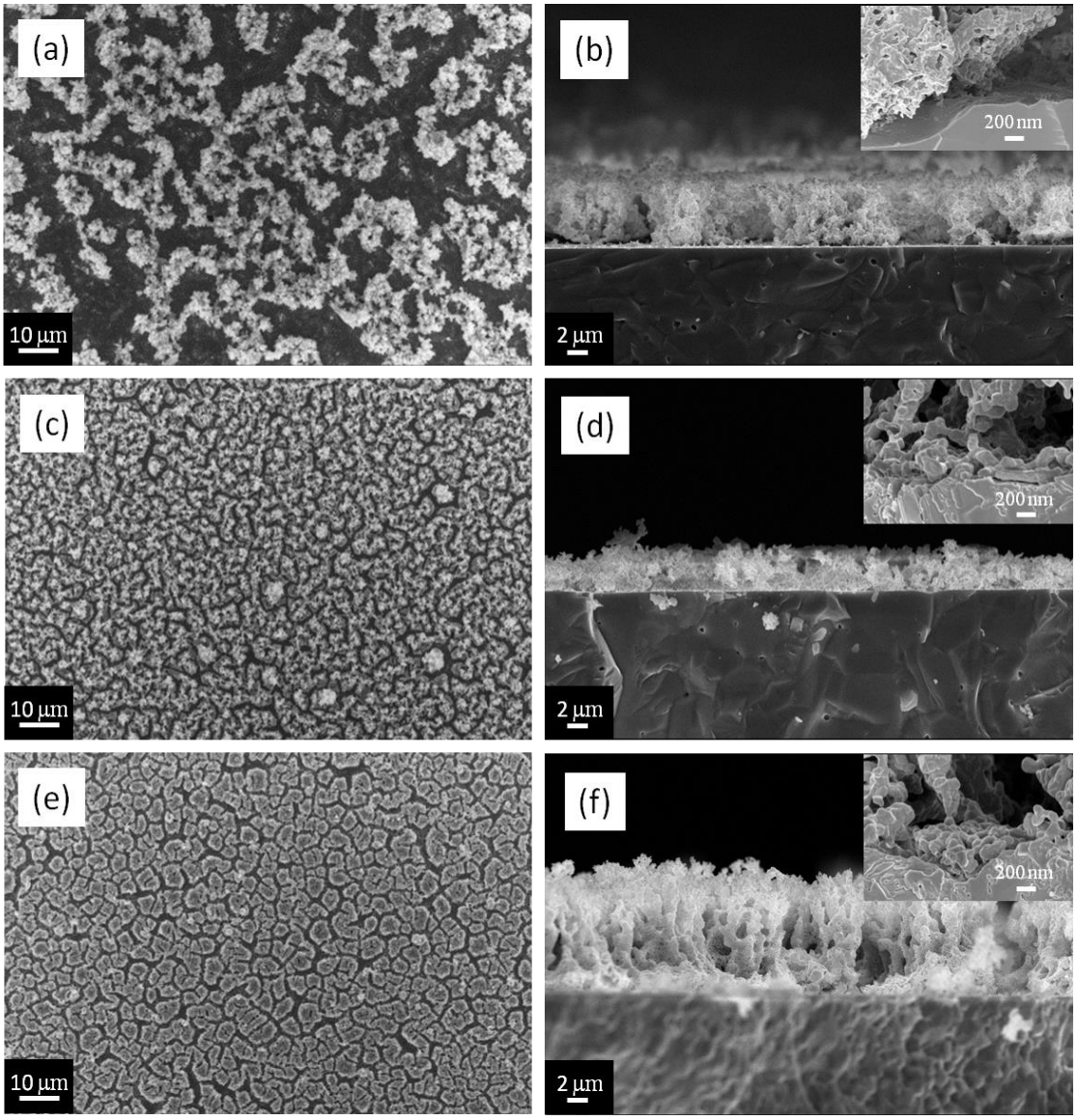

Fig. 4 SEM micrographs of calcined films (950 °C for 6 h) obtained with fixed substrate temperature T = 300 °C, nozzle to substrate distance 30 mm, flow rate 1.0 $mL.h^{-1}$, deposition time 1.33 h starting with solution of (a) EtOH, surface (b) EtOH, cross section (c) EtOH + H_2O (2:1), surface (d) EtOH + H_2O (2:1), cross section (e) EtOH + H_2O (1:2), surface (f) EtOH + H_2O (1:2), cross section.

This good adhesion was verified by a scotch-test. Indeed when a charged liquid droplet containing some water approaches the polished flat surface of the grounded substrate, it spreads much more than a finer droplet containing EtOH which evaporation rate is faster. In this way, these droplets form a continuous electrode layer on top of the substrate and that is why the adherence of the electrode to the electrolyte is improved when water is added without

the need of using high sintering temperatures. Indeed a calcination temperature of 950 °C for 6 h in air has been proved to be sufficient.

3.1.6. Architectural design of the LNO cathode

The electrochemical properties of the electrodes are influenced not only by their microstructure (percolation path between grains, particle size and porosity) and by the electrolyte-electrode interface contact for oxygen ion transfer, but also by an adequate current collection to enhance the electronic conductivity on the top layer. For the selected microstructures (shown here after in **Fig. 5**) the chosen ESD conditions were: nozzle-to-substrate distance, substrate temperature and flow rate, 50 mm, 350 °C, 1.5 $mL.h^{-1}$, respectively (**Table 1**), using a deposition time of 3 h to obtain thicker films. In order to study the effect of the LNO architectural design on its electrochemical properties, four different symmetrical cathodes have been prepared as shown schematically in **Fig. 5d, 5h, 5i and 5p**: (i) cathode 1 (sample 1, **Fig. 5a-5d**) consists of a porous 3-D coral microstructure of 20 μm thickness with small particle size (~ 100 nm, **Fig. S2**). This cathode, calcined at 950 °C for 6 h, was fabricated by ESD using EtOH based solution using the ESD conditions given in Table 1. However, the cathode/electrolyte interface is not continuous (**Fig. 5c**) and the contact between the top cathode and current collecting grid is rather rough. (ii) Cathode 2 (sample 2) has been fabricated with objective of improving the cathode/electrolyte interface, which plays a crucial role in the charge transfer process from cathode to electrolyte. As can be observed in **Fig. 5e-5h** a continuous thin dense layer is present, topped by a 3-D coral microstructure with larger particles (~ 150 nm), better density, better connectivity and better contact between cathode and grid. This cathode, 20 μm thick, was prepared by ESD using similar deposition conditions as those for cathode 1 (see **Table 1**) but from an EtOH-water solution (1:2). (iii) Cathode 3 (sample 3) has been fabricated by screen-printing (SP) only with the aim obtaining a flat surface to improve the contact between the grid and the cathode as shown in **Fig. 5i-5l**. This 20 μm thick cathode, calcined at 1050 °C for 2 h followed by 1100 °C for 0.5 h in air, **(Fig. 5j),** is characterized by discontinuous electrode/electrolyte interface. The average particle size is very large (~ 400 nm) in comparison to cathodes 1 and 2. Moreover, the total active surface with respect to cathode volume will be lower than for previous samples and hence less ORR is expected. (iv) A fourth innovative architecture was designed in cathode 4 (sample 4, **Fig. 5m-5p**) combining for the first time two well-established techniques, ESD and SP, to get a double LNO layer (dense thin and porous one in a single step by ESD topped by a

porous SP). The aim was to further improve the contact between the cathode and the grid of sample 2 by depositing a LNO current collecting layer (average particle size ~400 nm) by SP. This cathode was calcined at 950 °C for 6 h after the ESD in air and then 1050 °C for 2 h followed by 1100 °C for 0.5 h in air after the SP. As shown in **Fig. 5n**, the screen-printed layer is partially penetrating the ESD functional layer (average particle size ~ 150 nm) in a depth of approximately 8 µm.

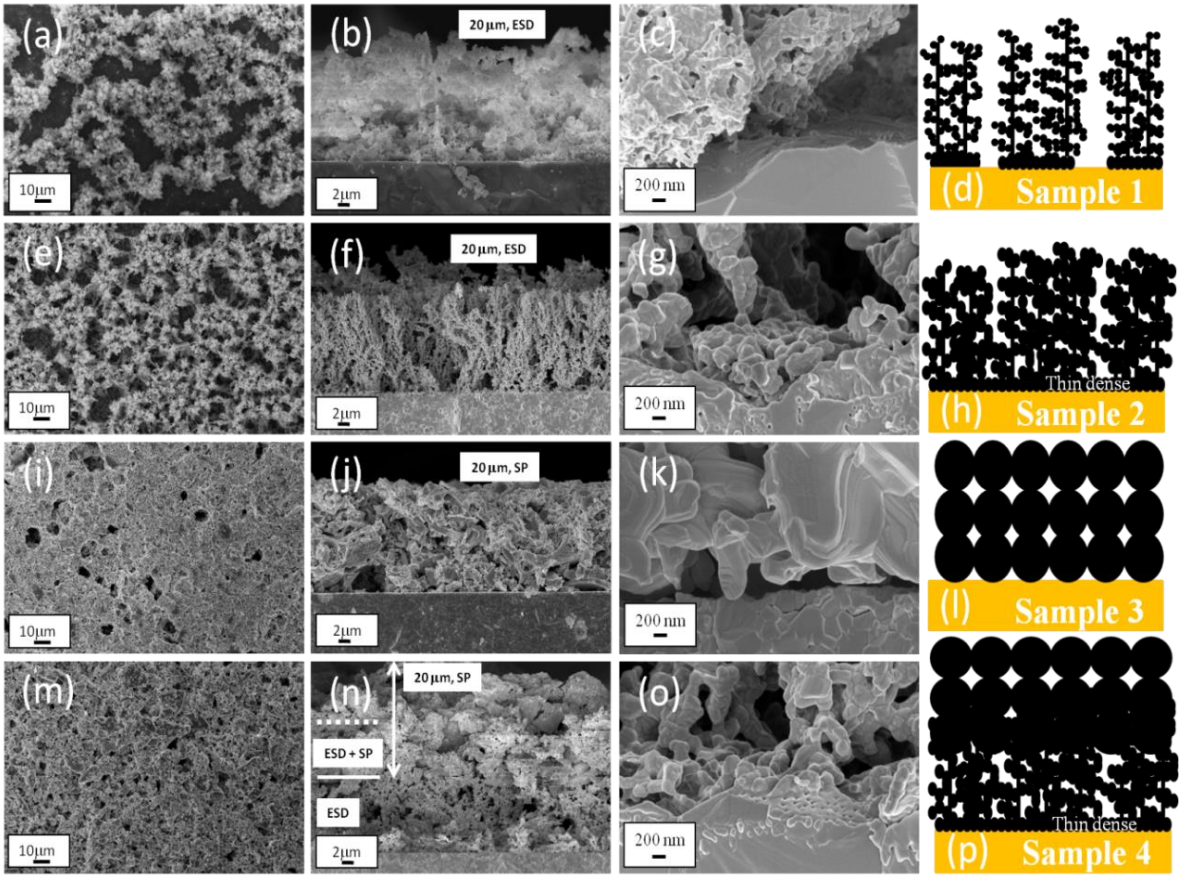

Fig. 5 Schematic and SEM micrographs of calcined films obtained with fixed substrate temperature T = 350 °C, nozzle to substrate distance 50 mm, flow rate 1.5 $mL.h^{-1}$, deposition time 3 h starting with solution of sample 1: (a) EtOH, surface, ESD (b), (c) EtOH, cross section, ESD (d) EtOH, ESD schematic diagram; sample 2: (e) EtOH + H_2O 1:2, surface, ESD (f), (g) EtOH + H_2O 1:2, cross section, ESD (h) EtOH + H_2O 1:2, ESD schematic diagram; sample 3: (i) SP surface (j), (k) SP cross section (l) SP schematic diagram; sample 4: (m) EtOH + H_2O, 1:2 ESD + SP, surface (n), (o) EtOH + H_2O, 1:2 ESD + SP, cross section (p) EtOH + H_2O, 1:2 ESD + SP, schematic diagram.

3.2. Electrochemical properties of the selected LNO cathodes

Typical experimental and fitted impedance diagrams, plotted in the Nyquist plane, recorded on symmetrical cells at 600°C in air for the four investigated electrodes (**Table 2**) are shown in **Fig. 6**. All experimental diagrams were fitted using a combination of several resistance-constant phase element parallel circuits, connected in series with an inductance L. This electrical element, appearing as a high-frequency (*HF*) tail below the real axis, represents the contribution of the connecting leads, measuring device and connecting wires to the measured total impedance [38]. The *HF* intercept of the diagrams on the real axis corresponds to the overall ohmic resistances (R_s), **Table 2**, including the resistive contributions of the electrolyte, electrode, leads and current collectors. At 600°C, R_s varies from 176.3 Ω cm² (sample 1) to 14.58 Ω cm² (sample 2) (**Fig. 6**). This variation corresponds to a much better contact at the electrolyte/electrode interface (sample 2) as shown in SEM micrographs (**Fig. 5g** compared to **Fig. 5c**). Consequently, the current constriction is lowered at the CGO/LNO interface leading to a reduction of the series resistance. This resistance also depends on the contact area with the gold grid. Indeed, R_s is further reduced to 7.58 Ω cm² at 600°C thanks to the flatness of the SP LNO layer (sample 3, **Fig. 5i-5j**) compared to the ESD coating (sample 2, **Fig. 5f**). For the double layer architecture (sample 4), when LNO ESD coral-type layer is topped by SP LNO (**Fig. 5n**), R_s is equal to 5.28 Ω cm² at 600°C (**Fig. 6d**), indicating that the screen-printed LNO actually acts as a current collector layer (CCL).

The electrode performance can be quantified by the polarization resistance $R_{pol} = R_{electrode} \times S/2$ (**Table 2**) where $R_{electrode}$ is measured from the difference between the value of the low frequency intercept of the electrode characteristic on the real axis and R_s. The surface area of each symmetrical electrode is referred to as S (**Table 2**). Regardless of both electrode microstructure and architecture, the electrode response is composed by two main elementary contributions at *HF* and low frequency (*LF*). For sample 4, an additional very small *LF* response was detected. Adding the LNO CCL (sample 4) decreases the relative contribution of the *HF* response to the total electrode impedance. Indeed, the frequency distribution of EIS spectra is shifted towards lower frequencies when a double LNO layer is used (**Fig. 6**). Moreover, the largest contribution to the polarization resistance is shifted from the *HF* to the *LF* response of the electrode when both sample contacts, at the electrode surface and at the electrode / electrolyte interface, are improved. At this stage, it is worth noting that the frequency distribution of the electrode characteristic for sample 4 is similar to that of sample 2

but remains different from that observed for sample 3 (**Fig. 6**). This suggests that the ORR is likely to occur mainly through the LNO layer deposited by ESD.

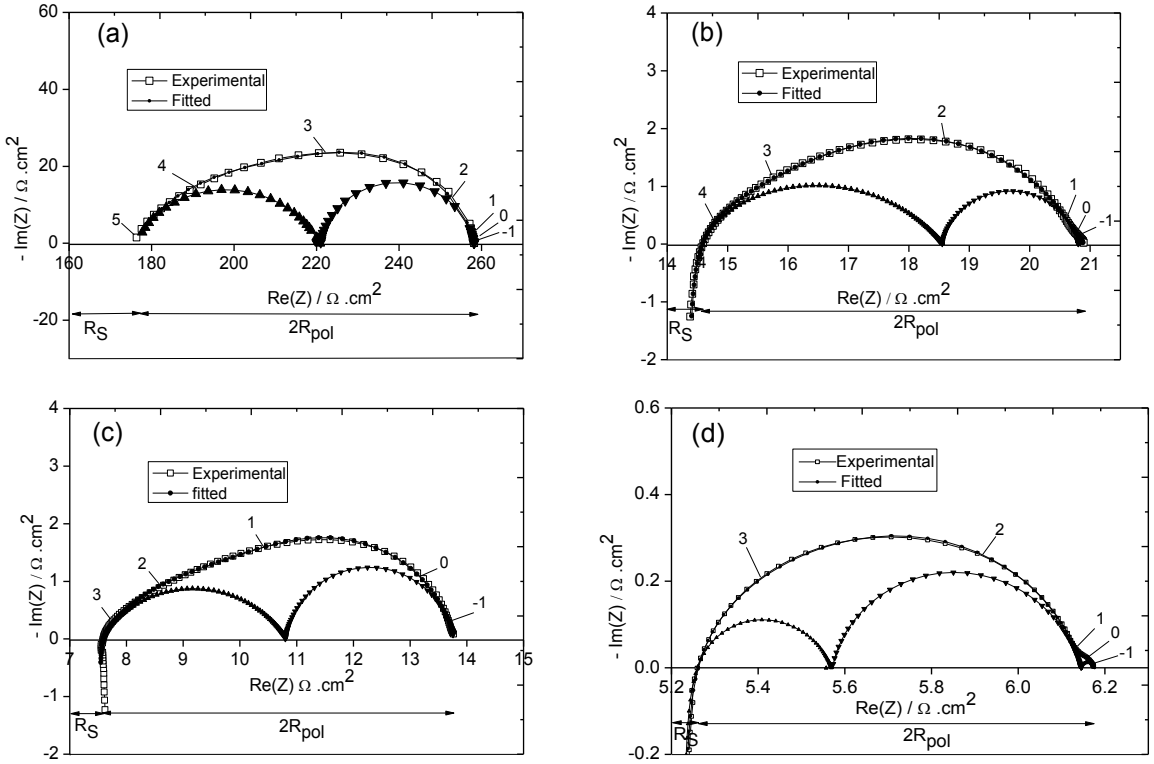

Fig. 6 Impedance spectra of the LNO cathode on CGO in symmetrical cells in air obtained at 600 °C in OCP conditions (a) sample 1 (b) sample 2 (c) sample 3 (d) sample 4. The numbers over the diagram indicate the logarithm of the measuring frequency.

As expected R_{pol} decreases as the temperature increases (**Fig. 7, Table 2**). R_{pol} is also reduced by improving the cathode/electrolyte interface (from sample 1 to sample 2) or/and the contact between the grid and the cathode (samples 3 and 4). Indeed, the R_{pol} value for sample 1 was found to be 40.73 Ω cm² at 600 °C (20.3 Ω cm² at 700 °C) whereas for sample 2 and 3, 3.33 and 3.53 Ω cm², respectively, at 600 °C (1.26 and 0.58 Ω cm² at 700 °C). For a single LNO layer deposited by ESD (sample 2) with an optimized electrode/electrolyte contact, R_{pol} decreases by a factor of 12 at 600 °C in comparison to sample 1, where this interface is not continuous (**Fig. 6**). When a single LNO layer is deposited by SP (sample 3), the surface planarity of the electrode leads to a good current collection, as also suggested by the corresponding decrease of R_s. The frequency distributions of the electrode characteristic for samples 1 and 2 are different: for sample 2 it is shifted towards lower frequencies, which suggests that the active volume of the ESD deposit increases in good agreement with the

microstructures (**Fig. 5a and 5e)**. As can be observed in **Fig. 5a and 5e,** there is a larger coverage in the case of sample 2. Moreover the contact between cathode and grid is much better in sample 2. As a consequence, sample 2 provides larger surface for electronic conduction and this can lead to faster ORR kinetics and hence shift towards lower frequency. Rather surprisingly, the polarization resistance for sample 3 is close to that recorded for sample 2 and even lower at higher temperatures (**Fig. 7**). Indeed, the average particle size of LNO is higher in the former electrode but the current collection is likely to be improved, as suggested by the lower corresponding series resistance. Since the microstructure of sample 3 is different (**Fig. 5**), the frequency distribution of the electrode characteristic varies. Moreover, as can be observed in **Fig. 6d**, a significant improvement in the R_p value as low as 0.42 Ω cm² at 600 °C (0.08 Ω cm² at 700 °C, **Fig. 7, Table 2**) has been obtained by further improving the current collecting efficiency of sample 2 by adding a SP layer on top, which favors a better contact between the sample and the gold grid (**Fig. 5n**). This is also in good agreement with of the R_s values.

This huge and significant decrease in polarization resistance of the LNO double-layer (sample 4), roughly 8 times lower than sample 2 at 600 °C (~16 times of R_p at 700 °C) can be attributed to the simultaneous presence of a CCL providing good contact between the grid and the cathode, a porous cathode functional layer (CFL) with a fine particle size (~150 nm) of large surface area and good connectivity and of a continuous thin and dense LNO layer providing the oxygen transfer to the electrolyte. The role of the CCL is to homogenize the current distribution in the whole volume of the CFL, by avoiding any current constrictions and by increasing the lateral percolation. To the best of our knowledge the obtained R_{pol} value (as low as 0.08 Ω cm² at 700 °C for sample 4) is far better than the minimum R_{pol} values reported in the literature for pure $La_2NiO_{4+\delta}$ cathode. For example R. Sayers et al. [15] reported R_{pol} values of 1.0 Ω cm² at 700 °C (SP) after the addition of a thin and dense LNO contact layer at the CGO/LNO interface. Vibhu et al. [18] have recently reported a R_{pol} value of 0.3 Ω cm² at 700 °C for a screen-printed LNO electrode (average particle size equal to 400 nm) on YSZ electrolyte, which is the reference in the literature at the moment for the pure LNO. Further improvement in the cathode performance has been recently reported by Nicollet et al. [39] when LNO was infiltrated inside the CGO backbone. A R_{pol} value as low as 0.05 Ω cm² was found at 700 °C for this LNO/CGO composite. The activation energies deduced from the Arrhenius plots of the polarization resistance (**Fig. 7**) are reported in **Table 2** and were found to be in good agreement with the values reported in literature [15, 16, 40]. The novel

and performant data obtained (R_p= 0.08 Ω cm² at 700 °C) indicates that an architectural design of LNO cathode with a controlled microstructure plays a major role in improving its performance.

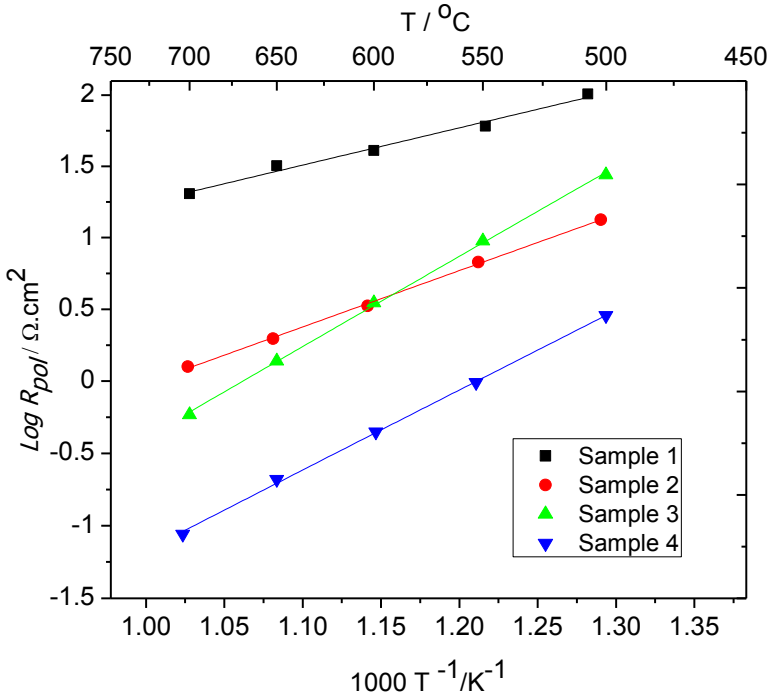

Fig. 7 Arrhenius plot of the R_{pol} value in air for LNO films (OCP conditions) (a) sample 1 (b) sample 2 (c) sample 3 (d) sample 4.

Table 2. Fabrication process, surface area (S), series resistance (R_S), polarization resistance (R_{pol}) and activation energy (E_a) values in air

Samples	Fabrication process	Surface area [cm²]	R_s at 600 °C [Ω cm²]	R_{pol} at 600 °C [Ω cm²]	R_{pol} at 700 °C [Ω cm²]	E_a [eV]
Sample 1	ESD-EtOH Single layer	2.00	176.3	40.73	20.3	0.52 ± 0.03
Sample 2	ESD-EtOH:H_2O, 1:2 Single layer	2.00	14.58	3.33	1.26	0.77 ± 0.01
Sample 3	SP Single layer	2.00	7.58	3.53	0.58	1.25 ± 0.02
Sample 4	ESD-EtOH:H_2O, 1:2 + SP Double layer	1.54	5.28	0.42	0.08	1.11 ± 0.02

3.3. Stability and reactivity

The long-term chemical stability of an LNO film grown on a CGO electrolyte and prepared by ESD starting from an EtOH-H_2O solution (1:2) and its reactivity with CGO have been studied by X-ray diffraction after heat treatments in air at 700, 800 and 1100 °C for 10 days (**Fig. 8**). In this study, we have selected sample 2, the one characterized by a thin dense layer, 200 nm thick, covered by a porous 3-D coral microstructure. Up to 800 °C, only pure $La_2NiO_{4+\delta}$ phase was detected with the presence of CGO from the substrate. No high-order Ruddlesden-Popper phases such as $La_3Ni_2O_7$ or $La_4Ni_3O_{10}$, nor La_2O_3 or NiO have been observed. The observed chemical stability of $La_2NiO_{4+\delta}$ with CGO at 800 °C for 10 days is in good agreement with previous data [17]. No significant changes were observed by XRD in powder mixtures after heating at 800 °C for 5 days, confirming no chemical reactivity between $Ln_2NiO_{4+\delta}$ and CGO under these conditions. However, the reactivity test on LNO with CGO electrolyte under severe conditions, after 1100 °C for 10 days indicated the decomposition of $La_2NiO_{4+\delta}$ into $La_3Ni_2O_7$ Ruddlesden-Popper phase, La_2O_3 and $La_{0.5}Ce_{0.5}O_2$. On the other hand, a total decomposition into $La_4Ni_3O_{10}$ phase has been reported after heating at 1150 °C for 1 h as reported by Philippeau et al. [17]. Montenegro-Hernandez et al. [42] studied the chemical reactivity of CGO with LNO by EIS measurements. They further studied this reactivity by Focused Ion Beam-Transmission Electron Microscopy (FIB-TEM) and STEM after EIS measurements (at 800 °C for 400 h). They observed an increase of the ASR values in LNO/CGO/LNO cells after 20 h at 750 °C, indicating the beginning of a chemical reaction with the formation of an insulating phase containing mainly Ce and La at the CGO/LNO interface and in the LNO grains. If such reactivity is developed over time, its effect should not be significant, at least during the IT-SOFC lifetime. An evidence of reactivity was also previously reported by Amow et al. [43] by X-ray diffraction when $La_2Ni_{0.9}Co_{0.1}O_4$ on CGO pellet was fired at 950 °C in air for two weeks, leading to a thermal decomposition into La_2O_3 and $La_3Ni_2O_7$. The compatibility of LNO with CGO powders was also tested by Sayers et al. [44] for 50:50 wt. % mixtures of CGO and LNO powders heat treated up to 1000 °C for 72 h in air. At 700 °C, there was no evidence of new phases formed after 72 h and above 1000 °C, interfacial reactions were taking place unambiguously. Since the typical cell fabrication temperatures are below 1000 °C (calcination at 950 °C for 6 h in air) and impedance measurements are performed only up to 700 °C, it should lead to a relatively stable LNO film with respect to CGO electrolyte. Moreover, the kinetics of the chemical reactivity strongly depends on the microstructure of the cathode, as reported by

Montenegro-Hernandez [41] in the case of $La_2NiO_{4+\delta}$ with CGO and by Figueiredo et al. [45] in the case of $LaCoO_3$ on YSZ where the film porosity may promote the chemical reactivity.

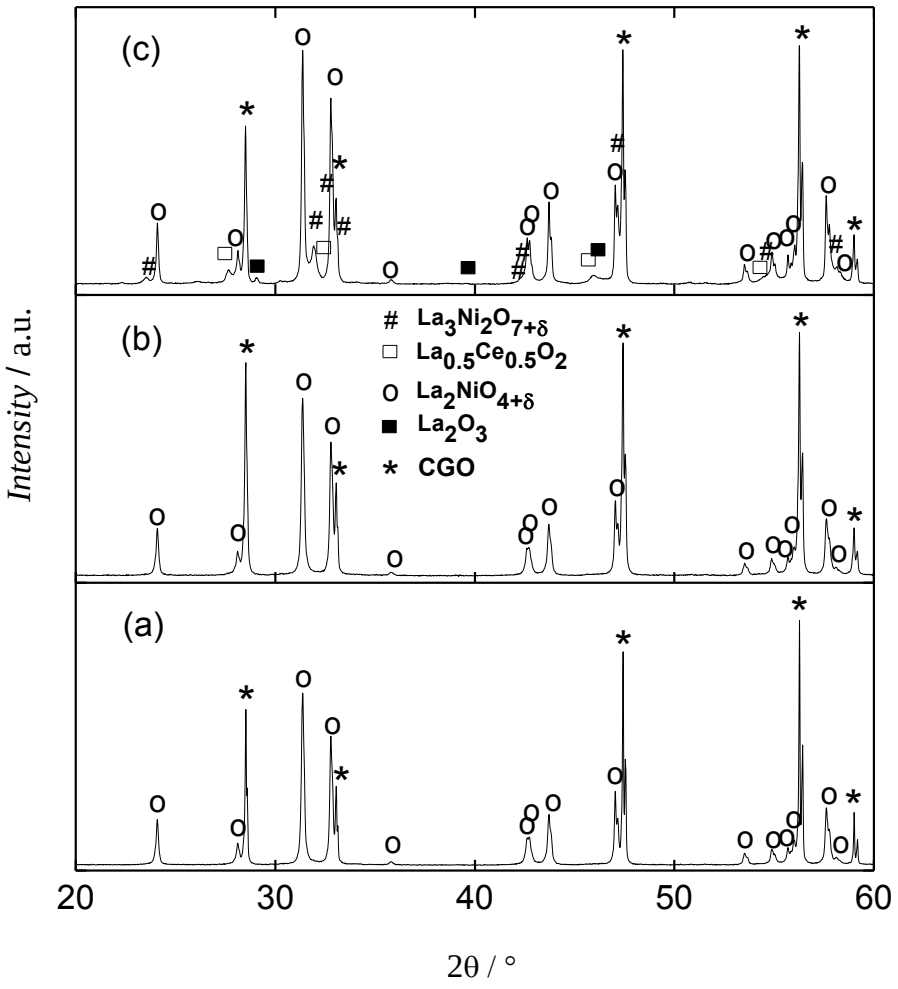

Fig. 8 XRD patterns of LNO film prepared by ESD (sample 2) after heat treatment for 10 days at (a) 700 °C, (b) 800 °C, (c) 1100 °C.

Indeed porosity is expected to improve the diffusion of molecular O_2. As a consequence, it can enhance the reactivity of LNO with CGO. In this architecture, the dense and thin LNO film could be acting as a barrier layer preventing the direct contact of the gaseous oxygen with the CGO electrolyte, and thus limiting the undesired chemical reactions. One can notice that the heat treatment at 800 °C in air for 10 days is not a sufficient criterion for stability of the electrode for use in SOFCs. However this study is important to mention as

preliminary results, 800°C being a relatively high temperature, which increases the chemical reactivity. Since our objective is to reduce the operating temperature of the SOFC, this LNO material should be a good candidate to be used at 600 °C or 700 °C. Such experiments will be continued using longer annealing times.

4. Conclusions

Different architectural designs based on electrostatic spray and screen-printing deposition were investigated to improve the electrochemical properties of LNO cathodes at moderated temperatures, improving the percolation, the cathode/electrolyte interface adhesion and the contact between the cathode and the current collecting grid. For this purpose various porous nanostructured $La_2NiO_{4+\delta}$ films were successfully coated by ESD on CGO substrates, from which two different microstructures were selected. The films consist of a 3-D coral-like microstructure with or without a thin (~200 nm) dense and continuous cathode/electrolyte interface layer and with a further difference in coverage, average particle size and percolation. A calcination step at only 950 °C for 6 h in air is sufficient for the crystallization of the films (in a pure orthorhombic LNO structural type) with fine particle sizes (100-150 nm) and a good adhesion on CGO. The R_{pol} decreases due to the presence of a thin dense LNO layer between the electrolyte and the porous LNO cathode, which was prepared by ESD in a single step. This thin dense contact enhances the oxygen ion transfer to the electrolyte. When this LNO film, formed by a thin dense interlayer covered by a 3D coral microstructure layer, is topped by a screen-printed porous LNO current collector film, a drastic reduction of the R_{pol} down to 0.08 $\Omega.cm^2$ at 700 °C was obtained, which to the best of our knowledge is so far the lowest value reported in the literature for the pure $La_2NiO_{4+\delta}$ cathode. This substantially improved electrochemical performance is related to a decrease of the ohmic and polarization resistances due to an improved electric contact between the cathode and the current collector. As highlighted throughout this work, the cathode architecture is of great importance for obtaining a good electrochemical performance, as the gas/solid and solid/solid interfaces are crucial for the ORR to take place. Moreover, $La_2NiO_{4+\delta}$ films are chemically stable and no reactivity between them and CGO electrolyte has been observed after a heat treatment at 800 °C in air for 10 days. In summary, this double layer (ESD + SP) $La_2NiO_{4+\delta}$ cathode is very promising and it seems that it is an optimistic strategy to enhance the cathode electrochemical properties for further research towards lowering the operating temperature of SOFCs.

Acknowledgements

This work was performed within the framework of the Centre of Excellence of Multifunctional Architectured Materials "CEMAM" n° AN-10-LABX-44-01 funded by the "Investments for the Future" Program. The authors would like to thank S. Coindeau and T. Encinas for XRD and R. Martin for SEM and EDX analyses in CMTC (Grenoble INP, France). M. Burriel also acknowledges financial support from the Spanish Economy and Competitiveness Ministry through the "Juan de la Cierva" fellowship program.

References:

[1] A. Aguadero, L. Fawcett, S. Taub, R. Woolley, K.-T. Wu, N. Xu, S.J. Skinner, Materials development for intermediate-temperature solid oxide electrochemical devices, Journal of Materials Science 47 (2012) 3925-3948.
[2] J. A. Kilner, M. Burriel, Materials for Intermediate-Temperature Solid-Oxide Fuel Cells, Annual Review of Materials Research 44 (2014) 365-393.
[3] A. Orera, P. R. Slater, New Chemical Systems for Solid Oxide Fuel Cells, Chemistry of Materials 22 (2010) 675-690.
[4] A. J. Jacobson, Materials for Solid Oxide Fuel Cells, Chemistry of Materials 22 (2010) 660-674.
[5] S.J. Skinner, J.A. Kilner, Oxygen diffusion and surface exchange in $La_{2-x}Sr_xNiO_{4+\delta}$. Solid State Ionics 135 (2000) 709-712.
[6] E. Boehm, J. M. Bassat, M.C. Steil, P. Dordor, F. Mauvy, J. C. Grenier, Oxygen transport properties of $La_2Ni_{1-x}Cu_xO_{4+\delta}$ mixed conducting oxides, Solid State Science 5 (2003) 973-981.
[7] F. Mauvy, C. Lalanne, J.M. Bassat, J.C. Grenier, H. Zhao, L. Huo, P. Stevens, Electrode properties of $Ln_2NiO_{4+\delta}$ ($Ln = La, Nd, Pr$) AC Impedance and DC Polarization Studies, J. Electrochem. Soc. 153 (2006) 1547-1553.
[8] A. Tarancón, M. Burriel, J. Santiso, S. J. Skinner, J.A. Kilner, Advances in layered oxide cathodes for intermediate temperature solid oxide fuel cells, Journal of Materials Chemistry 20 (2010) 3799-3813.
[9] H. Inaba, H. Tagawa, Ceria-based solid electrolytes, Solid State Ionics 83 (1996) 1-16.
[10] L.M. Tai, M.M. Nasrallah, H.U. Anderson, D.M. Sparlin, S.R. Sehlin, Structure and electrical properties of $La_{1-x}Sr_xCo_{1-y}Fe_yO_3$. Part 2. The system $La_{1-x}Sr_xCo_{0.2}Fe_{0.8}O_3$, Solid State Ionics 76 (1995) 273-283.
[11] L.M. Tai, M.M. Nasrallah, H.U. Anderson, D.M. Sparlin, S.R. Sehlin, Structure and electrical properties of $La_{1-x}Sr_xCo_{1-y}Fe_yO_3$.Part 1. The system $La_{0.8}Sr_{0.2}Co_{1-y}Fe_yO_3$, Solid State Ionics 76 (1995) 259-271.
[12] B.C.H. Steele, Appraisal of $Ce_{1-y}\ Gd_y\ O_{2-y/2}$ electrolytes for IT-SOFC operation at 500°C, Solid State Ionics 129 (2000) 95-110.

[13] G. Amow, I.J. Davidson, S.J. Skinner, A comparative study of the Ruddlesden-Popper series, $La_{n+1}Ni_nO_{3n+1}$(n=1, 2 and 3), for solid-oxide fuel-cell cathode applications, Solid State Ionics 177 (2006) 1205-1210.
[14] D. Huang, Q. Xu, F. Zhang, W. Chen, H.-X. Liu, J. Zhou, Synthesis and electrical conductivity of $La_2NiO_{4+\delta}$ derived from apolyaminocarboxylate complex precursor, Materials Letters 60 (2006) 1892-1895.
[15] R. Sayers, M. Rieu, P. Lenormand, F. Ansart, J.A. Kilner, S.J. Skinner, Development of lanthanum nickelate as a cathode for use in intermediate temperature solid oxide fuel cells, Solid State Ionics 192 (2011) 531-534.
[16] N. Hildenbrand, P. Nammensma, D.H.A. Blank, H. J.M. Bouwmeester, B. A. Boukamp, Influence of configuration and microstructure on performance of $La_2NiO_{4+\delta}$ intermediate-temperature solid oxide fuel cells cathodes, Journal of Power Sources 238 (2013) 442-453.
[17] B. Philippeau, F. Mauvy, C. Mazataud, S. Fourcade, J.C. Grenier, Comparative study of electrochemical properties of mixed conducting $Ln_2NiO_{4+\delta}$ (Ln=La, Pr and Nd) and $La_{0.6}Sr_{0.4}Fe_{0.8}Co_{0.2}O_{3-\delta}$ as SOFC cathodes associated to $Ce_{0.9}Gd_{0.1}O_{2-\delta}$, $La_{0.8}Sr_{0.2}Ga_{0.8}Mg_{0.2}O_{3-\delta}$ and $La_9Sr_1Si_6O_{26.5}$ electrolytes, Solid State Ionics 249 (2013) 17-25.
[18] V. Vibhu, A. Rougier, J.C. Grenier, J.M. Bassat, Mixed Nickelates $Pr_{2-X}La_xNiO_{4+\delta}$ Used as Cathodes in Metal Supported SOFCs, ECS Trans. 57 (2013) 2093-2100.
[19] K. Hayashi, O. Yamamoto, Y. Nishigaki, H. Minoura, Sputtered $La_{0.5}Sr_{0.5}MnO_3$–yttria stabilized zirconia composite film electrodes for SOFC, Solid State Ionics 98 (1997) 49-55.
[20] H.B. Wang, J.F. Gao, D.K. Peng, G.Y. Meng, Plasma deposition of $La_{0.8}Sr_{0.2}MnO_3$ thin films on yttria-stabilized zirconia from aerosol precursor, Mater. Chem. Phys. 72 (2001) 297-300.
[21] M. Burriel, G. Garcia, M. Rossell, A. Figueras, G. Van Tendeloo, J. Santiso, Enhanced High-Temperature Electronic Transport Properties in Nanostructured Epitaxial Thin Films of the $La_{n+1}Ni_nO_{3n+1}$ Ruddlesden-Popper Series (n) 1, 2, 3, ∞), Chem. Mater. 19 (2007) 4056-4062.
[22] G. Garcia, M. Burriel, J. Santiso, N. Bonanos, Electrical Conductivity and Oxygen Exchange Kinetics of La_2NiO_{4+d}Thin Films Grown by Chemical Vapor Deposition, J. Electrochem. Soc. 155 (2008) 28-32.
[23] G.L. Bertrand, G. Caboche, L.C. Dufour, Low-pressure-MOCVD $LaMnO_{3\pm d}$ very thin films on YSZ (100) optimized for studies of the triple phase boundary, Solid State Ionics 129 (2000) 219-235.
[24] T. Nguyen, E. Djurado, Deposition and characterization of nanocrystalline tetragonal zirconia films using electrostatic spray deposition, Solid State Ionics 138 (2001) 191-197.
[25] I. Taniguchi, R.C. van Landschoot, Schoonman, J. Fabrication of $La_{1-x}Sr_xCo_{1-y}Fe_yO_3$ thin films by electrostatic spray deposition, Solid State Ionics 156 (2003) 1-13.
[26] C.H. Chen, M.H.J. Emond, E.M. Kelder, B. Meester, Schoonman, J. Electrostatic Sol-Spray Deposition of Nanostructured Ceramic Thin Films, J. Aerosol. Sci. 30 (1999) 959-967.
[27] D. Marinha, C. Rossignol, E. Djurado, Influence of electrospraying parameters on the microstructure of $La_{0.6}Sr_{0.4}Co_{0.2}F_{0.8}O_{3-\delta}$ films for SOFCs, Journal of Solid State Chemistry 182 (2009) 1742-1748.

[28] D. Marinha, L. Dessemond, E. Djurado, Comprehensive Review of Current Developments in IT-SOFCs, Current Inorganic Chemistry 3 (2013) 2-22.
[29] J. Rodriguez-Carvajal, Recent advances in magnetic structure determination by neutron powder diffraction, Physica B 192 (1993) 55-69.
[30] R. Neagu, D. Perednis, A. Princivalle, E. Djurado, Initial Stages in Zirconia Coatings Using ESD, Chem. Mater. 17 (2005) 902-910.
[31] A. Lintanf, A. Mantoux, E. Blanquet, E. Djurado, Elaboration of Ta_2O_5 Thin Films Using Electrostatic Spray Deposition for Microelectronic Applications, J. Phys. Chem. C. 111 (2007) 5708-5714.
[32] C.H. Chen, E.M. Kelder, P.J.J.M. Van der Put, Schoonman, J. Morphology control of thin $LiCoO_2$ films fabricated using the electrostatic spray deposition (ESD) technique, J. Mater. Chem. 6 (1996) 765-771.
[33] A. Princivalle, E. Djurado, Nanostructured LSM/YSZ composite cathodes for IT-SOFC: A comprehensive microstructural study by electrostatic spray deposition, Solid State Ionics 179 (2008) 1921-1928.
[34] A. M. Gañan-Calvo, J. Davila, A. Barrero, Current and droplet size in the electrospraying of liquids. Scaling laws, J. Aerosol Science 28 (1997) 249-275.
[35] S. Mahiuddin, B. Minofar, J.M. Borah, , M.R. Das, P. Jungwirth, , Propensities of oxalic, citric, succinic, and maleic acids for the aqueous solution/vapour interface: Surface tension measurements and molecular dynamics simulations, Chemical Physics Letters 462 (2008) 217–221.
[36] R.P.A. Hartman, J-P. Borra, J.C.M. Marijnissen, B. Scarlett, Development of electrohydrodynamic sprays related to space charge effects, J. of Aerosol Sci. 27 (1996) 177-178.
[37] J.A.D. Lange, Handbook of Chemistry, 14th edn., Mc Graw-Hill Inc. New York. 1992.
[38] C. Fu, K. Sun, N. Zhang, X. Chen, D. Zhou, electrochemical characteristics of LSCF-SDC composite cathode for intermediate temperature SOFC, Electrochim. Acta 52 (2007) 4589-4594.
[39] C. Nicollet, A. Flura, V. Vibhu, A. Rougier, J.M. Bassat, J.C. Grenier, $La_2NiO_{4+\delta}$ infiltrated into gadolinium doped ceria as novel solid oxide fuel cell cathodes: Electrochemical performance and impedance modeling, Journal of Power Sources 294 (2015) 473-482.
[40] J.A. Kilner, C.K.M. Shaw, Mass transport in $La_2Ni_{1-x}Co_xO_{4+\delta}$ oxides with the K_2NiF_4 sturcture, Solid State Ionics 154 (2002) 523-527.
[41] A. Montenegro-Hernandez, J. Vega-Castillo, L. Mogni, A. Caneiro, Thermal stability of Ln_2 $NiO_{4+\delta}$ (Ln: La, Pr, Nd) and their chemical compatibility with YSZ and CGO solid electrolytes, International Journal of Hydrogen Energy 36 (2011) 15704-15714.
[42] A. Montenegro-Hernandez, A. Soldati, L. Mogni, H. Troiani, A. Schreiber, F. Soldera, A. Caneiro, Reactivity at the $Ln_2NiO_{4+\delta}$/electrolyte interface (Ln = La, Nd) studied by Electrochemical Impedance Spectroscopy and Transmission Electron Microscopy, Journal of Power Sources 265 (2014) 6-13.

[43] G. Amow, P.S. Whitfield, I.J. Davidson, R.P. Hammond, C.N. Munnings, S.J. Skinner, Structural and sintering characteristics of the $La_2Ni_{1-x}Co_xO_{4+\delta}$ series, Ceramics International 30 (2004) 1635-1639.

[44] R. Sayers, J. Liu, B. Rustumji, S.J. Skinner, Novel K_2NiF_4-Type Materials for Solid Oxide Fuel Cells: Compatibility with Electrolytes in the Intermediate Temperature Range, Fuel Cells 8 (2008) 338-343.

[45] M. Figueiredo, J.A. Labrincha, J.R. Frade, F.M.B. Marques, Reactions between a zirconia-based electrolyte and $LaCoO_3$-based electrode materials, Solid State Ionics 101 (1997) 343-349.

Supporting Information

Compositional analysis by EDX has been given in **Fig. S1**. SEM surface view of calcined LNO films (950 °C for 6 h) are given at larger magnification in Fig. S2and S3to evaluate the ESD process parameters effect on particle size.

Fig.S1.Typical EDX spectrum of the LNO film deposited on CGO substrate by ESD after calcination at 950°C for 6 h in air.

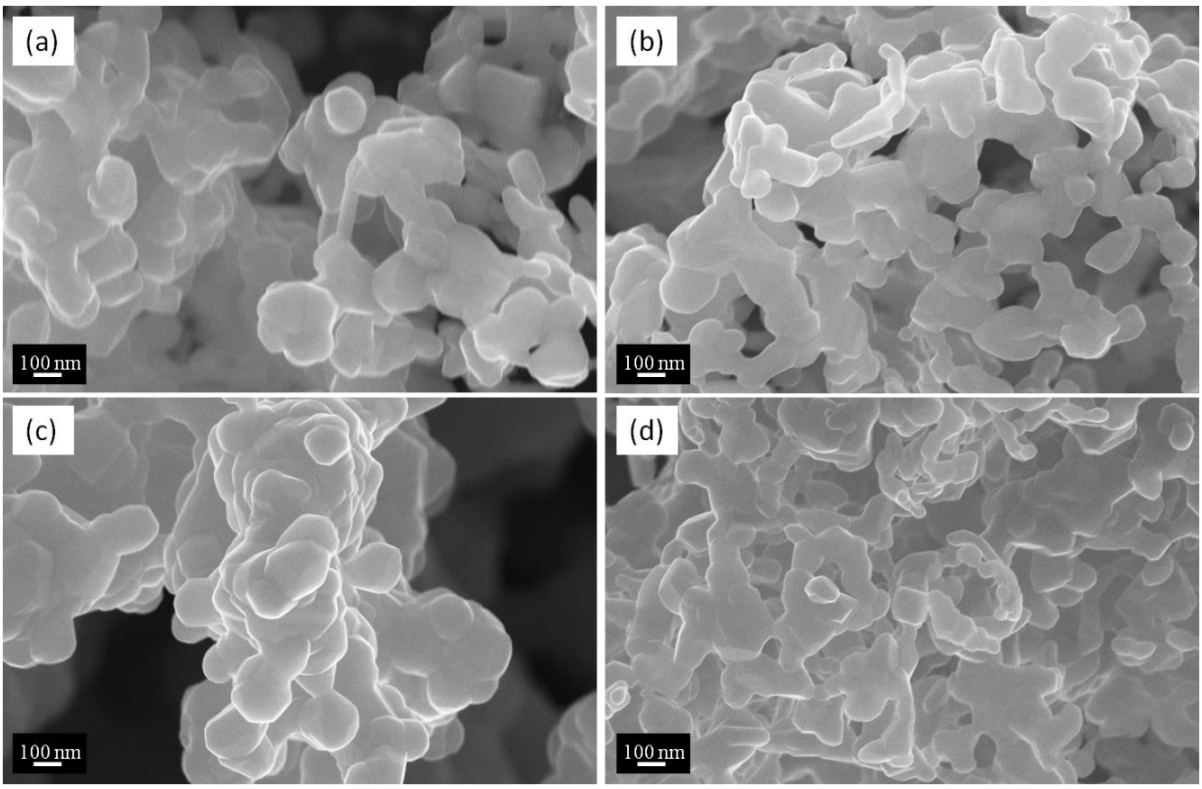

Fig. S2 SEM surface microstructures (larger magnification) of the calcined LNO films (950 °C for 6 h) deposited by ESD at 300°C, 30 mm and 1.0 $mL.h^{-1}$ after deposition time of: (a) 1.33 h, (b) 2.17 h, (c) 4 h, (d) 6.67 h.

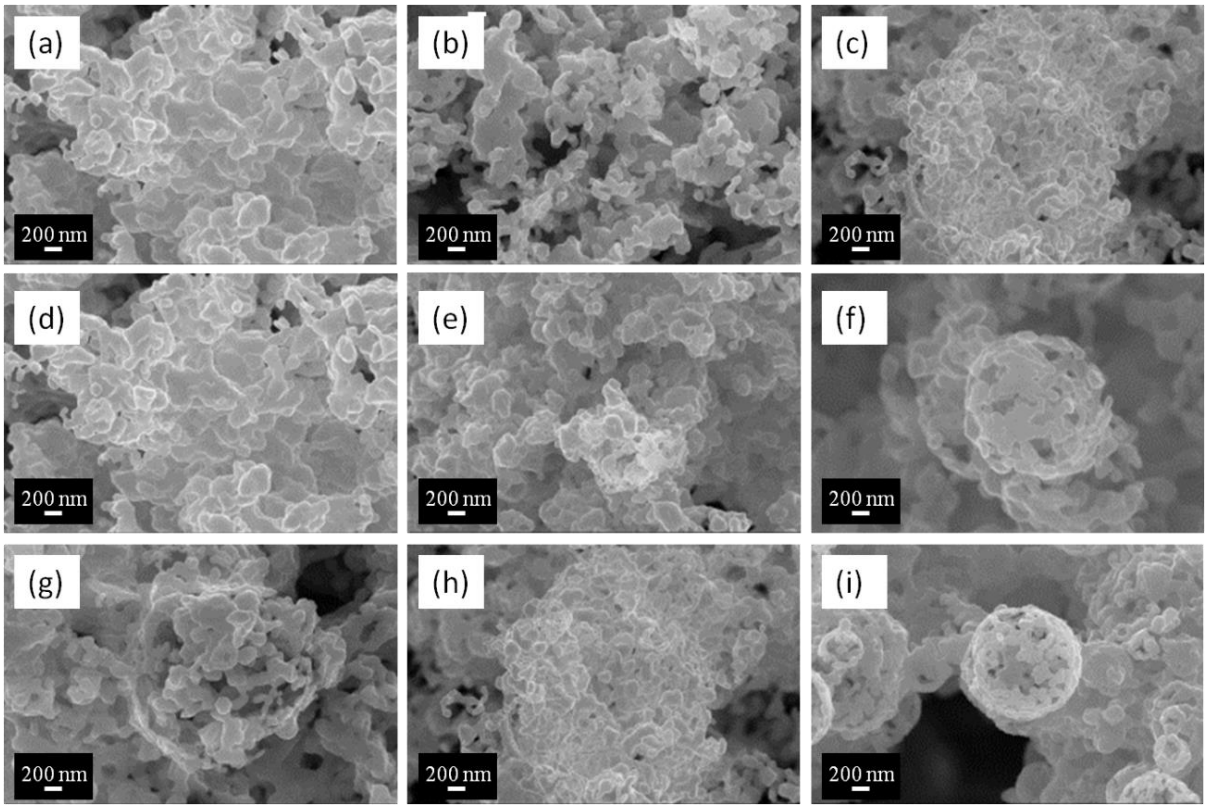

Fig. S3 SEM surface microstructures (larger magnification) of the calcined LNO films (950 °C for 6 h) using pure EtOH and coated at: nozzle-to-substrate distance of (a) 20 mm (b) 30 mm and (c) 50 mm and at fixed 1.0 $mL.h^{-1}$, 300 °C and 1.33 h; at: substrate temperature of (d) 300°C (e) 400°C (f) 450°C and at fixed 1.0 $mL.h^{-1}$, 30 mm and 1 h ; at flow rate of (g) 0.5 $mL.h^{-1}$ (h) 1.0 $mL.h^{-1}$ and (i) 1.5 $mL.h^{-1}$, and at fixed 300 °C, 30 mm and 2 h.

Chapter 3

Efficient 3-D coral $La_{2-x}Pr_xNiO_{4+\delta}$ SOFC cathodes: a compromise in electrochemical performance and chemical stability

R. K. Sharma, Seng-Kian Cheah M. Burriel, L. Dessemond, J.-M. Bassat and E. Djurado, submitted to *J. Mater. Chem. A*.

Efficient 3-D coral $La_{2-x}Pr_xNiO_{4+\delta}$ SOFC cathodes: a compromise in electrochemical performance and chemical stability

Rakesh K. Sharma[a, b, c], Seng-Kian Cheah[a, b], Mónica Burriel[d], Laurent Dessemond[a, b], Jean-Marc Bassat[c], Elisabeth Djurado[a, b*]

[a] Univ. Grenoble Alpes, LEPMI, F-38000 Grenoble, France
[b] CNRS, LEPMI, F-38000 Grenoble, France
[c] ICMCB, CNRS, Université Bordeaux, 33608 PESSAC, France
[d] Catalonia Univ. Grenoble Alpes, CNRS, LMGP, F-38000 Grenoble, France

*Corresponding author: Elisabeth Djurado
E-mail: elisabeth.djurado@lepmi.grenoble-inp.fr, Tel: +33-476826684; Fax: +33-476826777

Abstract:

Architecturally designed $La_{2-x}Pr_xNiO_{4+\delta}$ (with x = 0, 0.5, 1 and 2) cathodes on $Ce_{0.9}Gd_{0.1}O_{2-\delta}$ (CGO) electrolyte have been prepared with a view to taking advantage of the complimentary properties of the two extreme compositions $La_2NiO_{4+\delta}$ and $Pr_2NiO_{4+\delta}$, i.e. superior stability of $La_2NiO_{4+\delta}$ and higher electronic conductivity of $Pr_2NiO_{4+\delta}$. The design consists of a stacking of two layers starting with a 3-D tree-like microstructure (~20 μm thick) over a thin dense base layer (~100 nm) fabricated in one step by electrostatic spray deposition (ESD) and then topped by a screen-printed (SP) current collecting layer of the same composition. X-ray diffraction confirms the formation of a complete solid solution crystallizing in a single phase orthorhombic structure with Fmmm space group. The chemical stability and polarisation resistance (R_{pol}) decrease by increasing the Pr content. Among the complete $La_{2-x}Pr_xNiO_{4+\delta}$ solid solution, $LaPrNiO_{4+\delta}$ shows the best compromise between electrochemical properties (the lowest R_{pol} value available in the literature for this composition, 0.12 Ω cm^2 at 600 °C) and chemical stability in air (up to 30 days at 700 °C). Moreover, an anode supported single cell (Ni-3YSZ/Ni-8YSZ/8YSZ/CGO) including $LaPrNiO_{4+\delta}$ double layered electrode shows a maximum power density of 438 mW cm^{-2} at 700 °C.

Keywords: $La_{2-x}Pr_xNiO_{4+\delta}$ solid solution, Electrostatic Spray Deposition, IT-SOFC, EIS.

1. Introduction

Solid oxide fuel cells (SOFCs) convert chemical energy directly into electric power in a highly efficient way. The main objective of SOFC devices is to reduce the operating temperature from 1000 °C to intermediate temperatures (500 -700°C). However, the electrochemical activity of the cathode deteriorates dramatically with decreasing temperature. Thus there has been considerable attention on the investigation of efficient oxygen electrodes or cathodes which show good cathodic performance in the intermediate-temperature range.[1, 2]

In this context, mixed ionic-electronic conductors (MIEC), particularly, A_2MO_4 oxides (A = rare earth, alkaline earth; M = transition metal) with K_2NiF_4-type structure have attracted much attention[3, 4] due to their interesting structure, transport and catalytic performance.[5, 6] The K_2NiF_4-type structure consists of a combination of AMO_3 perovskite and AO rock-salt layers arranged alternately.[7] They can accomodate hyperstoichiometric oxygen in interstitial lattice sites in the rocksalt layers of the structure. Ni-based K_2NiF_4-type oxides present high oxygen diffusivity and surface reaction rate[5, 8] and also show higher thermochemical stability than perovskite-type oxide based cathodes.[9] Dailly et al. have reported that the Ruddlesden-Popper-type nickelate compounds such as $Ln_2NiO_{4+\delta}$ (Ln = La, Nd and Pr) are promising cathode materials for IT-SOFC.[10] The polarization resistance (R_{pol}) value at 700 °C, was found to decrease from 5.2 to 1.5 and 0.6 Ω cm^2 for $La_2NiO_{4+\delta}$, $Nd_2NiO_{4+\delta}$ and $Pr_2NiO_{4+\delta}$, respectively. However the R_{pol} value is still too high since the targeted value is expected to be around 0.15 Ω cm^2 for a good cathode.[11] There are several strategies to minimize it, such as the control of the microstructure and the design of the electrode's architecture.[12] For instance, it is possible to maximize the electrocatalytic activity by adding a dense base-layer with small particle size adjacent to the electrolyte.[13] This thin dense layer has been shown to improve the electrolyte/electrode contact and hence enhance the oxygen transfer to the electrolyte. Sayers et al. have reported a decrease in the R_{pol} value of $La_2NiO_{4+\delta}$ cathode from 7.4 to 1.0 Ω cm^2 at 700 °C when a compact $La_2NiO_{4+\delta}$ (~1-2 μm) has been used prior to porous SP electrode.[14] Hildenbrand et al. have also shown that the insertion of a dense base-layer improves the $La_2NiO_{4+\delta}$ electrode footprint, lowers the sintering temperature and enlarges the triple phase boundary (TPB) region. Consequently a decrease of R_{pol} of ~ 30 % at 600 °C (from 1.2 to 0.85 Ω cm^2) has been reported for $La_2NiO_{4+\delta}$ cathode.[15] Recently, Sharma et al. [12] reported the lowest R_{pol} values down to 0.42 and 0.08 Ω cm^2 at 600 °C for $La_2NiO_{4+\delta}$ and $Pr_2NiO_{4+\delta}$, respectively. The cathodes consisted of an architecturally designed 3D coral-like microstructure grown on $Ce_{0.9}Gd_{0.1}O_{2-\delta}$ (CGO) electrolyte with a thin (~100 nm) dense and

continuous cathode/electrolyte interface layer. Another approach to improve the electrochemical performance is to increase the surface area of the bulk electrode to enhance the number of active surface sites.[16] The most promising $Pr_2NiO_{4+\delta}$ electrode has been obtained for a mean particle size of ~ 0.4 μm (R_{pol} value down to 0.08 Ω cm^2 at 600 °C).[17] Although $Pr_2NiO_{4+\delta}$ exhibits excellent electrochemical properties at intermediate temperatures[17], it has a rather poor chemical stability in comparison to $La_2NiO_{4+\delta}$.[18] In fact $Pr_2NiO_{4+\delta}$ decomposes to $Pr_4Ni_3O_9$ and $PrO_{1.71}$ at 800 °C.[19, 20]

The preparation of efficient oxygen electrode materials which present very low degradation rates is still a challenge. A little attention has been paid to the substitution on the A-site of the A_2BO_4 oxides in order to find the best electrochemical and stability properties.[21, 22] So this work aims to investigate Pr doped lanthanum nickelates, $La_{2-x}Pr_xNiO_{4+\delta}$ with $0 \leq x \leq 2$ by controlling the architecture as single and double layered electrode using electrostatic spray deposition (ESD) and screen-printing (SP). The phase structure, microstructure, chemical stability and electrochemical properties are discussed with the aim of finding the best compromise between chemical stability and electrochemical performance.

2. Experimental

2.1. Film preparation and powder synthesis

Pr doped $La_2NiO_{4+\delta}$ films ($La_{2-x}Pr_xNiO_{4+\delta}$ with x = 0, 0.5, 1 and 2) have been deposited on CGO ($Ce_{0.9}Gd_{0.1}O_{2-\delta}$) substrates by electrostatic spray deposition (ESD) in a vertical set-up configuration[23, 24] and by screen-printing (SP). The ESD technique is a method for coating films based on the principle of electrostatic atomization. A positive high voltage is applied to the stainless steel nozzle from which positively charged droplets are generated and directed to the grounded substrate. For the films fabricated by ESD, precursor solutions of 0.02 M (total cation concentration) in the mixture of ethanol and water (1:2) (C_2H_5OH, Prolabo, 99.9%, referred as EtOH) for x = 0, 0.5, 1 and 2 were prepared. Predetermined amount of $La(NO_3)_3.6\ H_2O$ (Acros Organics, 99%), $Pr(NO_3)_3.6\ H_2O$ (Acros Organics, 99%) and $Ni(NO_3)_2\ 6\ H_2O$ (Fisher Scientific, 98%) salts and citric acid, 20 mol. % in excess [$C_6H_8O_7$, 99.9%, Alfa Aesar] acting as a chelating agent were used as precursors. During the ESD deposition, the voltage was fixed to approximately 13 kV. A film of each composition was deposited for 180 minutes at a substrate temperature, nozzle to substrate distance and flow rate of 350 °C, 50 mm and for 1.5 mL h^{-1}, respectively, values optimized in our previous work.[12] As-deposited

films for $0 \leq x \leq 1$ were annealed in air at 950 °C for 6 h while a heat treatment at 1100 °C for 4 h was required to get crystallization of the $Pr_2NiO_{4+\delta}$ films. For the ink preparation for the electrodes prepared by SP, $La_{2-x}Pr_xNiO_{4+\delta}$ powders with x = 0, 0.5, 1 and 2 have been synthesized at 150 °C by the auto-combustion method using the same precursor solution as for the ESD process but using pure ethanol as a solvent. The crystallization of the powders was obtained by sintering using the same conditions as for corresponding ESD films. The $La_{2-x}Pr_xNiO_{4+\delta}$ ink was prepared by mixing this crystalline powder into a commercial dispersant (KD2921, Zschimmer and Schwarz).

2.2. Symmetric and single cell preparation

Single layer (ESD) and double layer (ESD+SP) cathodes were fabricated on CGO electrolyte as symmetrical cells (electrode//CGO//electrode) and their electrochemical performance has been evaluated by electrochemical impedance spectroscopy (EIS). Dense pellets of CGO, made by pressing discs (Ø = 19.6 mm in diameter, 1.2 mm thick) of commercial powder (Solvay) and subsequently fired at 1400 °C for 4 h, were used as the electrolyte. The double layer cathode was prepared in two different steps: i) in a first step, a single layer cathode was deposited on both sides of CGO substrate by ESD and sintered and ii) in a second step, a screen-printed current collecting layer (CCL) was coated on the single layer ESD cathode and sintered in air for 2 h at 1050 °C in air followed by 0.5 h at 1100 °C. The cathode area is 2.0 cm^2 for the single layer and 1.54 cm^2 for the double layer architecture. In addition a complete cell was fabricated starting from a commercial anode supported half cell (supplied by HC Starck producer) made of a 500 μm thick Ni-3YSZ anode topped by a 8-10 μm thick Ni-8YSZ functional layer and a 5 μm thick 8YSZ electrolyte membrane (Ø = 40 mm). A CGO layer of 5 μm thickness (Ø = 40 mm) was first deposited as a barrier layer on Ni-3YSZ//Ni-8YSZ//8YSZ support by ESD. The selected ESD conditions used to coat the dense CGO thin layer had been previously optimized[25] and are the following: The total concentration of salts ($Ce(NO_3)_3 \cdot 6H_2O$ (Prolabo rectapur, 99.5%) and $Gd(NO_3)_3 \cdot 6H_2O$ (Aldrich Chemical Company Inc, 99.9%) salts in adequate stoichiometry) was fixed at 0.005 M in diethylene glycol monobutyl ether, known as butyl carbitol ($C_8H_{17}O_2OH$, Acros Organics, >99%). The substrate temperature, nozzle to substrate distance and flow rate were fixed at 300 °C, 45 mm and 0.5 mL h^{-1}, respectively, for a deposition time of 15 minutes. A sintering for 2 h in air at 800 °C was sufficient to obtain crystalline CGO. Then the double-

layered $LaPrNiO_{4+\delta}$ cathode (active area = 1.54 cm^2) was deposited by ESD followed by SP in the same way as the double layer symmetric cell.

2.3. Physico-chemical characterization

The crystal structure of the powders and films was determined by X-ray diffraction (XRD, Philips X'Pert-MPD system, Cu Kα radiation, λ =1.54056 Å) in the Bragg–Brentano configuration. The ageing test of the $La_{2-x}Pr_xNiO_{4+\delta}$ films was performed in air at 700 °C and 800 °C up to 30 days and the stability was checked by XRD. Each X-ray pattern was refined by profile matching using the Fullprof software[26] in order to determine the lattice parameters. Scanning electron microscopy (ZEISS Ultra 55 instrument) with a field emission gun (FEG) and energy-dispersive X-ray spectroscopy (EDX) analyzer, using an acceleration voltage of 20 keV, were used for the evaluation of the film surface and cross-sectional morphology, and for the composition analysis, respectively. The particle size of the electrodes was estimated from the SEM images using an image analysis tool (Image J software). Inductively coupled plasma mass spectroscopy (ICP-MS) was also used for more precise composition analysis. The oxygen overstoichiometry (δ) of the $La_{2-x}Pr_xNiO_{4+\delta}$ samples (powder scratched from the ESD films) was determined by thermogravimetry measurements (TGA-Q50 thermogravimetric analyzer) under flowing 5% H_2-Ar gas. Data were collected from 20 to 800 °C at 30 °C h^{-1}. The oxygen content was determined by the weight change of $La_{2-x}Pr_xNiO_{4+\delta}$ after reduction in appropriate ratio into La_2O_3, Pr_2O_3 and Ni.

2.4. Electrochemical measurements

2.4.1. Symmetrical cells characterization

The electrochemical properties of the symmetrical cells were characterized by Electrochemical Impedance Spectroscopy (EIS). EIS measurements were carried out using an autolab potentiostat-galvanostat (PGSTAT 302N) in air, from 500 to 700°C, in the frequency range from 0.05 Hz to 100 kHz. The measurements were performed with a signal amplitude of 0.02 V at open circuit potential (OCP), using gold grids (Heraeus, 1024 meshes cm^{-2} woven from 0.06 mm dia. wire) as the current collectors. The EIS diagrams were normalized to the electrode area and fitted using equivalent circuits with the ZView® software (Scribner Associates) were. The polarization resistance (R_{pol}) values were calculated by subtracting the high frequency (HF) intercept from the low frequency (LF) intercept on the real axis of the electrode impedance in the Nyquist plane. The ageing of the $LaPrNiO_{4+\delta}$ cathode was carried

out at 700 °C in OCV condition as well as under polarization (195 mA cm^{-2}) at 600 °C over 500 h in air.

2.4.2. Single cells characterization

The single cell was mounted into the measurement setup (supplied by Fiaxell), with flows of Ar on the cathode and anode sides, respectively. Prior to the single cell measurements, the anode was reduced using the following procedure: after heating in Ar (100 mL min^{-1}) up to 800 °C, the anode side was progressively flushed with hydrogen gas at a flow rate of 80 mL min^{-1}. After 10 h, 3 % water vapor was introduced on anode side along with the hydrogen. On the cathode side, synthetic air was supplied as oxidant at a flow rate of 200 mL min^{-1}. The electrochemical measurements and ageing study were carried out using an autolab potentiostat-galvanostat (PGSTAT 302N) and current booster. The impedance diagrams were recorded at OCV from 550 °C to 800 °C in 50 °C steps. The ageing of the single cell at 700 °C was performed at a potential of 0.7 V.

3. Results and discussion

3.1. Structural properties of $La_{2-x}Pr_xNiO_{4+\delta}$ ($0 \leq x \leq 2$) films

The XRD patterns of the $La_{2-x}Pr_xNiO_{4+\delta}$ ($0 \leq x \leq 2$) films deposited by ESD on the CGO pellet (**Fig. 1 and Fig. S1-S3**) show the presence of two single phases: $Ce_{0.9}Gd_{0.1}O_{2-\delta}$ (ICDD # 04-013-6577) from the substrate and $La_2NiO_{4+\delta}$ (ICDD # 01-074-9394) from the film without any impurities. All $La_{2-x}Pr_xNiO_{4+\delta}$ ($0 \leq x \leq 2$) compositions could be accurately fitted with a single orthorhombic Fmmm space group as shown in **Fig. 1** for $LaPrNiO_{4+\delta}$ and for the remaining compositions in **Fig. S1-S3**.This indicates that the substitution of La by Pr results in a complete solid solution. The lattice parameters and space group for the different compositions are given in **Table 1**. This substitution leads to a linear decrease of the cell parameters and cell volume due to the smaller ionic radius of praseodymium ($r(Pr^{3+})$ = 1.126 Å) with comparison to the one of lanthanum $r(La^{3+})$ =1.16 Å.[27] However other authors[22] have shown the existence of two different space groups, both with orthorhombic structure for the $La_{2-x}Pr_xNiO_{4+\delta}$ solid solution, namely a La-rich one from x = 0 to 0.5 with Fmmm space group, and a Pr-rich one from x = 1.0 to 2.0 with Bmab space group. In the composition range $0.5 < x < 1$, the authors have reported the coexistence of both space groups. Moreover, both space groups, Fmmm and Bmab have been reported for $Pr_2NiO_{4+\delta}$ in the literature.[22, 28] This

work reports for the first time the presence of a complete solid solution. This is probably the consequence of very reactive fine grains (~200 nm, **Fig. S4**),

Table 1. Cell parameters, volume (a, b, c and V) and space group for $La_{2-x}Pr_xNiO_{4+\delta}$ ($0 \leq x \leq 2$)

Sample	a (Å)	b (Å)	c (Å)	V (Å^3)	Space Group
$La_2NiO_{4+\delta}$	5.458(9)	5.462(7)	12.689(2)	378.39	Fmmm
$La_{1.5}Pr_{0.5}NiO_{4+\delta}$	5.448(8)	5.458(4)	12.621(1)	375.37	Fmmm
$LaPrNiO_{4+\delta}$	5.422(5)	5.451(3)	12.604(7)	372.59	Fmmm
$Pr_2NiO_{4+\delta}$	5.394(6)	5.450(8)	12.447(9)	366.02	Fmmm

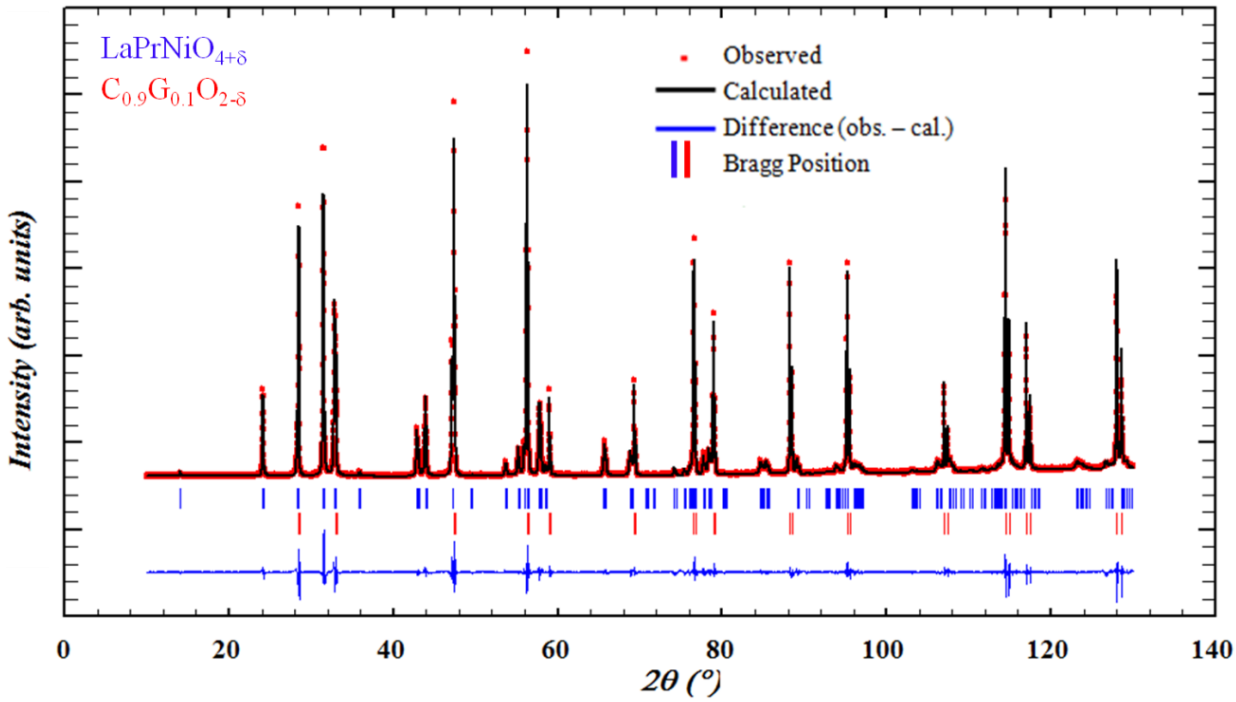

Fig. 1 FULLPROF refinement of the XRD patterns of the $LaPrNiO_{4+\delta}$ film deposited by ESD on a CGO pellet (Fitting parameters: $\chi^2 = 8.52$, Bragg R-factor = 1.45 and RF-factor = 0.98 for $LaPrNiO_{4+\delta}$; Bragg R-factor = 1.33 and RF-factor = 0.70 for CGO.

3.2. Microstructural properties of the $La_{2-x}Pr_xNiO_{4+\delta}$ ($0 \leq x \leq 2$) films

For the ESD process, the microstructure of the obtained films strongly depends on the size of the spray droplets impacting the substrate. It is possible to control the droplet size through the ESD deposition parameters, such as the solution flow rate the distance between the substrate and the nozzle and substrate temperature.[29] Regardless of the Pr content, all the $La_{2-x}Pr_xNiO_{4+\delta}$ films are approximately 20 μm thick and show a similar porous 3-D coral type microstructure, as shown in **Fig. S4**. As an example, the microstructure and schematic diagram of the $LaPrNiO_{4+\delta}$ cathode are shown in **Fig. 2(a)-(c)** and **Fig. 2d**, respectively. Such coral microstructures are the consequence of the preferential landing of the aerosol droplets on the CGO substrate, as nearly dry aerosol droplets impact the substrate. Indeed, the droplets undergo a decrease in size due to the long flight time for the large nozzle to substrate distance (50 mm) and due to the solvent evaporation, since the substrate is heated at 350 °C.[30] This 3-D coral microstructure is highly porous with sub-micron sized grains (~ 150 nm for x = 1 and ~ 200 nm for x = 2) and has uniformly distributed micro-pores throughout the different Pr content as shown in **Fig. S4 (b), (f), (j)** and **(n)**. A larger crystal growth is expected for $Pr_2NiO_{4+\delta}$ in comparison to $La_{2-x}Pr_xNiO_{4+\delta}$, $0 \leq x < 1$) since a higher sintering temperature is required to obtain the pure $Pr_2NiO_{4+\delta}$ crystallized phase (1100 °C for 4 h for $Pr_2NiO_{4+\delta}$ against 950 °C for 6 h for $La_2NiO_{4+\delta}$). A thin dense base-layer (~ 100 nm thick) is also present at the electrolyte-electrode interface for all Pr contents, as shown in **Fig. S4 (d), (h), (p)** and **(l)**. This thin dense layer appears due to the spreading of the first ESD droplets of precursor solution arriving on the CGO substrate, as reported previously.[12] A large spreading is obtained on a smooth surface and then a rough surface is progressively appears with time. Indeed, as time deposition is increases, the charges on the substrate surface induced by the strong electrostatic field applied concentrate more where the curvature is larger.[31] So, the charged droplets arriving at the surface will be more attracted towards these more curved areas and a coral-type growth appears. This is referred to as ‘‘preferential landing’’. A porosity of approximately 84 ± 2 vol. % was estimated for all electrodes by comparing the apparent film density with the theoretical density. The apparent density was obtained by weighing the CGO substrate before and after the film deposition and measuring the film thickness and diameter. These values are in good agreement with the ones estimated (from 67 to 87 vol. %) by 3D volume reconstruction using X-ray nanotomography for a CGO/LSCF ($La_{0.6}Sr_{0.4}Co_{0.2}Fe_{0.8}O_{3-\delta}$) film with a similar coral microstructure, as previously reported by

Sar et al.[32] Such large porosity with fine microstructure is required for the triple-phase boundary (TPB) increase and beneficial for the transport of oxygen gas molecules.

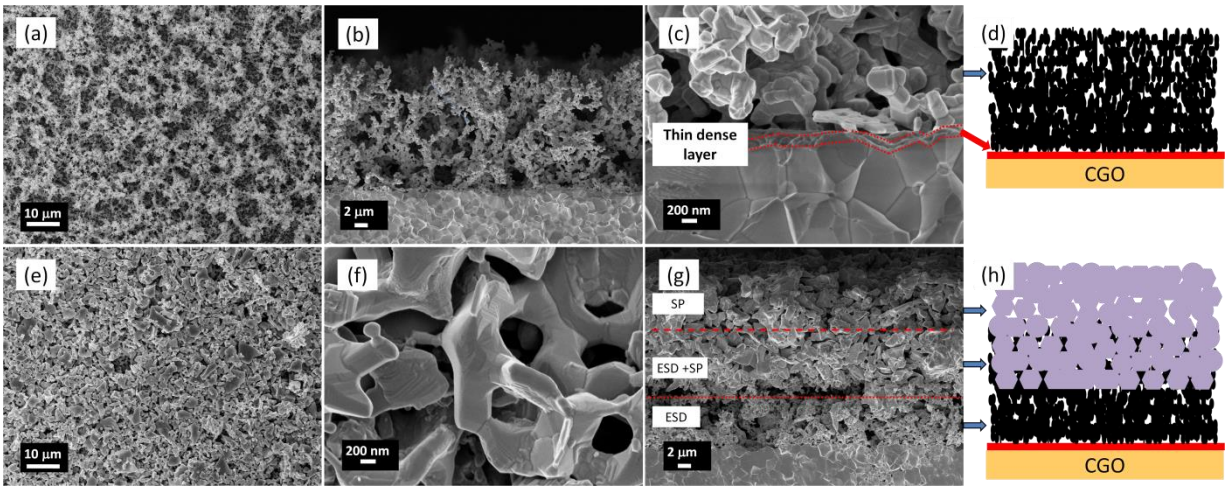

Fig. 2 SEM micrographs of the $LaPrNiO_{4+\delta}$ electrode on a CGO substrate, single layer: (a) surface, (b, c) cross section, (d) schematic diagram; and double layer: (e) surface, (f, g) cross section, (h) schematic diagram.

A double layer architecture of $La_{2-x}Pr_xNiO_{4+\delta}$ ($0 \leq x \leq 2$) films has been proposed by stacking a SP layer on the top of an ESD one of the same composition, previously deposited on CGO. The microstructure of the double layer cathodes are shown in **Fig. S5**. **Fig. 2(e)-(g)** and **Fig. 2h** show the microstructure and schematic diagram of the $LaPrNiO_{4+\delta}$ cathode. It is obvious that the SP layer improves the flatness of the air-electrode interface and hence will increase the contact between the current collecting grid and electrode. Moreover, the 20 µm thick SP layer partially penetrates (~ 50 %) the 3-D coral type electrode without damaging it, as shown in **Fig. S5 (c)**, **(f)**, **(i)** and **(l)**. This SP layer is expected to improve the lateral percolation as well. The average particle size of the screen-printed layer sintered in the same conditions for all electrodes is of approximately 450 nm (**Fig. 2(f)** and **Fig. S5**).

3.3. Compositional properties of $La_{2-x}Pr_xNiO_{4+\delta}$ ($0 \leq x \leq 2$) films

Inductively coupled plasma mass spectrometry (ICP-MS) and EDX, used for the quantitative analysis, confirm the presence of only La, Pr and Ni elements (**Table 2**). **Table 2** also shows that the La/Ni, Pr/Ni and La/Pr ratios are in good agreement with the theoretical values.

Table 2. EDX and ICP-MS quantitative analyses of $La_{2-x}Pr_xNiO_{4+\delta}$ (with x = 0, 0.5, 1 and 2) films

			$La_2NiO_{4+\delta}$	$La_{1.5}Pr_{0.5}NiO_{4+\delta}$	$LaPrNiO_{4+\delta}$	$Pr_2NiO_{4+\delta}$
La/Ni	Theoretical		2.0	1.5	1.0	-----
	Experimental	ICP-MS	1.99	1.43	0.99	-----
		EDX	1.99	1.58	1.09	-----
Pr/Ni	Theoretical		-----	0.5	1.0	2.0
	Experimental	ICP-MS	-----	0.45	0.99	1.98
		EDX	-----	0.48	1.01	2.06
La/Pr	Theoretical		-----	-----	1.0	-----
	Experimental	ICP-	-----	3.17	0.99	-----
		EDX	-----	3.28	1.08	-----

The oxygen over-stoichiometry (δ), determined by TGA, was determined from the TGA curves (**Fig. 3**).

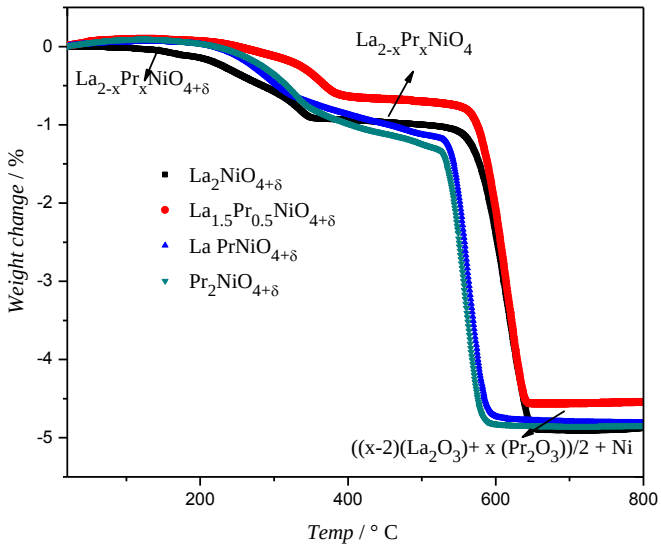

Fig. 3 TGA curves of the four solid solution samples.

As previously reported[33], two weight changes are observed: the first one occurs around 350 °C, corresponding to the reduction of Ni^{3+} into Ni^{2+} (the oxygen over-stoichiometry being reduced down to $\delta = 0$). The second weight loss is assigned to the complete reduction of $La_{2-x}Pr_xNiO_{4+\delta}$ into La_2O_3, Pr_2O_3 and Ni. The δ value has been calculated from both weight change values using the mole conservation principle. The oxygen over-stoichiometry, δ, was found to be 0.16, 0.18, 0.22 and 0.24 for $La_2NiO_{4+\delta}$, $La_{1.5}Pr_{0.5}NiO_{4+\delta}$, $LaPrNiO_{4+\delta}$ and $Pr_2NiO_{4+\delta}$, respectively. These values are in good agreement with the ones previously reported in the literature.[22]

3.4. Effect of praseodymium content on the stability and compatibility of $La_{2-x}Pr_xNiO_{4+\delta}$ with CGO

In order to study the effect of the Pr content on the stability and compatibility of the $La_{2-x}Pr_xNiO_{4+\delta}$ single layers on CGO substrates, heat treatments have been performed for 30 days in air at 700 °C (**Fig. 4a**) and 800 °C (**Fig. 4b**). Interestingly, two types of behavior were observed depending on the composition. La-rich phases with $x = 0$ ($La_2NiO_{4+\delta}$) and $x = 0.5$ ($La_{1.5}Pr_{0.5}NiO_{4+\delta}$) are highly stable at 700 °C and 800 °C in air. No structural modification was found in the detection limit of XRD which, in agreement with Solis *et al*.[34]who reported no decomposition of $La_2NiO_{4+\delta}$ and $La_{1.5}Pr_{0.5}NiO_{4+\delta}$ powders after 2 weeks at 750 °C in air. This was also confirmed recently by Vibhu *et al.* who reported no decomposition after one month at 700 °C and 800 °C in air.[35] However Vibbhu *et al.* have reported a decomposition of $LaPrNiO_{4+\delta}$ phase into $(La, Pr)_4Ni_3O_{10+\delta}$, $(La, Pr)NiO_3$ and Pr_6O_{11} phases at 700 °C after 30 days.[35] In this work, $LaPrNiO_{4+\delta}$ phase is found to be stable at 700 °C after 30 days since no secondary phases can be observed by XRD (**Fig. 4a**). The decomposition has been also observed but at 800 °C after 30 days **(Fig. 4b)**. In the case of $Pr_2NiO_{4+\delta}$, the decomposition in air takes place at both temperatures giving rise to $PrNiO_{3-\delta}$, Pr_6O_{11}, NiO phases (which amount increases with annealing temperature) along with some residual traces of $Pr_2NiO_{4+\delta}$. No traces of $Pr_4Ni_3O_{10+\delta}$ phase was detected contrary to the literature.[35]

These results reveal that $La_{2-x}Pr_xNiO_{4+\delta}$ films (x = 0, 0.5 and 1) present a good chemical compatibility with CGO electrolyte for the intermediate operating temperature and particularly at 700 °C. $LaPrNiO_{4+\delta}$ oxide, which presents a long term chemical stability at 700 °C, has been selected as the optimized composition. It requires to be electrochemically investigated as oxygen electrode and then tested in a full cell.

.

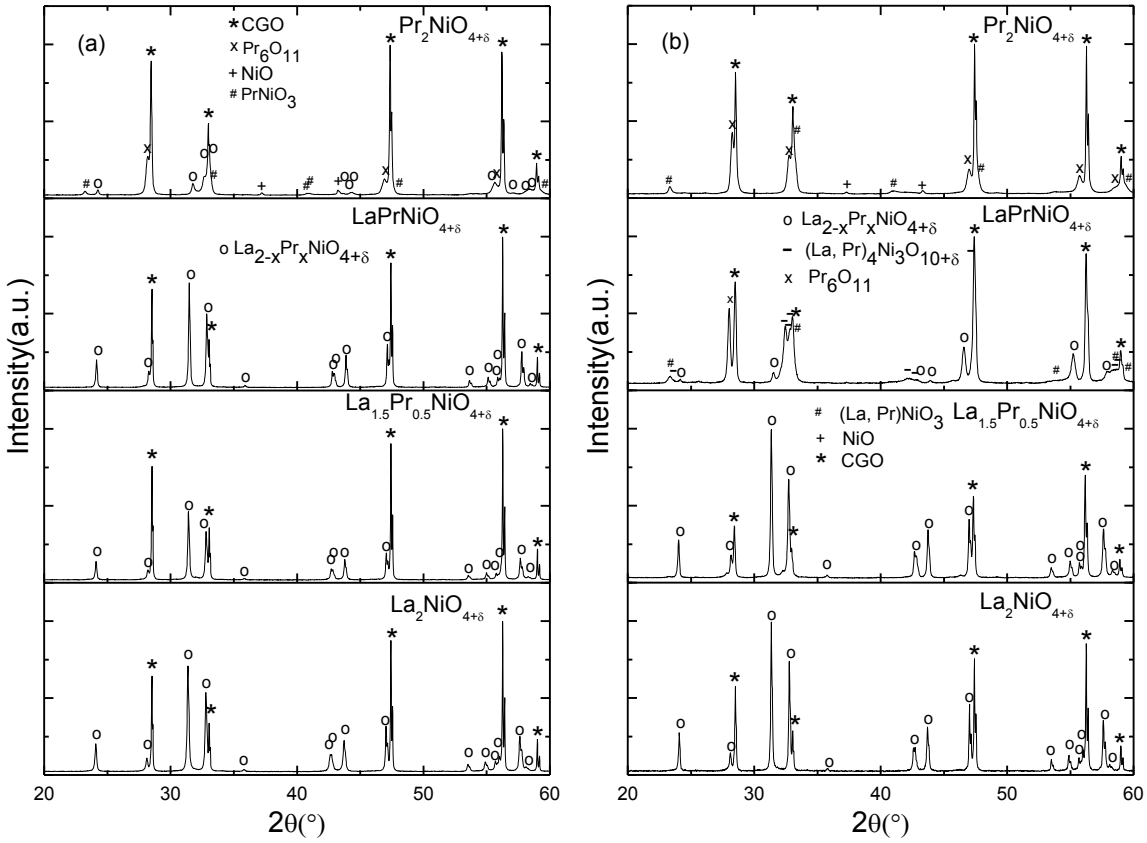

Fig. 4 XRD patterns of the single layer $La_{2-x}Pr_xNiO_{4+\delta}$ films on CGO electrolyte; after heat treatments for 30 days in air at (a) 700 °C and (b) 800 °C

3.5. Electrochemical properties

In this section, the electrochemical properties of single layer and double layer cathodes were studied by EIS. These measurements have been performed as a function of temperature and the results are discussed comparing the sets of data obtained for the single layer and double layer cathodes. Finally, single cell measurements for $LaPrNiO_{4+\delta}$ cathode (i-V curves were performed recording at operating temperatures between 600 °C and 750 °C, in the steps of 50 °C).

3.5.1 Symmetrical cells performance

The impedance diagrams were fitted using ZView® software with an equivalent circuit, consisting of a combination of several resistances (R)-constant phase element (CPE) parallel circuits, connected in series with an inductance (L). This electrical element (L), appearing as a

high frequency tail below the real axis, represents the contribution of the connecting leads, measuring device and connecting wires to the measured total impedance.[36] The high frequency intercept of the diagrams on the real axis corresponds to the overall ohmic resistance (R_s), including the resistive contributions of the electrolyte, electrode, leads and current collectors. The ohmic resistance (R_s) has been subtracted in order to facilitate comparison between the resistance polarization values (R_{pol}) of the investigated electrodes. According to the selected analysis, the electrode response is composed by two or three main elementary contributions located at high frequency (P1), medium frequency (P2) and low frequency (P3) depending upon the composition of the cathodes and temperature. For the single layer electrodes, two processes for 500 °C ≤ T ≤ 650 °C (P1 and P2) and three processes (P1, P2 and P3) at 700 °C are distinguishable. As far as the double layer cathodes are considered, there are two processes (P1 and P2) for 500 °C ≤ T < 600 °C and three processes for 600 °C ≤ T ≤ 700 °C (P1, P2 and P3) for $La_2NiO_{4+\delta}$ and $La_{1.5}Pr_{0.5}NiO_{4+\delta}$ whereas for $LaPrNiO_{4+\delta}$ and $Pr_2NiO_{4+\delta}$, there are two processes (P1 and P2) for 500 °C ≤ T < 600 °C and two processes (P2 and P3) for T ≥ 600 °C. At higher temperatures, T ≥>650 °C, as all processes are shifted toward higher frequencies, the process P1 is hidden by the inductance of the wires and hence could not be distinguished from P2 and P3.

The processes P1 (high frequency arc) and P2 (middle frequency arc) were fitted using three parallel R//CPE elements. The origin of process P1 is likely due to the charge transfer at the electrode/electrolyte interface whereas the process P2 is can be associated with various electrode processes such as adsorption of gaseous oxygen O_2, dissociation of O_2 and charge transfer-diffusion (O^{2-}) in the electrode.[36-38] The process P3 (low frequency arc, fitted by R//CPE) is due to a gas impedance due to either porous electrodes or the experimental set-up.[39-40]

As can be seen in **Table 3** the addition of a SP layer leads to a significant decrease in the series resistance (from single layer to double layer) regardless of the composition of the electrode. For instance, at 600°C, the R_s value decreases from 14.58 down to 5.43 Ω cm²when a screen-printed layer is added on the top of the single layer $La_2NiO_{4+\delta}$ (**Table 3**). Indeed, R_s depends upon the intimate contact at the electrode/electrolyte and current collector/electrode interfaces. Due to the presence of a thin dense layer (**Fig. S4**), the electrode - electrolyte contact area is of 100 % for the single layer cathode but the contact between electrode and current collector gold grid is poor.

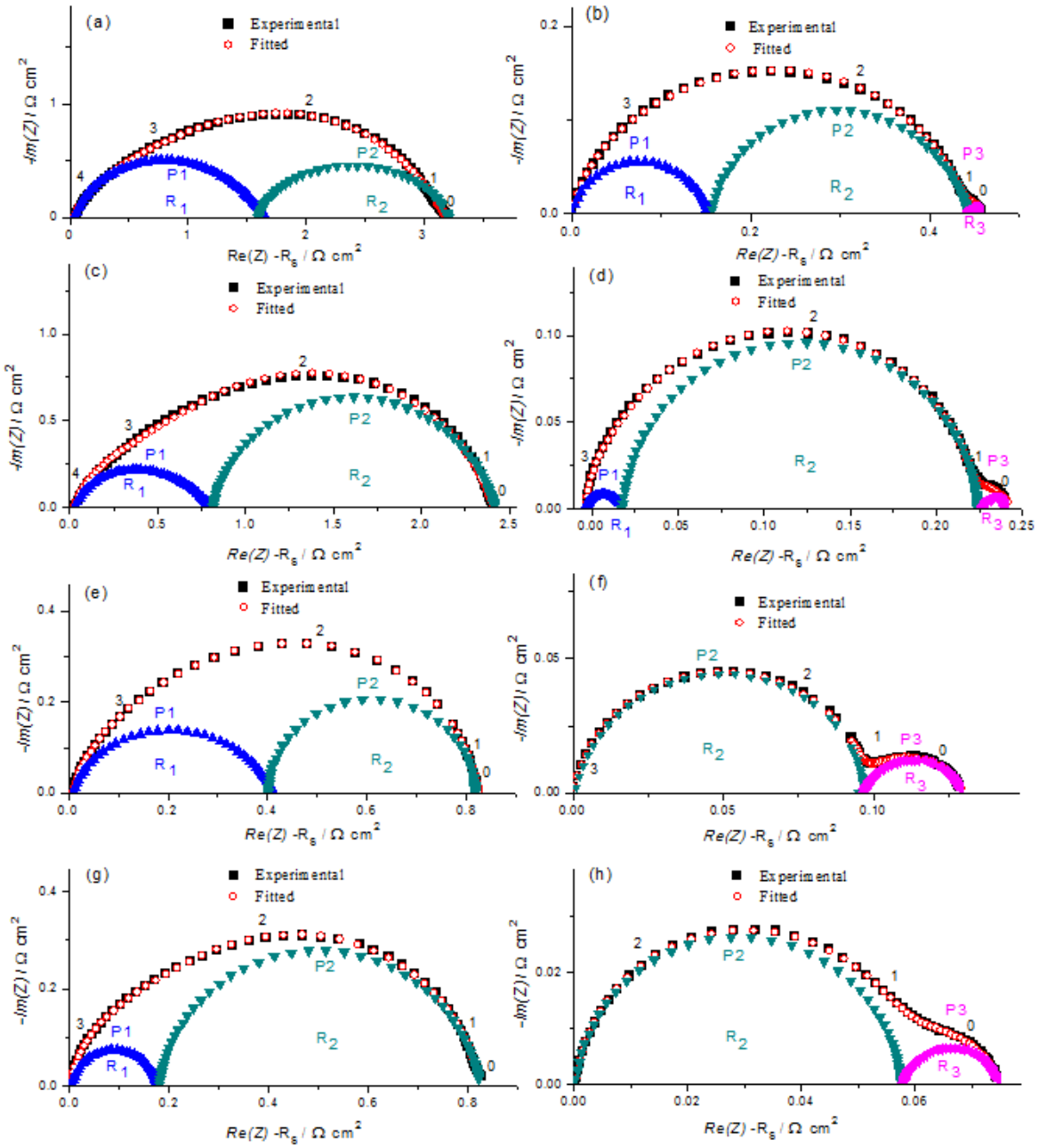

Fig. 5 Nyquist impedance diagrams at 600 °C in air at OCV: $La_2NiO_{4+\delta}$ (a) single layer, (b) double layer; $La_{1.5}Pr_{0.5}NiO_{4+\delta}$ (c) single layer, (d) double layer; $LaPrNiO_{4+\delta}$ (e) single layer, (f) double layer and $Pr_2NiO_{4+\delta}$ (g) single layer, (h) double layer. The numbers indicate the logarithm of the measuring frequency.

Therefore, when a gold grid as a current collector (single layer), the current lines are not well distributed through the electrode volume, leading to a significant current constriction effect in the vicinity of the electrode/electrolyte interface. As a consequence, the R_s values of

the single layer cathodes are large. Once the screen-printed layer is added (**Fig. 3**), a much better contact area between grid and electrode is achieved, which results in a homogeneous distribution of the current lines within the electrode. Thus, a decrease of the current constriction effect in the vicinity of the electrode/electrolyte interface is expected. An argument that further supports this assumption is the decrease in the series resistance when a screen-printing layer is added (**Table 3**).

The total R_{pol}, calculated for all temperatures (500 - 700 °C range) in air for the single and double layer electrodes are shown in **Fig. 6a**. Regardless of the temperature, the R_{pol} value decreases by substituting La by Pr. Indeed, the R_{pol} values at 600°C for $La_2NiO_{4+\delta}$, $La_{1.5}Pr_{0.5}NiO_{4+\delta}$, $LaPrNiO_{4+\delta}$ and $Pr_2NiO_{4+\delta}$ were 3.33, 2.37, 1.63 and 0.83 Ω cm², respectively. As the microstructure for all single layer cathodes, is similar (**Fig. S4**), the decrease in R_{pol} is related to an improvement in transport properties (electronic and ionic conductivity) of $La_{2-x}Pr_xNiO_{4+\delta}$ over $La_2NiO_{4+\delta}$.[22] It can also be noticed that the P1 and P2 contributions also decrease when the Pr amount is increased. Despite the favorable microstructural parameters (thin dense layer, smaller grain, large porosity), a relatively poor performance is obtained for the single layer electrode. As mentioned above there is large current constriction effect due to very low contact area between Au grids and highly porous 3D coral microstructure. When the contact between the gold grids and electrode is improved by adding screen-printed CCL of same composition (**Fig. 2** and **Fig. S5**), the current constriction effect is minimized. As a consequence, a drastic reduction in R_{pol} has been obtained for the double layer cathodes with values equal to 0.42, 0.23, 0.12 and 0.08 Ω cm² for $La_2NiO_{4+\delta}$, $La_{1.5}Pr_{0.5}NiO_{4+\delta}$, $LaPrNiO_{4+\delta}$ and $Pr_2NiO_{4+\delta}$, respectively, at 600 °C. As shown in **Fig. 5**, the frequency distribution of the electrode impedance is not modified by adding the CCL, indicating that the ORR remains the same. This enhancement can be related to the use of a CCL which homogenizes the current distribution along the cathode functional layer (CFL), activating a larger cathode volume.

The activation energies deduced from the Arrhenius plots of the polarization resistance R_{pol} (**Fig. 6a**) and given in **Table 3** and are in good agreement with the values reported in literature.[14, 15, 22] To the best of our knowledge, the R_{pol} values obtained for the double layer cathodes, as low as 0.42, 0.23, 0.12 and 0.08 Ω cm² at 600 °C for $La_2NiO_{4+\delta}$, $La_{1.5}Pr_{0.5}NiO_{4+\delta}$, $LaPrNiO_{4+\delta}$ and $Pr_2NiO_{4+\delta}$,respectively, are much lower than the minimum

R_{pol} values previously reported for pure $La_2NiO_{4+\delta}$ (0.93 Ω cm² at 600 °C) and $Pr_2NiO_{4+\delta}$ (0.15 Ω cm² at 600 °C) based cathodes by Vibhu et al.[22]

In order to identify the origin of the difference in the R_{pol} values, the thermal variations of the resistances R_1, R_2 and R_3, related to the three processes P1, P2 and P3, are plotted in **Fig. 6a-d**, respectively. Interestingly, R_{pol}, R_1 and R_2 for both the single and double layer cathodes decrease by increasing the Pr amount and the temperature, while the R_3 for the double layer cathodes remains almost constant. The activation energies corresponding to the three processes (R_1, R_2 and R_3) are given in **Table 4**.

Table 3. Comparison of R_s, R_{pol} values at 600 °C and activation energy (E_a) of the $La_{2-x}Pr_xNiO_{4+\delta}$ electrodes (estimated error for resistances is < 5%)

Electrodes	R_S [Ω cm²]		R_{Pol} [Ω cm²]		E_a [eV]	
	Single layer	Double layer	Single layer	Double layer	Single layer	Double layer
$La_2NiO_{4+\delta}$	14.56	5.43	3.33	0.42	0.77	1.09
$La_{1.5}Pr_{0.5}NiO_{4+\delta}$	10.02	5.62	2.37	0.23	0.63	1.08
$LaPrNiO_{4+\delta}$	9.51	5.71	1.63	0.12	0.63	0.80
$Pr_2NiO_{4+\delta}$	8.32	4.35	0.83	0.08	0.66	0.78

Table 4. Activation energy (Ea) values corresponding to R_1, R_2 and R_3

Electrodes	E_a [eV]				
	Single layer		Double layer		
	R_1	R_2	R_1	R_2	R_3
$La_2NiO_{4+\delta}$	0.50 ± 0.04	0.98 ± 0.04	1.11 ± 0.04	1.10 ± 0.07	0.22 ± 0.07
$La_{1.5}Pr_{0.5}NiO_{4+\delta}$	0.55 ± 0.04	0.64 ± 0.06	1.17 ± 0.10	1.03 ± 0.04	0.04 ± 0.02
$LaPrNiO_{4+\delta}$	0.70 ± 0.11	0.64 ± 0.04	----	0.94 ± 0.03	0.07 ± 0.005
$Pr_2NiO_{4+\delta}$	0.80 ± 0.04	0.64 ± 0.08	----	0.83 ± 0.01	0.07 ± 0.003

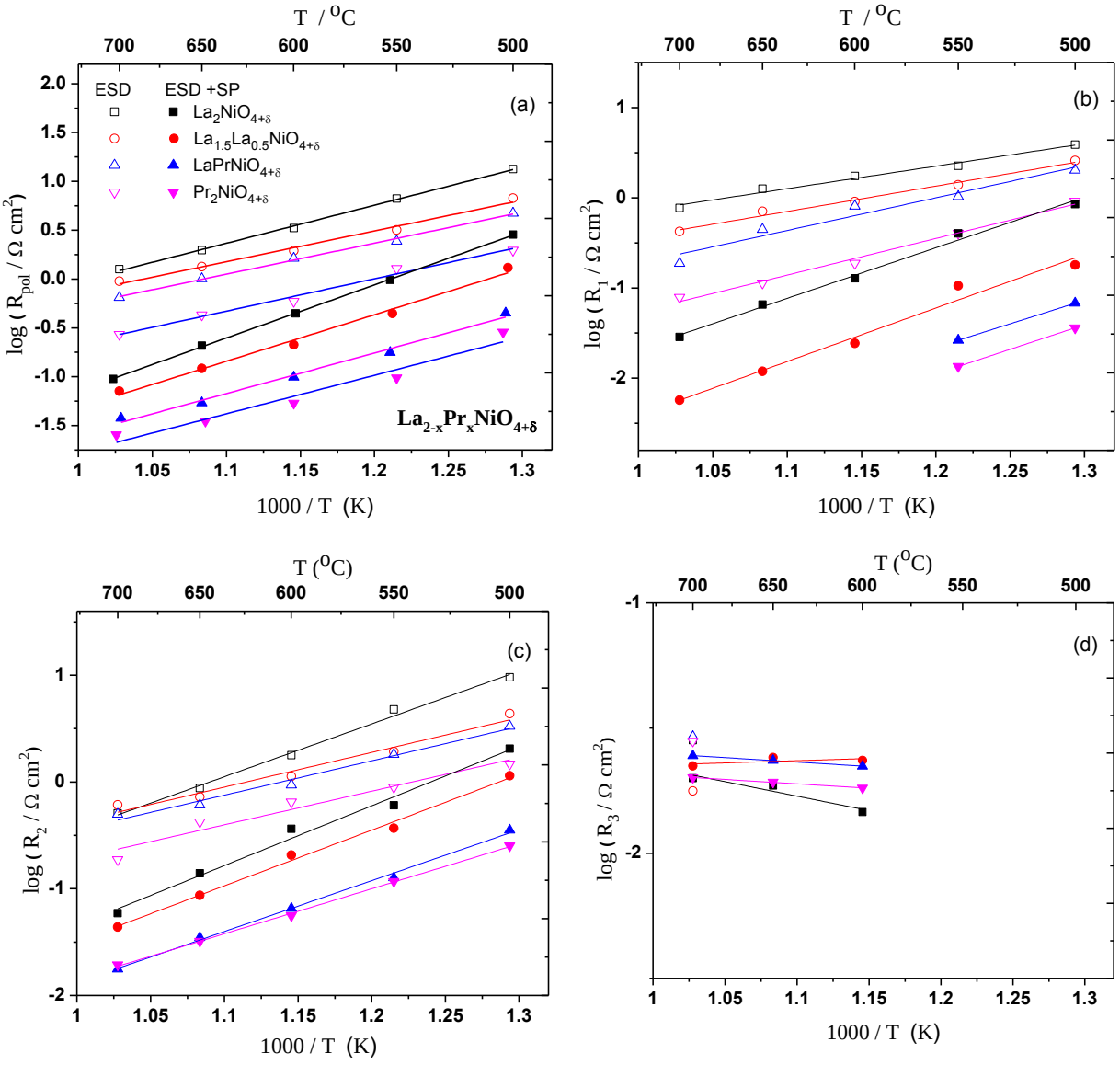

Fig. 6 Arrhenius plot of the electrodes: a) R_{pol}, b) R_1, c) R_2, d) R_3.

One can notice (**Table 4**) that activation energy values corresponding to R_2 process, decreases with the increasing amount of Pr especially for the double layer cathode. This could be due to better transport properties of $La_{2-x}Pr_xNiO_{4+\delta}$ over $La_2NiO_{4+\delta}$.[22] However, for larger Pr contents, the R_1 and R_2 values for the double layer decrease much faster with temperature compared to the single layer resistance values. The relaxation frequency and capacitance related to the different processes involved for both architectures (single layer and double layer) are compared in **Fig. 7a-f**.

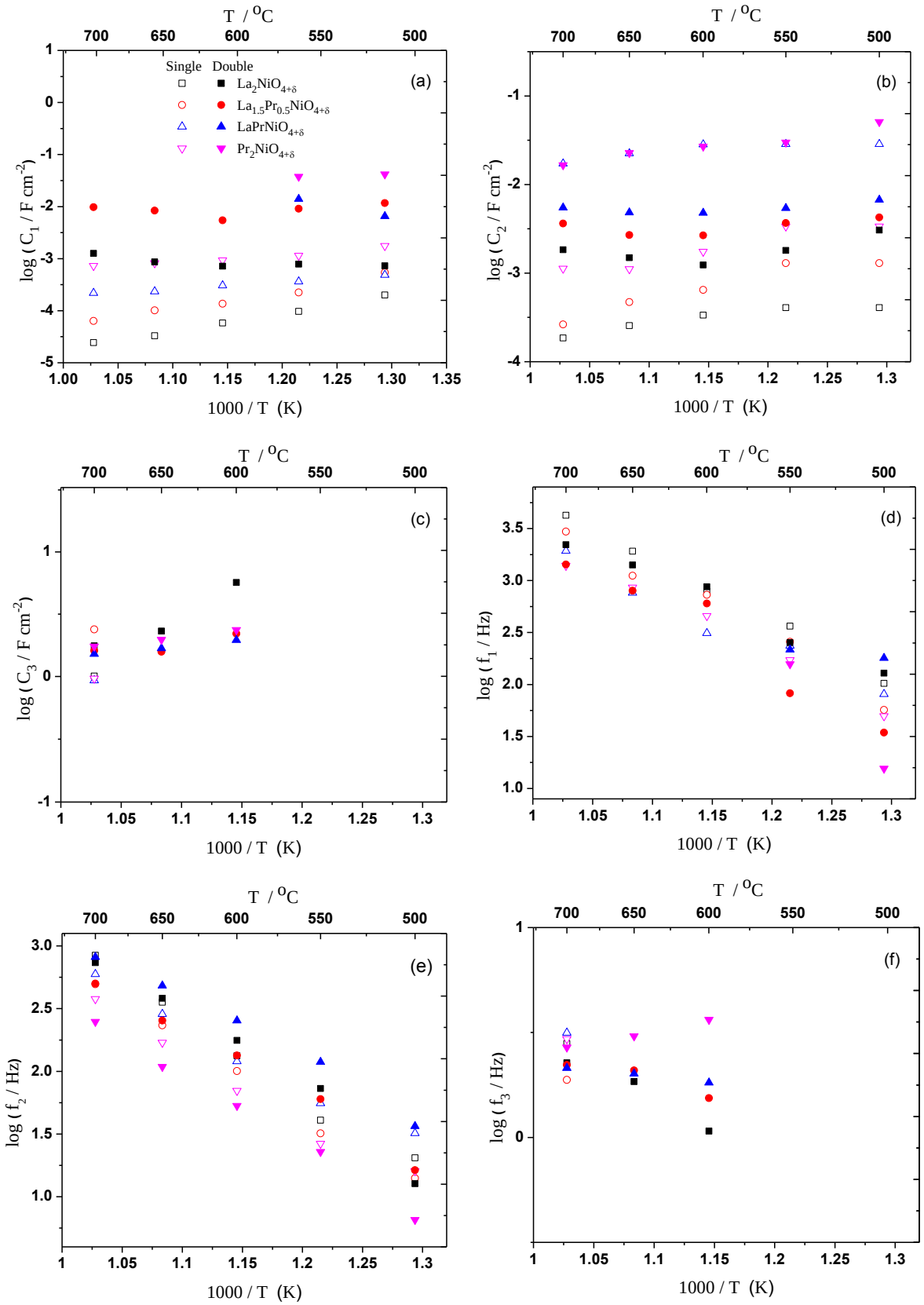

Fig. 7 Arrhenius plot of the capacitance and frequency corresponding to processes P1, P2 and P3: a) C_1, b) C_2, c) C_3, d) f_1, e) f_2 and g) f_3.

The capacitance associated to process P1 is nearly temperature independent (**Fig. 7a**) which is in good agreement with the behavior of an interfacial capacitance coupled with a charge transfer process.[41] Since current constriction effects occur at the current collector/electrode interface (for single layer electrodes), the existence of a contribution due to this interface in the high frequency region is expected.[42] Nevertheless, elementary impedance responses are similar for all investigated electrodes as shown by the evolution of the apex frequencies as a function of the reciprocal temperature (**Fig. 7d-e**).

The R_2 values are always larger than the R_1 ones, suggesting that the oxygen desorption or adsorption process is the rate-limiting step for the ORR.[43-45] As shown in **Fig. 6d**, the magnitude of the process P3 (R_3) observed at low frequency (~1 Hz, **Fig.7f**) does not vary with temperature significantly. Moreover, the P3 contribution is characterized by high capacitance values, of the order of F cm^{-2} (**Fig.7c**). Such contribution has been attributed to the O_2 gas diffusion process through the porous electrode.[46-47] This is further in agreement with the small activation energy corresponding to this process, as shown in **Table 4** even if these values are very scarce with respect to literature.

Finally, the long term aging has been carried out on $LaPrNiO_{4+\delta}$ cathode for 500 h at 700 °C in air at OCV followed by 600 °C for 500 h in air under polarization, -195 mA cm^{-2}. The polarization resistance does not show a significant variation at OCV indicating no significant thermal degradation of the studied assembly. Whereas under polarization a slight decrease with time, particularly for the first 250 h, has been observed (**Fig. 8**) probably, suggesting an enhancement of the electrochemical properties.

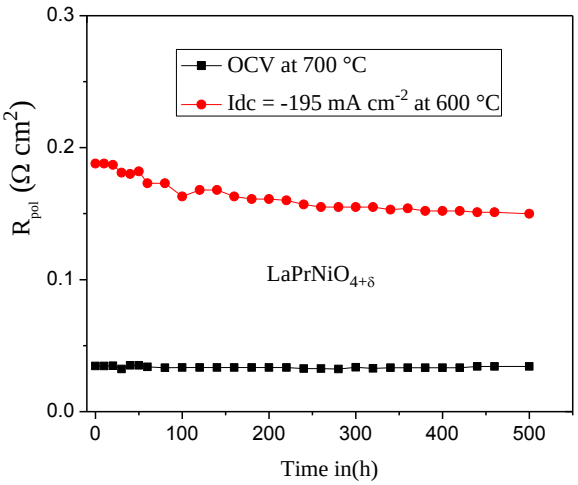

Fig. 8 R_{pol} vs. time for the $LaPrNiO_{4+\delta}$ electrode at OCV (700 °C) and under polarization (-195 mA cm^{-2}) at 600 °C.

3.5.2. $LaPrNiO_{4+\delta}$ single cell performance

The open circuit voltage (OCV) was around 1.06 V, in good agreement with the Nernst's law. The i-V characteristic was measured from OCV down to 0.2 V at 600 °C, 650 °C, 700 °C and 750 °C. **Fig. 9** shows the cell voltage as a function of the current density, as well as the resulting power density at 600 °C, 650 °C, 700 and 750 °C. The cell performance is reaching maximum power densities of 323 mW cm^{-2} at 650 °C and 438 mW cm^{-2} at 700 °C.

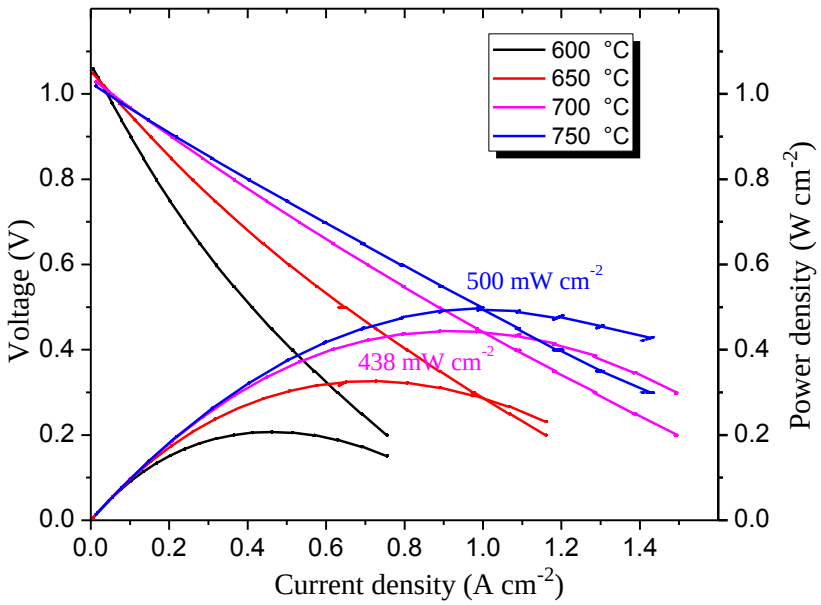

Fig. 9 Performance of a single cell consisting in a commercial half-cell (Ni-3YSZ/Ni-8YSZ/8YSZ/CGO) and $LaPrNiO_{4+\delta}$ as the cathode; i-V curves and resulting power densities.

Moreover, this performance is very close to the best performing cell based on $Pr_2NiO_{4+\delta}$ cathode (250 - 400 mW cm^{-2} at 600 °C).[17] Nevertheless, the performance of the anode-supported cell can be affected by several factors, such as the electrode and anode-support microstructures, electrolyte thickness and nature.[48-51] Indeed a thinner electrolyte has been reported to improve cell performances.[48] For instance, a maximum peak power density was obtained at 500 °C surpassing 500 mW cm^{-2}, for the YSZ-based anode-supported SOFC (1 µm YSZ/ 200 nm CGO).[51] In the future, a more efficient fuel cell based on this $LaPrNiO_{4+\delta}$ cathode could be obtained by incorporating a ~1 µm thick CGO electrolyte.

Following the i-V measurements, the cell was aged for 408 h at 700 °C at a voltage 0.7 V (current density of 0.3 A cm^{-2}). The current density started at around 0.75 mA cm^{-2},

followed by a decrease, and after 408 h the current density was around 0.60 mA cm^{-2} (degradation rate ~ 20%).

4. Conclusions

This work reports the structural, microstructural, electrochemical properties and chemical stability of $La_{2-x}Pr_xNiO_{4+\delta}$ films as a function of Pr content (x mol. %) for their use as SOFC cathodes. Original 3-D coral type $La_{2-x}Pr_xNiO_{4+\delta}$ (x = 0, 0.5, 1 and 2) films were successfully prepared on $Ce_{0.9}Gd_{0.1}O_{2-\delta}$ (CGO) substrates by electrostatic spray deposition. Single-phase solid solution with orthorhombic structure (Fmmm space group) is obtained in the entire range of compositions. An over-stoichiometry δ value equal to 0.16, 0.18, 0.22 and 0.24 is obtained under air for x = 0, 0.5, 1 and 2, respectively. The chemical stability decreases with increasing Pr content, as detected by XRD. For the first time, $La_{2-x}Pr_xNiO_{4+\delta}$ films were stable for 30 days at 700 °C up to x = 1 and, as expected, they were also stable at 800 °C, in this case for a lower Pr content (x = 0 and 0.5). A decrease in R_{pol} is recorded at 600 °C from 3.33, 2.37, 1.67, to 0.83 Ω cm^2 by increasing the Pr content from x = 0, 0.5, 1 to 2 in the $La_{2-x}Pr_xNiO_{4+\delta}$ solid solution. A further improvement in R_{pol} is obtained for architecturally designed $La_{2-x}Pr_xNiO_{4+\delta}$ cathodes (ESD + SP), reaching values down to 0.42, 0.21, 0.12 and 0.08 Ω cm^2 for x = 0, 0.5, 1 and 2 at 600 °C, respectively. These values are the lowest available in the literature for each composition, to the best of our knowledge. Finally, the $LaPrNiO_{4+\delta}$ phase is quite stable in symmetrical cell during long term operation (after 500 h at 700 °C in OCP and after 500 h at 600 °C under polarization, -195 mA cm^{-2}). An anode supported single cell (Ni-3YSZ/Ni-8YSZ/8YSZ/CGO) with $LaPrNiO_{4+\delta}$ double layer cathode produced maximum power density of 438 and 323 $mWcm^{-2}$ at 700 °C and 650 °C, respectively. It has shown a degradation rate of 20 % for 408 h at 700 °C. It can be then concluded that the $LaPrNiO_{4+\delta}$ is the optimized composition to be used as a very promising oxygen electrode since it shows the best compromise in between electrochemical behavior and chemical stability.

Acknowledgements

This work was performed within the framework of the Centre of Excellence of Multifunctional Architectured Materials "CEMAM" n° AN-10-LABX-44-01 funded by the "Investments for the Future" Program. The authors would like to thank S. Coindeau and T.

Encinas in CMTC (Grenoble INP, France) for XRD analyses. We would also like to thanks Rachel Martin for SEM and EDX analyses.

References:

[1] W. Zhou, R. Ran and Z. P. Shao, *Journal of Power Source*s, 2009, **192**, 231.

[2] X.W. Meng, S.Q. Lu¨, Y. Ji, T. Wei and Y.L. Zhang, *Journal of Power Sources*, 2008, **183**, 581.

[3] J. P. Martinez, D. M. Lopez, J.C. Ruiz-Morales, B.E. Buergler, P. Nunez and L. J. Gauckler, *Journal Power Sources*, 2006, **159**, 914.

[4] H.L. Zhao,W. Shen, Z.M. Zhu, X. Li and Z.F.Wang, *Journal Power Sources*, 2008, **182**, 503.

[5] S.J. Skinner and J.A. Kilner, *Solid State Ionics*, 2000, **135**, 709.

[6] E. Boehm, J. M. Bassat, M.C. Steil, P. Dordor, F. Mauvy and J. C. Grenier, *Solid State Science*, 2003, **5**, 973.

[7] G. Amow, P.S. Whitfield, I.J. Davidson, R.P. Hammond, C.N. Munnings and S.J. Skinner, *Ceram. Int.*, 2004, **30**, 1635.

[8] A. Tarancón, M. Burriel, J. Santiso, S. J. Skinner and J. A. Kilner, *J. Mater. Chem.*, 2010, **20**, 3799.

[9] J. A. Kilner and M. Burriel, *Annu. Rev. Mater. Res.*, 2014, **44**, 365.

[10] J. Dailly, S. Fouread, A. Largeteau, F. Mauvy, J.C. Grenier and M. Marrony, *Electrochim. Acta*, 2010, **55**, 5847.

[11] N. P. Brandon, S.J. Skinner and B.C.H. Steele, *Ann. Rev. Mat. Res.*, 2003, **33**, 183.

[12] R. K. Sharma, M. Burriel, L. Dessemond, V. Martin, J.M. Bassat and E. Djurado, *Journal of Power Sources*, 2016, **316**, 17.

[13] M.L. Fontaine, C. Laberty-Robert, F. Ansart and P. Tailhades, *J. Power Sources*, 2006, **156**, 33.

[14] R. Sayers, M. Rieu, P. Lenormand, F. Ansart, J.A. Kilner and S.J. Skinner, *Solid State Ionics*, 2011, **192**, 531.

[15] N. Hildenbrand, P. Nammensma, D.H.A. Blank, H.J.M. Bouwmeester and B.A. Boukamp, *J. Power Sources*, 2013, **238**, 442.

[16] D. Marinha, L. Dessemond, J.S. Cronin, J.R. Wilson, S. A. Barnett and E. Djurado, *Chem. Mater.* 2011, **23**, 5340.

[17] C. Ferchaud, J.C. Grenier, Y.Z. Steenwinkel, M.M.A. van Tuel, F.P.F. van Berkel and J.M. Bassat, *Journal of Power Sources*, 2011, **196**, 1872.

[18] A. Flura, S. Dru, C. Nicollet, S. Furcade, A. Rougier, J.M. Bassat and J.C. Grenier, presented at FDFC 2013,Karlsruhe Germany, April, 2013.

[19] P. Odier, C. Alloncon and J.M. Basst, *J. Solid State Chem.*,2000, **153**, 381.

[20] A.V. Kovalevky, V.V. Kharton, A.A. Yarmchenko, V.V. Pivak, E.N. Naumovich and J.R. Frade, *J. Eur. Ceram. Soc.*, 2007, **27**, 4269.

[21] J. Yang, J. Cheng, Q. Jiang, Y. Wang, R. Wang and J. Gao, *International Journal of Hydrogen Energy*, 2012, **37**, 1746.

[22] V. Vibhu, A. Rougier, C. Nicollet, A. Flura, J.C. Grenier and J-M. Bassat, *Solid State Ionics*, 2015, **278**, 32.

[23] C.H. Chen, M.H.J. Emond, E.M. Kelder, B. Meester and J. Schoonman, *J. Aerosol. Sci.*, 1999, **30**, 959.

[24] D. Marinha, L. Dessemond and E. Djurado, *Current Inorganic Chemistry,* 2013, **3**, 2.

[25] G. Constantin, C. Rossignol, J. P. Barnes, and E. Djurado, *Solid State Ionics*, 2013, **235**, 36.

[26] J. Rodriguez-Carvajal, Phys. B, 1993, **192**, 55.

[27] R.D. Shannon, *Acta Crystallogr. Sect. A*, 1976, **32**, 751.

[28] B. Philippeau, F. Mauvy, C. Mazataud, S. Fourcade and J.C. Grenier, *Solid State Ionics*, 2013, **249-250**, 17.

[29] R. Neagu, D. Perednis, A. Princivalle and E. Djurado, *Solid State Ionics*, 2006, **177**,1981.

[30] C.H. Chen, E.M. Kelder, P.J.J.M. van der Put and J. Schoonman, *J. Mater. Chem.*, 1996, **6**, 765.

[31] B.-H. Hwang, C.-L. Chang, C.-S. Hsu and C.-Y. Fu, *J. Phys. D: Appl. Phys.*, 2007, **40**, 3448.

[32] J. Sar, O. Celikbilek, J. Villanova, L. Dessemond, C. L. Martin and E. Djurado, *Journal of the European Ceramic Society*, 2015, **35**, 4497.

[33] J.A. Kilner and C.K.M. Shaw, *Solid State Ionics*, 2002, **154-155**, 523.

[34] C. Solis, L. Navarrete and J. M. Serra, *Journal of Power Sources*, 2013, **240**, 691.

[35] V. Vibhu, J-M. Bassat, A. Flura, C. Nicollet, J.C. Grenier and A. Rougier, *ECS Trans*. 2015, **68**, 825.

[36] C. Fu, K. Sun, N. Zhang, X. Chen and D. Zhou, *Electrochim. Acta*, 2007, **52**, 4589.

[37] S.B. Adler, *Solid State Ionics*, 2000, **135**, 603.

[38] M.J. Escudero, A. Aguadero, J.A. Alonso and L. Daza, *J. Electroanal. Chem.*, 2007, **611**, 107.

[39] T. Jacobsen, P.V. Hendriksen and S. Koch, *Electrochimica Acta*, 2008, **53**, 7500.

[40] W.G. Bessler, *Journal of the Electrochemical Society*, 2006, **153**, A1492.

[41] S.P. Jiang, W. Wang and Y.D. Zhen, *Journal of Power Sources*, 2005, **147**, 1.

[42] X.C. Lu and J.H. Zhu, *Solid State Ionics*, 2007, **178**, 1467.

[43] Z. Lou, J. Qiao, Y. Yan, J. Peng, Z. Wang and T. Jiang, *Int J Hydrogen Energy*, 2012, **37**, 11345.

[44] S. Huang , Q. Lu, S. Feng, G. Li and C.Wang, *Adv. Energy Mater*, 2011, **1**, 1094.

[45] H. Gu, H. Chen, L. Gao and L. Guo, *Electrochim Acta*, 2009, **54**, 7094.

[46] L. Mogni, N. Grunbaum, F. Prado and A. Caneiro, *J. Electrochem. Soc.*, 2011, **158**, B202.

[47] S. Pang, X. Jiang, X. Li, Q. Wang and Z. Su, *J. Power Sources*, 2012, **204**, 53.

[48] H.-S. Noh, J.-W. Son, H. Lee, H.-S. Song, H.-W. Lee and J.-H. Lee, *J. Electrochem. Soc*., 2009, **156**, B1484.

[49] H.-S. Noh, H. Lee, B.-K. Kim, H.-W. Lee, J.-H. Lee and J.-W. Son, *J. Power Sources*, 2001, **196**, 7169.

[50] D.-H. Myung, J. Hong, K. Yoon, B.-K. Kim, H.-W. Lee, J.-H. Lee and J.-W. Son, *Journal of Power Sources*, 2012, **206**, 91.

[51] H.-S. Noh, K. J. Yoon, B.-K. Kim, H.-J. Je, H.-W. Lee, J.-H. Lee and Ji-W. Son, *Journal of Power Sources*, 2014, **247**, 105.

Supporting information

FULLPROF refinements of the XRD patterns of the $La_{2-x}Pr_xNiO_{4+\delta}$ (x=0, 0.5 and 2) films prepared by ESD on a CGO pellet.

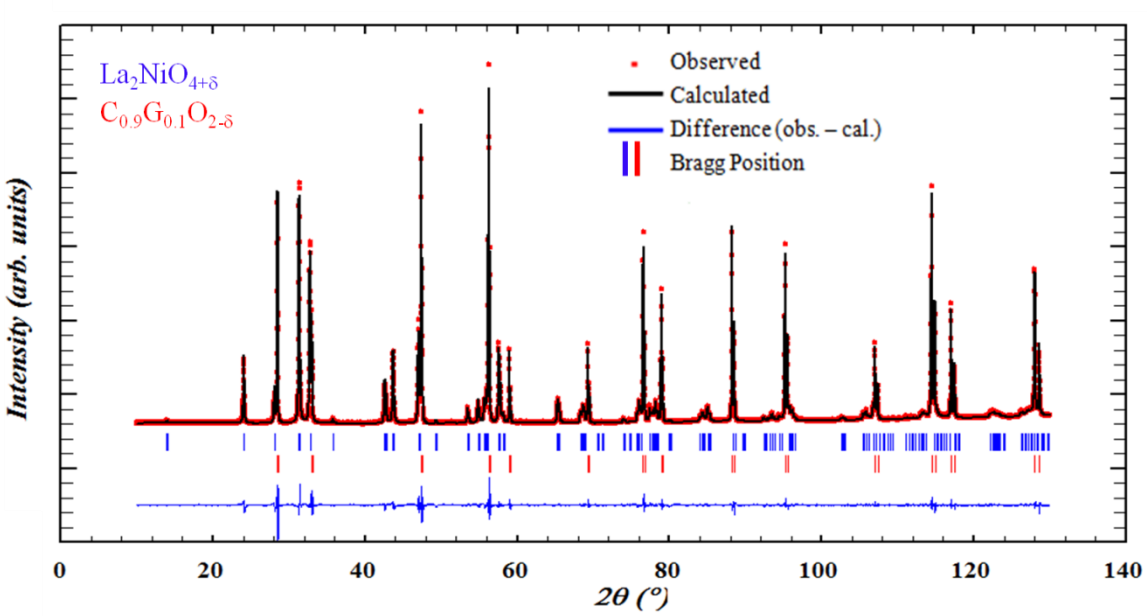

Fig. S1 FULLPROF refinement of the XRD patterns of $La_2NiO_{4+\delta}$ film deposited by ESD on a CGO pellet (Fitting parameters: χ^2 = 6.99, Bragg R-factor = 1.22 and RF-factor = 0.752 for $La_2NiO_{4+\delta}$; Bragg R-factor = 1.84 and RF-factor = 1.00 for CGO).

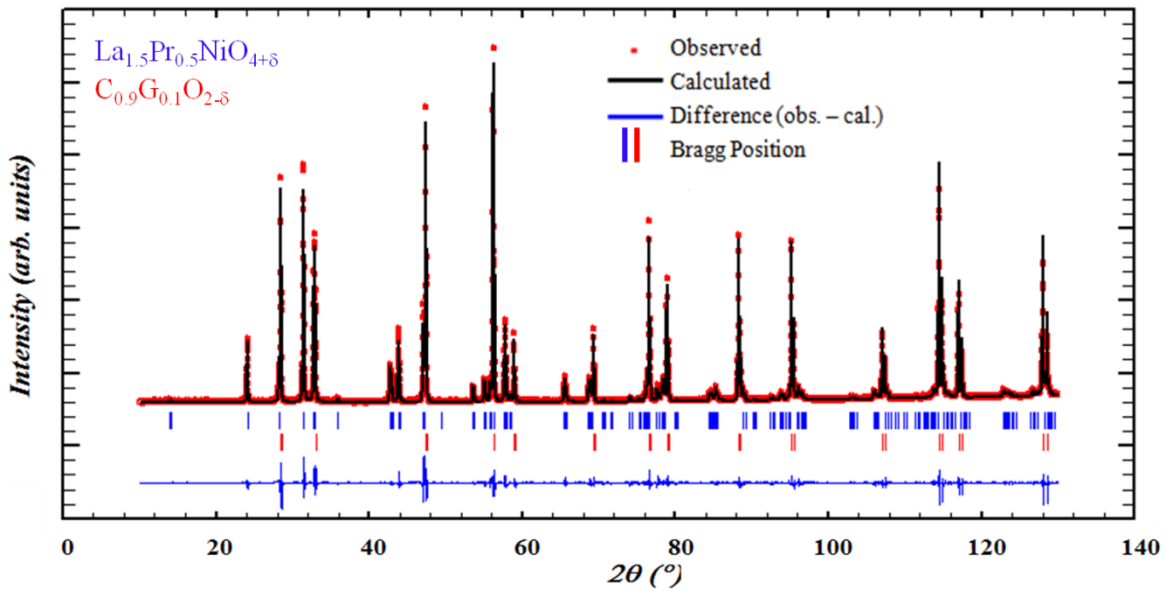

Fig. S2 FULLPROF refinement of the XRD patterns of $La_{1.5}Pr_{0.5}NiO_{4+\delta}$ film deposited by ESD on a CGO pellet (Fit parameters: χ^2 = 7.44, Bragg R-factor = 1.36 and RF-factor = 0.99 for $La_{1.5}Pr_{0.5}NiO_{4+\delta}$; Bragg R-factor = 1.48 and RF-factor = 0.77 for CGO).

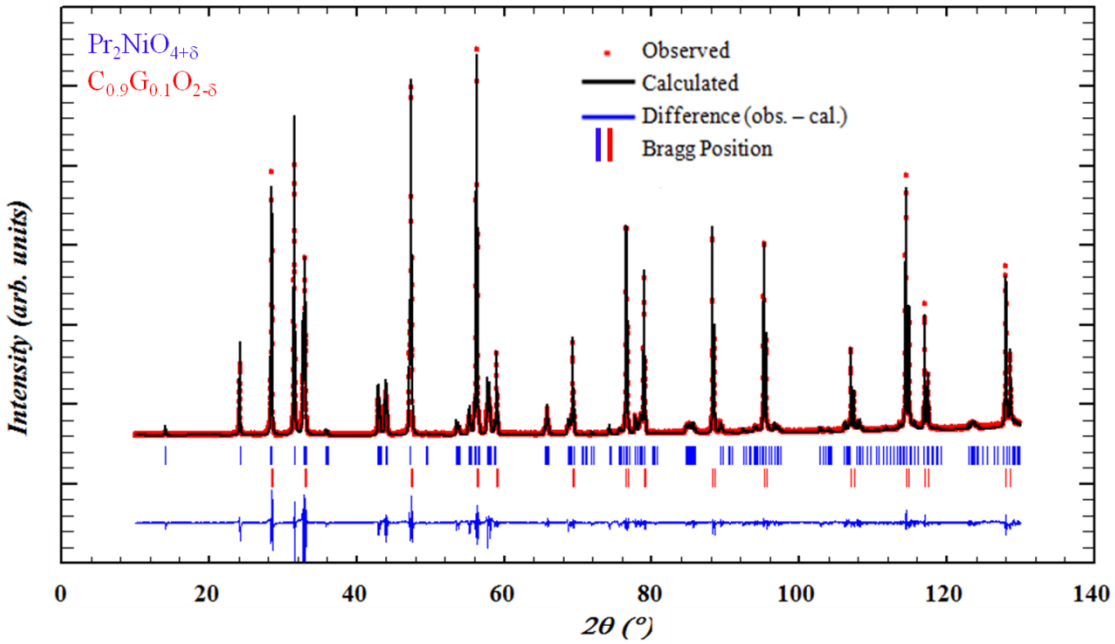

Fig. S3 FULLPROF refinement of the XRD patterns of $Pr_2NiO_{4+\delta}$ film deposited by ESD on a CGO pellet (Fit parameters: χ^2 = 10.3, Bragg R-factor = 1.09 and RF-factor = 0.67 for $Pr_2NiO_{4+\delta}$; Bragg R-factor = 0.83 and RF-factor = 0.49 for CGO).

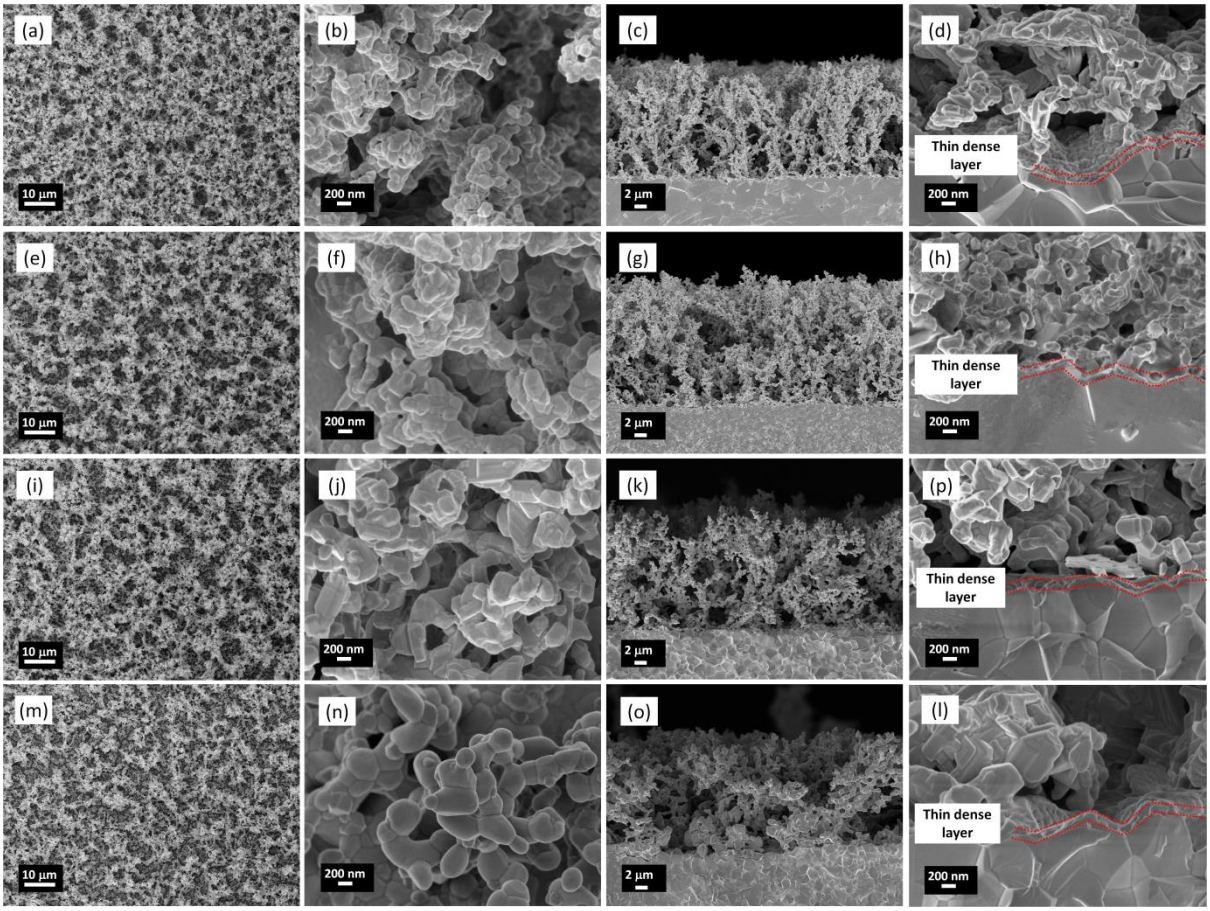

Fig. S4 SEM micrographs of the $La_{2-x}Pr_xNiO_{4+\delta}$ ($0 \leq x \leq 2$) single layer films on a CGO substrate, $La_2NiO_{4+\delta}$: (a, b) surface, (c, d) cross section; $La_{1.5}Pr_{0.5}NiO_{4+\delta}$: (e, f) surface, (g, h) cross section; $LaPrNiO_{4+\delta}$: (i, j) surface, (k, l) cross section and $Pr_2NiO_{4+\delta}$: (m, n) surface, (o, p) cross section.

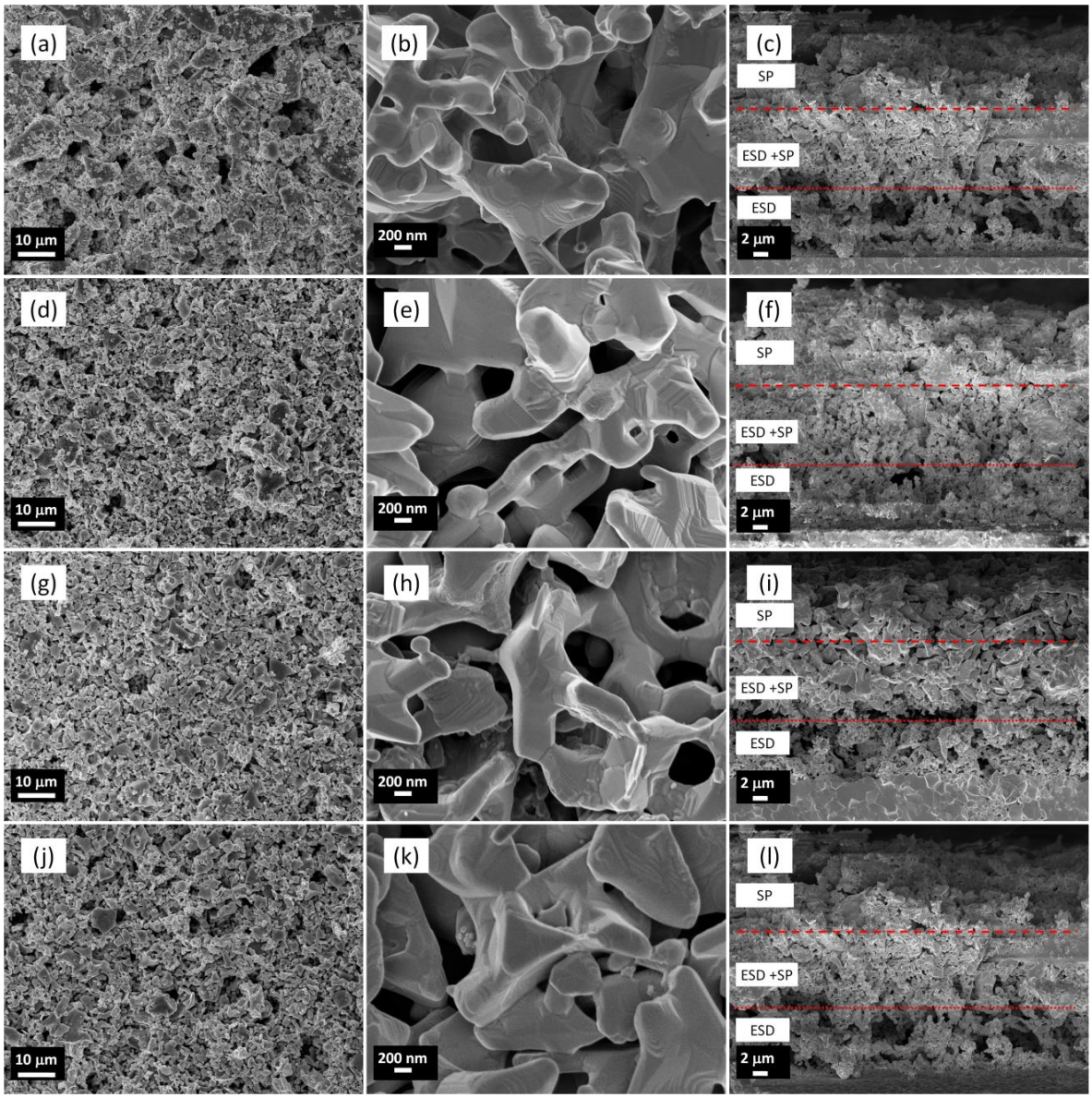

Fig. S5 SEM micrographs of the $La_{2-x}Pr_xNiO_{4+\delta}$ ($0 \leq x \leq 2$) double layer films on a CGO substrate, $La_2NiO_{4+\delta}$: (a, b) surface, (c) cross section; $La_{1.5}Pr_{0.5}NiO_{4+\delta}$: (d, e) surface, (f) cross section; $LaPrNiO_{4+\delta}$: (g, h) surface, (i) cross section and $Pr_2NiO_{4+\delta}$: (j, k) surface, (l) cross section.

Chapter 4

$La_4Ni_3O_{10-\delta}$ as an efficient solid oxide fuel cell cathode: electrochemical properties versus microstructure

R. K. Sharma, M. Burriel and E. Djurado, *J. Mater. Chem. A*, 2015, **3**, 23833-23843.
DOI: 10.1039/C5TA07862H

$La_4Ni_3O_{10-\delta}$ as an efficient solid oxide fuel cell cathode: electrochemical properties versus microstructure

R. K. Sharma[a, b], M. Burriel[c, d] and E. Djurado[a, b]

[a] Univ. Grenoble Alpes, LEPMI, F-38000 Grenoble, France
[b] CNRS, LEPMI, F-38000 Grenoble, France
[c] ICMCB, CNRS, Université Bordeaux, 33608 PESSAC, France
[d]Catalonia Univ. Grenoble Alpes, CNRS, LMGP, F-38000 Grenoble, France

*Corresponding author: Elisabeth Djurado
E-mail: elisabeth.djurado@lepmi.grenoble-inp.fr, Tel: +33-476826684; Fax: +33-476826777

Abstract:

The higher-order Ruddlesden-Popper phase $La_4Ni_3O_{10-\delta}$ is prepared for the first time by electrostatic spray deposition (ESD) on CGO ($Ce_{0.9}Gd_{0.1}O_{2-\delta}$) electrolyte and evaluated as Intermediate Temperature Solid Oxide Fuel Cell cathode. Different and innovative microstructures are obtained by varying the deposition time, nozzle to substrate distance, substrate temperature, solution flow rate, concentration and solvents. Single phase $La_4Ni_3O_{10-\delta}$ films crystallize in an orthorhombic layered Ruddlesden-Popper (n=3) structure after calcination at 950 °C for 8 h in air and is maintained after further sintering at 1100 °C for 6 h in air. The surface morphology, observed by SEM-FEG, is strongly influenced by the solution concentration, the nature of the solvents and the deposition temperature. The electrochemical properties are found to be strongly dependent on the microstructure of the cathode films. The lowest polarization resistance values obtained for the double layer (3-D coral-type film by ESD topped by a screen-printed layer) cathode are 2.01, 0.30 and 0.05 $\Omega.cm^2$ at 600 °C, 700 °C and 800 °C, respectively. To the best of our knowledge, this $La_4Ni_3O_{10-\delta}$ cathode shows the best performance reported to date for this composition.

1. Introduction

The main objective of the current research on solid oxide fuel cells (SOFCs) is the lowering of the operating temperature from above 900 °C down to 700 °C (intermediate temperatures) in order to increase their lifetime and reduce the overall cost. However, the fuel cell performance degrades at lower temperature because of the larger overpotentials generated at the cathodic side and the larger ohmic losses in the electrolyte. Hence, the search for new mixed ionic-electronic conducting(MIEC) cathode materials is key, especially for improving the performance of Intermediate Temperature Solid Oxide Fuel Cells (IT-SOFCs) working at 500–700 °C.[1-5] The Ruddlesden-Popper (RP) family compounds with general formula ($La_{n+1}Ni_nO_{3n+1}$; n=1, 2, 3) have been suggested to be promising candidates for cathode materials [6-8]. The total conductivity of RP phases has been found to increase with *n*. [6, 7, 9-11] In particular, the $La_3Ni_2O_{7-\delta}$ and $La_4Ni_3O_{10-\delta}$ compounds possess higher conductivity compared with $La_2NiO_{4+\delta}$ and also higher relative stabilities, which potentially could make them more suitable cathode materials for IT-SOFCs. [6, 7, 12] As an example, the $La_4Ni_3O_{10-\delta}$ electrode performance of symmetrical cells with $La_{.9}Sr_{.1}Ga_{.8}Mg_{.2}O_{3-\delta}$ electrolyte was found the lowest one of the series (1 Ω cm^2 at 1073 K). Nickelates have also received much attention because they exhibit high kinetics with a surface exchange coefficient of 1.3 x 10^{-7} $cm.s^{-1}$ measured at 700°C.[13] Moreover, it is worth to mention that the thermal expansion coefficient of $La_4Ni_3O_{10-\delta}$ (13.2 x 10^{-6} K^{-1}) has been reported to be close to the common SOFC electrolyte materials such as the ceria based electrolytes (CGO) (13.4 x 10^{-6} K^{-1}) in air. [6] The similar TEC values guarantees the thermo-mechanical compatibility between cell components.

Despite of the fact that several methods have been used for the synthesis of $La_4Ni_3O_{10-\delta}$: Pechini routes[6], nitrate and citrate routes[15, 16], solid-state routes [7, 17], and continuous hydrothermal flow synthesis method [18]; the higher members of the $La_{n+1}Ni_nO_{3n+1}$series, particularly n=2 and 3 are difficult to synthesize as a pure phase because they normally require prolonged homogenization and reheating procedures. [6, 15, 17] For example Amow *et al.* prepared $La_4Ni_3O_{10-\delta}$ by the Pechini method at 1050 °C over 6 days with one intermittent regrinding step, [6, 19] whereas Takahashi *et al.* synthesized $La_4Ni_3O_{10-\delta}$ by heating La_2O_3 and NiO at 1050 °C over 6 days with one intermittent regrinding step.[7] Furthermore, Zhang *et al.* prepared the same composition by calcinations at 1100 °C for 4 ~ 5 days in air, also with several grinding processes. [16]

This article reports, for the first time, the facile preparation of pure $La_4Ni_3O_{10-\delta}$ films on CGO substrate by electrostatic spray deposition (ESD) followed by sintering in air. A systematic study of the effect of the ESD process parameters, such as deposition time, nozzle-to-substrate distance, substrate temperature, and the precursor solution, on the film microstructure is presented in order to optimize the $La_4Ni_3O_{10-\delta}$ electrode microstructure, required to improve the electrochemical performance. The electrochemical properties in air are investigated by electrochemical impedance spectroscopy (EIS) versus the microstructure for high performance IT-SOFCs applications.

2. Experimental

To prepare the solutions containing precursors with a La:Ni mole ratio of 4:3 stoichimetric amounts of nickel nitrate hexahydrate (Ni $(NO_3)_2$ $6H_2O$, 99.9%, Aldrich) and lanthanum nitrate hexahydrate ($La(NO_3)_3$ $6H_2O$, 99.9%, Alfa Aesar) were added to citric acid ($C_6H_8O_7$, 99.9%, Alfa Aesar) and ethanol (CH_3CH_2OH, >99.9%, prolabo, referred to as EtOH) into a 30 mL ethanol, ethanol-butyl carbitol ($C_4H_9(OCH_2CH_2)_2OH$, Acros Organics, 99+%, referred to as BC) (1:2), and ethanol-distilled water (1:2) solution with vigorous stirring over 3h. The total concentration of metal ions was varied from 0.005 M to 0.02M. The conductivity of each of the prepared solution was measured and is included in **Table 1** together with the boiling points and surface tension. [20]

Electrostatic spray deposition (ESD), with several advantages over conventional deposition techniques such as a simple set-up and the use of inexpensive precursors, has been used to deposit $La_4Ni_3O_{10-\delta}$ films on $Ce_{0.9}Gd_{0.1}O_{2-\delta}$ (CGO) substrates (~19 mm in diameter) in a vertical set-up configuration [19, 21] under ambient atmosphere. ESD is based on electrohydrodynamic laws where a precursor solution is pumped through a metallic nozzle at a controlled flow rate. The solution is then atomized by applying a high voltage that generates an electrical field between the nozzle and the substrate. The electrical field generates the aerosol and directs it towards the substrate where the droplets spread, dry and decompose to form the film. The ESD raw coatings are amorphous. To crystallize the films a calcination step at 950 °C for 8 h in air was carried out after the deposition. The effect of the ESD process parameters (**Table 2**) such as deposition time, concentration, nature of the solvent, substrate temperature, nozzle to substrate distance and solution flow rate were investigated to control the film microstructure.

X-ray diffraction (XRD, Philips X'Pert-MPD system, Cu K_α radiation, λ=1.54056 Å) was used to determine the crystal structure.The phase identification was carried out using International Centre for Diffraction data (ICDD). The positions of X-ray diffraction peaks as well as the cell parameters were obtained by refinement using Fullprof software. [22] Field emission scanning electron microscopy (ZEISS Ultra 55 instrument with field emission gun (FEG) was used for the morphology evaluation of the film surfaces and cross-sections and Energy-dispersive X-ray spectroscopy (EDX) for the composition analysis. Four symmetrical cells, cathode/ CGO electrolyte / cathode, were used for the electrochemical studies.

Table 1. Solvent composition, concentration, conductivity, boiling points and surface tensions of the precursor solutions [20]

Solutions	Solvent(s)	Solution concentration [$mol \cdot L^{-1}$]	Solution conductivity [$mS.cm^{-1}$]	Boiling point [°C]	Surface tension [$mN.m^{-1}$]
S_A	EtOH+ BC(1:2)	0.02	0.06	168	27
S_B	EtOH, 100 %	0.005	0.16	78	21
S_C	EtOH, 100 %	0.01	0.19	78	21
S_D	EtOH, 100 %	0.02	0.26	78	21
S_E	EtOH + H_2O (1:2)	0.02	3.34	93	55

Ink for the screen-printing of the current collecting layer (CCL) was prepared using the KD2921 (Zschimmer and Schwarz) solvent and nickelate powder, previously synthesized by sintering (950 °C/ 8 h in air) of amorphous powder obtained by the heating of the ESD precursor solution at 150 °C. For the double layer cathode, the $La_4Ni_3O_{10-\delta}$-based CCL was screen printed (SP) on the ESD films deposited on the CGO electrolyte (see **Table 3**) and then sintered under air at 1050 °C for 2h followed by 1100 ° C for 0.5 h. The cathode area of each ESD prepared cathode was of 2.0 cm^2 whereas for the double layer (ESD + SP) of 1.54 cm^2. Electrochemical Impedance Spectroscopy (EIS) measurements were carried out with a PARSTAT 302N in a symmetrical two-electrode configuration in air between 500 and 800 ºC. The measurements were performed in the frequency range from 50 mHz to 100 kHz with

signal amplitude of 0.02 V at open-circuit voltage, using Au grids (Heraeus, 1024 meshes/cm^2 woven from 0.06 mm dia. wire) as current collectors. The impedance diagrams were fitted to equivalent circuits using the ZView® software (Scribner Associates).

Table 2. ESD process parameters investigated to control the film microstructure

Process parameters	Substrate temperature [°C]	Deposition time [h]	Flow rate [$mL.h^{-1}$]	Nozzle-to-substrate distance [mm]	Nature of solvent(s)	Solution concentration [M]
Deposition time	350	0.5 1.5 2.0 3.0	1.5	50	EtOH	0.02
Solution concentration	350	3.0	1.5	50	EtOH	0.005 0.01 0.02
Nature of solvent(s)	350	3.0	1.5	50	EtOH EtOH:H_2O, 1:2 EtOH:BC, 1:2	0.02
Substrate temperature	300 350 400	3.0	1.5	50	EtOH:H_2O, 1:2	0.02
Nozzle-to-substrate distance	350	3.0	1.5	30 50	EtOH:H_2O, 1:2	0.02

3. Results and discussion

3.1. Structural characterization and elemental analysis

All the films were sintered at 950 °C for 8 h in air and a pure orthorhombic cell, structure which was maintained after sintering at 1100ºC, as confirmed by XRD. **Fig. 1** shows the typical FULLPROF refinement of the XRD pattern of the film sintered at 950 °C for 8 h in air followed by sintering of 1100 °C for 6 h in air. No impurities or secondary phases can be observed even after the second calcination at 1100°C. All diffraction peaks matched well those of $La_4Ni_3O_{10-\delta}$ phase (ICDS #04-009-2594) and were indexed to an orthorhombic unit cell with the Fmmm space group (N° 69). The cell parameters of a = 5.413(2) Å, b = 5.462(3) Å and c = 27.960 (5) Å, deduced from Fullprof software refinement, are found to be in good agreement with previously reported values. [6, 15, 17] The EDX spectrum, shown in Fig 2, confirmed the presence of La, Ni and O elements in the film with a La/Ni ratio of 1.28 ± 0.05, as expected.

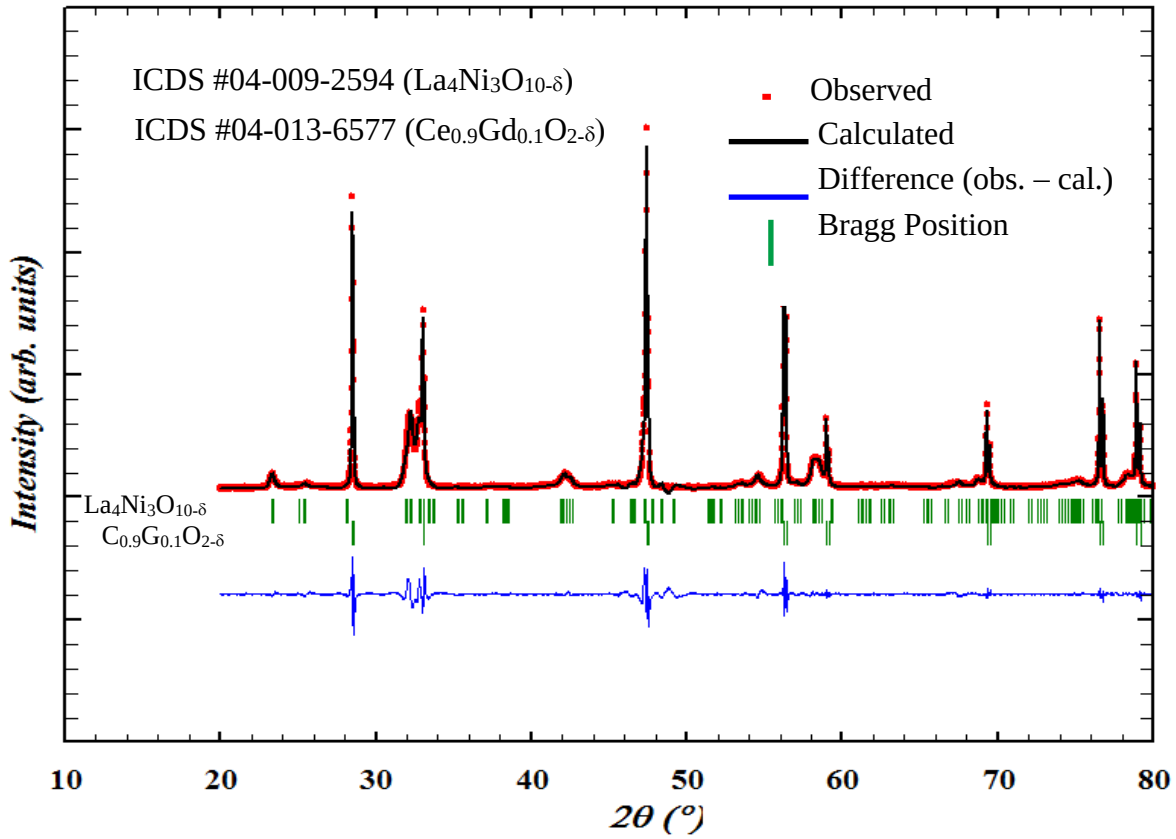

Fig. 1 FULLPROF refinement of the XRD patterns of $La_4Ni_3O_{10-\delta}$ film deposited by ESD at 350 °C on a CGO substrate and after calcination at 950 °C/ 8 h + 1100 °C/ 6 h in air.

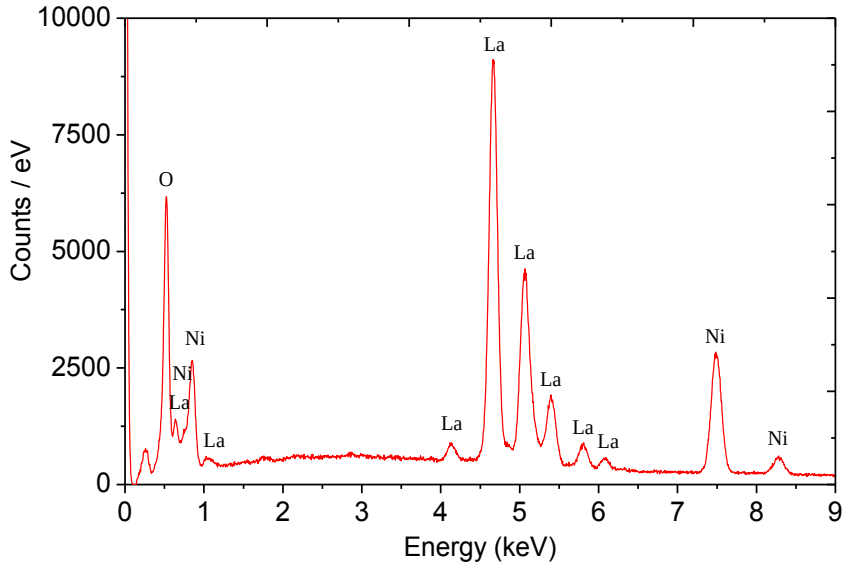

Fig. 2 Typical EDX spectrum of the $La_4Ni_3O_{10-\delta}$ film calcined at 950 °C for 8 h in air.

3.2. Microstructural characterization

In a first step, ESD was systematically investigated for the preparation of various microstructures depending on five process parameters (see **Table 2**).The microstructure of the film deposited by this technique highly depends on the size of the droplets impacting the heated substrate. The droplet size is determined by the substrate temperature, the droplet flight time between the needle and the substrate during transport of the aerosol spray, and the precursor solution flow rate. Therefore the size of the droplets can be easily tuned in a controlled manner by changing the deposition parameters. Several studies have modelled how the solution properties and the deposition parameters determine the droplet size formed at the nozzle, [23, 24] being the Gañan-Calvo's relationship the most consensual one [25]:

$$d \sim \left(\frac{\rho \varepsilon_0 Q^3}{\gamma K} \right)^{1/6} \qquad \text{(Equation 1)}$$

where d is the droplet diameter, ρ the density, ε_0 the vacuum permeability, Q the flow rate, γ the surface tension and K the electrical conductivity of the solution.

3.2.1. Influence of the deposition time

To study the evolution of the film growth and microstructure, $La_4Ni_3O_{10-\delta}$ films have been prepared at 350 °C varying the deposition time from 0.5 to 3 h while maintaining a pure EtOH solution, a nozzle to substrate distance of 50 mm, a flow rate of1.5 mL/h and a concentration of the precursor solution of 0.02 M (see **Table 2**). A significant evolution of the surface morphology is evidenced over time (**Fig. 3**), especially between 0.5 h (**Fig. 3-c**) and 1.5 h (**Fig. 3-f**). As the deposition time was raised, an increase in particle agglomeration resulted from preferential landing of the aerosol droplets and from the lack of wetting on the substrate[26] due to the nearly dry aerosol droplets. With increasing time, a larger number of droplets arrive on the substrate changing the smooth surface of the original substrate and creating some irregularities with higher curvature. The charges on the substrate surface induced by the strong applied electrostatic field concentrate more where the curvature is greater.[27] So the charged droplets arriving at the surface will be more attracted towards these more curved areas. This is referred to as ‘‘preferential landing’’. This action will cause particle agglomeration, especially when the droplets are small and light. Hwang *et al.*[27] have shown that when the substrate roughness is increased, preferential landing is promoted

leading to particle agglomeration. In our case, several agglomerates are clearly visible after 0.5 h of deposition due to the preferential attraction (**Fig. 3a**) and this agglomeration increases with increasing time as shown in **Fig.3d**, **3g** and **3j**.The thickness was found to be about 6 µm in average after 0.5 h (**Fig. 3c**), 15µm after 1.5 h (**Fig. 3f**), 18 µm after 2 h (**Fig. 3i**) and 26 µm after 3 h (**Fig. 3l**).

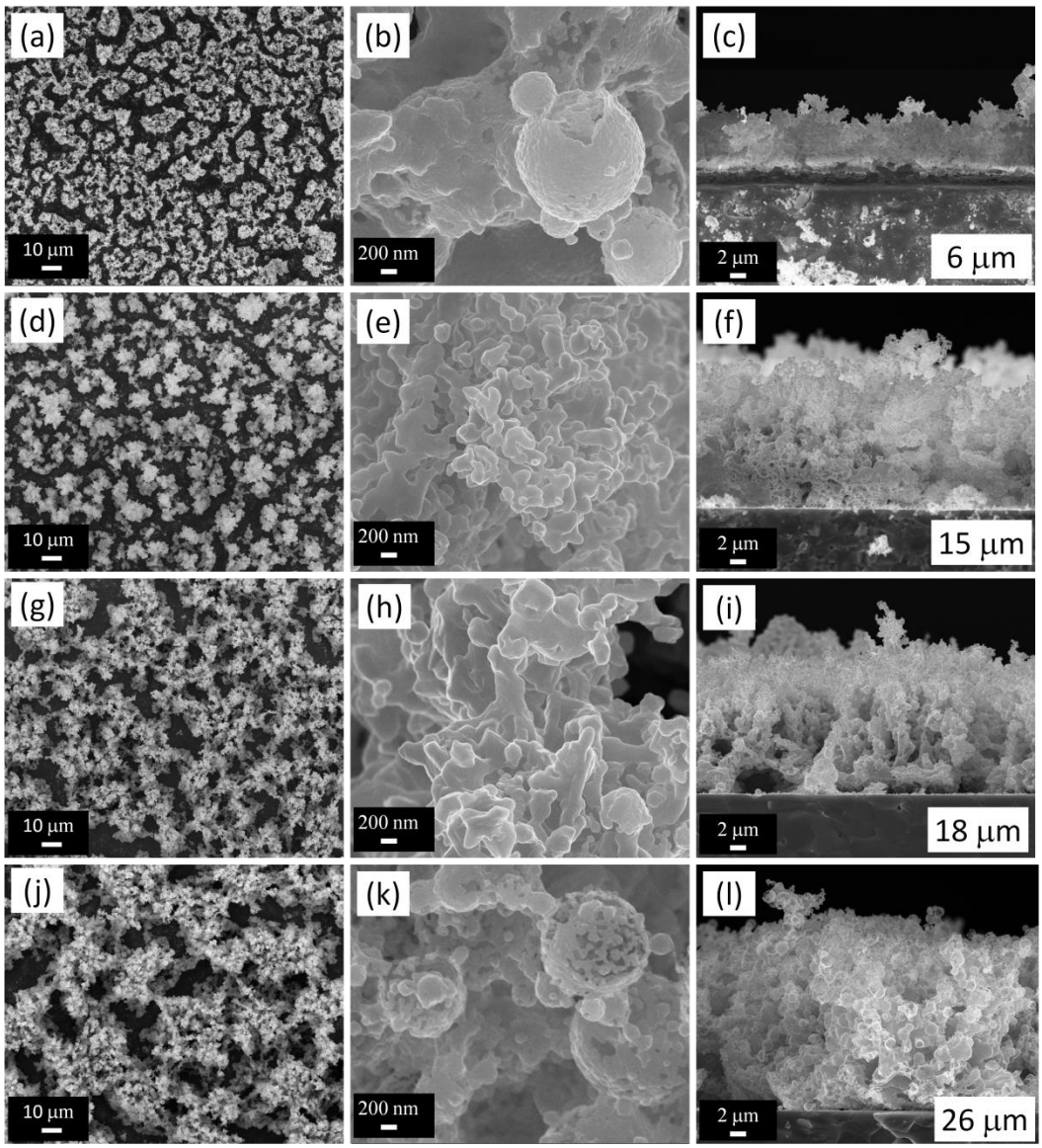

Fig. 3 SEM micrographs of the calcined (950°C for 8 h in air) ESD films using EtOH and 0.02 M salt concentration at T=350 °C, for a distance nozzle to substrate of 50 mm and a flow rate of 1.5 $mL.h^{-1}$ after deposition time of: 0.5 h (a, b) surface, (c) cross section; 1.5 h (d, e) surface, (f) cross section; 2 h (g, h) surface, (i) cross section; 3 h (j, k) surface, (l) cross section.

3.2.2. Influence of the precursor solution concentration

The influence of the precursor concentration on the film morphology was studied for different salt concentrations of 0.005, 0.01 and 0.02 M (Figure 4). The other ESD deposition parameters were maintained constant at a flow rate of 1.5 $mL.h^{-1}$, substrate temperature of 350 °C, 3 h deposition time, nozzle-to-substrate distance equal to 50 mm and using pure ethanol as the solvent (see **Table 2**). The measured electrical conductivity of the precursor solution decreases with the precursor concentration as shown in Table 1, in good agreement with previous observations.[11] Having considered capillary equilibrium, liquid continuity and moment and charge continuity at the jet, Gañan-Calvo deduced the following relation for polar liquids:

$$d \sim \varepsilon_r^{1/6} \left(\frac{Q}{K} \right)^{1/3} \qquad \text{(Equation 2)}$$

where ε_r, d and Q are the relative permittivity of the solution, the diameter of the droplets emitted at the jet (the primary droplet size) and the flow rate of the solution, respectively. As a result, the primary droplet size depends on these 3 parameters. Thus for a given flow rate (in this case, 1.5 $mL.h^{-1}$), the droplet size depends only on the conductivity of the solution provided that the permittivity of the solution is kept constant. For the ethanol solution, the permittivity is approximately 2×10^{-10} F m^{-1}. [20]

As evidenced in **Fig. 4a-d**, a similar "cauliflower" like microstructure has been observed for the solution of concentration 0.005 and 0.01 M. Since the conductivity of the solution is quite similar (**Table 1**), a closed morphology with primary particle size of ~ 100 nm can be observed. When the concentration of the solution is increased to 0.02 M, some large, very porous and connected agglomerates are visible (**Fig. 4e**, **4f**). These round-shape agglomerates consist of finer particles of an approx. 50 nm diameter size. According to equation 2, a higher concentration and hence a higher conductivity (passing to 0.26 $mS.cm^{-1}$) will result in a smaller droplet size. They are smaller and lighter so their movement direction can be changed considerably by the attraction of induced charges at the substrate surface to form agglomerates.

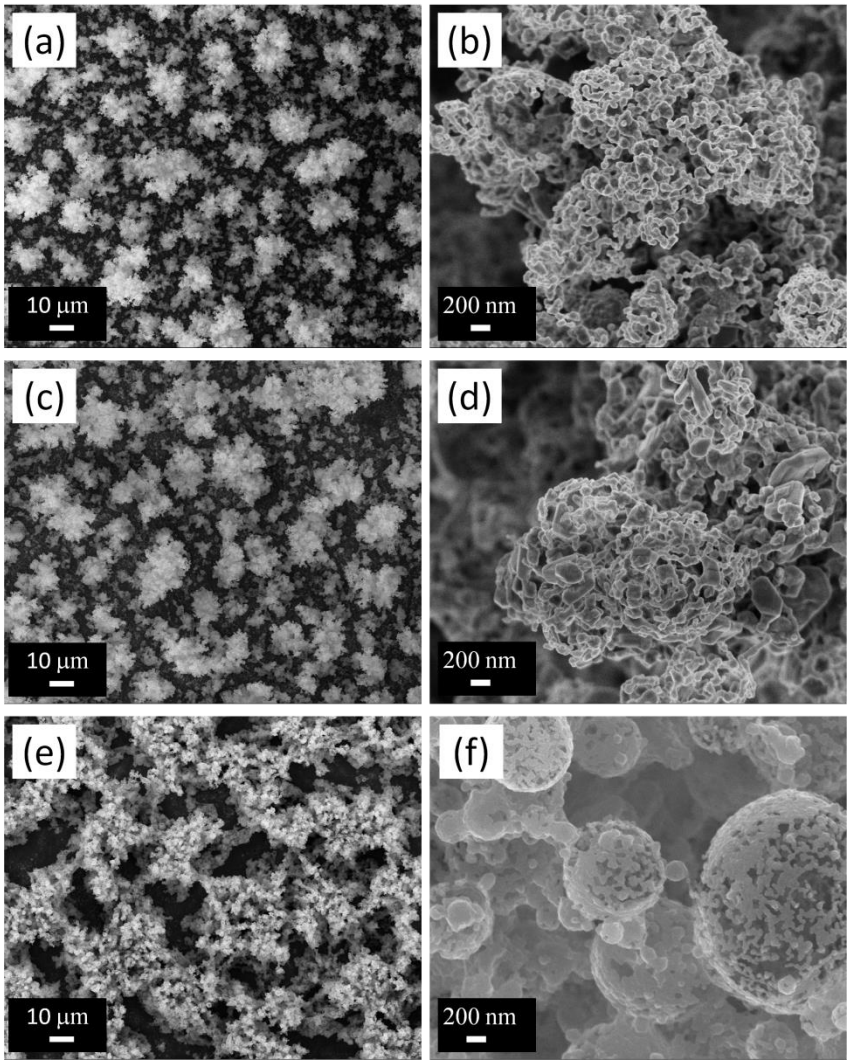

Fig. 4 SEM surface micrographs (at 2 different magnifications) of calcined (950 °C for 8 h in air) $La_4Ni_3O_{10-\delta}$ ESD films obtained with a solution concentration of (a), (b) 0.005 M; (c) (d) 0.01 M; (e), (f) 0.02 M, using pure EtOH at T=350 °C for a nozzle to substrate distance of 50 mm and a flow rate of 1.5 $mL.h^{-1}$ and after deposition time of 3 h.

3.2.3. Influence of the solvent composition

The physico-chemical properties of the precursor solution also play an important role in the ESD process and especially on the droplet size, which determines the morphology of the coating. In particular, the boiling point, conductivity and surface tension are crucial factors affecting both the evaporation of the solvents during the transport and the spreading of the droplets that impact the substrate. By changing the solvent composition, the layer morphology may also be modified. At a fixed optimized concentration of 0.02 M three different solvent compositions of EtOH: BC(1:2), EtOH 100% and EtOH: water (1:2),

referred to as S_A, S_D and S_E (Table 1) have been selected to study their effect on the evolution of the $La_4Ni_3O_{10-\delta}$ film morphology. In this study, the other process parameters: substrate temperature, solution flow rate, nozzle-to-substrate distance and deposition time were fixed at 350 °C, 1.5 $mL.h^{-1}$, 50 mm and 3h, respectively (**Table 2**). The resulting microstructures are shown in **Fig. 5**.

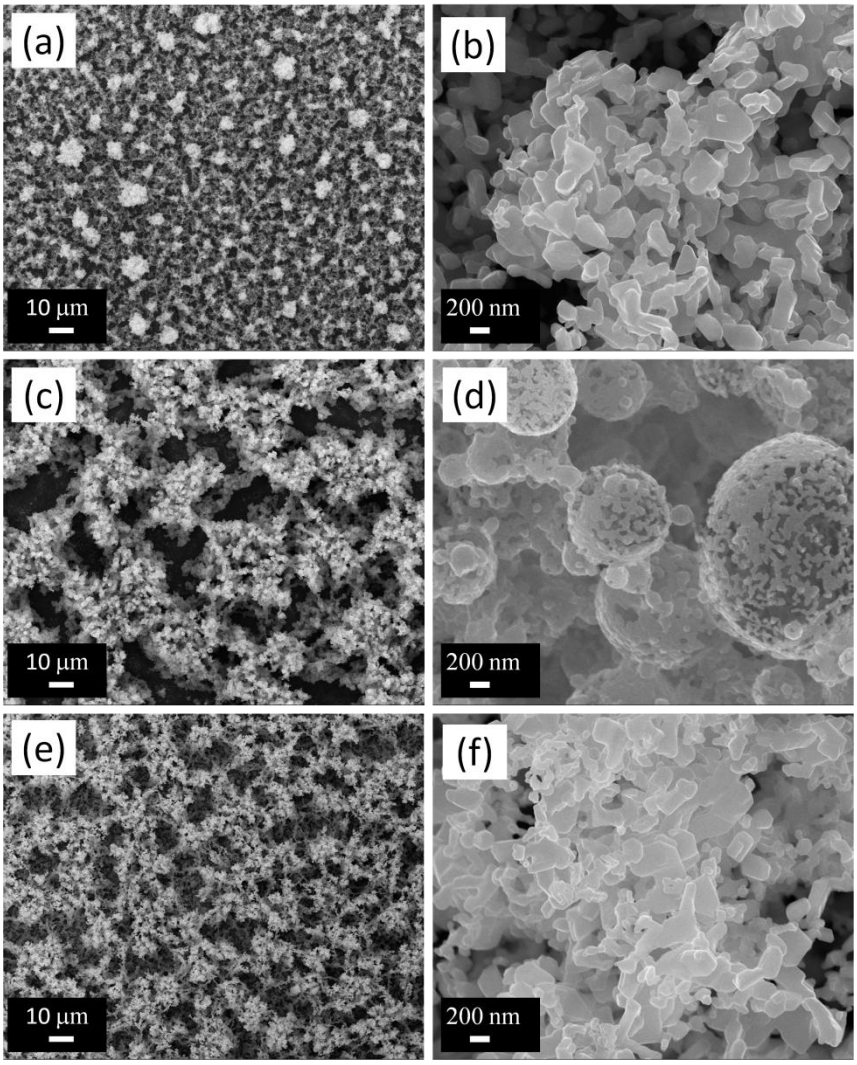

Fig. 5 SEM surface micrographs (at 2 different magnifications) of calcined (950 °C for 8 h in air) $La_4Ni_3O_{10-\delta}$ ESD films obtained with solution of (a), (b) S_A: EtOH + BC (1:2); (c), (d) S_D: EtOH; (e), (f) S_E: EtOH + H_2O(1:2) with a solution concentration of 0.02 M at T=350 °C for a nozzle to substrate distance of 50 mm and a flow rate of 1.5 $mL.h^{-1}$ and after deposition time of 3 h.

A larger particle size (~200 nm) can be observed (**Fig. 5a**, **5b**) when BC is added to EtOH (S_A) in comparison to our previous investigation with S_D (**Fig. 5c**, **5d**) (~50 nm). According to equation 1, since the conductivity has been drastically reduced to 0.06 $mS.cm^{-1}$ and the surface tension is of the same order of magnitude (**Table 1**), the droplet size is expected to be larger in S_A, being mainly proportional to $K^{-1/6}$. These larger particles also originate from the higher boiling point of the EtOH:BC (1:2) solution (S_A, **Table 1**). Considering that the evaporation rate for S_A is slower than that of S_D (pure EtOH), a slower drying process is expected. The large liquid droplets of S_A are expected to spread much more on the heated substrate than the smaller and drier droplets of S_D. Consequently, the coating obtained from S_A (**Fig. 5a, 5b**) presents a porous connected net with larger particles than the net of round shape agglomerates with finer grains in S_D (**Fig. 5c, 5d**). The addition of H_2O in EtOH (S_E) leads to a higher conductivity of the precursor solution and larger surface tension (Table 1) than in S_D and S_A and, consequently, to a decrease in the droplet size (see Equation 1). However, the particle size observed in **Figures 5e** and **5f** (150 nm) is not as small as the one in S_D (50 nm, **Fig. 5d**). Indeed, we also have to consider the boiling point of S_E which is larger than in the case of S_D (93 °C against 78 °C, **Table 1**). This is the factor which is countering the effect of conductivity and surface tension parameters and may lead to intermediate final particle sizes (~150 nm) for S_E (**Fig. 5f**). In these conditions, a porous reticulation is observed with particle size ranging from ~200 nm (S_A) (**Fig. 5b**), ~ 50 nm (S_D) (**Fig. 5d**) and ~ 150 nm (S_E) (**Fig. 5f**).

3.2.4. Influence of the substrate temperature

The substrate deposition temperature has been reported to be a main parameter, since the entire pyrolysis processes take place at or near the substrate surface.[28] The temperature plays a role in conditioning the drying rate of the droplets during the flight, the rate at which they dry once deposited on the substrate, the way in which the droplets spread on the surface have an effect in the resulting microstructure. As observed by Nguyen *et al.*[29], a mere 5 °C difference is sufficient to modify the droplet size and thus, to radically change the resulting microstructure. For the solution S_E, the evolution of the surface microstructure of the $La_4Ni_3O_{10-\delta}$ films deposited at different temperatures ranging from 300 °C to 400 °C is shown in **Fig. 6**. The precursor solution concentration, nozzle-to-substrate distance, flow rate and deposition time were fixed at 0.02 M, 50 mm, 1.50 $mL.h^{-1}$ and 3 h, respectively. At 300 °C, cracks have been observed (**Fig. 6a**) which could be due to stresses developed during the

drying process of a large quantity of liquid present on the substrate at this low temperature. When large droplets impact the heated substrate, simultaneous spreading and drying processes occurs. Consequently, large particles of approx.100 x 400 nm are obtained. As the deposition temperature was raised to 350 °C, the arriving droplets contained less solvent. Therefore the drying step is more homogeneous and smaller connected particles of ~ 150 nm are visible. The cracks disappeared and a porous reticulated $La_4Ni_3O_{10-\delta}$ film is observed. An increase in particle agglomeration (**Fig. 6c**) resulted from preferential landing of the aerosol droplets and from the lack of wetting on the substrate [26] due to the nearly dry aerosol droplets. At higher temperatures drier particles arrive on the substrate changing the surface of the original substrate and creating some irregularities with higher curvature. On further increasing the temperature to 400 °C, no change in the particle size has been observed (**Fig. 6d** and **6e**).

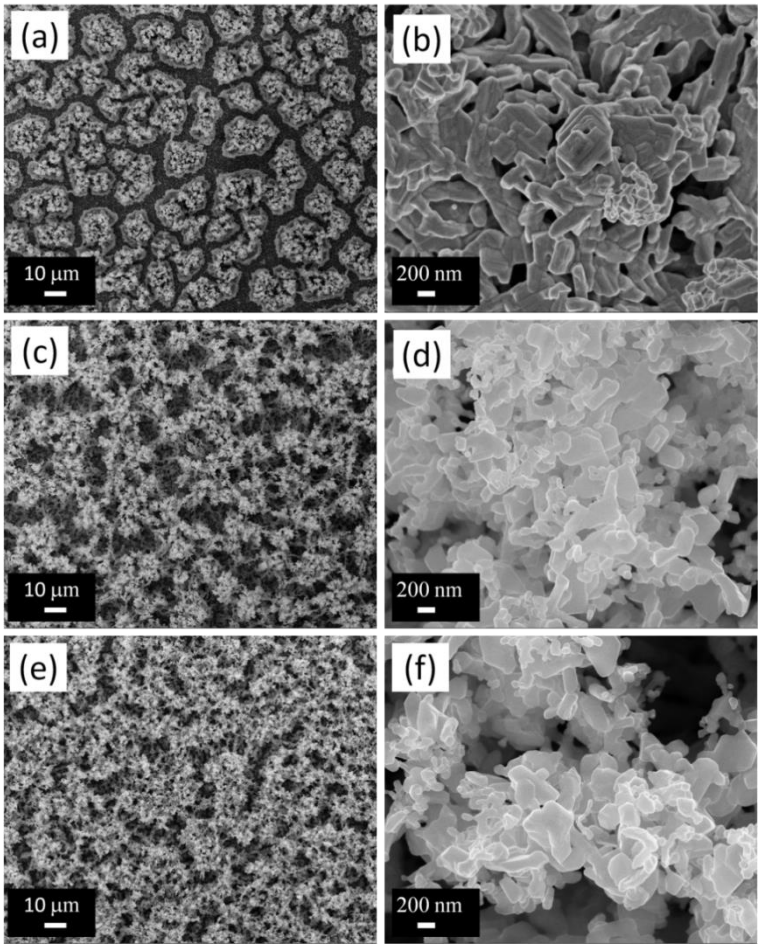

Fig. 6 SEM surface micrographs (at two different magnifications) of calcined (950°C for 8 h in air) $La_4Ni_3O_{10-\delta}$ films obtained by ESD at deposition temperatures of: (a), (b) 300 °C; (c), (d) 350 °C; (e), (f) 400 °C with a solution concentration of 0.02 M for a nozzle to substrate distance of 50 mm and a flow rate of 1.5 $mL.h^{-1}$ and after deposition time of 3 h.

3.2.5. Effect of the nozzle to substrate distance

The amount of precursor solution arriving onto the substrate is also controlled by the nozzle to substrate distance. The shorter the distance, the larger the amount of precursor solution deposited. Therefore we could expect to control the film porosity by changing the nozzle to substrate distance in the same way as the influence of temperature in terms of quantity of solution arriving on the substrate. **Fig. 7** shows surface morphologies of $La_4Ni_3O_{10-\delta}$ films deposited at two different nozzle-to-substrate distances of 30 and 50 mm using solution S_E (**Tables 1** and **2**). The solution flow rate, substrate temperature and total deposition time were fixed at 1.5mL.h^{-1}, 350 °C and 3 h, respectively. The reticulated microstructures of the films deposited at 30 and 50 mm are quite similar but are composed of nanostructured particles of ~ 200 nm at only 30 mm and slightly smaller, ~150 nm for 50 mm (**Fig. 7a-b** and **7c-d**, respectively). As the nozzle to substrate distance increases, it takes a longer time for the droplets to reach the substrate, allowing for a greater solvent evaporation and resulting in drier and smaller droplets when impacting the substrate. In both cases a 3-D coral-type microstructure has been obtained with a slightly more porous microstructure at 50 mm, with smaller connected particles.

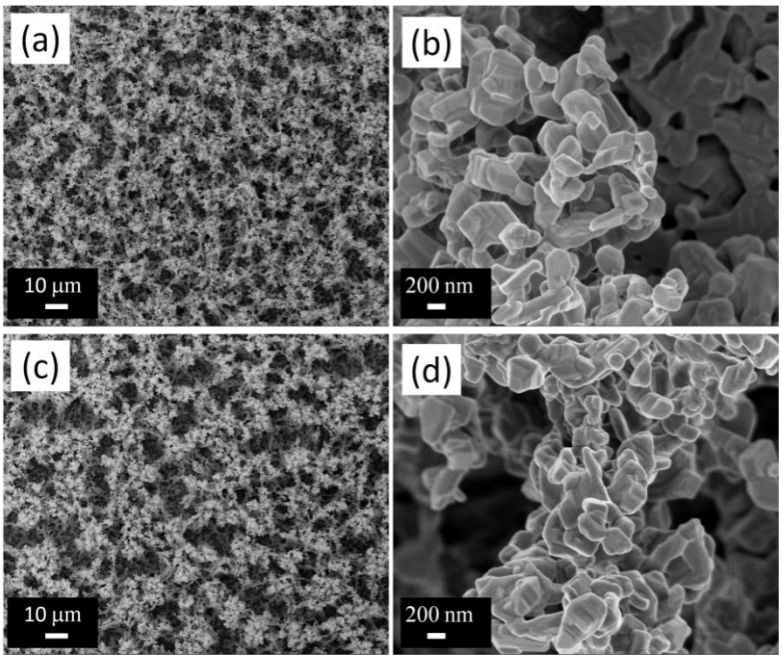

Fig. 7 SEM surface micrographs (at 2 different magnifications) of the calcined (950°C for 8 h in air) $La_4Ni_3O_{10-\delta}$ films obtained at a deposition temperature of 350 °C, a deposition time of 3 h, a flow rate of 1.5 mL.h^{-1} and a nozzle to substrate distance of: (a), (b) 30 mm; (c), (d) 50 mm with a S_E solution of concentration 0.02 M.

3.2.6. Selected $La_4Ni_3O_{10-\delta}$ films microstructures for electrochemistry

The electrochemical properties of the oxygen electrodes depend on their microstructure (percolation path between grains, particle size, porosity), on the electrolyte-electrode interface contact for oxygen ion transfer and on the current collection, to enhance the electronic conductivity. In order to study the effect of the $La_4Ni_3O_{10-\delta}$ films microstructure on their electrochemical properties, we have selected three ESD film microstructures, which differ qualitatively in terms of the percolation path inside the electrode and of the quality of the contact at the $La_4Ni_3O_{10-\delta}$ / CGO interface. These specimens consist of "isolated cauliflowers" (sample 1, **Fig. 8a-b**), connected round agglomerates (sample 2, **Fig. 8d-e**) and 3D coral-type microstructure (sample 3, **Fig. 8g-h**). The films were deposited at a substrate temperature, nozzle to substrate distance, flow rate and deposition time of, 350 °C, 50 mm, 1.5 $mL.h^{-1}$ and 3h, respectively. The other ESD parameters such as nature of the solvents and concentration of the precursor solution used for such microstructures are given in **Table 3**, along with some characteristics of the microstructure. The porosity of the films was estimated by comparing the apparent film density with the $La_4Ni_3O_{10-\delta}$ theoretical density. The apparent density was obtained by weighing the CGO substrates before and after the ESD film deposition and measuring the film thickness and diameter. A porosity of approximately 95, 92 and 86 vol. % was estimated for the isolated cauliflower, connected round agglomerates and 3-D coral type microstructures, respectively. This large porosity indicates that plenty of space is available for oxygen molecules to transport in ESD film. These values are in good agreement with the porosity reported by Sar et. al. using FIB-SEM on the CGO/LSCF ($La_{0.6}Sr_{0.4}Co_{0.2}Fe_{0.8}O_{3-\delta}$) film also deposited by ESD. [30] Further all three electrodes are characterized by an average particle size varying from 50 nm (sample 2, **Fig. 4f**), to 100 nm (sample 1, **Fig. 4d**) to 150 nm (sample 3, **Fig. 5f**) with a difference in percolation and in the presence or absence of a continuous thin dense cathode layer between the electrolyte and the porous cathode. It is obvious from **Fig. 8c** and **8f** that samples 1 and 2 do not have the continuous thin dense layer, whereas sample 3 (3-D coral-type microstructure) and sample 4 (3-D coral-type microstructure topped by SP layer) do present a continuous and adherent interface (**Fig. 8i**). The origin of this thin dense layer is the lower evaporation rate and larger amount of the liquid in the charged droplet of EtOH + water (1:2) based precursor solution (used for samples 3 and 4) in comparison to the finer and almost dry droplets of the EtOH based solution (used for samples 1 and 2). As a consequence, the charged liquid droplets containing water, spread much more on the polished flat surface of the grounded substrate

than a finer droplets containing EtOH. This leads to the formation of a continuous thin dense layer also improving the adherence of the electrode-electrolyte interface without the need of using high sintering temperatures. Clearly, the percolation path in sample 2, composed of connected round agglomerates, is better than that of the isolated cauliflowers (sample 1). The percolation path is further improved for sample 3, with a 3-D coral-type microstructure. In order to further improve the lateral percolation and to ensure a better contact between the current collecting grid and the cathode, a double layer cathode (sample 4, **Fig. 8j**) was prepared by screen-printing (SP) a 20 μm thick current collecting layer of $La_4Ni_3O_{10-\delta}$ on the top of the functional 3-D coral cathode (20 μm thick) **(Fig.8g** and **8h**). As shown in **Fig.8k**, the screen-printed layer with primary particle size of 600 nm is partially penetrating the ESD functional layer in a depth of approximately 10μm. The total double layer thickness is 30 μm.

Table 3 Sample, microstructure, ESD coating conditions, sintering conditions (in air) and cathode thickness and particle size of the selected films for electrochemical measurements

Samples	Microstructure	Nature of solvent(s)	Concentration of solution(s) [M]	Flow rate [$mL.h^{-1}$]	Sintering Temperature [°C]	Thickness of the cathode [μm]	Particle size [nm]
Sample 1	Isolated cauliflowers	S_C	0.01	1.5	950/ 8h	38	100
Sample 2	Connected round agglomerates	S_D	0.02	1.5	950/ 8h	26	50
Sample 3	3-D coral-type	S_E	0.02	1.5	950/ 8h	24	150
Sample 4	Double layer (3-D coral-type + SP)	S_E	0.02	1.5	950/ 8h 1050/ 2h+ 1100/ 0.5h	30	150 (ESD), 600 (SP)

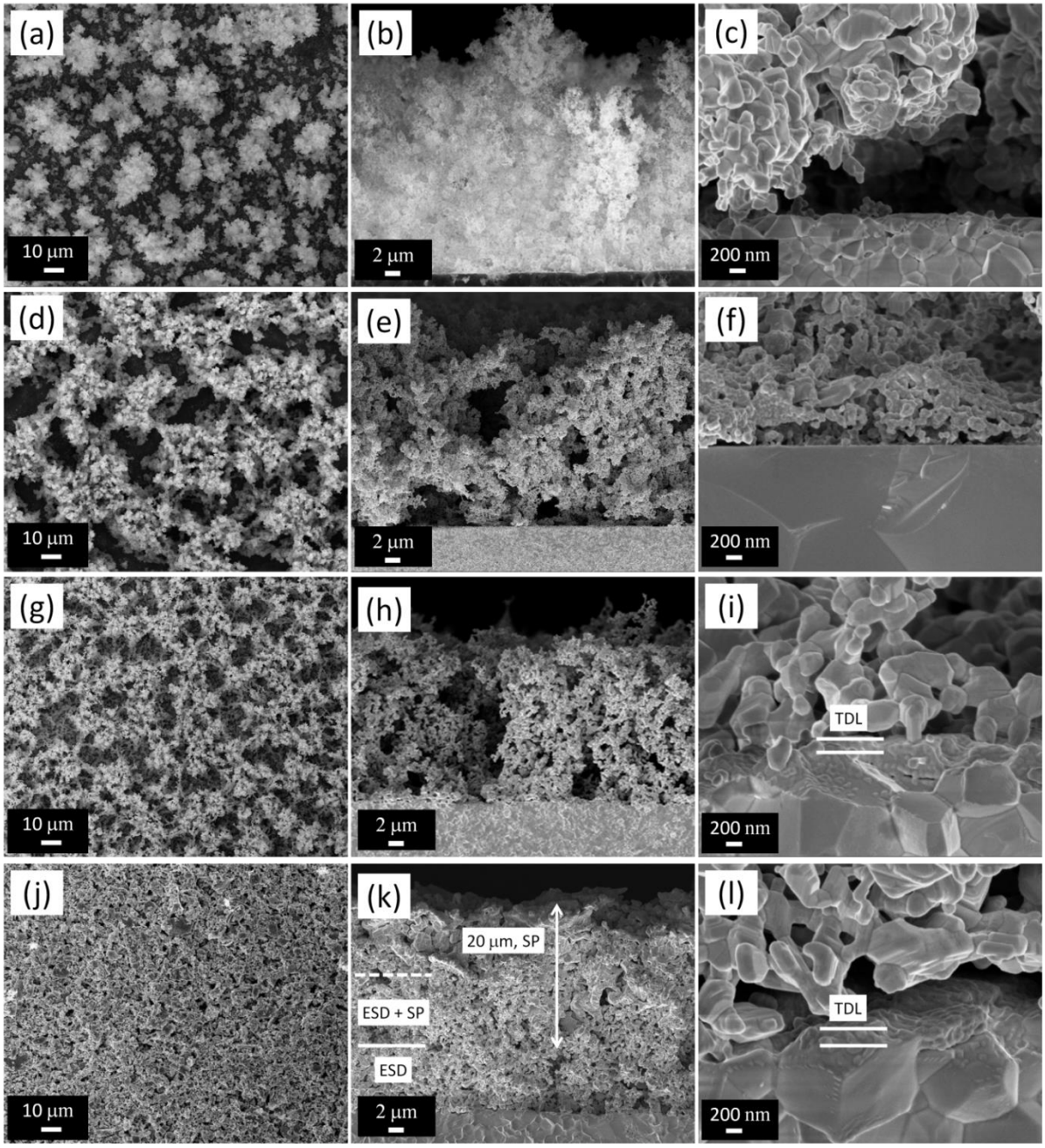

Fig. 8 SEM micrographs of the $La_4Ni_3O_{10-\delta}$ cathode, sample 1: (a) surface, (b) cross section, (c) cross section of a selected region with discontinuous interface; sample 2: (d) surface, (e) cross section , (f) cross section of a selected region with discontinuous interface; sample 3: (g) surface, (h) cross section, (i) interface with a thin dense layer (TDL); sample 4 (double layer cathode (ESD + SP)): (j) surface (k) cross section, (l) interface with a thin dense layer (TDL). Samples 1-3 were calcined at 950 °C for 8 h in air whereas sample 4 at 950 °C for 8 h (after ESD) + 1050 °C for 2 h + 1100 °C for 0.5 h (after SP in air).

3.3. Electrochemical properties

The electrochemical properties of the four selected $La_4Ni_3O_{10-\delta}$ electrodes (samples 1-4, Table 3) deposited as symmetrical cells on CGO were investigated by EIS in air between 500 and 800 ºC at open circuit potential (OCP). **Fig. 9** shows the impedance spectra of the four selected cathodes at 700°C presented on a Nyquist plot and **Fig. 10** shows the equivalent electrical circuit model used to fit the impedance spectra. All experimental diagrams were fitted using a series combination of two resistance-constant phase element parallel circuits (R1//CPE1 at high frequency, *HF* / (LF for sample 4), and R2//CPE2 at low frequency, *LF* / (very low frequency for sample 4)) connected in series with an inductance L1 and with series resistance R_s. The *HF* intercept of the diagrams on the real axis corresponds to the overall ohmic resistances (R_s, **Table 4**), including the resistive contributions of the electrolyte, electrode, leads, cathode and electrolyte interface and contact between electrode and grid. At 700 °C, R_s decreases from 31.97Ω.cm² (sample 1), to 20.73 and 17.78 Ω.cm² (samples 2 and 3, respectively) (**Fig. 9**). This significant variation in R_s from sample 1 to sample 2 can be attributed to an improved contact between the electrode and the current collecting grid (surface view, **Fig 8a** compared to **Fig. 8d**). From samples 2 to 3 the contact at electrolyte/electrode interface improves, increasing the number of contact points between the cathode and the electrolyte (**Fig 8i** compared to **Fig. 8f**) due to the presence of a continuous thin dense layer. Indeed in the cases of sample 2 and 3, the constriction effect of the current lines is lowered since the contact between electrode and grid as well as interface between electrolyte and electrode both are better in comparison to sample 1 characterized by isolated cauliflowers. As we can see in **Fig. 8c** and **8f**, samples 1 and 2 do not have continuous thin dense layer of cathode between the electrolyte and cathode, as is the case for sample 3 and sample 4 (**Fig. 8i** and **8l**). A much lower R_s value could be expected for sample 3 in comparison sample 2 due to better contact of electrode with electrolyte at the interface (presence of thin dense layer, **Fig.8l**), however it is not found due to the poor contact between the electrode and the grid and hence to poor current collection (**Fig. 8g**). A clear reduction of R_s down to 3.43 Ω.cm² (sample 4, **Table 4**, **Fig. 9d**) is obtained when the ESD coral-type film is topped by a SP $La_4Ni_3O_{10-\delta}$ layer. This SP layer leads to a flatter electrode surface (**Fig. 8j**) and hence to a better contact resulting in a better current collection. This means that SP $La_4Ni_3O_{10-\delta}$ layer acts as a current collector layer (CCL). The polarization resistance (R_{pol}) which is used to quantify the magnitude of the electrode reaction, is defined as

$R_{pol} = R_{electrode} \times S/2$

where $R_{electrode}$ is the resistance difference measured between the value of the low frequency intercept of the electrode characteristic on the real axis and R_s. The surface area of each symmetrical electrode is referred to as S and given in **Table 4**. According to the analysis, all electrode responses (samples 1-3) can be separated into two arcs (*HF* and *LF* ones respectively). The *HF* contribution is usually attributed to the charge transfer from the electrode to the electrolyte while the *LF* one is associated with the diffusion resistance, including the adsorption-desorption of oxygen, oxygen diffusion at the gas-cathode interface, and the surface diffusion of intermediate oxygen species. [31]

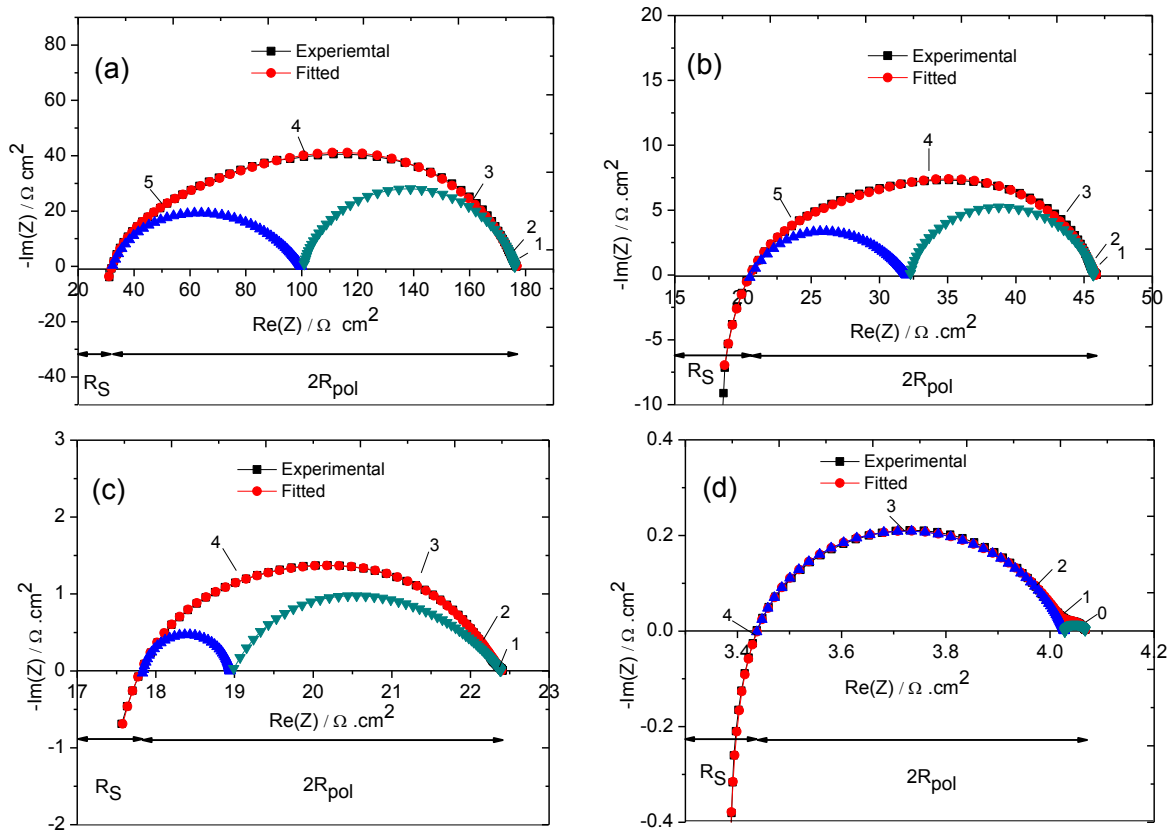

Fig. 9 Nyquist plots for the $La_4Ni_3O_{10-\delta}$/CGO/$La_4Ni_3O_{10-\delta}$ cells with different microstructure recorded in air at 700 °C in OCP conditions: (a) sample 1 (b) sample 2 (c) sample 3 (d) sample 4. The numbers over the diagram indicate the logarithm of the measuring frequency.

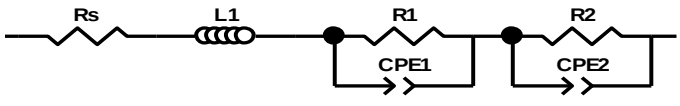

Fig. 10 Equivalent electrical circuit model used for impedance spectra fitting.

Table 4. Microstructures, surface area (S), series resistance (R_S), polarization resistance (R_{pol}) and activation energy (E_a) values in air for the 4 investigated samples

Samples	Microstructure	Surface area [cm^2]	R_S at 700 °C [Ω cm^2]	R_{pol} at 700 °C [Ω cm^2]	R_{pol} at 800 °C [Ω cm^2]	E_a [eV]
Sample 1	Isolated cauliflowers	2.00	31.97	72.41	18.86	1.16
Sample 2	Connected round agglomerates	2.00	20.73	12.78	4.20	0.91
Sample 3	3-D coral-type	2.00	17.78	2.21	0.84	0.72
Sample 4	Double layer (3-D coral-type + SP)	1.54	3.43	0.30	0.05	1.32

Regardless of electrode microstructure, R_{pol} decreases by improving the percolation of the isolated cauliflowers (from sample 1 to sample 2) and decreasing the particle size from 100 nm to 50 nm (**Table 4**). Indeed, the R_{pol} value for the "isolated cauliflower" cathode (sample 1) was found to be 72.41 Ω cm² at 700 °C whereas for the "connected round agglomerates" cathode (sample 2) 12.78 Ω cm². In SOFC operation, the cathode is devoted to reducing the available oxygen molecules into oxygen ions, O^{2-}, especially in the vicinity of triple phase boundary (TPB) points. Consequently, the electronic conductivity must be maximized and sufficient porosity is required to facilitate gas permeation. The microstructure of the cathode is therefore fundamental in enabling access of oxygen, electrons and ionic species between the cathode and the electrolyte, as well as expanding the number of TPB sites by increasing the total cathode surface area. For the 3-D coral-type microstructure the R_{pol} value is further reduced to 2.21 Ω cm² at 700 °C (sample 3, **Table 4**) favored by a simultaneous improvement of the percolation path (**Fig. 8g**) and of the electrode/electrolyte contact (**Fig. 8h**), whereas the particle size is around 150 nm. This is believed to result from the increase in the number of contact points between the CGO substrate and the porous cathode layer due to the presence of the intermediate thin dense cathode layer. The beneficial impact of the addition of an interfacial layer at the electrode-electrolyte has also been previously reported in the literature.[32, 33] A decrease of the area specific resistance from 0.67 Ω cm^2 to 0.21 Ω cm^2 at 600°C was measured when 200 nm of $La_{0.6}Sr_{0.4}Co_{0.2}Fe_{0.8}O_{3-\delta}$ was deposited on TZ3Y (3% yttria-doped zirconia) electrolyte substrate by pulsed laser deposition

(PLD) prior to the screen-printing of the porous LSCF cathode.[32] In addition a decrease by 35% of the ASR was also reported using a $La_2NiO_{4+\delta}$ electrode when a dense thin electrode layer was added by PLD between the TZ3Y electrolyte and screen-printed porous electrode.[33] The presence of this layer is expected to improve the oxygen transfer towards the electrolyte.

It can be observed that by the addition of the $La_4Ni_3O_{10-\delta}$ current collecting layer (CCL) (sample 4) decreases the relative contribution of the *HF* response to the total electrode impedance. Indeed, for this double layer cathode, sample 4, only 1 arc is observed in the frequency range from 10 to 10^4 Hz in the plot (**Fig. 9d**). This is primarily caused by the total domination by R_{pol} (LF) and hence the low-frequency response of the sample 4 could be thought to be the rate-limiting step for this double layer cathode. On the other hand, a very small contribution at very low frequencies, appears at high temperatures (≥ 700 °C) and does not vary as the temperature is increased. Moreover the capacitance corresponding to this LF contribution is very high (of the order of 3.3 F cm^{-2}), which suggests that it is related with bulk processes such as the O_2 diffusion in the gas phase.[34]

A drastic improvement in the R_{pol} to a value as low as 0.30 Ω cm^2 at 700 °C (**Fig.9d**) has been measured when the 3-D coral-type microstructure was topped by a $La_4Ni_3O_{10-\delta}$ SP layer (**Fig. 8**). To the best of our knowledge this R_{pol} value is the lowest reported to date in the literature for $La_4Ni_3O_{10-\delta}$ cathode. [35] This double cathode is characterized by a porous cathode functional layer (CFL) with a fine particle size (~150 nm) of large surface area and good connectivity, as well as a good contact between the flat electrode surface (**Fig. 8j**) and the gold grid. In addition, this microstructure also possesses a good electrolyte/electrode contact (continuous thin and dense $La_4Ni_3O_{10-\delta}$ layer (**Fig. 8l**) improving the oxygen diffusion towards the electrolyte), as proved by the low R_s value. This decrease in R_{pol} of roughly ~7 times at 700 °C (16 times at 800 °C) in comparison to sample 3, can be attributed to the presence of a CCL which homogenizes the current distribution along the cathode functional layer (CFL), activating the whole volume of the cathode by avoiding any current constrictions and by increasing the lateral percolation. Remarkably, the R_{pol} obtained (0.05 Ω cm^2 at 800 °C) of the double layer $La_4Ni_3O_{10-\delta}$ cathode developed here on an CGO electrolyte is lower than those for cathodes of the same composition reported elsewhere deposited by brush coating on LSGM and by screen-printing on YSZ electrolyte (1.0 and 0.15 Ω cm^2, respectively, at 800 °C).[6, 36] The R_{pol} (0.30 Ω cm^2 at 700 °C) also presents a better performance than those of the composite and functionally graded composite of $La_2NiO_{4+\delta}/La_4Ni_3O_{10-\delta}$ on a LSGM electrolyte at 700 °C (0.62 and 0.52 Ω cm^2, respectively)

[37, 38] and even lower than the CGO /$La_4Ni_3O_{10-\delta}$ composite 0.435 Ω cm^2, at 700 °C. [39] As expected, R_{pol}–decreases when the temperature increases (**Fig.11**, Table 4). The activation energies deduced from the Arrhenius plots (**Fig. 11**) are given in Table 4 and are in good agreement with the values reported in the literature. [6, 36, 39] Our study highlights the importance of the microstructure in improving the cathode performance and puts this $La_4Ni_3O_{10-\delta}$ double layer microstructure as the best cathode reported to date for this composition.

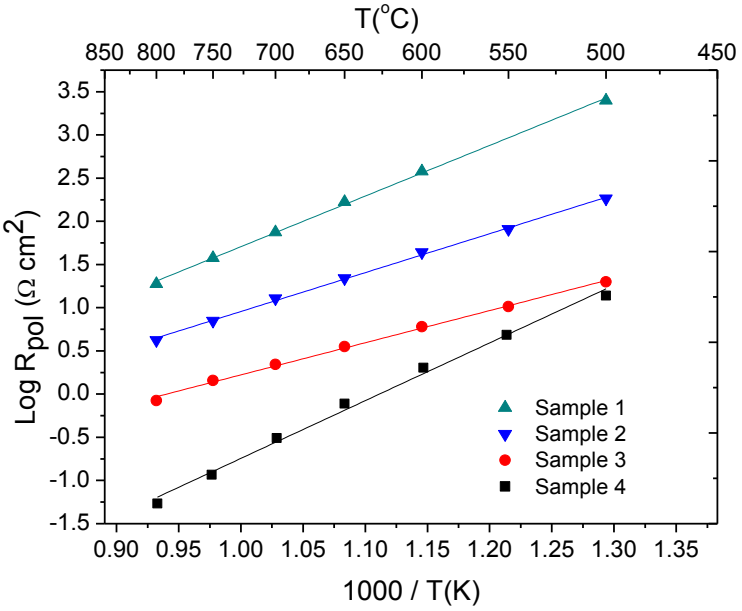

Fig. 11 Arrhenius plot of the R_{pol} in air for $La_4Ni_3O_{10-\delta}$ electrodes (OCP conditions) on CGO electrolyte,(a) sample 1, isolated cauliflower (b) sample 2, connected round agglomerates (c) sample 3, 3-D coral type (d) sample 4, double layer cathode (3-D coral type + SP).

4. Conclusions

This paper reports the fabrication of porous, continuous and crack-free $La_4Ni_3O_{10-\delta}$ cathodes on $Ce_{0.9}Gd_{0.1}O_{2-\delta}$ substrate by electrostatic spray deposition. Pure single phase $La_4Ni_3O_{10-\delta}$ films were obtained after calcination at 950 °C for 8 h in air, crystallizing in an orthorhombic symmetry. Various microstructures such as isolated cauliflowers, connected round agglomerates and 3-D coral-type films, have been obtained by optimizing the ESD key process parameters. Longer deposition times, favored preferential landing of the aerosol droplets and particle agglomeration. By increasing the substrate temperature and the nozzle to substrate distance, continuous and porous films can be obtained. The addition of 67% vol. water to pure ethanol gives a 3-D coral type microstructure with a continuous, dense thin

layer adjacent to the electrolyte. It has been clearly shown that the electrochemical properties of these $La_4Ni_3O_{10-\delta}$ cathodes strongly depend upon the microstructure. R_{pol} improves from 74.94 to 12.78 and then to 2.21 $\Omega.cm^2$ by changing the microstructure from isolated cauliflowers to connected round agglomerates and then to the 3-D coral-type microstructure, thanks to an improved percolation path and a better electrolyte/electrode contact. Moreover the R_{pol} value of the 3-D coral-type microstructure decreases down to 0.30 $\Omega.cm^2$ at 700 °C after improving the current collection by adding a $La_4Ni_3O_{10-\delta}$ SP layer on top. To the best of our knowledge, this polarization resistance value is the lowest for this composition in the present literature.

Acknowledgments

This work was performed within the framework of the Centre of Excellence of Multifunctional Architectured Materials "CEMAM" n° AN-10-LABX-44-01funded by the "Investments for the Future" Program. The authors would like to thank S. Coindeau and T. Encinas for XRD and R. Martin for SEM and EDX analyses in CMTC (Grenoble INP, France). M.B. also acknowledges financial support from the Spanish Economy and Competitiveness Ministry through the “Juan de la Cierva” fellowship program.

References:

[1] J. H. Kim, M. Cassidy, J. T. S. Irvine and J. Bae, *Chem. Mater.*, 2010, **22**, 883.
[2] G. Kim, S. Wang, A. J. Jacobson, L. Reimus, P. Brodersen and C. A. Mims, *J. Mater. Chem.*, 2007, **17**, 2500.
[3] S. Park, S. Choi, J. Shin, and G. Kim, *RSC Adv.*, 2014, **4**, 1775.
[4] J. A. Kilner and M. Burriel, *Annual Review of Materials Research*,2014, **44**,365
[5] J.A. Kilner and C.K.M. Shaw, *Solid State Ionics*, 2002, **154**, 523.
[6] G. Amow, I. J. Davidson, and S. J. Skinner, *Solid State Ionics*, 2006, **177**, 1205.
[7] Z. Lou, J. Peng, N. Dai, J. Qiao, Y. Yan, Z. Wang, J. Wang and K. Sun, *Electrochemistry Communications*, 2012, **22**, 97.
[8] S. Takahashi, S. Nishimoto, M. Matsuda and M. Miyake, *Journal of the American Ceramic Society*, 2010, **93**, 2329.
[9] G. Amow and S.J. Skinner, *J. Solid State Electrochem.*, 2006, **10**, 538.
[10] M. Burriel, G. Garcia, M. Rossell, A. Figueras, G. Van Tendeloo and J. Santiso, *Chem.Mater.*, 2007, **19**,4056.
[11] O. Wilhelm, S.E. Pratsinis, D. Perednis and L.J. Gauckler, *Thin Solid Films*, 2005, **479**, 121.
[12] A. Wold and R.J. Arnott, *Journal of Physics and Chemistry of Solids*, 1959, **9**, 176.

[13] A.Tarancón, M. Burriel, J. Santiso, S. J. Skinner and J.A. Kilner, *Journal of Materials Chemistry*, 2010, **20**, 3799.
[14] R. Sayers, R.A. De Souza, J.A. Kilner and S.J. Skinner, *Solid State Ionics* 2010,**181**, 386
[15] M.D. Carvalho, F.M.A. Costa, I.D.S. Pereira, A. Wattiaux, J.M. Bassat, J.C. Grenier and M. Pouchard, *J. Mater. Chem.*, 1997, **7**, 2107.
[16] Z. Zhang and M. Greenblatt, J Solid State Chem. 1995, **117**, 236.
[17] C.D. Ling, D.N. Argyriou, G. Wu and J.J. Neumeier, *J. Solid State Chem.*, 2000, **152**, 517.
[18] X. Weng, P. Boldrin, I. Abrahams, S.J. Skinner and J.A. Darr, Chem Mater., 2007, **19**, 4382.
[19] C.H. Chen, M.H.J. Emond, E.M. Kelder, B. Meester and J. Schoonman, *J. Aerosol. Sci.*, 1999, **30** 959.
[20] R.C. Weast, *Handbook of Chemistry and Physics*, 56th edn., CRC Press, 1975, E-56.
[21] D. Marinha, L. Dessemond and E. Djurado, *Current Inorganic Chemistry*, 2013, **3**, 2.
[22] J. Rodriguez-Carvajal, *Phys. B*, 1993, **192**, 55.
[23] J. F. Delamora and I.G. Loscertales, *J. Fluid Mech.*,1994, **260**, 155.
[24] O. Wilhelm, L. Madler and S.E. Pratsinis, *J. Aerosol Sci.*,2003, **34**, 815.
[25] A.M. Gañan-Calvo, J. Davila and A. Barrero, *J. Aerosol Sci.*, 1997, **28**, 249.
[26] C.H. Chen, E.M. Kelder, P.J.J.M. van der Put and J. Schoonman, *J. Mater. Chem.*, 1996, **6**, 765.
[27] B.-H. Hwang, C.-L. Chang, C.-S. Hsu and C.-Y. Fu, *J. Phys. D: Appl. Phys.*, 2007, **40**, 3448.
[28] R. Neagu, D. Perednis, A. Princivalle and E. Djurado, *Surf. Coat. Technol.*, 2006, **200**, 6815.
[29] T. Nguyen and E. Djurado, *Solid State Ionics*, 2001, **138**, 191.
[30] J. Sar, O. Celikbilek, J. Villanova, L. Dessemond, C. L. Martin and E. Djurado, *Journal of the European Caramic Society*, 2015 (in press).
[31] S. B. Adler, *Solid State Ionics*, 2000, **135**, 603.
[32] N. Hildenbrand, B. A. Boukamp, P. Nammensma, D. H. A. Blank, *Solid State Ionics*, **192** (2011) 12.
[33] N. Hildenbrand, P. Nammensma, D.H.A. Blank, H.J.M. Bouwmeester, B.A. Boukamp, *J. Power Sources*, **238** (2013) 442.
[34] X. Xu, Z. Jiang, X. Fan and C. Xia, *Solid State Ionics*, 2006, **177** 2113.
[35] C. Peter, A. Weber and E. Ivers-Tiffée, *Journal of the Electrochemical Society*, 2008, **155**, B730.
[36] Z. Lou, N. Dai, Z. Wang ,Y. Dai, Y. Yan, J. Qiao, J. Peng, J. Wang and K. Sun, *J Solid State Electrochem.*, 2013, **17**, 2703.
[37] R. J. Woolley and S. J. Skinner, *Journal of Power Sources*, 2013, **243**, 790.
[38] R. J. Woolley and S. J. Skinner, *Solid State Ionics*, 2014, **255**, 1.
[39] S. Choi and G. Kim, *Journal of the Korean Ceramic Society*, 2014, **51**, 265.

Chapter 5

Influence of $Ce_{0.9}Gd_{0.1}O_{2-\delta}$ (CGO) addition on electrochemical properties of nickelates based cathodes

Chapter 5

Part I: Design of interfaces in efficient $Ln_2NiO_{4+\delta}$ (Ln = La, Pr) cathode for SOFCs application

R. K.Sharma, M. Burriel, L. Dessemond, J.-M. Bassat and E. Djurado, *J. Mater. Chem. A*, 2016, 4, 12451-12462.
DOI: 10.1039/C6TA04845E

Design of interfaces in efficient $Ln_2NiO_{4+\delta}$ (Ln = La, Pr) cathode for SOFCs application

R. K. Sharma[a, b, c], M. Burriel[d], L. Dessemond[a, b], J.M. Bassat[c], E. Djurado[a, b*]

[a] Univ. Grenoble Alpes, LEPMI, F-38000 Grenoble, France
[b] CNRS, LEPMI, F-38000 Grenoble, France
[c] ICMCB, CNRS, Université Bordeaux, 33608 PESSAC, France
[d]Catalonia Univ. Grenoble Alpes, CNRS, LMGP, F-38000 Grenoble, France

*Corresponding author: Elisabeth Djurado
E-mail: elisabeth.djurado@lepmi.grenoble-inp.fr, Tel: +33-476826684; Fax: +33-476826777

Abstract

In this work, a novel architecture of $Ln_2NiO_{4+\delta}$ (LnNO; Ln = La, Pr) cathodes is prepared on $Ce_{0.9}Gd_{0.1}O_{2-\delta}$ (CGO) electrolyte by sequentially using screen-printing (SP) and electrostatic spray deposition (ESD) techniques for the first time. Both LnNO samples crystallize into a single Fmmm orthorhombic layered Ruddlesden-Popper structure. The role of the electrode/air and electrode/electrolyte interfaces has been evaluated by impedance spectroscopy. A drastic reduction in polarization resistance (R_{pol}) from 3.33 to 0.42 Ω cm^2 and from 0.83 to 0.08 Ω cm^2 is obtained at 600 °C for LaNO and PrNO, respectively, when the ESD electrode (with a dense thin, ~ 100 nm, LnNO sub-layer) is topped by a SP current collector. A further R_{pol} reduction down to 0.16 and 0.04 Ω cm^2 is successfully obtained for LaNO and PrNO, respectively, when the LnNO sub-layer is replaced by a thicker (~3 μm) porous CGO/LnNO composite sub-layer. This composite sub-layer is playing a main role on obtaining the best electrochemical properties of nickelates available in the literature, to the best of our knowledge. Moreover, values of polarization resistance for both electrodes are constant at 650 °C for 15 days in air, proving their suitability as SOFC cathodes at this intermediate temperature.

Keywords: SOFC cathode, nickelate, interfaces, ESD, impedance spectroscopy

1. Introduction

Mixed ionic-electronic conductors (MIEC) with K_2NiF_4-type structure have been intensively studied[1, 2] as promising IT-SOFC cathode materials due to their attractive electrochemical performance.[3-8] It has been reported that the Ruddlesden-Popper-type nickelate compounds such as $Ln_2NiO_{4+\delta}$ (Ln = La, Pr and Nd) show sufficient electronic conductivity due to the metal mixed valence (~ 80 to 100 S cm^{-1}) and good ionic transport properties.[9, 10] Indeed, they can accomodate hyperstoichiometric oxygen in interstitial lattice sites in the rocksalt layers of the structure.[11] In addition, the lanthanide nickelates show a promising electrocatalytic activity for oxygen reduction reaction (ORR).[12] They exhibit high values of surface exchange and diffusion coefficients (k* and D*) compared to perovskites.[12-13] Moreover, they are characterized by low thermal expansion coefficient (TEC) values,[2, 3, 14] that are comparable to the most commonly used electrolytes, such as yttria stabilized zirconia (YSZ) and gadolinia doped ceria (CGO).[15-17] However the polarization resistance (R_{pol}) is still too high and its minimization is required to be used as cathodes for SOFC. Several strategies to improve the electrochemical performance have been explored including the addition of a dense base-layer between the electrolyte and the porous electrode, the control of the microstructure, the introduction of an ionically conducting phase to form a composite electrode and the design of the electrode's architecture. For instance, it is possible to fabricate a layer adjacent to the electrolyte with a smaller particle size to maximize the electrocatalytic activity in this region.[18] This sub-layer can be made denser than the bulk porous electrode with a view to improving the electrolyte/electrode contact and to enhance the oxygen transfer to the electrolyte. Thus, the R_{pol} value for $La_2NiO_{4+\delta}$ was found to decrease from 7.4 to 1.0 Ω cm^2 at 700 °C, as reported by Sayers et al.[19] and it was decreased by ~30% at 600 °C (from 1.2 to 0.85 Ω cm^2) with respect to the best porous cell as reported by Hildenbrand.[20] Another approach is to increase the surface area of the bulk electrode to enhance the number of active surface sites yielding better electrochemical performances.[21] The most promising $Pr_2NiO_{4+\delta}$ electrode, has been reported for a mean particle size of ~ 0.4 μm (R_{pol} value down to 0.08 Ω cm^2 at 600 °C).[22] Moreover, composite cathodes, consisting of a matrix phase cathode (electronic conducting or MIEC) and a second phase electrolyte, are gaining importance not only due to further reduction in the R_{pol} valuem but also to good cathode-electrolyte adhesion properties.[23-25] Composite electrodes preparation via infiltration is one of the most effective methods used to increase the triple phase boundary (TPB) area and to improve the cathode efficiency at lower temperature.[26, 27] Recently Nicollet et al.[27, 28] have

studied two different composite cathodes based on $La_2NiO_{4+\delta}$ and $Pr_2NiO_{4+\delta}$ infiltrated into a Gd-doped ceria backbone. Very low R_{pol} values of 0.15 Ω cm^2 for $La_2NiO_{4+\delta}$ and 0.075 Ω cm^2 for $Pr_2NiO_{4+\delta}$ at 600 °C were found in comparison to pure $La_2NiO_{4+\delta}$ (0.93 Ω cm^2 at 600 °C)[29] and $Pr_2NiO_{4+\delta}$ (0.15 Ω cm^2 at 600 °C)[29] cathodes deposited by screen-printing on YSZ electrolyte. On the other hand, the infiltration procedure demands several repeated impregnation-calcination steps which limits its use for industrial applications.[30, 31] Recently, we reported a drastic reduction of the R_{pol} from 3.33 to 0.42 Ω cm^2 at 600 °C when a 3-D coral nanocrystalline $La_2NiO_{4+\delta}$ film (mean particle size ~ 150 nm) with a continuous nanometric dense interfacewas topped by a $La_2NiO_{4+\delta}$ current collector.[32]

In this study, we propose for the first time, an alternative fabrication route for $Ln_2NiO_{4+\delta}$ (LnNO; Ln = La, Pr) electrode on CGO electrolyte, in three steps, as follows: A first thin porous CGO film is deposited by SP and sintered. Then, in a second step, it is covered by a 3-D LnNO porous coral-type microstructure by ESD and sintered. A third LnNO layer is topped by SP as a current collector and sintered. The innovative triple layer architecture of the full LnNO electrode resides on the presence of a CGO: LnNO composite thin porous sub-layer (3-4 μm thick) as a consequence of the penetration of the ESD LnNO film into the first SP CGO sub-layer. This new architecture is used with the objective of decreasing the polarization resistance by improving the electrode/electrolyte contact and enlarging the TPB region. A comparison of the electrochemical properties of the triple layer LnNO electrodes on CGO with two other architectures is performed: a single ESD LnNO layer and a double ESD+SP LnNO layer.

2. Experimental

2.1.Materials and solution preparation

Dense CGO ($Ce_{0.9}Gd_{0.1}O_{2-\delta}$) pellets made by pressing discs (20 mm diameter and 1.2 mm thickness) of commercial powder (Solvay) and subsequently fired at 1400 °C for 4 h were used as electrolyte. Nickel nitrate hexahydrate [Ni $(NO_3)_2$ $6H_2O$, 99.9%, Aldrich], Lanthanum nitrate hexahydrate [La $(NO_3)_3$ ·$6H_2O$, 99.9%, Alfa Aesar], Praseodymium nitrate hexahydrate [Pr $(NO_3)_3$.6 H_2O, 99.9%, Aldrich] citric acid [$C_6H_8O_7$, 99.9%, Alfa Aesar], and ethanol (CH_3CH_2OH, >99.9%, Prolabo) were used as precursors. ESD precursor solutions of 0.02 M (total cation concentration) were prepared in the mixture of 30 ml of ethanol and water (1:2) by adding the stoichiometric amount of $La(NO_3)_3$.6 H_2O, $Pr(NO_3)_3$.6 H_2O and $Ni(NO_3)_2$ 6 H_2O salts and citric acid (20 mol. % in excess). For the SP layers, the CGO and

the LnNO current collector, inks based on KD2921 (Zschimmer and Schwarz) solvent were prepared with commercial CGO powder (Solvay) and with LnNO (Ln = La and Pr) powders obtained by auto-combustion. For this process same precursor solution was used as in ESD process, but prepared in pure EtOH. Then solutions were heated at 150 °C till the completion of auto-combustion process in order to obtain amorphous powders. These amorphous powders were sintered at 950 °C for 6 h (LaNO) and 1100 °C for 4 h (PrNO) in air, respectively, in order to obtain crystallized and single-phase powders.

2.2.Cathode preparation and characterization

The preparation process of the triple layer cathode can be described in three steps interspersed with heat treatments (**Table 1,** samples 5 and 6). A first CGO base-layer porous film is deposited by SP on CGO electrolyte and sintered at 1200 °C for 4 h in air. Then, it is covered by a LnNO (Ln = La, Pr) porous film using the ESD technique, described elsewhere.[33, 34] The optimized ESD conditions in order to obtain a 3-D coral type microstructure are those previously reported in [31]: deposition time of 180 minutes, substrate temperature of 350 °C, nozzle to substrate distance of 50 mm and flow rate of 1.5 mL/h. This LnNO ESD film partially penetrates into the first CGO porous film leading to a denser CGO-LnNO composite base-layer. The crystallization of this LnNO ESD coating is obtained after a heat treatment of only 2 h at 900 °C for LaNO. In the case of PrNO a heat treatment at 1000 °C for 2 h followed by another one at 1050 °C for 2 h in air is required. No reactivity was observed between LnNO and CGO at these temperatures. The third and final step is the deposition of the LnNO current collecting layer (CCL) by SP, calcined at 1050 °C for 2 h in air. Both sintered electrodes, 30 μm thick, present a good adhesion onto the CGO electrolyte as demonstrated by the tape test. The cathode area is 1.54 cm^2.

Two other LnNO electrodes have been prepared on CGO electrolyte with a single ESD layer (**Table 1**, samples 1 and 2) and a double layer (ESD +SP) configuration (**Table 1**, samples 3 and 4).

Table 1. Sample identification, composition and deposition technique, surface area and sintering conditions of the prepared cathodes on CGO electrolyte

Samples (architecture)	Composition (Technique)	Surface area [cm^2]	Sintering in air Temperature / time
Sample 1 (single layer)	LaNO (ESD)	2.00	950 °C / 6 h
Sample 2 (single layer)	PrNO (ESD)	2.00	1100 °C / 4 h
Sample 3 (double layer)	LaNO (ESD) + LaNO (SP)	1.54	950 °C / 6 h + 1050 °C / 2 h + 1100 °C / 0.5 h
Sample 4 (double layer)	PrNO (ESD) + PrNO (SP)	1.54	1100 °C / 4 h 1050 °C / 2 h + 1100 °C / 0.5 h
Sample 5 (triple layer)	CGO (SP) + LaNO (ESD) + LaNO (SP)	1.54	1200 °C / 4h 900 °C / 2 h 1050 °C / 2 h
Sample 6 (triple layer)	CGO (SP) + PrNO (ESD) + PrNO (SP)	1.54	1200 °C / 4h 1000 °C / 2 h +1050 °C / 2 h 1050 °C / 2 h

Six symmetrical cells were prepared with the single, double and triple layer electrode on both sides of the CGO electrolyte in order to be analyzed by impedance spectroscopy. Electrochemical impedance diagrams were recorded between 500 and 700 °C in air in the frequency range from 0.05 Hz to 100 kHz with an ac signal amplitude of 0.02 V at open circuit potential (OCP) by using a PGSTAT 302N (Eco Chemie). Gold grid (Heraeus, 1024 meshes cm^{-2} woven from 0.06 mm dia. wire) was used as current collector. The data were fitted using equivalent circuits with the Zview® software (Scribner Associates) and were normalized to the electrode area. The crystal structure was determined using powder X-ray diffraction (XRD, Philips X'Pert-MPD system, Cu Kα radiation, λ= 1.54056 Å) in Bragg-Brentano configuration. The XRD patterns were refined using Fullprof software in order to determine the lattice parameters.[35] Surface and cross-sectional morphology of the cathodes was characterized using a scanning electron microscope (ZEISS Ultra 55 instrument with field emission gun, FEG). The particle size of the electrodes was estimated from the SEM images using an image analysis tool (Image J software). The composition analysis was

performed by energy-dispersive X-ray spectroscopy (EDX) using acceleration voltage equal to 20 keV. Oxygen overstoichiometry (δ) of $La_2NiO_{4+\delta}$ and $Pr_2NiO_{4+\delta}$ samples (powder scratched from ESD films) was determined by thermogravimetry measurements (TGA-Q50 instrument) under flowing 5% H_2–Ar gas. Data were collected from 25 to 800 °C at the heating rate of 0.5 °C min^{-1}. Long-term stability measurements were also carried out on the LnNO triple layer cathodes at 650 °C for 15 days in air.

3. Results and discussion

3.1. Structural characterization of the LnNO films

Fig. 1 shows XRD patterns of the LaNO and PrNO films deposited by ESD and SP on a CGO electrolyte previously recovered by a screen-printed CGO porous layer (samples 5 and 6, **Table 1**).

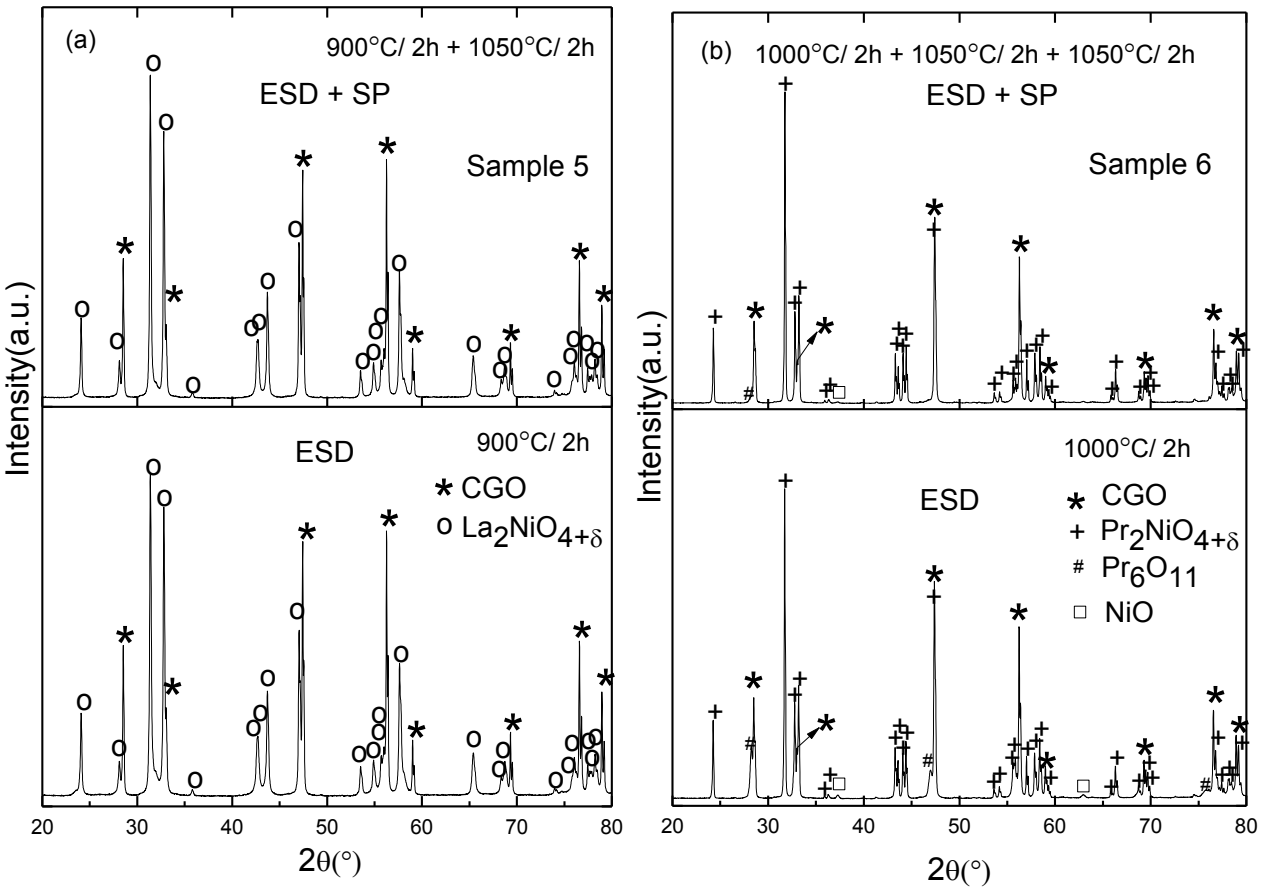

Fig. 1 XRD patterns of the LnNO films coated by ESD and SP on CGO electrolyte previously recovered by a SP CGO sub-layer: (a) $La_2NiO_{4+\delta}$ and (b) $Pr_2NiO_{4+\delta}$.

For LaNO film, no impurities or secondary phases have been observed neither for the ESD film after sintering at 900 °C for 2 h, nor for the sample 5, after sintering at 900 °C for 2 h followed by 1050 °C for 2 h in air . All diffraction peaks matched well those of the $La_2NiO_{4+\delta}$ phase (ICDD # 01-074-9394) and those of the $Ce_{0.9}Gd_{0.1}O_{2-\delta}$ phase (ICDD # 04-013-6577) originating from both the substrate and the SP sub-layer. In the case of $Pr_2NiO_{4+\delta}$ prepared by ESD, some traces of Pr_6O_{11} and NiO appear as intermediate phases after sintering at 1000 °C for 2 h along with the CGO phase (ICDD # 04-013-6577) coming from both the substrate and the SP sub-layer. Then, after a successive sintering at 1050 °C for 2 h in air (sample 6), they recombine leading to the pure $Pr_2NiO_{4+\delta}$ phase (ICDD #04-014-1778)). No structural modification was detected when the $Pr_2NiO_{4+\delta}$ CCL film was successively screen-printed onto the ESD layer and sintered again at 1050 °C for 2 h. Both LnNO films crystallize in an orthorhombic unit cell with the Fmmm space group (N° 69). The cell parameters, determined from Fullprof software refinement (**Fig. S1** and **S2**), are a = 5.457(3) Å, b = 5.462(8) Å and c = 12.690 (6) Å for $La_2NiO_{4+\delta}$ and a = 5.391 (4) Å, b = 5.453 (8) Å and c = 12.446 (3) Å for $Pr_2NiO_{4+\delta}$, in good agreement with previously reported values.[29]

Moreover, the oxygen overstoichiometry (δ) determined by TGA (**Fig. S3**) was found to be 0.16 and 0.24 for $La_2NiO_{4+\delta}$ and $Pr_2NiO_{4+\delta}$, respectively which is in good agreement with the literature.[29]

3.2. Microstructural characterization of the LnNO films with different architectures

As described in **Table 1**, one can consider six LnNO electrodes deposited on CGO electrolyte with different architectural designs: *the single layer*: coral-type ESD LnNO layer (sample 1: LaNO and sample 2: PrNO), *the double layer*: ESD + SP LnNO layer (sample 3: LaNO and sample 4: PrNO) and *the triple layer*: characterized by the CGO-LnNO composite base-layer, the ESD LnNO coral-type layer and the SP LnNO current collecting layer (sample 5: LaNO and sample 6: PrNO). In the following, a microstructural study of the LnNO electrode is focused on the construction of the electrode starting by the single, then the double to end with the triple layer architecture. The electrical performance of the triple layer architecture is then investigated and compared to both the single and the double layer electrodes.

Fig. 2 shows SEM surface and cross section images of the samples 1 (LaNO) and 2 (PrNO). Whatever the rare-earth composition (La or Pr), both the samples 1 and 2 are

approximately 20 μm thick and show a porous 3-D coral type microstructure, as previously reported by Sharma et al. for LaNO.[32] The ESD process obeys to electrohydrodynamic atomization laws of liquids to produce an aerosol from a liquid precursor which is then directed to a heated substrate. Thus, the microstructure of the resulting film is strongly dependent on the size of the droplets impacting the heated substrate. The droplet size can be controlled through the ESD deposition parameters such as solution flow rate, distance between the substrate and the nozzle and substrate temperature.[36] ESD is a promising and low-cost process which allows a good reproducibility of the coatings. Using similar ESD conditions to the ones reported in our previous article[32] the porous 3-D coral-type microstructure is obtained (substrate temperature of 350 °C, nozzle to substrate distance of 50 mm and flow rate of 1.5 mL/h). This porous microstructure is the consequence of preferential landing of the aerosol droplets on the CGO substrate since nearly dry aerosol droplets impact the substrate.[37] The charges on the substrate surface induced by the strong applied electrostatic field concentrate more where the curvature is greater.[38] So, the charged droplets arriving at the surface will be more attracted towards these more curved areas. This is referred to as ‘‘preferential landing’’. This action is the main route for the particle agglomeration, especially when the droplets are small and light. Hwang *et al.*[38] have shown that when the substrate roughness increases, preferential landing is promoted leading to particle agglomeration. The average particle size of samples 1 (LaNO) and 2 (PrNO) is estimated to be ~ 150 nm (**Fig. 2b**) and ~ 200 nm (**Fig. 2f**), respectively. The crystal growth is expected to be larger for PrNO in comparison to LaNO since a higher sintering temperature is required to obtain the pure $Pr_2NiO_{4+\delta}$ crystallized phase (1100 °C for 4 h for PrNO compared to 950 °C for 6 h for LaNO). The presence of a thin dense base-layer at the electrolyte-electrode interface, ~ 100 nm thick, can be observed in **Fig. 2d** and **Fig. 2h**, for both sample 1 and sample 2, respectively. As reported previously, [32] this first thin dense interlayer is deposited at the beginning of the ESD process. As a consequence, the first charged liquid droplets containing the precursors solution spread on the polished flat surface of the grounded substrate. The spreading is larger if the precursor solution is characterized by a low evaporation rate. This happens with an EtOH + water (1:2) based precursor solution due to a larger amount of liquid in the charged droplets impacting the substrate. This leads to the formation of a continuous thin dense layer which also facilitates the adhesion of the electrode-electrolyte interface without the need of high sintering temperatures.

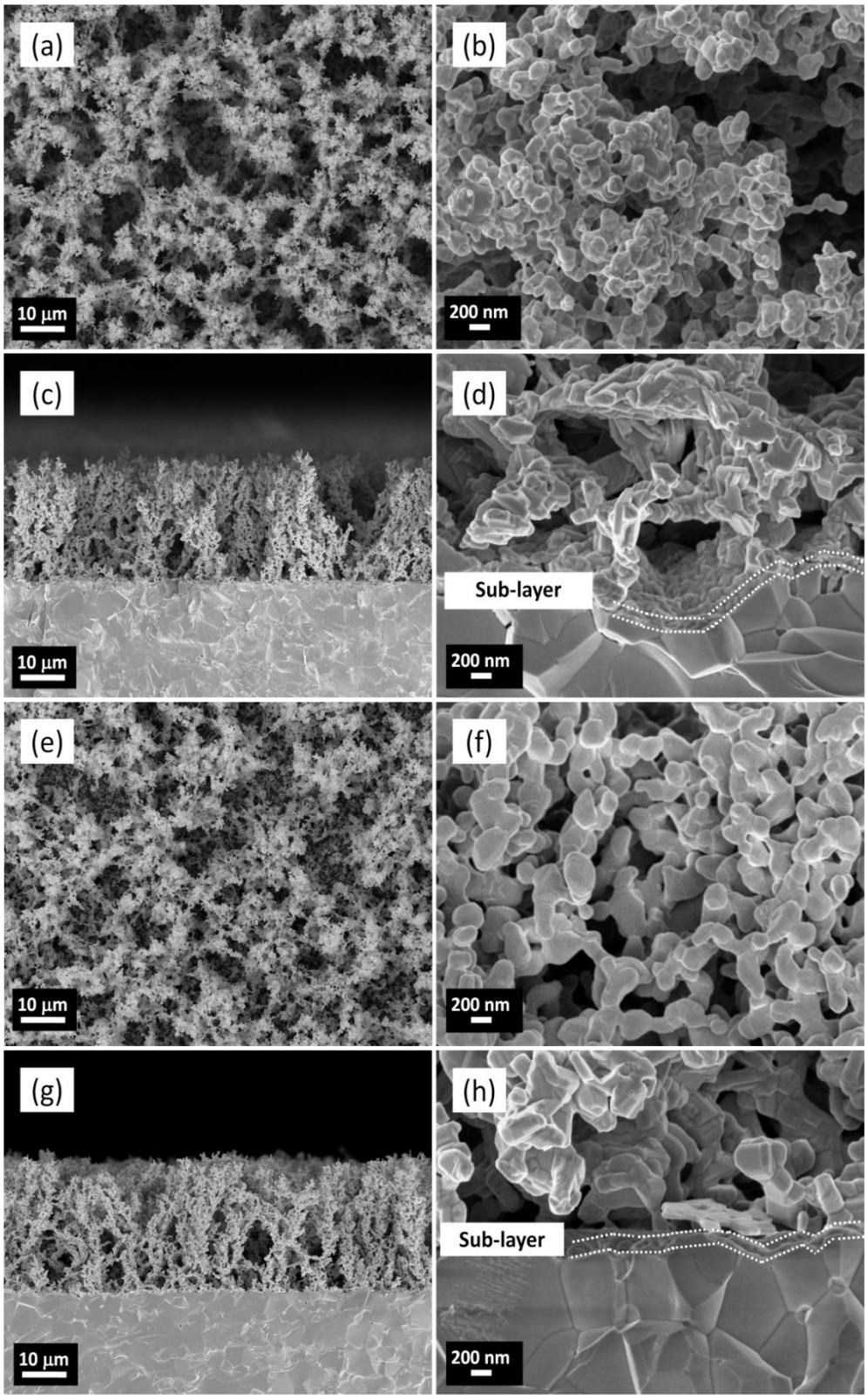

Fig. 2 SEM micrographs of sample 1: (a, b) surface, (c, d) cross section and sample 2: (e, f) surface, (g, h) cross section.

In order to further improve the flatness and contact between the current collecting grid and the electrode, double layer architecture, samples 3 (LaNO) and 4 (PrNO) were prepared by depositing a screen-printed CCL of similar composition on top of the samples 1 and 2, respectively (**Fig. 3**). The current collecting layer, 20 μm thick, partially penetrates (~ 50 %) the 3-D coral type electrode which further improves the lateral percolation. The average particle size of the screen-printed layer sintered in the same conditions is approximately 450 nm for both compositions.

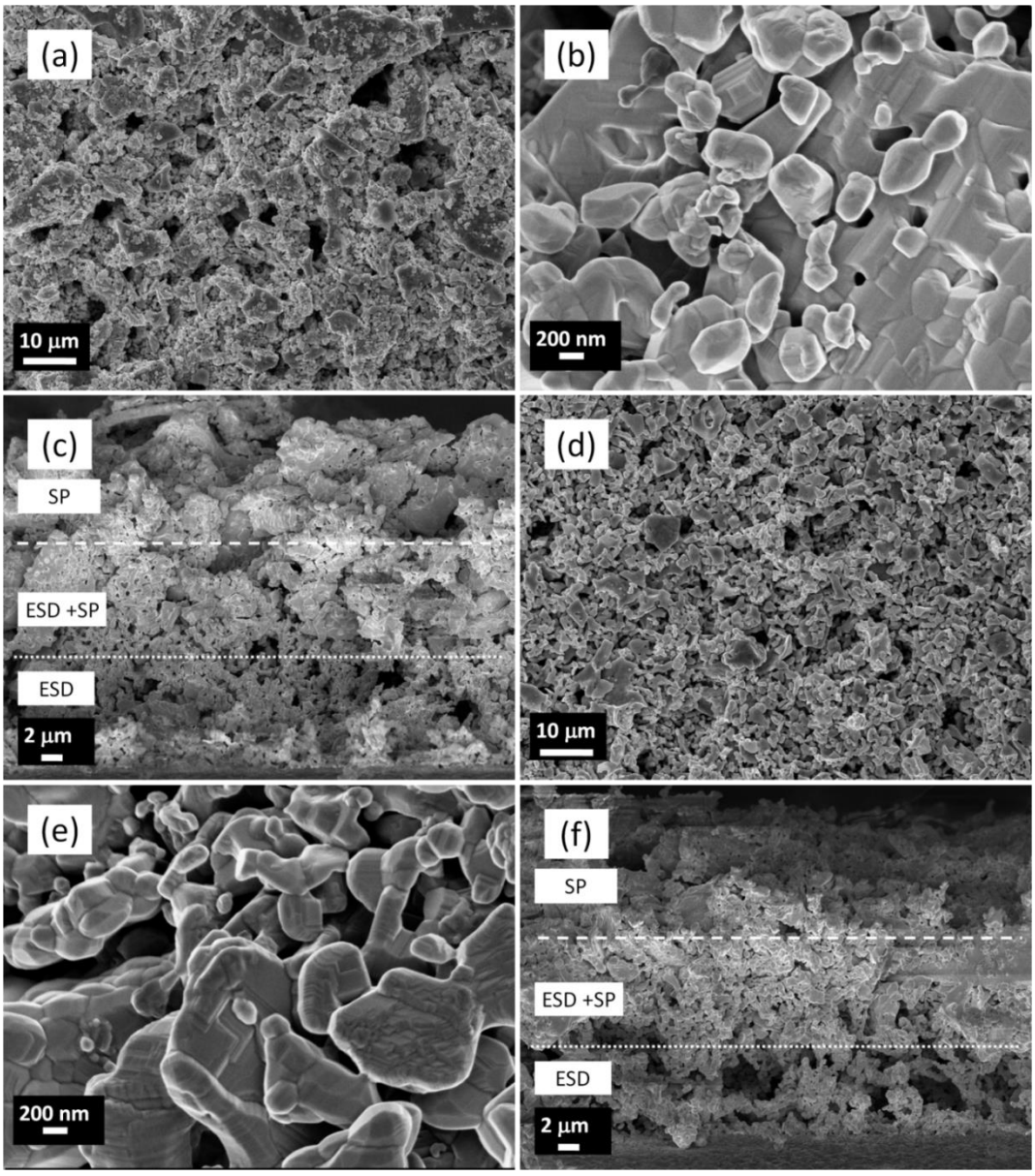

Fig. 3 SEM micrographs of sample 3: (a,b) surface, (c) cross section and sample 4: (d,e) surface, (f) cross section.

Finally, we have designed another cathodes, samples 5 (LaNO) and 6 (PrNO) by modifying the thin dense sub-layer. It consists of a triple layer electrode obtained by inserting a CGO-LnNO composite base-layer onto the electrolyte (**Table 1**). **Fig. 4** shows the SEM micrographs of sample 6, the cross section, the composite base-layer and a schematic of the triple layer design on CGO substrate. Similar morphologies can be observed in sample 5 (**Fig. S4**). A compact base-layer, ~ 3-4 μm thick, is observed. It is the result of the penetration of the electrosprayed LnNO into an initial porous SP LnNO layer forming a base-layer of CGO-LnNO composite, similarly to the infiltration process.[31] The formation of the CGO-LnNO composite of the base-layer was confirmed by EDX in the base-layer region. As an example, EDX signal, collected from an area estimated to 1 μm x 1 μm located in the centre of the sub-layer, is shown in **Fig. 5**.

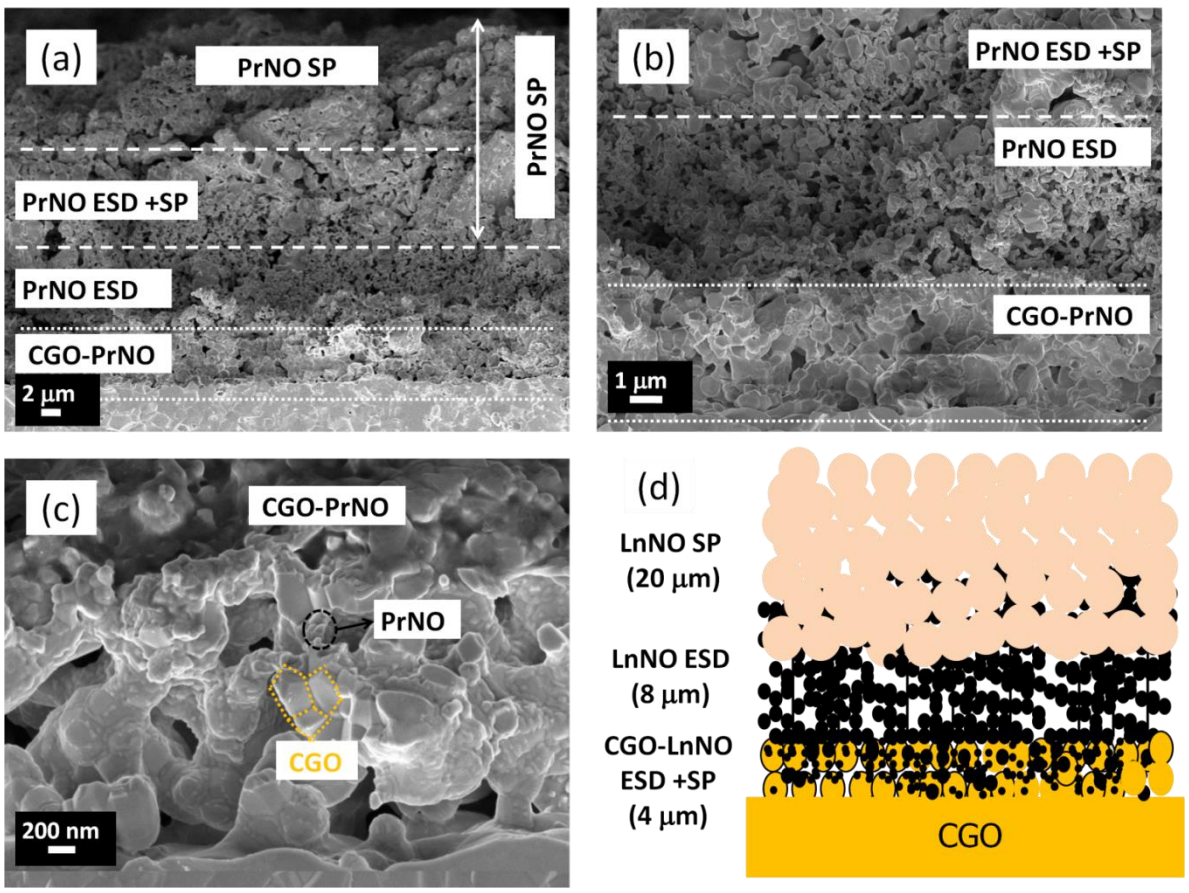

Fig. 4 SEM micrographs of sample 6: (a), (b) cross section, (c) CGO-PrNO sub-layer on CGO electrolyte, (d) schematic of the triple layer design.

The LnNO electrodes with the different designs are characterized by a heterogeneous porosity, larger in the ESD part than the SP one. An estimation of the porosity of the ESD

single layer has been performed by comparing the apparent film density with the LnNO theoretical density. The apparent density was obtained by weighing the CGO substrate before and after the LnNO film deposition and measuring the film thickness and diameter. A porosity of approximately 84 vol. % was estimated. This large porosity indicates that plenty of space is available for oxygen molecules to transport especially in the ESD film. These values are in good agreement with the porosity reported by Sar et al.[39] using FIB-SEM on the CGO/LSCF film also deposited in our group by ESD.

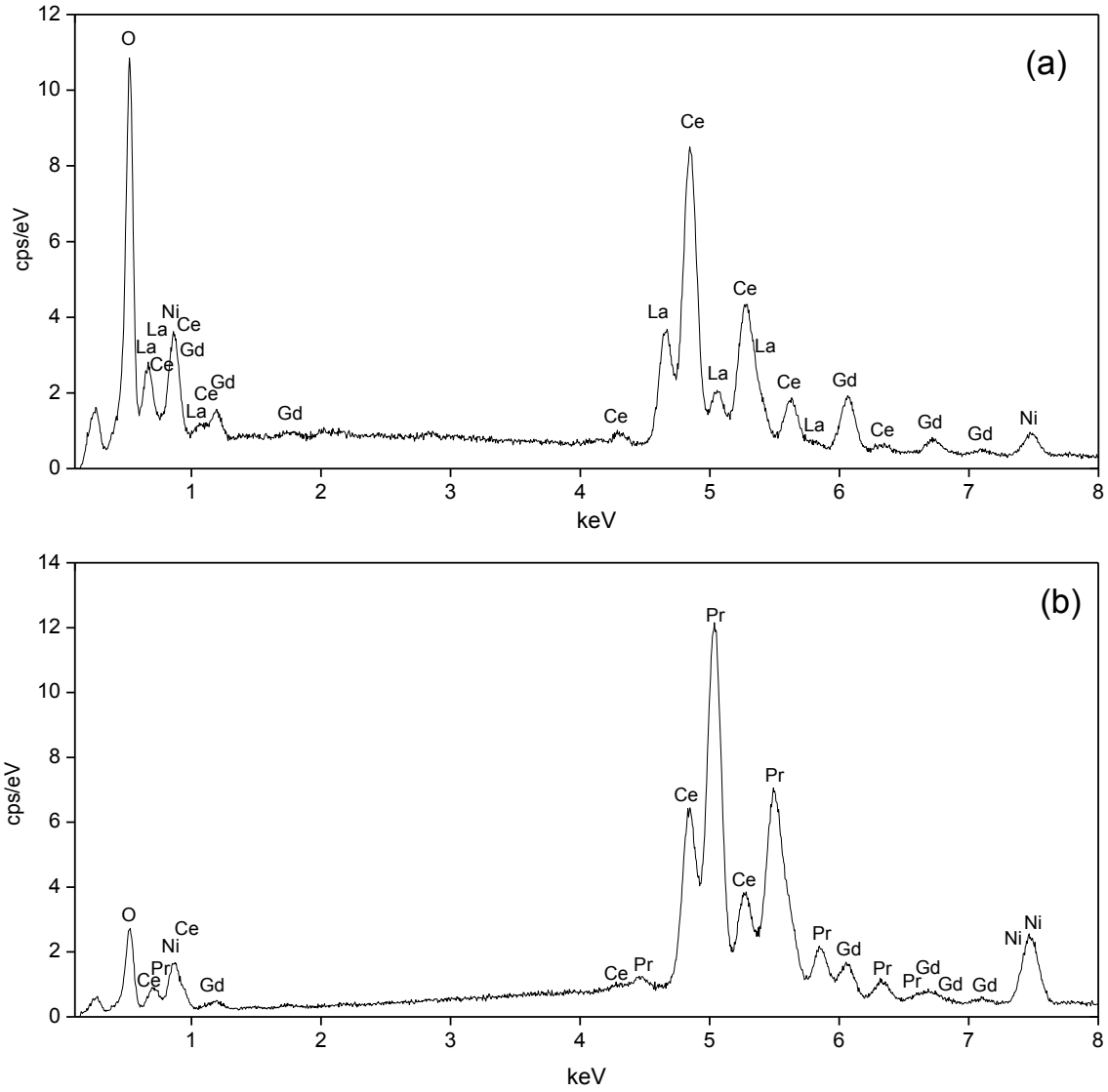

Fig. 5 EDX analysis of the sub-layer region in the LnNO triple layer electrode: (a) sample 5, (b) sample 6.

3.3.Electrochemical properties and stability

The electrochemical properties of the electrodes (samples 1-6, **Table 1**) deposited symmetrically on CGO were investigated by impedance spectroscopy in air at OCV over the temperature range 500 - 700 ºC. In the following, the electrical properties of the single and the double layer electrode architecture are first presented and then followed by the ones of the triple layer electrode. The impedance diagrams were fitted with an equivalent circuit, as shown in **Fig. 6**, consisting of a combination of several resistances (R)-constant phase element (CPE) parallel circuits, connected in series with an inductance (L) using ZView® software. This electrical element (L), appearing as a high frequency tail below the real axis, represents the contribution of the connecting leads, measuring device and connecting wires to the measured total impedance.[40] The high frequency intercept of the diagrams on the real axis corresponds to the overall ohmic resistance (R_s), including the resistive contributions of the electrolyte, electrode, leads and current collectors. The electrode performance can be quantified by the polarization resistance R_{pol} ($2R_{pol} = 2R_1 + 2R_2 + 2R_3$), which is the difference between the real axis intercepts of the impedance arc. According to the selected analysis, the electrode response is composed by two or three main elementary contributions located at high frequency (1), medium frequency (2) and low frequency (3) depending upon the temperature and composition of the cathodes. The medium frequency arc resistance can be associated with various electrode processes such as adsorption of gaseous oxygen O_2, dissociation of O_2 and charge transfer-diffusion (O^{2-}) in the electrode whereas the high frequency arc is usually attributed to the charge transfer at the electrode/electrolyte interface.[40, 41, 42] The low frequency contribution can be related to a gas impedance due to either porous electrodes or the experimental set-up.[43, 44]

Typical experimental and fitted impedance diagrams, plotted in the Nyquist plane are shown in **Fig. 7a** and **Fig. 7b** for the samples 1 and 3, respectively. Similar data were obtained for the PrNO electrodes (samples 2 and 4). The ohmic resistance (R_s) has been subtracted in order to facilitate comparison between the resistance polarization values (R_{pol}) of the different samples. It is worth mentioning the important effect of the screen-printed CCL layer on the R_s. Adding a SP layer results in a significant decrease of the series resistance regardless of the composition of the electrode. For instance, at 600°C, R_s varies from 14.58 Ω cm² (sample 1) down to 5.43 Ω cm² (sample 2, not shown in **Fig. 7**). Indeed, R_s depends upon the intimate contact at the electrode/electrolyte and current collector/electrode interfaces. Increasing the

contact area at both interfaces yields a homogeneous current distribution within the volume of the electrode, i.e. a lower constriction effect of the electrical current lines. As can be seen in **Fig. 2d** and **Fig. 2h** for single layer electrodes, a thin dense layer can be also evidenced at the electrode/electrolyte interface for sample 3 and sample 4. Nevertheless, by using only a gold grid as a current collector (samples 1 and 2), the current lines are not well distributed through the electrode volume. Once the screen-printed layer is added (**Fig. 3**), an homogeneous distribution of current lines within the electrode can be thus anticipated as well as a decrease of the constriction effect of the current lines in the vicinity of the electrode/electrolyte interface. An argument that further supports this assumption is that the series resistance recorded for both triple layer electrodes is not modified (**Table 2**). Accordingly, any variation of the polarization resistance between the double (samples 3 and 4) and triple layer (samples 5 and 6) electrodes is expected to be related mainly to the electrode morphology.

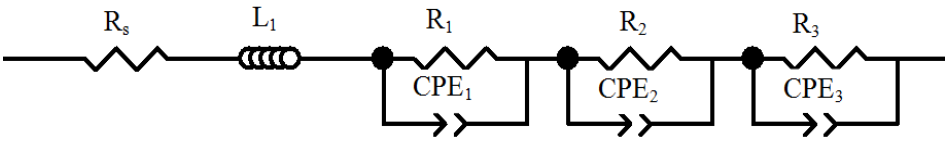

Fig. 6 Equivalent electrical circuit model used for impedance spectra fitting.

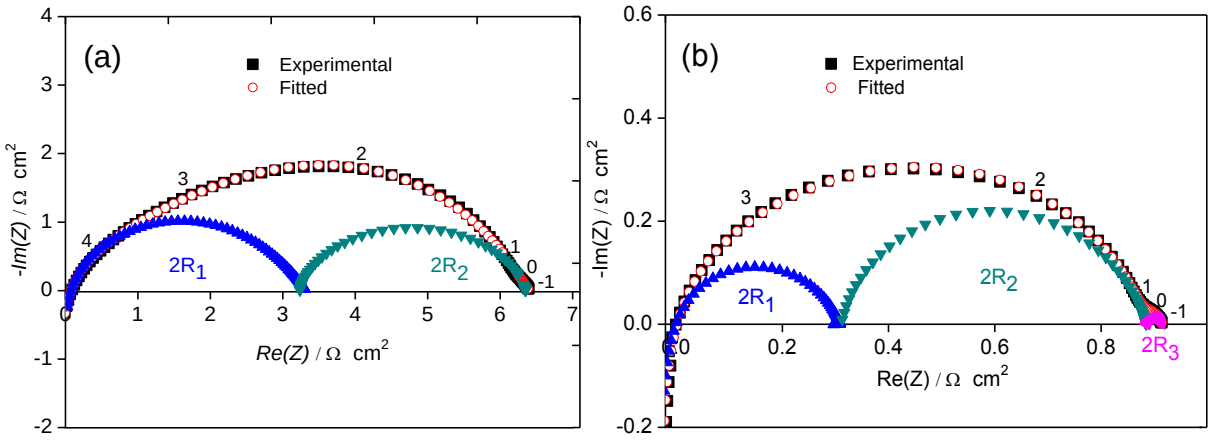

Fig. 7 Nyquist plots recorded at 600 °C in air at OCV: (a) sample 1 and (b) sample 3. The numbers indicate the logarithm of the measuring frequency.

As previously reported[20, 45], the presence of a thin dense layer at the cathode/electrolyte interface (samples 1 and 2) favors the oxygen transfer from the cathode towards the electrolyte and hence leads to better electrode performance. For instance, the polarization resistance was reported to decrease from 0.67 to 0.21 Ω cm^2 and from 1.2 to 0.85 Ω cm^2 at 600 °C for LSCF and LaNO, respectively, when a thin dense layer was deposited by PLD on the TZ3Y electrolyte prior to the screen-printed porous electrode.[20, 45] It is not the case for samples 1 and 2, indeed, the R_{pol} values are found to be 3.33 and 0.83 Ω cm^2 at 600 °C (Table 2), respectively. These values are found to be higher than the lowest values reported in the literature[51], (2.20 Ω cm^2, LaNO and 0.28 Ω cm^2, PrNO) (see **Table 3**). The coral microstructure of samples 1 and 2 is highly porous (**Fig. 2a** and **Fig. 2e**) and the contact area with Au grids is too low and thus the whole electrode volume is not totally active for the ORR. Regardless of the electrode microstructure and the related behavior, the oxygen reduction reaction (ORR) from molecular oxygen O_2 into oxygen ions, O^{2-} requires the O_2 supply to the active reaction sites. Consequently, sufficient porosity is needed to facilitate gas permeation and the electronic conductivity must be also maximized at the same time to improve the current collection. This could be the reason for the relatively poor performance of samples 1 and 2. In order to improve the contact between cathode and the grids and hence the effective electronic conductivity of the cathode sheet, the double layer cathodes (samples 3 and 4) were fabricated by depositing a SP layer of the respective composition on the top of the 3-D coral microstructure as a current collector and studied. As for the series resistance, a drastic improvement in R_{pol} is obtained when adding a $La_2NiO_{4+\delta}$ (sample 3) and $Pr_2NiO_{4+\delta}$ SP layer (sample 4), respectively (**Fig. 7**). Double layer cathodes show much better performance: 0.42 Ω cm^2 at 600 °C (sample 3) and 0.08 Ω cm^2 at 600 °C (sample 4), respectively. At 600 °C the R_{pol} decreases by a factor of 8 for sample 3 and factor of 10 for sample 4. This is also in good agreement with the improvement in R_s values.

This drastic improvement of electrode performance (**Table 2**) of sample 4 over sample 3 (or sample 2 over sample 1) is also due to better mixed ionic-electronic conductivity as well as diffusion properties of PrNO in comparison to LaNO for similar architecture. Indeed these properties are dependent upon oxygen nonstoichiometry (δ); the higher the δ, larger the ionic conductivity and diffusion. From TGA (**Fig. S3**), PrNO shows larger oxygen nonstoichiometry (δ = 0.24) in comparison to LaNO (δ =0.16) in good agreement with the literature.[29]As shown in **Fig. 7**, the frequency distribution of the electrode impedance is not

modified by adding the CCL, indicating that the ORR remains the same. In order to further reduce the R_{pol} values, a composite sub-layer was added for samples 5 and 6 (**Fig. 4**). For a given electrode composition the frequency distribution of the electrode impedance is not strongly modified (**Fig. 8**). The ORR is likely to remain similar.

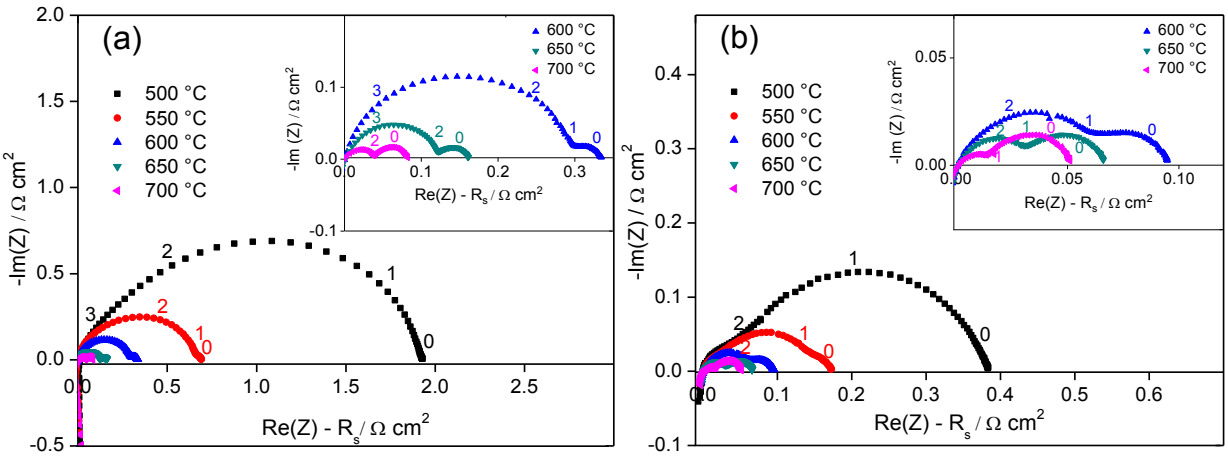

Fig. 8 Nyquist Plots recorded as a function of the temperature (from 500 to 700 ºC) at OCV; (a) sample 5 and (b) sample 6. Inset picture is a zoom-in of the high temperature plot. The numbers indicate the logarithm of the measuring frequency.

On the other hand, the shape of the electrode characteristic is modified since a third elementary contribution (labeled as 3) is clearly observed for temperatures higher than 550 °C (**Table 2**). The fitted and experimental spectra at 600 °C from the inset of **Fig. 8b,** is shown in **Fig. S5.** In order to assess the robustness of the fittings, capacitances and exponents of CPE for all 6 architectures are further given in **Table S1.** It must be emphasized that the R_{pol} value decreases further down to 0.04 Ω cm^2 for sample 5 (LaNO) and to 0.02 Ω cm^2 for sample 6 (PrNO) at 700 °C, respectively. Once again such improvement in sample 6 over sample 5 is due to the better mixed ionic-electronic conductivity and diffusion property of PrNO since architecture is similar (**Fig. 4**, **Fig. S4**). Remarkably, the obtained R_{pol} values are lower than those reported in the literature for LnNO based cathodes (**Table 3)**. When a compact composite layer of CGO and LnNO is inserted between the electrolyte and the double layer cathode), a significant decrease in both the high and medium frequency resistances (R_1 and R_2) is observed. Since the series resistances do not vary between double and triple layer electrodes for temperatures higher than 500 °C (**Table 2**), it can be assumed that the

constriction effect at the electrode/electrolyte interface is minimized in the chosen temperature range. By considering that the SP layer acts as an optimized current collector for both types of electrodes, and that the microstructure of the ESD and SP layers remains unchanged (**Figures 3** and **4**), one could infer that the polarization resistance remains the same. Nevertheless, adding CGO enhances the ionic conductivity adjacent to the electrolyte and a better contact between CGO and LnNO can be anticipated.[20, 23] The improvement of the electrode performance is likely to be mainly related to the increase of the active electrode thickness by inserting a composite layer. These results are in good agreement with the work previously reported by Nicollet et al.[27, 28] for the composite electrodes, LaNO and PrNO infiltrated into a Gd-doped ceria backbone. Low R_{pol} values of 0.15 Ω cm^2 for LaNO and 0.08 Ω cm^2 for PrNO at 600 °C were reported. Thus the proposed cathodes in this work could be considered as a potential cathode material for IT-SOFC.

Table 2. Comparison of R_s, R_{pol}, R_1, R_2, R_3 values (Ω cm^2) of the three architectures for LaNO and PrNO electrodes (estimated error is < 5 %)

Temperature [°C]	LaNO cathodes														
	Single layer (sample 1)					Double layer (sample 3)					Triple layer (sample 5)				
	R_s	R_{pol}	R_1	R_2	R_3	R_s	R_{pol}	R_1	R_2	R_3	R_s	R_{pol}	R_1	R_2	R_3
500	22.78	13.38	3.86	9.52	---	8.25	2.85	0.82	2.03	---	7.61	0.97	0.29	0.68	---
550	18.96	7.00	2.24	4.76	---	6.40	1.01	0.38	0.63	---	6.35	0.35	0.11	0.23	0.01
600	14.56	3.32	1.63	1.69	---	5.43	0.42	0.11	0.30	0.01	5.28	0.16	0.04	0.11	0.01
	PrNO cathodes														
	Single layer (sample 2)					Double layer (sample 4)					Triple layer (sample 6)				
	R_s	R_{pol}	R_1	R_2	R_3	R_s	R_{pol}	R_1	R_2	R_3	R_s	R_{pol}	R_1	R_2	R_3
500	14.28	2.38	0.91	1.47	---	6.30	0.32	0.12	0.20	---	7.26	0.23	0.10	0.13	---
550	10.74	1.30	0.56	0.74	---	4.76	0.14	0.06	0.08	---	5.50	0.08	0.03	0.04	0.01
600	8.32	0.83	0.18	0.65	---	4.35	0.08	---	0.07	0.01	4.59	0.04	---	0.03	0.01

As could be expected, R_1 and R_2 decrease by increasing the temperature (**Table 2**). The R_2 values are always larger than those of R_1 (at least a factor of 2 between 500 and 700 °C)

suggesting that the oxygen desorption or adsorption process is the rate-limiting step for the ORR.[46-48] As shown in **Table 2**, the magnitude of the (R_3) low frequency contribution (~1 Hz) almost does not vary with temperature. Moreover this contribution is characterized by high capacitance values, C ≈ 2.6 F cm^{-2} for the LaNO and ≈ 3.3 F cm^{-2} for the PrNO cathode, respectively. Such contribution has been attributed to the O_2 gas diffusion process through the porous electrode.[49, 50]

Table 3 Comparison of minimum R_{pol} value obtained in this study with values reported in the literature for LnNO (Ln= La, Pr) cathode

Cathode	Electrolyte	R_{pol} [Ω cm^2]	T [°C]	Reference
LaNO infiltrated CGO	CGO	0.15	600	Nicollet et al.[27]
PrNO infiltrated CGO	CGO	0.07	600	Nicollet et al.[28]
LaNO	CGO	2.20	600	Philippeau et al.[51]
PrNO	CGO	0.28	600	
LaNO	YSZ	0.93	600	Vibhu et al.[29]
PrNO	YSZ	0.15	600	
Triple layer LaNO	CGO	0.16	600	Present work
Triple layer PrNO	CGO	0.04	600	

The activation energies deduced from the Arrhenius plots of the polarization resistance R_{pol} (**Fig. 9**) are in good agreement with the values reported in literature.[19, 20, 27] To the best of our knowledge, the R_{pol} value obtained (as low as 0.04 Ω cm² at 700 °C for sample 5 and as low as 0.02 Ω cm² at 700 °C for sample 6) is far better than the minimum R_{pol} values previously reported for pure $La_2NiO_{4+\delta}$ and $Pr_2NiO_{4+\delta}$ based cathodes, as shown in **Table 3**. Moreover, all the results have been found to be reproducible. Such excellent performance of triple layer cathodes indicates that an architectural design of LnNO (Ln = La, Pr) cathodes plays a major role in improving their performance by enhancing the electrode to electrolyte charge transfer as well as the ORR. Finally, the polarization resistance stability was evaluated for two electrodes (samples 5 and 6) for 360 h at 650 °C and neither of the cathodes shows any significant variation in the polarization resistance at OCV, as shown in **Fig. 10**. Further studies are in progress to evaluate the stability of these nanostructured electrodes after long-term operation under polarization and to test the performance in fuel cells.

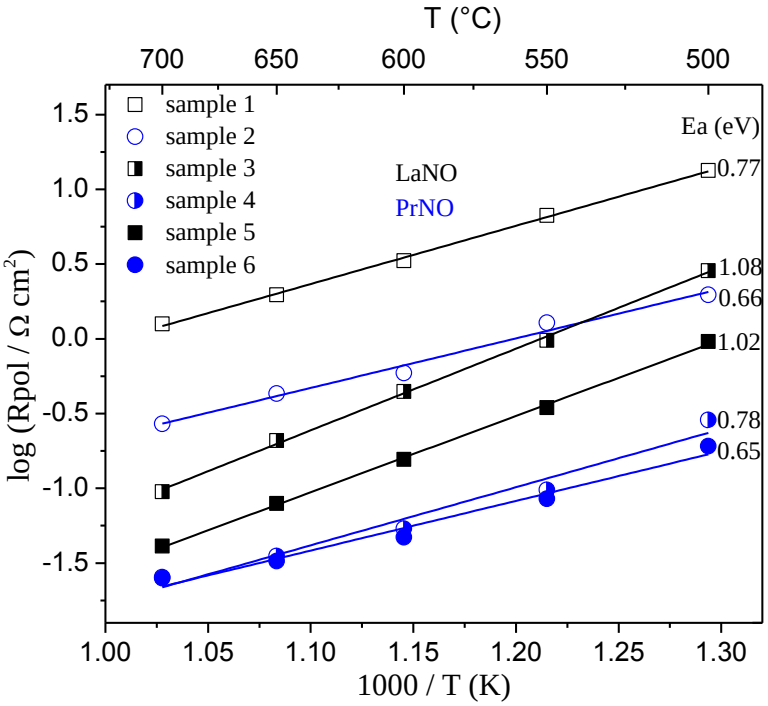

Fig. 9 Arrhenius plot of the R_{pol} in air for six electrodes (OCV conditions) on CGO electrolyte.

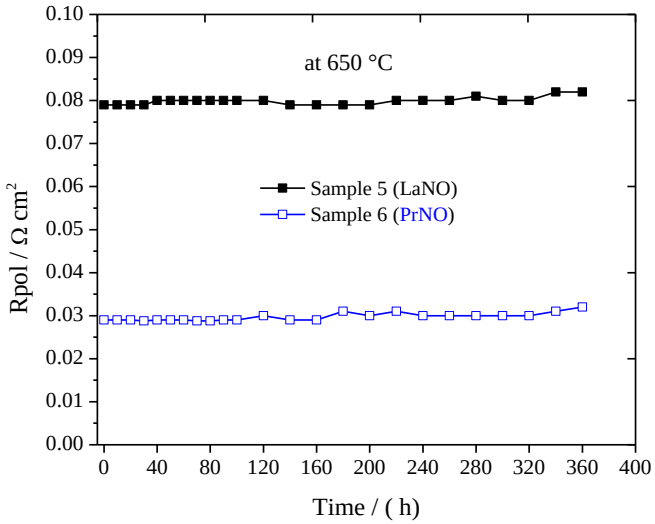

Fig. 10 Variation in the polarization resistance of samples 5 and 6 at 650 °C in OCV condition.

In summary, electrostatic spray deposition could be an effective method for commercial production of large-area electrodes for SOFCs with a series of advantages

compared to the wet infiltration process, including easy industrial implementation, less preparation steps and low cost. Moreover, this method may be applicable to other electrochemical systems, such as solid electrolyzers, batteries, and supercapacitors.

4. Conclusions

This study demonstrates that the presence of a thin composite layer of CGO and LnNO in between electrolyte and the double layer LnNO cathodes deposited via SP and ESD procedures, respectively, is a very innovative route to improve significantly the electrochemical performance. Single phase of the prepared electrode crystallized in orthorhombic (Fmmm) has been confirmed by XRD. During the growth of the 3-D coral microstructure of LnNO on the top of thin compact CGO film, the precursor solution penetrates the compact CGO layer and leads to the formation of CGO and LnNO composite. In this work, cathodes containing CGO-LnNO composite sub layer displayed polarization resistances as low as 0.16 Ω cm^2 at 600 °C (0.04 Ω cm^2 at 700 °C) for LaNO and 0.04 Ω cm^2 at 600 °C (0.02 Ω cm^2 at 700 °C) for PrNO, which are among the best values reported so far for SOFC cathodes. The lowest values, found for these composite cathodes are due to the higher ionic conductivity of the composites, larger number of active points close to electrolyte, and larger contact area between CGO and LnNO which facilitate the charge transfer from the cathode to the electrolyte. In addition, the R_{pol} values for both electrodes were found to be constant at 650 °C for 15 days, further proving their suitability to be used as SOFC cathode.

Acknowledgements

This work was performed within the framework of the Centre of Excellence of Multifunctional Architectured Materials "CEMAM" n° AN-10-LABX-44-01 funded by the "Investments for the Future" Program.

References:

[1] A. Chroneos, D. Parfitt, J.A. Kilner and R.W. Grimes, *J. Mater. Chem.,* 2010, **20**, 266.
[2] D. Pérez-Coll and A. Aguadero, *Fuel Cells*, 2011, **11**, 91.
[3] V.V. Kharton, E.V. Tsipis, A.A. Yaremchenko and J.R. Frade, *Solid State Ionics*, 2004, **166**, 327.

[4] F. Mauvy, J.M. Bassat, E. Boehm, P. Dordor and J.P. Loup, *Solid State Ionics*, 2003, **158**, 395.
[5] F. Mauvy, E. Boehm, J.M. Bassat, J.C. Grenier and J. Fouletier, *Solid State Ionics*, 2007, **178**, 1200.
[6] Q. Li, H. Zhao, L. Huo, L. Sun, X. Cheng and J-C. Grenier, *Electrochemistry Communications*, 2007, **9**, 1508.
[7] A. Aguadero, J.A. Alonso, M.J. Escudero and L. Daza, *Solid State Ionics*, 2008, **179**, 393.
[8] F. Mauvy, J.M. Bassat, E. Boehm, J.P. Manaud, P. Dordor and J.C. Grenier, *Solid State Ionics*, 2003, **158**, 17.
[9] J.M. Bassat, P. Odier, A. Villesuzanne, C. Marin and M. Pouchard, *Solid State Ionics*, 2004, **167**, 341.
[10] E. Boehm, J. Bassat, P. Dordor, F. Mauvy, J. Grenier and P. Stevens, *Solid State Ionics*, 2005, **176**, 2717.
[11] C. Munnings, S.J. Skinner, G. Amow, P. Whitfield and I. Davidson, *Solid State Ionics*, 2005, **176**, 1895.
[12] A. Tarancón, M. Burriel, J. Santiso, S. J. Skinner and J. A. Kilner, *J. Mater. Chem.*, 2010, **20**, 3799.
[13] K. Yakal-Kremski, L. V. Mogni, A. Montenegro-Hernández, A. Caneiro and S.A. Barnett, *Journal of The Electrochemical Society*, 2014, **161**, F1366.
[14] A. M. Daroukh, V.V. Vashook, H. Ullmann, F. Tietz and Arual Raj I., *Solid State Ionics*, 2003, 158, 141.
[15] V.V. Kharton, A.P. Viskup, A.V. Kovalesvsky, E.N. Naumovich and F.M.B. Marques, *Solid State Ionics*, 2001, **143**, 337.
[16] X. Dong, Z. Wu, X. Chang, W. Jin and N. Xu, *Ind. Eng. Chem. Res.*, 2007, **46**, 6910.
[17] A.P. Khandale and S.S. Bhoga, *J. Power Sources*, 2010, **195**, 7974.
[18] M.L. Fontaine, C. Laberty-Robert, F. Ansart and P. Tailhades, *J. Power Sources*, 2006, **156**, 33.
[19] R. Sayers, M. Rieu, P. Lenormand, F. Ansart, J.A. Kilner and S.J. Skinner, *Solid State Ionics*, 2011, **192**, 531.
[20] N. Hildenbrand, P. Nammensma, D.H.A. Blank, H.J.M. Bouwmeester and B.A. Boukamp, *J. Power Sources*, 2013, **238**, 442.
[21] D. Marinha, L. Dessemond, J.S. Cronin, J.R. Wilson, S. A. Barnett and E. Djurado, *Chem. Mater.* 2011, **23**, 5340.
[22] C. Ferchaud, J.C. Grenier,Y. Zhang-Steenwinkel, M.M.A. Van Tuel, F. P.F. Van Berkel and J.M. Bassat, *Journal of Power Sources*, 2011, **196**, 1872.
[23] C. Jin and J. Liu, *J. Alloys Compd.*, 2009, **474**, 573.
[24] S.J. Skinner and G. Amow, *Journal of Solid State Chemistry*, 2007, **180**, 1977.
[25] C. Tealdi, C. Ferrara, L. Malavasi, P Mustarelli, C Ritter and G. Chiodelli, *Physical Review B*, 2010, **82**, 174118.
[26] S. Choi, S. Yoo, J.-Y. Shin and G. Kim, *J. Electrochem. Soc.*, 2011, **158**, B995.
[27] C. Nicollet, A. Flura, V. Vibhu, A. Rougier, J-M. Bassat and J.C. Grenier, *Journal of Power Sources*, 2015, **294**, 473.

[28] C. Nicollet, A. Flura, V. Vibhu, S. Fourcade, A. Rougier, J-M. Bassat and J.C. Grenier, *Journal of Solid State Electrochem*, 2016, 1.
[29] V. Vibhu, A. Rougier, C. Nicollet, A. Flura, J.C. Grenier and J-M. Bassat, *Solid State Ionics*, 2015, **278**, 32.
[30] Y. Huang, J. M. Vohs and R. J. Gorte, John Wiley & Sons, Inc., Hoboken, NJ, 2006; Vol. 179.
[31] D. Ding, X. Li, S. Lai, K. Gerdes and M. Liu, *Energy Environ. Sci.* 2014, **7**, 552.
[32] R. K. Sharma, M. Burriel, L. Dessemond, V. Martin, J.M. Bassat and Elisabeth Djurado, *Journal of Power Sources*, 2016, **316**, 17.
[33] C.H. Chen, M.H.J. Emond, E.M. Kelder, B. Meester and J. Schoonman, *J. Aerosol. Sci.*, 1999, **30**, 959.
[34] D. Marinha, L. Dessemond and E. Djurado, *Current Inorganic Chemistry*, 2013, **3**, 2.
[35] J. Rodriguez-Carvajal, *Phys. B*, 1993, **192**, 55.
[36] R. Neagu, D. Perednis, A. Princivalle and E. Djurado, *Solid State Ionics*, 2006, **177**, 1981.
[37] C.H. Chen, E.M. Kelder, P.J.J.M. van der Put and J. Schoonman, *J. Mater. Chem.*, 1996, **6**, 765.
[38] B.-H. Hwang, C.-L. Chang, C.-S. Hsu and C.-Y. Fu, *J. Phys. D: Appl. Phys.*, 2007, **40**, 3448.
[39] J. Sar, O. Celikbilek, J. Villanova, L. Dessemond, C. L. Martin and E. Djurado, *Journal of the European Caramic Society*, 2015, **35**, 4497.
[40] C. Fu, K. Sun, N. Zhang, X. Chen and D. Zhou, *Electrochim. Acta*, 2007, **52**, 4589.
[41] S.B. Adler, *Solid State Ionics*, 2000, **135**, 603.
[42] M.J. Escudero, A. Aguadero, J.A. Alonso and L. Daza, *J. Electroanal. Chem.*, 2007, **611**, 107.
[43] T. Jacobsen, P.V. Hendriksen and S. Koch, Electrochimica Acta, 2008, **53**, 7500.
[44] W.G. Bessler, Journal of the Electrochemical Society, 2006, **153**, A1492.
[45] N. Hildenbrand, B. A. Boukamp, P. Nammensma and D.H.A. Blank, *Solid State Ionics*, 2011, **192** 12.
[46] Z. Lou, J. Qiao, Y. Yan, J. Peng, Z. Wang and T. Jiang, *Int J Hydrogen Energy*, 2012, **37**, 11345.
[47] S. Huang , Q. Lu, S. Feng , G. Li and C.Wang, *Adv. Energy Mater*, 2011, **1**, 1094.
[48] H. Gu, H. Chen, L. Gao and L. Guo, *Electrochim Acta*, 2009, **54**, 7094.
[49] L. Mogni, N. Grunbaum, F. Prado and A. Caneiro, *J. Electrochem. Soc.*, 2011, **158**, B202.
[50] S. Pang, X. Jiang, X. Li, Q. Wang and Z. Su, *J. Power Sources*, 2012, **204**, 53.
[51] B. Philippeau, F. Mauvy, C. Mazataud, S. Fourcade and J.C. Grenier, *Solid State Ionics*, 2013, **249-250**, 17.

Supporting information

Table S1. Capacitances (F cm^{-2}) and exponents of CPE for all six architectures (estimated error is < 5 %)

Sample	CPE_1			CPE_2			CPE_3		
	n	Q	C_1	n	Q	C_2	n	Q	C_3
Sample 1	0.5552	0.0051	$5.8x10^{-5}$	0.8224	0.0022	$3.3x10^{-3}$	-----	-----	-----
Sample 2	0.8805	0.0049	$9.3x10^{-4}$	0.9036	0.0063	$1.8x10^{-3}$	-----	-----	-----
Sample 3	0.7529	0.0092	$7.1x10^{-4}$	0.8062	0.0074	$1.2x10^{-3}$	0.9719	9.23	5.6
Sample 4	-----	-----	-----	0.9435	0.0531	$2.6x10^{-2}$	0.8242	5.34	2.6
Sample 5	0.9055	0.0088	$3.3x10^{-3}$	0.8827	0.0093	$3.9x10^{-3}$	0.8454	5.79	2.6
Sample 6	-----	-----	-----	0.7688	0.1609	$2.4x10^{-2}$	0.8387	7.50	3.3

FULLPROF refinement of the XRD patterns of the $Ln_2NiO_{4+\delta}$ (Ln = La, Pr) films prepared by ESD on a screen printed CGO layer on a CGO pellet.

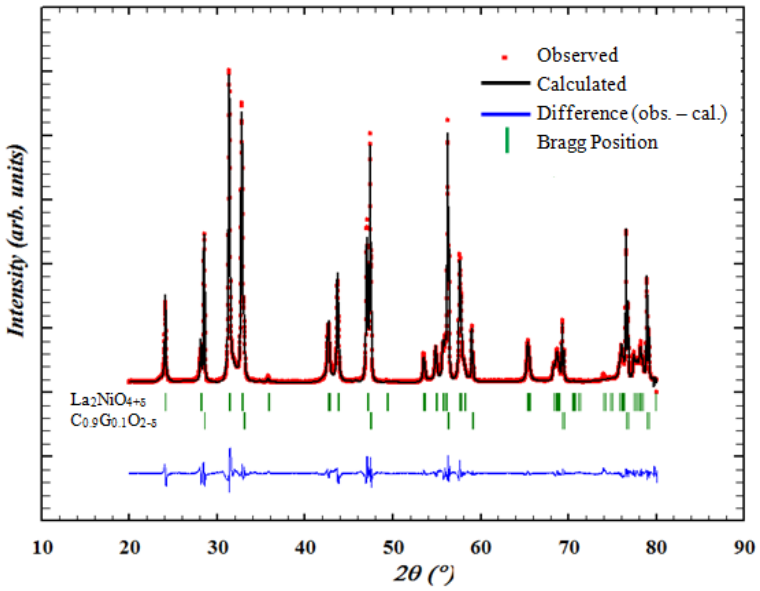

Fig. S1 FULLPROF refinement of the XRD patterns of $La_2NiO_{4+\delta}$ film deposited by ESD on a screen printed CGO layer on a CGO pellet (Fit parameters: χ^2 = 12.2, Bragg R-factor = 1.272 and RF-factor = 0.637for $La_2NiO_{4+\delta}$; Bragg R-factor = 0.925 and RF-factor = 0.442 for CGO).

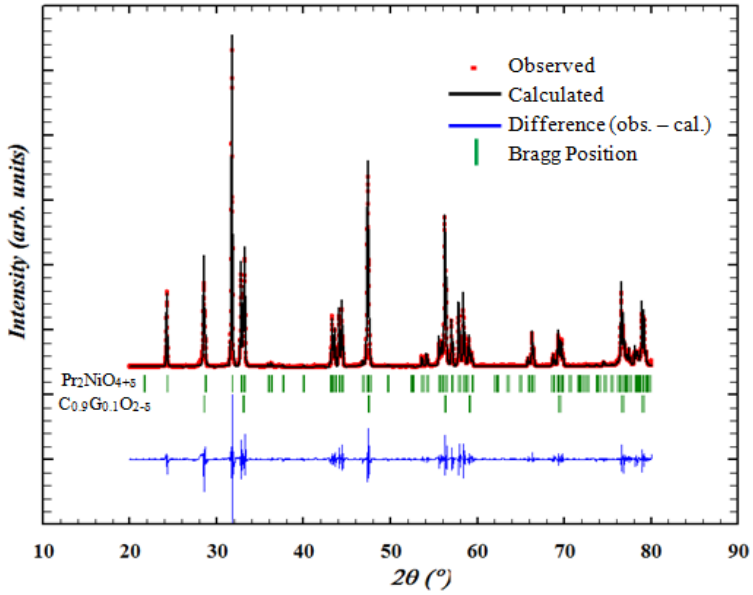

Fig. S2 FULLPROF refinement of the XRD patterns of $Pr_2NiO_{4+\delta}$ film deposited by ESD on a screen printed CGO layer on a CGO pellet (Fit parameters: χ^2 = 26.2, Bragg R-factor = 1.13 and RF-factor = 0.601 for $Pr_2NiO_{4+\delta}$; Bragg R-factor = 0.556 and RF-factor = 0.319 for CGO).

Oxygen overstoichiometry by TGA:

TGA curves of $La_2NiO_{4+\delta}$and $Pr_2NiO_{4+\delta}$ are shown in **Fig. S3**. Two weight changes are observed: the first one occurs around 350°C, corresponding to the reduction of Ni^{3+} into Ni^{2+} (the oxygen overstoichiometry being reduced down to δ = 0). The second weight loss characterizes the complete reduction of LnNO into La_2O_3, Pr_2O_3 and Ni. The δ value has been calculated from both values of the weight changes using mole conservation principle.

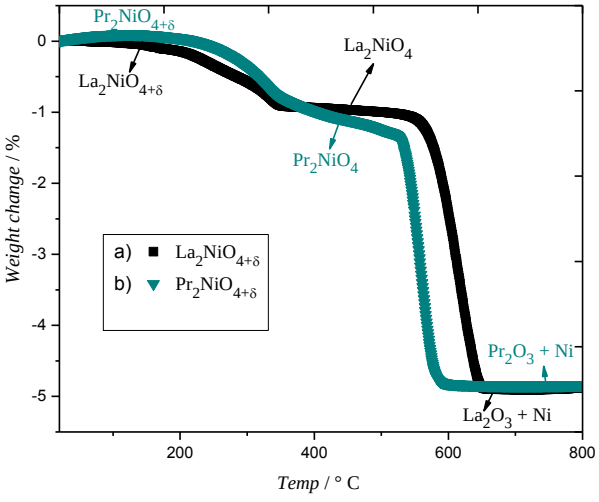

Fig. S3 TGA curves of$La_2NiO_{4+\delta}$and $Pr_2NiO_{4+\delta}$.

Micrographs of sample 5:

Fig. S4 shows the SEM micrographs of sample 5, the LaNO cross section and the CGO-LaNO composite base-layer of the LaNO triple layer design on CGO substrate using sequentially SP and ESD.

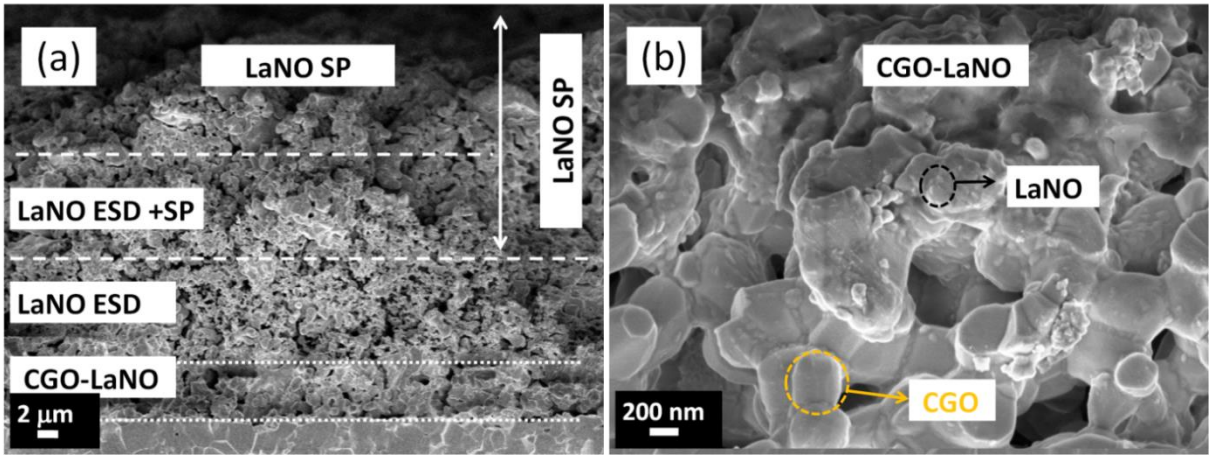

Fig. S4 SEM micrographs of sample 5: (a) cross section, (b) CGO-LaNOsub-layer on CGO electrolyte.

The experimental and fitted impedance spectra at600 °C from the inset of **Fig. 8b**, is shown in **Fig. S5** along with capacitances and exponents of CPE for all 6 architectures in Table S1.

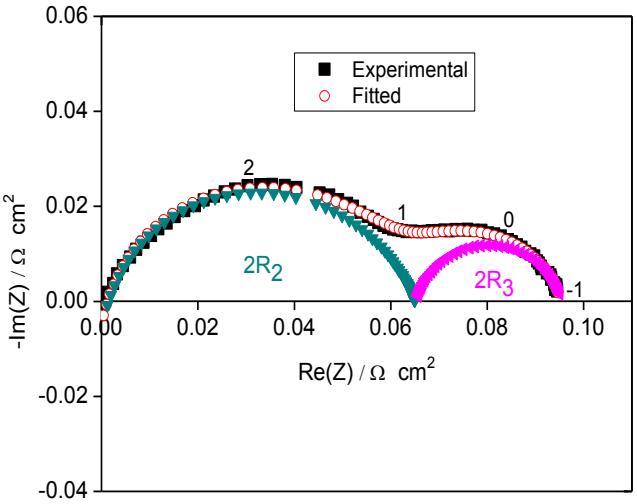

Fig. S5 Nyquist plots recorded at 600 °C in air at OCV for sample 6. The numbers indicate the logarithm of the measuring frequency.

Chapter 5

Part II: $La_{n+1}Ni_nO_{3n+1}$ (n = 2 and 3) phases and composites for solid oxide fuel cell cathodes: facile synthesis and electrochemical properties

R. K. Sharma, M. Burriel, L. Dessemond, J.-M. Bassat and E. Djurado, *Journal of Power Sources*, 2016, 325, 337-345.
DOI: http://dx.doi.org/10.1016/j.jpowsour.2016.06.047

$La_{n+1}Ni_nO_{3n+1}$ (n = 2 and 3) phases and composites for solid oxide fuel cell cathodes: facile synthesis and electrochemical properties

Rakesh K. Sharma[a, b], Mónica Burriel[c], Laurent Dessemond[a], Jean-Marc Bassat[b], Elisabeth Djurado[*, a]

[a] Univ. Grenoble Alpes, CNRS, LEPMI, F-38000 Grenoble, France
[b]CNRS, Université Bordeaux, Institut de Chimie de la Matière Condensée de Bordeaux, 87 Av. du Dr Schweitzer, 33608 PESSAC Cedex,France
[c]Univ. Grenoble Alpes, CNRS, LMGP, F-38000 Grenoble, France

**Corresponding author:* Elisabeth Djurado
E-mail: elisabeth.djurado@lepmi.grenoble-inp.fr, Tel: +33-476826684; Fax: +33-476826777

Abstract:

In this work we present a modified citrate-nitrate route using citric acid as a chelating agent as an effective and facile strategy to obtain nanocrystalline $La_3Ni_2O_{7+\delta}$ (L3N2) and $La_4Ni_3O_{10-\delta}$ (L4N3) powders for the preparation of solid oxide fuel cell cathodes. Both samples crystallize in a Fmmm orthorhombic layered $La_{n+1}Ni_nO_{3n+1}$ Ruddlesden-Popper structure, with n = 2 and 3, respectively. The oxygen non-stoichiometry, determined by TGA is equal to 0.05 and 0.06 for L3N2 and L4N3, respectively. The thermal expansion coefficient values of L3N2 and L4N3 are 11.0 x 10^{-6} K^{-1} and 11.5 x 10^{-6} K^{-1}, respectively. This study focused on L3N2, L4N3 and on novel composite electrodes with CGO ($Ce_{0.9}Gd_{0.1}O_{2-\delta}$): L3N2-CGO and L4N3-CGO with a view to taking advantage of their complimentary properties, i.e. high ionic conductivity of CGO and high electronic conductivity of $La_{n+1}Ni_nO_{3n+1}$ (n = 2 and 3). A significant improvement of the polarization resistance, from 1.0 to 0.03 Ω cm^2 and from 1.5 to 0.52 Ω cm^2 at 700 °C, is obtained when 50 wt. % CGO is added to L3N2 and L4N3, respectively. In addition, the L3N2-CGO composite shows good long-term stability at 900 °C for 2 weeks in air, confirming its suitability as a SOFC cathode.

Keywords: IT-SOFCs, mixed electronic ionic conducting oxides, lanthanum nickelate, composite, AC impedance.

1. Introduction

Solid oxide fuel cell (SOFC) based electrochemical devices convert chemical energy into electrical energy efficiently with low pollutant emissions [1 - 4]. Recently, rare earth nickelates ($La_{n+1}Ni_nO_{3n+1}$, with n=1, 2 and 3) have been considered to be promising materials for IT (intermediate temperature)-SOFC cathode applications [5 - 9] because of many important advantages such as high mixed ionic and electronic conductivity [10 - 12], moderate temperature expansion coefficient (TEC) [8], and high electrocatalytic activity under oxidizing conditions [8, 9, 13]. The Ruddlesden–Popper (RP) phases, with the general formula $La_{n+1}Ni_nO_{3n+1}$, are composed of *n* finite layers of the perovskite $LaNiO_3$ along the *c*-axis separated by LaO rock salt-like layers [14]. As a consequence of their layered framework, the La:Ni ratio varies throughout the RP series, leading to very different electronic conductivity and they can accommodate a range of oxygen non-stoichiometry. According to previous reported results, the overall electrical conductivity of $La_{n+1}Ni_nO_{3n+1}$ at 500-700 °C was found to increase systematically with *n* [9, 15, 16] (from 63, 100 to 250 S cm^{-1} at 600°C for n=1, 2 to 3, respectively) thanks to a larger number of perovskite layers, which govern the electronic conduction pathways located in the NiO_6 octahedra of these RP phases. For a given phase, the electronic conductivity also increases with the Ni^{3+} content, governed by the oxygen non-stoichiometry, which can vary depending on the preparation method [15, 16]. Furthermore, it has also been reported that $La_{n+1}Ni_nO_{3n+1}$ (n>1) oxides grown on $La_{0.9}Sr_{0.1}Ga_{0.8}Mg_{0.2}O_{3-\delta}$ (LSGM) or on ($Ce_{0.9}Gd_{0.1}O_{2-\delta}$) (CGO) electrolyte exhibit good long-term stability in air (at 900 °C for 2 weeks) [8]. In contrast, a similar aging treatment of $La_2NiO_{4.15}$ on CGO has revealed its degradation [17]. As a consequence, it seems that the higher order Ruddlesden–Popper (RP) structures such as $La_3Ni_2O_{7+\delta}$ (L3N2) and $La_4Ni_3O_{10-\delta}$ (L4N3) could be more suitable cathodes than $La_2NiO_{4+\delta}$ (L2N1) for IT-SOFC applications [11, 17].

In some cases the electrochemical properties of the cathode can be further improved by adding a pure ionic conductor phase, such as demonstrated for yttria stabilized zirconia (YSZ) in strontium doped lanthanum manganate [18, 19], doped ceria in $Pr_{0.7}Sr_{0.3}Co_{0.9}Cu_{0.1}O_{3-\delta}$ [18-20], doped lanthanum gallate in $La_{0.6}Sr_{0.4}Co_{0.2}Fe_{0.8}O_{3-\delta}$ (LSCF) [21, 22] and samarium-doped ceria or gadolinium-doped ceria in LSCF [23-25]. For example, the polarization resistance of the composite cathode, LSCF-CGO, 60: 40 wt. % was about seven times lower than that of the pure LSCF [26]. As for the nickelates, Choi et al. reported a

decrease in the polarization resistance (R_{pol}) for the composite cathodes $La_{n+1}Ni_nO_{3n+1}$ (*n* = 1, 2, and 3)-YSZ prepared by infiltration from 0.120 down to 0.068 Ω cm^2 at 750 °C by increasing *n* from 1 to 3 [13]. These R_{pol} values are significantly lower than those reported for pure $La_{n+1}Ni_nO_{3n+1}$ at the same temperature: 0.2 Ω cm^2 for *n* = 1 [27], 0.39 Ω cm^2 for *n* = 2 [28] and 0.26 Ω cm^2 for *n* = 3 [29]. In addition the good performance of a 50:50 wt.% L2N1-L4N3 composite cathode has been reported taking advantage of the specific properties of each phase, i.e. a high ionic conductivity for L2N1 and a high total conductivity for L4N3 [30]. The 50 wt. % L2N1-L4N3 composite presents the lowest R_{pol} value with comparison to pure L2N1 and L4N3 materials at 700 °C of 0.62 Ω. The authors also reported that the total conductivity of L4N3 is much better than that of the L2N1-L4N3 composite.

The cathode performance is usually evaluated by measuring the polarization resistance value, which is not only influenced by the choice of the material itself, but also by its microstructure. The processing conditions used in the synthesis of the La–Ni–O phases are of considerable interest, as these can affect their properties as cathode materials in IT-SOFCs devices [8, 16, 17, 31, 32]. Up to now, various methods have been reported in the literature such as the nitrate and citrate routes [16, 33], the continuous hydrothermal flow synthesis (CHFS) method [16, 17, 34–38], solid-state synthesis [16, 35], the Pechini method [8] and pulsed laser deposition [39]. The synthesis of pure and single phase higher members of the $La_{n+1}Ni_nO_{3n+1}$ series, particularly *n* = 2 and 3, is difficult due to prolonged homogenization and reheating procedures which have to be restricted to limited temperatures because of possible transformation into L2N1 at higher temperatures [8, 16, 35, 40]. For example, the synthesis of the pure L4N3 phase from metal oxide powders takes up to 4–5 days at 1100 ºC under air with intermittent grinding and reheating steps [41]. Recently, Lou et. al. reported the direct and fastest method for the synthesis of L3N2 [28] and L4N3 [29] via sol-gel route by using F127, a poly (ethylene oxide)–poly (propylene oxide)–poly (ethylene oxide) (PEO–PPO–PEO) tri-block copolymer as a chelating agent. In order to get a gel, a first heating at 100 °C for 24 h is required followed by 2 sintering steps, at 1150 °C for 12 h and at 1025 °C for 12 h in air for obtaining pure L3N2 and L4N3 phases, respectively. Thus, the synthesis of such complex materials in a faster and more efficient way constitutes a challenge.

In the present work, we describe the direct, efficient and single-step synthesis of the $La_{n+1}Ni_nO_{3n+1}$ phases (with *n*= 2 and 3) from a nitrate non-aqueous precursor solution. We have investigated the structural parameters, oxygen content, TEC of the pure L3N2 and L4N3

Ruddlesden–Popper systems as well as the electrochemical properties of cathodes deposited on $Ce_{0.9}Gd_{0.1}O_{2-\delta}$ (CGO) electrolyte. Moreover, the electrochemical properties of the cathode can be enhanced significantly when an ionic conductor is added in the range 40-60 wt% [18-26]. Therefore, novel composite cathodes consisting of 50 wt.% of CGO and 50 wt.% of $La_{n+1}Ni_nO_{3n+1}$ phases (with n= 2 and 3) denoted by L3N2-CGO and L4N3-CGO, respectively, have been deposited by screen-printing on a dense CGO electrolyte and their electrochemical properties evaluated.

2. Experimental

2.1. Synthesis process and characterization

$La_{n+1}Ni_nO_{3n+1}$ (with n = 2 and 3) powders were prepared by a citric acid complexation method. Stoichiometric amounts of nickel nitrate hexahydrate [$Ni(NO_3)_26H2O$, 99.9%, Aldrich] and lanthanum nitrate hexahydrate [$La(NO_3)_36H2O$, 99.9%, Alfa Aesar] were completely dissolved in ethanol (CH_3CH_2OH, >99.9%, Prolabo) with vigorous stirring over 1 h, and then an excess amount (20 % per mole) of citric acid [$C_6H_8O_7$, 99.9%, Alfa Aesar] was mixed into the solution under the stirring conditions. The solution was then heated up to 150 ℃ with constant stirring until the auto combustion occurred. The as-prepared powder was subsequently calcined at 950 °C for 8 h and at 1050 °C for 4 h in order to obtain the L3N2 and L4N3 phases, respectively. The crystal structure was determined by powder X-ray diffraction using Bragg-Brentano configuration (XRD, Philips X'Pert-MPD system, Cu Kα radiation, λ= 1.54056 Å). The lattice parameters were extracted from Rietveld refinement of the XRD patterns using Fullprofsuite [42]. Commercial CGO ($Ce_{0.9}Gd_{0.1}O_{2-\delta}$) powder (Solvay) was used for the composite and electrolyte preparation.

The oxygen content (at room temperature) of the two considered oxides was determined by thermogravimetric analysis performed under flowing 5% H_2–Ar gas using a TGA-Q50 thermogravimetric analyzer. For this purpose, data were collected in the 20 – 900 °C temperature range at the heating rate of 0.5 °C min^{-1}. The oxygen content was determined by measuring the weight change of the starting materials on complete reduction into La_2O_3 and Ni. With the aim of determining the TEC of the materials, the thermal variations of the relative expansion (dL/L) of the $La_{n+1}Ni_nO_{3n+1}$ pellets (density 64% of theoretical value) were carried out in the temperature range 25 – 900 °C using a differential dilatometer (Netzsch-402 DIL402C).

L3N2, L4N3, L3N2-CGO and L4N3-CGO cathodes were screen-printed symmetrically on both sides of the CGO electrolyte pellets for the electrochemical studies. CGO electrolyte pellets were made by pressing discs (20 mm diameter and 1.2 mm thickness) which were fired at 1400 °C for 4 h. Inks based on KD2921 (Zschimmer and Schwarz) solvent were prepared with the L3N2, L4N3, L3N2-CGO and L4N3-CGO powders. The pure L3N2 and L4N3 nickelate cathodes, were sintered at 1000 °C for 4 h under air while the composite cathodes were sintered at 1000 °C/1 h + 1050 °C /1 h under air. These sintering temperatures were selected to avoid the delamination of the cathode on the CGO electrolyte. The area of the L3N2 and L4N3 electrodes was of 2.0 cm^2 and that of the corresponding composites was 1.54 cm^2. Electrochemical impedance diagrams were recorded on symmetric cells at open circuit potential (OCP) between 500 and 750 °C in air using a PGSTAT 302N (Eco Chemie). The measuring frequency ranged from 50 mHz to 100 kHz, and the AC amplitude was fixed to 20 mV. Gold grid (Heraeus, 1024 meshes/cm^2 woven, 0.06 mm dia. wire) was used as current collector. The impedance diagrams were normalized to the electrode area and analyzed using equivalent circuits using Zview® software. Long-term measurements on the L3N2-CGO composite cathode were performed at 900 °C for 2 weeks in air. The surface and cross-sectional morphology of the cathodes was characterized using a scanning electron microscopy (ZEISS Ultra 55 instrument with field emission gun (FEG)). The particle size (diameter) of the electrodes was estimated from the SEM images using ImageJ software.

3. Results and discussion

3.1. Structural characterization

Fig. 1 shows the XRD patterns of the L3N2 and L4N3 powders calcined at 1050 °C for 4 h and at 950 °C for 8 h, respectively. Both XRD patterns can be clearly indexed as pure $La_3Ni_2O_{7+\delta}$ and $La_4Ni_3O_{10-\delta}$ orthorhombic phase structure with the Fmmm space group (69). The XRD patterns of the L3N2 + CGO and L4N3 + CGO composite films screen-printed on a CGO electrolyte and calcined at 1000 °C/1 h + 1050 °C /1 h in air, are shown in **Fig. S1**. For these composite films, neither reactivity between L3N2 and CGO, between L4N3 and CGO, nor phase decomposition have been observed. The refined unit cell parameters of the orthorhombic L3N2 and L4N3 phases, summarized in Table 1, are in good agreement with previously reported data [8, 16, 35]. With the method described in this work it is possible to obtain the pure $La_{n+1}Ni_nO_{3n+1}$ oxide phases (n=2 and 3) after calcination for relative short

times (4 and 8 h, respectively) and at quite low temperatures (1050 °C and 950 °C, respectively) without the need of any intermediate grinding steps, as required in earlier reports [9, 16]. As can be seen in **Table 2**, the preparation of pure $La_3Ni_2O_{7+\delta}$ and $La_4Ni_3O_{10-\delta}$ by the citrate route, using citric acid as chelating agent requires thermal treatment at lower temperatures and for shorter duration in comparison to the nitrate one, showing the importance of citric acid as a chelant.

Table 1. Lattice parameters a, b, c and space groups of L3N2 and L4N3

Samples	a [Å]	b [Å]	c [Å]	V [Å^3]	Space Group
L3N2	5.404(9)	5.452(4)	20.496(1)	603.86(5)	Fmmm
L4N3	5.413(2)	5.462(3)	27.960(5)	826.65(9)	Fmmm

Table 2. Comparison of the different synthesis routes for $La_{n+1}Ni_nO_{3n+1}$ including solvent, chelant and reaction temperature / time

	Route	Solvent	Chelant	Reaction temp/time [°C / h]	Formulation	Reference
L3N2	nitrate	water		1150 °C/ 72 h	$La_3Ni_2O_{6.93}$	[16]
	nitrate-citrate	water	citric acid	1080 °C/ 48 h	$La_3Ni_2O_{7.03}$	
	modified nitrate-citrate	ethanol	citric acid	1050 °C /4 h	$La_3Ni_2O_{7.05}$	this work
L4N3	nitrate	water		1150 °C /336 h	$La_4Ni_3O_{9.75}$	[16]
	nitrate-citrate	water	citric acid	1080 °C / 48 h	$La_4Ni_3O_{10.02}$	
	modified nitrate-citrate	ethanol	citric acid	950 °C /8 h	$La_4Ni_3O_{9.94}$	this work

As shown in **Table 2**, Carvalho et al. [16] reported a reduction in the thermal treatments from 1150 °C / 72 h to 1080 °C/ 48 h for L3N2 and from 1150 °C / 336 h to 1080 °C/ 48 h for L4N3. The authors reported smaller powder grain sizes and higher reactivity when the powders were prepared by the citrate route in comparison to the nitrate one. This can be explained by the fact that citric acid forms complexes with Ni^{2+} and La^{3+} through coordination bonds [43], bringing the reaction partners sufficiently close to each other. However, since water was used as solvent, both methods still required intermittent grinding steps. In this work

we have used ethanol instead of water as a solvent. The citrate-complex method is significantly altered by the solvent [44], for instance in the work reported by Ding et al. [44], smaller particles were formed by the lower polarity of EtOH and its high dissolving capacity compared to H_2O. In addition, EtOH has a lower dielectric constant than H_2O (25.3 against 78.54) [45] which helps accelerate the homogeneous complexing process. Thus, the solute-solvent interaction between ethanol and the precursors plays an important and positive role in the synthesis process.

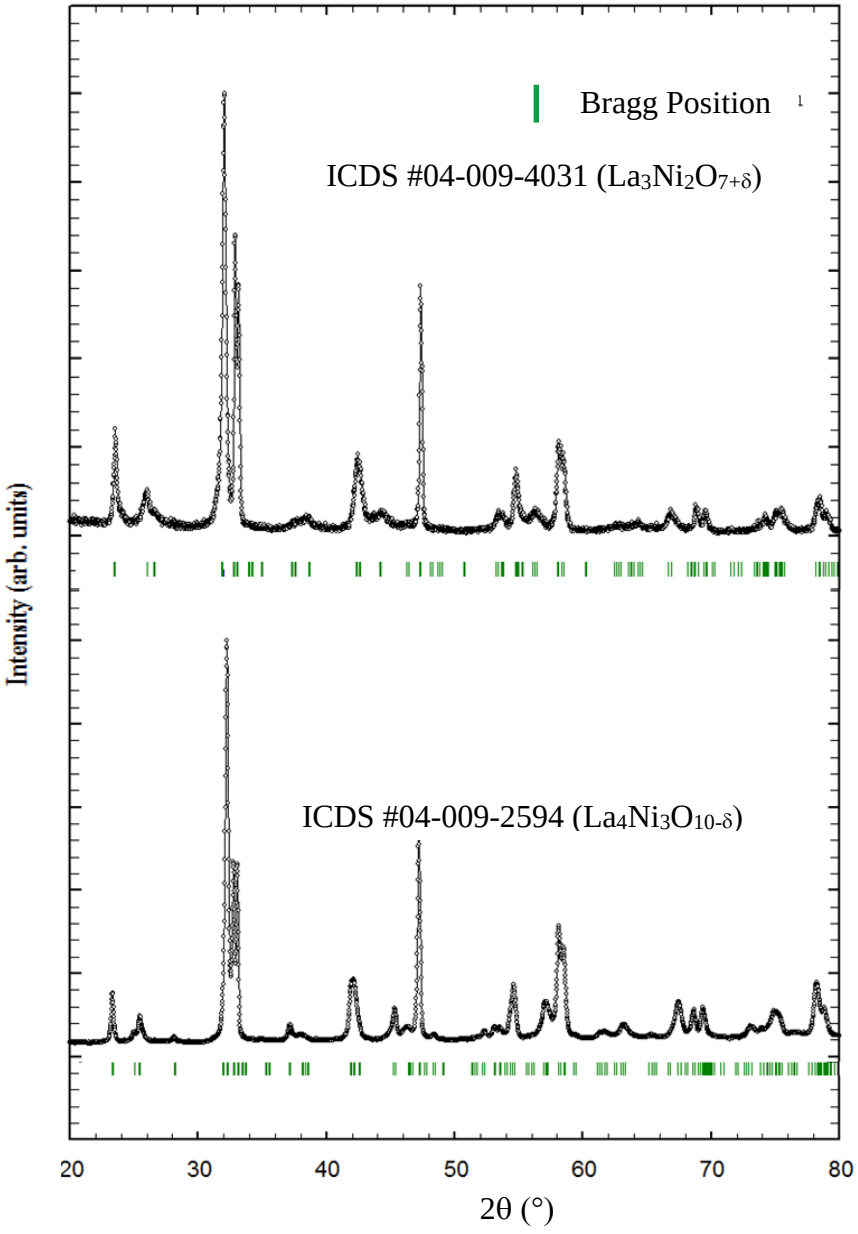

Fig. 1 XRD patterns of the L3N2 and L4N3 powders.

3.2.Oxygen content analysis by TGA

The oxygen non-stoichiometry (δ) was calculated using the the TGA results performed under reducing conditions (5% H_2/ 95% Ar atmosphere). As shown in **Fig. 2**, two weight changes are observed: the first one occurs around 350 °C, corresponding to the reduction of Ni^{3+} into Ni^{2+} (*i.e.* the stabilization of intermediate phases corresponding to $La_3Ni_2O_{6.5}$ and $La_4Ni_3O_9$, respectively). The second weight loss characterizes the complete decomposition of the material, i.e., the reduction of L3N2 and L4N3 into La_2O_3 and Ni. The δ value has been calculated from the total weight loss using the mole conservation principle. The oxygen non-stoichiometry (δ) was found to be 0.05 and 0.06 for L3N2 and L4N3, respectively. The obtained oxygen stoichiometry for both L3N2 and L4N3 is in agreement with similar compositions previously prepared by the nitrate method [16, 35, 46].

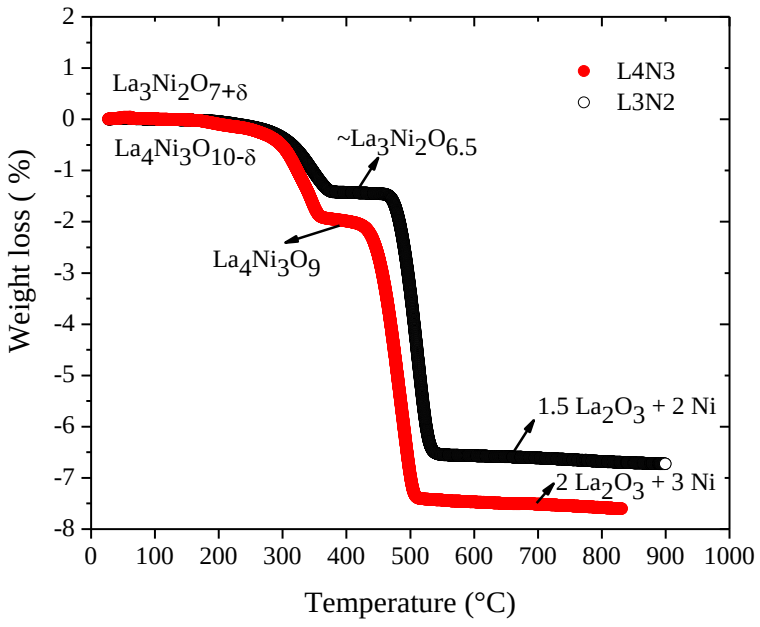

Fig. 2 TGA curve of L3N2 and L4N3 powders recorded under 5% H_2/ 95% Ar atmosphere.

3.3. Thermal expansion

The dilatometric data recorded in this study are shown in **Fig. 3**. The dL/L evolution is linear in the range from 250 to 800 °C. In this temperature range the thermal expansion coefficients were found to be ~11.0 x 10^{-6} K^{-1} for L3N2 and ~11.5 x 10^{-6} K^{-1} for L4N3, in good agreement with previously reported values [8, 29]. These values are close to those of

CGO (~11 × 10^{-6} K^{-1}), ensuring the adequate use of these materials as cathodes on CGO electrolyte in the intermediate temperature range from a thermo-mechanical point of view.

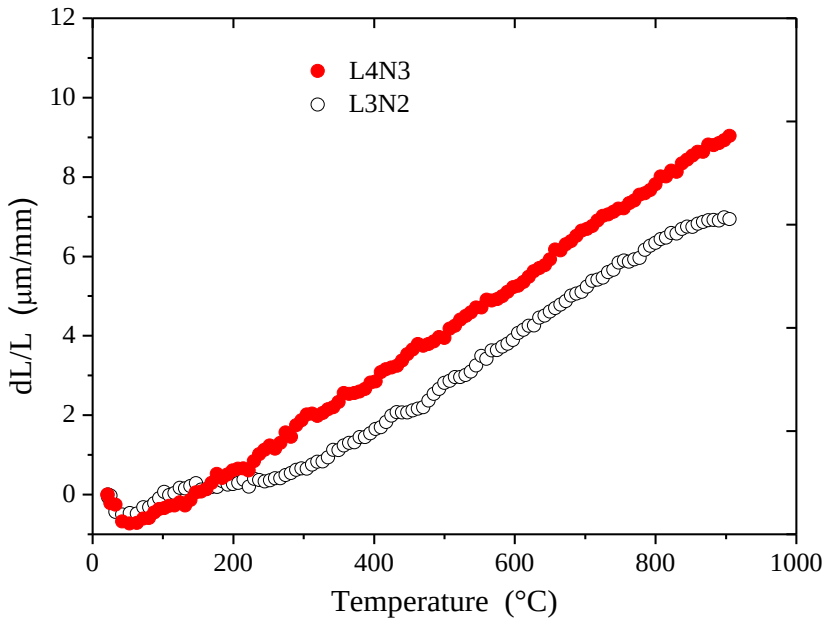

Fig. 3 Thermal expansion curve of samples measured from 25 to 900 °C under air for L3N2 and L4N3 pellets.

3.4. Microstructural characterization

The SEM images in **Fig. 4** show the surface micrographs and the cross-sectional views of the sintered screen-printed L3N2, L4N3 cathodes and of the L3N2 -CGO and L4N3-CGO composite cathodes. All the electrodes exhibit a porous microstructure which is expected to be beneficial for gaseous oxygen diffusion. Both L3N2 and L4N3 electrode are comprised of particles with well-defined flat facets. The L3N2 cathode (**Fig. 4a-4c**) displays a uniform particle size distribution (300-450 nm) and well interconnected particles. In comparison, the L4N3 cathode (**Fig. 4d-4f**) lacks interconnectivity and presents a broader distribution of particle sizes (350-800 nm) with a series of voids throughout. For the composite cathodes, it is possible to distinguish between the L3N2 (or L4N3) and the CGO particles constituting the composites. The CGO particles are rounded in shape and much smaller (100 nm) in comparison to the L3N2 and L4N3 ones, as shown in **Fig. 4h** and **Fig. 4k**, respectively. While the composite electrodes were prepared under the same conditions, the CGO and L3N2

particles are homogeneously distributed and well connected with each other (**Fig. 4h**), while for the L4N3-CGO composite both phases are not as homogeneously mixed as in the L3N2-CGO composite (**Fig. 4k**), meaning that a larger number of conduction pathways are expected in L3N2-CGO composite. The thickness of all cathodes is in between 28-34 μm as shown in **Fig. 4c, 4f, 4i, 4l**. All the electrodes are well-adhered to the electrolyte and no cracks or delamination has been observed for any of the investigated cathodes.

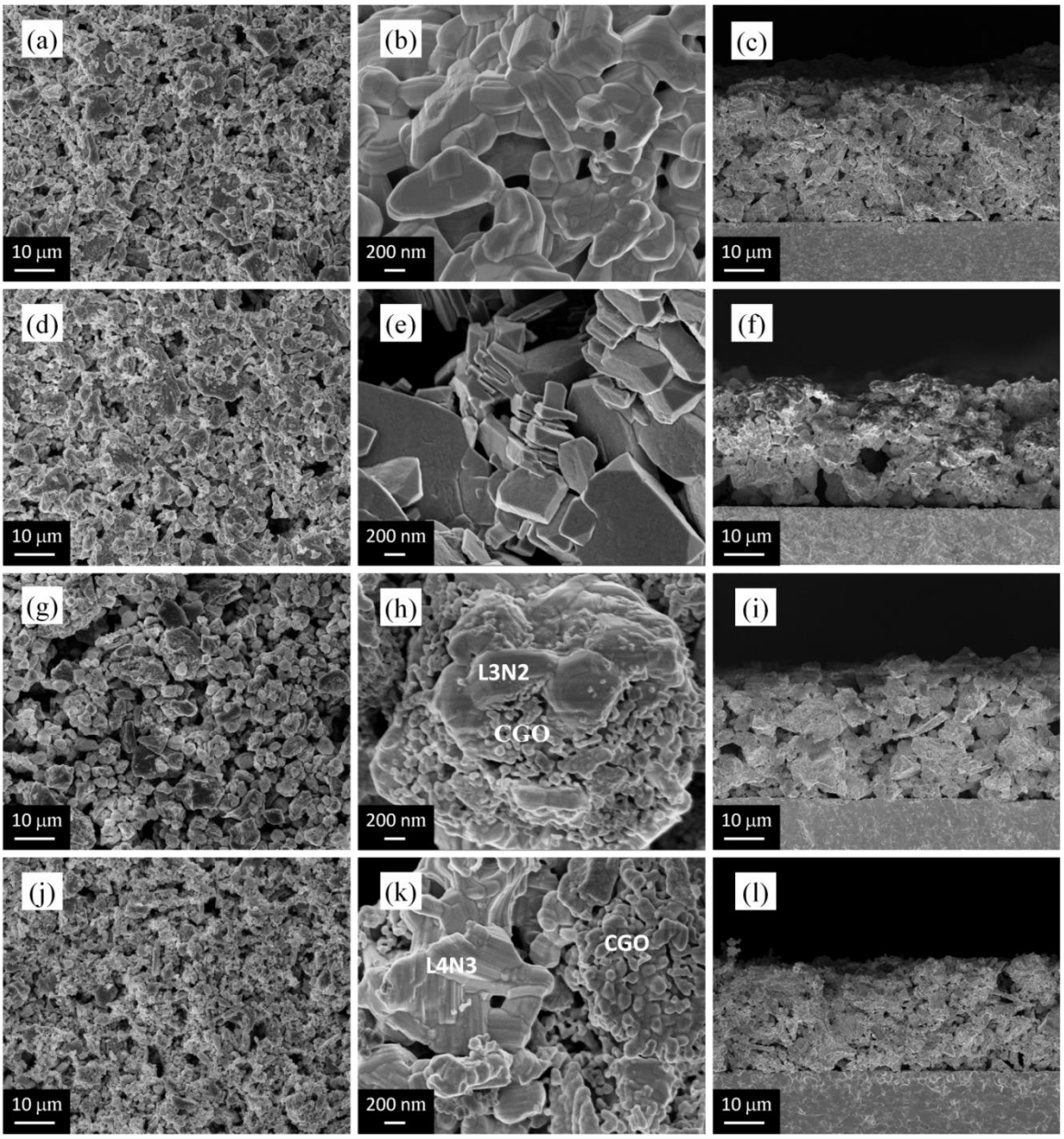

Fig. 4 SEM micrographs of the L3N2 films: a), b) surface views and c) cross section; L4N3 films: d), e) surface views and f) cross section; L3N2-CGO: g), h) surface view and i) cross section; and L4N3-CGO composites: j), k) surface views and l) cross section.

3.5. Electrode performances

For the determination of the performance of the investigated cathodes, the electrochemical impedance diagrams were fitted using an equivalent circuit consisting of an inductive element (L_1) in series with a resistance R_s and successive R//CPE elements connected in series, as shown in **Fig. 5**. Since the ideal response of a capacitor is rarely observed in operating conditions, the capacitors have been replaced by Constant Phase Elements (CPE). As an example the characteristic experimental and fitted impedance diagrams recorded at 600 °C for the 4 different cathode compositions are shown in **Fig. 6**.

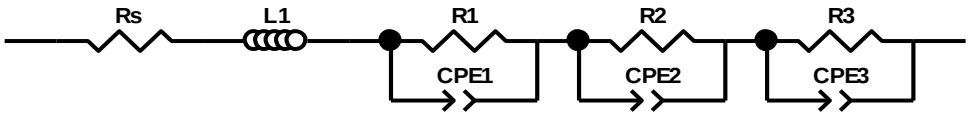

Fig. 5 Equivalent circuit used for the fitting of the electrochemical impedance diagrams.

According to the chosen analysis, the impedance diagrams of L3N2 could be resolved into two arcs, whatever the temperature is, (corresponding to the high and medium frequency ranges and labelled as 1 and 2, respectively) whereas the impedance diagrams of the L3N2-CGO cathode could be separated into three arcs, including an additional low frequency contribution (labelled as 3), whatever the temperature is. The polarization resistance (R_{pol}) of a given cathode is the sum of the elementary electrode resistances R_1, R_2 and R_3. For both the L4N3 and the L4N3-CGO composite cathodes, three arcs can be systematically identified in the chosen experimental conditions. The high frequency arc (referred to as 1) is usually attributed to the charge transfer at the electrode/electrolyte interface [47, 48] while the medium frequency one (referred to as 2) can be associated with various electrode processes such as adsorption of O_2, dissociation of O_2 and charge transfer-diffusion (O^{2-}) in the electrode. As shown in **Fig. 6c** and **6d**, a small third contribution at very low frequencies (referred to as 3), appears at temperatures higher than 600 °C and its magnitude barely varies with the measuring temperature. This contribution is characterized by high capacitance values: ≈ 2.4 F cm^{-2} for L3N2-CGO and ≈ 1.2 F cm^{-2} for the L4N3-CGO cathode, respectively. Such a response can be assigned to the O_2 gas diffusion through the porous electrode [49, 50]. On the contrary, the magnitude of the low frequency contribution for the L4N3 cathode (**Fig. 6b**) is temperature-dependent with similar capacitance values of the order of ≈ 10^{-1} F cm^{-2} till 650 °C. At 700°C, the magnitude of this capacitance is larger, ≈ 1.6 F cm^{-}

^{2}. At this stage, its interpretation becomes complex and requires additional experiments. It is worth mentioning that the frequency distribution of the electrode impedance is not modified by adding CGO (**Fig. 6**). This indicates that the whole electrode reaction mechanism remains nearly identical for a pure and the corresponding composite cathodes. The low frequency contribution (referred to as 3) in the L3N2-CGO response appears due to the strong enhancement of the electrode reaction rate for composite cathodes. The polarization resistance of L3N2-CGO electrode is 27 times lower than for L3N2at 600 °C (**Table 3**).

At 700 °C, R_{pol} is of 1.0 and 1.5 Ω cm^2 for the L3N2 and L4N3 electrodes, respectively. The polarization resistance of L3N2 is close to that reported by Lou et al. [28] for a screen-printed cathode on YSZ electrolyte (0.97 Ω cm^2 at 700 °C). The R_{pol} value of the L4N3 cathode is significantly lower than that of a brush-coated electrode on a LSGM electrolyte (14.4 Ω cm^2 at 700 °C) [8], but higher than that reported by Lou et al. [29] for L4N3 screen-printed on YSZ (0.53 Ω cm^2 at 700 °C). However, attention should be paid when making a direct comparison of different porous cathodes. Even the same compositions prepared by different methods can significantly vary due to differences on the starting materials and fabrication processes and thus to differences in the corresponding microstructures [51].

Despite the fact that the electric conductivity of L4N3 [29] is reported to be higher than that of L3N2 [28], we have observed that the polarization resistance of the L4N3 electrode is higher in comparison to L3N2 in the measured temperature range (**Fig. 7**). Constriction effect of the current lines in L4N3 electrode is expected to be lower than in the L3N2 electrode because of its higher electrical conductivity reported in the literature. As a consequence, a higher effective active volume should be expected in the electrode reaction for L4N3 and hence should lead to a lower polarization resistance. But this is not the case. Therefore, this indicates that the electronic conductivity of the electrode material is not the limiting factor in the cathode reaction and probably microstructural properties have to be taken into account. Hence the lower R_{pol} value of L3N2 is likely to be due to a smaller particle size in comparison to that of L4N3 (**Fig. 4**), increasing the effective active area for the oxygen reduction. Moreover, the L4N3 electrode exhibits a broad distribution of particle sizes with a series of voids throughout, which yields a lower interconnectivity between particles and thus to less conduction pathways in comparison with the L3N2 cathode (**Fig. 4e** and **Fig. 4b**).

A large improvement in performance has been observed when CGO is added to both the L3N2 and L4N3 cathodes (**Fig. 7**). At 600 °C, R_{pol} decreases by a factor of 27 for the L3N2-CGO electrode and by a factor of 2.3 for L4N3-CGO compared to the single L3N2 and L4N3 electrodes (**Table 3**). Such improvement is due to a significant enhancement of the effective ionic conductivity of the electrode. In fact the addition of CGO to the electrode is expected to break the interconnectivity of the electrode particles and hence to increase the solid phase tortuosity. But the electrical performances are not degraded even if a lower effective electronic conductivity of the electrode material is expected. Indeed, the number of TPB sites for the oxygen reduction is increased in the volume of the electrode when adding CGO. Then, the active surface area of the electrode is enlarged. In addition, in the L3N2-CGO composite, L3N2 and CGO are homogeneously mixed as seen in **Fig. 4** and display a good interconnectivity. One can expect a greater number of conduction pathways in this composite in comparison to pure L3N2 as well as in L4N3 and the L4N3-CGO composite cathode. As a consequence of a larger TPB density, the efficiency of an effective surface area for the oxygen reduction is enhanced for this composite electrode. This is also clearly evidenced by the decrease of both resistances R_1 and R_2 which have been attributed to the resistances of the electrode/electrolyte charge transfer and the one of the electrode reaction (**Table 3**).

Table 3. Electrode composition, total and elementary polarization resistances (at 600 °C) and activation energy of the polarization resistance for L3N2 and L4N3 cathodes and their corresponding composite electrodes

Samples	Rpol [Ω cm^2]	R_1 [Ω cm^2]	R_2 [Ω cm^2]	R_3 [Ω cm^2]	Ea [eV]
L3N2	3.59	1.13	2.46	----	0.97
L3N2-CGO	0.13	0.04	0.08	0.02	1.06
L4N3	6.17	2.33	3.38	0.46	1.37
L4N3-CGO	2.67	0.95	1.69	0.03	1.25

However, the microstructure of the L4N3-CGO composite is less ideal since the CGO and L4N3 particle distributions and interconnectivity could be improved. As shown in **Fig. 4k**, L4N3 and CGO are not mixed randomly but separated in blocks. Therefore, according to **Fig.**

4, one can expect a lesser TPB density in the L4N3-CGO composite in comparison to L3N2-CGO composite. The small decrease in the polarization resistance for the L4N3-CGO electrode obtained when adding CGO (**Fig. 6**) supports this assumption. As the value of the low frequency contribution (R_3), is two times larger for L4N3-CGO than for L3N2-CGO, an improvement of the performance can also be expected by improving the homogeneity in particle size and porosity of the electrode material (**Fig. 4**). In comparison to the literature, the polarization resistance obtained for the L3N2-CGO composite electrode (0.03 Ω cm^2 at 700 °C) is much lower than that reported (0.112 Ω cm^2 at 750 °C) by Choi et al. [13] for an infiltrated L3N2-YSZ composite on YSZ electrolyte, whereas the L4N3-CGO composite electrode does not show such a good performance (0.52 Ω cm^2 at 700 °C) as the L4N3-YSZ electrode prepared by infiltration on a YSZ electrolyte (0.13 Ω cm^2 at 700 °C) reported by Kim et al. [52]. As the R_2 values were always larger than R_1 over the temperature range 500-750 °C, interface processes such as oxygen adsorption and diffusion on the cathode surface, as well as oxygen$^-$ diffusion in the cathode bulk can be regarded as the rate-determining steps for the oxygen reduction reaction [53, 54].

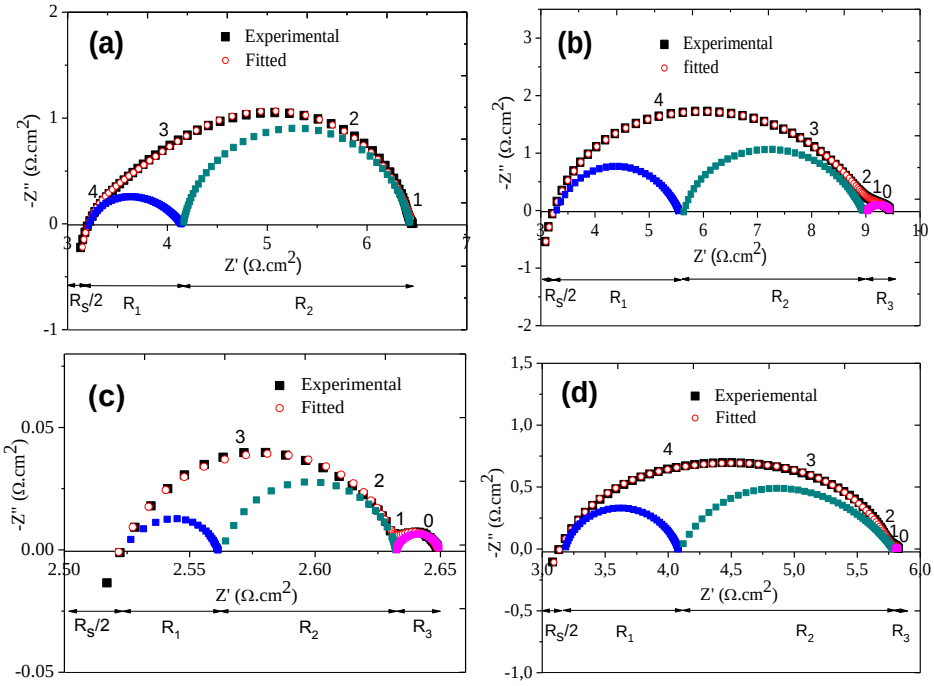

Fig. 6 Typical experimental and fitted impedance diagrams at 600 °C in air; a) L3N2; b) L4N3; c) L3N2-CGO; d) L4N3-CGO.

For all the investigated cathodes, the activation energy values E_a (**Table 3**), determined from the Arrhenius diagrams of R_{pol} (**Fig. 7**), are in rather good agreement with literature data [28, 29]. The introduction of CGO does not significantly modify these values, suggesting that the limiting electrode reaction mechanism remains similar.

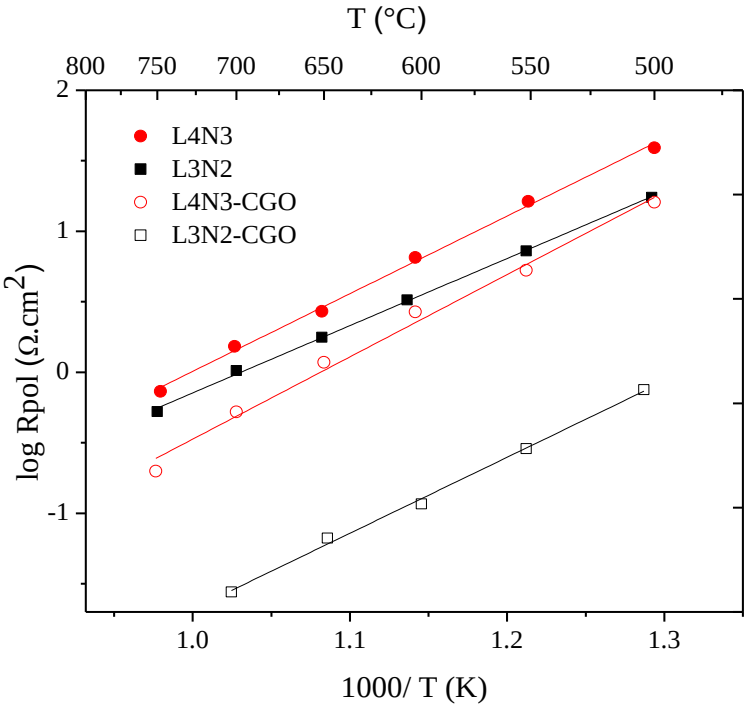

Fig.7 Arrhenius plot of the polarization resistance in air from 500 to 750 ºC for the four cathode investigated compositions

3.6. Chemical stability and compatibility with CGO

The L3N2-CGO composite has been selected to investigate the long-term chemical stability and compatibility with CGO because it presents the best electrochemical performance among all samples. For this purpose, X-ray diffraction of the composite was recorded after a heat treatment at 900 °C for 2 weeks in air. The XRD patterns of the as prepared CGO-L3N2 composite and after the long heat treatment are shown in **Fig. 8**. Nicely, the presence of only the L3N2 and the CGO phases coming from the composite and the substrate are observed both before and after the heat treatment. Possible additional peaks corresponding to reactivity between CGO and L3N2 or decomposition of L3N2 into new phases have not been observed after the heat treatment within the detection limit of XRD. However, as a consequence of reactivity between L3N2 and CGO, an amorphous phase or

secondary phases in regions at the nanometer scale may be present. One can assume that no amorphisation has been detected since the intensity of the XRD peaks remains similar before and after anneal (**Fig. 8**).

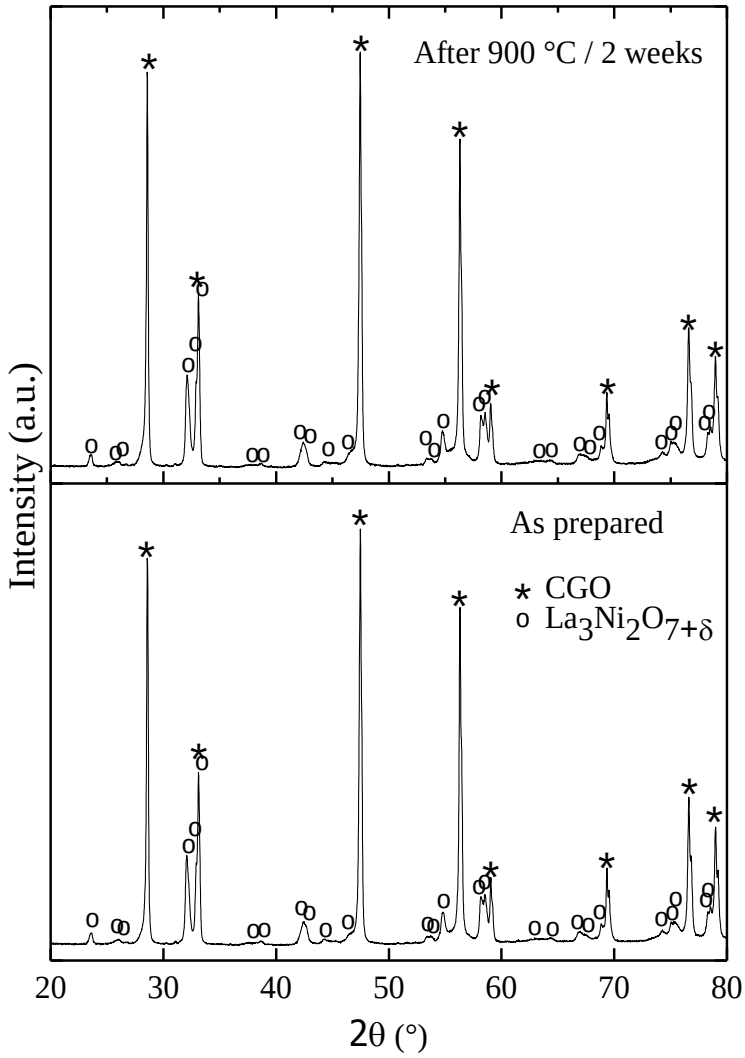

Fig. 8 XRD patterns of the L3N2-CGO composite film prepared by SP on a CGO electrolyte before and after a heat treatment of 2 weeks duration at 900 °C in air.

However, A. Montenegro-Hernández et al. [55] have reported the amorphous material formation at the interface and surrounding the cathode by analyzing the La_2NiO_4/CGO interface by FEG TEM and EDS. Therefore, a further detailed investigation into long-term stability has to be carried out for L3N2-CGO composite cathode. Our results are in good agreement with those of Amow et al. [8] who have shown no impurity formation by XRD

when L3N2 was heated at 900 °C for 2 weeks in air in contrast to previously reported data for $La_2NiO_{4+\delta}$ [56, 57]. This can be explained by the increased Ni^{3+} content in L3N2 compared to $La_2NiO_{4+\delta}$, which is more stable in air at lower temperatures. Therefore, in addition to the promising cathode performance, L3N2-CGO composite also shows long-term chemical stability and compatibility with a CGO, which makes this composite a promising cathode for IT-SOFC.

4. Conclusions

Single phase high-order RP phases, $La_3Ni_2O_{7+\delta}$ and $La_4Ni_3O_{10-\delta}$, were prepared for the first time by a modified citrate–nitrate route using citric acid as the chelating agent and ethanol as the solvent. This modified route has proved to be a facile and direct synthesis method. L3N2 is found to be slightly over stoichiometric ($\delta = 0.05$) whereas L4N3 is slightly oxygen deficient ($\delta = 0.06$). Dilatometric measurements reveal that the TECs of L3N2 (11.0×10^{-6} K^{-1}) and L4N3 (11.5×10^{-6} K^{-1}) match well that of CGO (12.2×10^{-6} K^{-1}). To evaluate these materials and based composites as cathodes for IT-SOFCs, L3N2, L4N3, L3N2-CGO and L4N3-CGO oxide-based symmetrical cells were prepared and electrochemically measured. L3N2 and L4N3 cathodes present typical R_{pol} values of 1.0 and 1.5 Ω cm^2 at 700 °C, respectively. An addition of CGO drastically reduces the R_{pol} value, especially in the case of L3N2 matrix (0.03 against 0.52 Ω cm^2 at 700 °C). Moreover, the L3N2-CGO composite cathode is chemically stable and no chemical reactivity between L3N2 and CGO has been observed after a heat treatment at 900 °C in air for 2 weeks. These preliminary results suggest that L3N2-CGO composite prepared from the facile proposed method is a promising cathode material for IT-SOFCs. Hence this new modified citrate–nitrate preparation method seems to be very versatile for the synthesis of higher order lanthanum nickelate based RP phases for IT-SOFC cathodes.

Acknowledgements

This work was performed within the framework of the Centre of Excellence of Multifunctional Architectured Materials "CEMAM" n° AN-10-LABX-44-01.

References:

[1] A. Aguadero, L. Fawcett, S. Taub, R. Woolley, K.-T. Wu, N. Xu, S. J. Skinner, Materials development for intermediate-temperature solid oxide electrochemical devices, Journal of Materials Science 47 (2012) 3925-3948.
[2] J. A. Kilner, M. Burriel, Materials for intermediate-temperature solid-oxide fuel cells, Annual Review of Materials Research 44 (2014) 365-393.
[3] A.Orera, P. R. Slater, New Chemical Systems for Solid Oxide Fuel Cells, Chemistry of Materials 22 (2010) 675-690.
[4] A. J. Jacobson, Materials for solid oxide fuel cells, Chemistry of Materials 22 (2010) 660-674.
[5] A.Tarancón, M. Burriel, J. Santiso, S. J. Skinner, J.A. Kilner, Advances in layered oxide cathodes for intermediate temperature solid oxide fuel cells, Journal of Materials Chemistry 20 (2010) 3799-3813.
[6] S. Chaianansutcharit, K. Hosoi, J. Hyodo, Y.-W. Ju, T. Ishihara, Ruddlesden Popper oxides of $LnSr_3Fe_3O_{10-\delta}$ (Ln = La, Pr, Nd, Sm, Eu, and Gd) as active cathodes for low temperature solid oxide fuel cells, J. Mater. Chem. A 23 (2015) 12357-12366.
[7] J.A. Kilner, C.K.M. Shaw, Mass transport in $La_2Ni_{1-x}Co_xO_{4+\delta}$ oxides with the K_2NiF_4 structure, Solid State Ionics 154 (2002) 523-527.
[8] G. Amow, I.J. Davidson, S.J. Skinner, A comparative study of the Ruddlesden-Popper series, $La_{n+1}Ni_nO_{3n+1}$ (n = 1, 2 and 3), for solid-oxide fuel-cell cathode applications, Solid State Ionics 177 (2006) 1205-1210.
[9] S. Takahashi, S. Nishimoto, M. Matsuda, M Miyake, Electrode properties of the Ruddlesden–Popper Series, $La_{n+1}Ni_nO_{3n+1}$ (n= 1, 2, and 3), as intermediate-temperature solid oxide fuel cells, J Am Ceram Soc. 93 (2010) 2329-2333.
[10] M. Burriel, G. Garcia, M. Rossell, A. Figueras, G. Van Tendeloo, J. Santiso, Enhanced high-temperature electronic transport properties in nanostructured epitaxial thin films of the $La_{n+1}Ni_nO_{3n+1}$ Ruddlesden−Popper series (n = 1, 2, 3, ∞), Chem. Mater. 19 (2007) 4056-4062.
[11] S. J. Skinner, J. A. Kilner, Oxygen diffusion and surface exchange in $La_{2-x}Sr_xNiO_{4+\delta}$, Solid State Ionics 135 (2000) 709-712.
[12] J. Wan, J. B. Goodenough, J. H. Zhu, $Nd_{2-x}La_xNiO_{4+\delta}$, A mixed ionic/electronic conductor with interstitial oxygen, as a cathode material, Solid State Ionics 178 (2007) 281-286.
[13] S. Choi, S. Yoo, J.-Y. Shin, G. Kim, High Performance SOFC Cathode Prepared by Infiltration of $La_{n+1}Ni_nO_{3n+1}$ (n = 1, 2, and 3) in Porous YSZ, Journal of the Electrochemical Society 158 (2011) B995-B999.
[14] P.J. Lacorre, Passage from T-type to T′-type arrangement by reducing $R_4Ni_3O_{10}$ to $R_4Ni_3O_8$ (R = La, Pr, Nd), J. Solid State Chem. 97 (1992) 495-500.

[15] J.C. Park, D.K. Kim, S. H. Byeon, D. Kim, XANES study on Ruddlesden-Popper phase, $La_{n+1}Ni_nO_{3n+1}$ (n = 1, 2, and ∞), J. Synchrotron Radiation 8 (2001) 704-706.
[16] M.D. Carvalho, F.M.A. Costa, I.D. Pereira, A. Wattiaux, J.M. Bassat, J.C. Grenier, M. Pouchard, New preparation method of $La_{n+1}Ni_nO_{3n+1-\delta}$ (n=2, 3), J. Mater. Chem. 7 (1997) 2107.

[17] G. Amow, S.J. Skinner, Recent developments in Ruddlesden–Popper nickelate systems for solid oxide fuel cell cathodes, J. Solid State Electrochem. 10 (2006) 538-546.
[18] M.J. Jørgensen, S. Primdahl, C. Bagger, M. Mogensen, Effect of sintering temperature on microstructure and performance of LSM–YSZ composite cathodes, Solid State Ionics 139 (2001) 1-11.
[19] J.-D. Kim, G.-D. Kim, J.-W. Moon, Y.-I. Park, H.-W. Lee, K. Kobayashi, M. Nagai, C.-E. Kim, Characterization of LSM-YSZ composite electrode by ac impedance spectroscopy, Solid State Ionics 143 (2001) 379-389.
[20] C. Zhu, X. Liu, D. Xu, D. Wang, D. Yan, L. Pei, T. Lü, W. Su, Electrochemical performance of $Pr_{0.7}Sr_{0.3}Co_{0.9}Cu_{0.1}O_{3-\delta}$–$Ce_{0.8}Sm_{0.2}O_{1.9}$ composite cathodes in intermediate-temperature solid oxide fuel cells**,** J. Power Sources 185 (2008) 212-216.
[21] Y. Lin, S.A. Barnett, $La_{0.9}Sr_{0.1}Ga_{0.8}Mg_{0.2}O_{3-\delta}$-$La_{0.6}Sr_{0.4}Co_{0.2}Fe_{0.8}O_{3-\theta}$ composite cathodes for intermediate-temperature solid oxide fuel cells, Solid State Ionics 179 (2008) 420-427.
[22] B. Liu, Y. Zhang, L. Zhang, Characteristics of $Ba_{0.5}Sr_{0.5}Co_{0.8}Fe_{0.2}O_{3-\delta}$–$La_{0.9}Sr_{0.1}Ga_{0.8}Mg_{0.2}O_{3-\delta}$ composite cathode for solid oxide fuel cell, J. Power Sources 175 (2008) 189-195.
[23] J. Harris, C. Metcalfe, M. Marr, J. Kuhn, O. Kesler, Fabrication and characterization of solid oxide fuel cell cathodes made from nano-structured LSCF-SDC composite feedstock, Journal of Power Sources 239 (2013) 234-243.
[24] S. Lee, H. S. Song, S. H. Hyun, J. Kim, J. Moon, LSCF-SDC core-shell high-performance durable composite cathode, Journal of Power Sources 195(1) (2010) 118-123.
[25] J.H. Kim, H. Kim, $Ce_{0.9}Gd_{0.1}O_{1.95}$ supported $La_{0.6}Sr_{0.4}Co_{0.2}Fe_{0.8}O_{3-\delta}$ cathodes for solid oxide fuel cells, Ceramics International 38 (2012) 4669-4675.
[26] Y. Leng, S. H. Chan, Q. Liu, Development of LSCF–GDC composite cathodes for low-temperature solid oxide fuel cells with thin film GDC electrolyte, Int. J. Hydrogen Energy 33 (2008) 3808-3817.
[27] V. Vibhu, A. Rougier, C. Nicollet, A. Flura, J.-C. Grenier, J.-M. Bassat, $La_{2-x}Pr_xNiO_{4+\delta}$ as suitable cathodes for metal supported SOFCs, Solid State Ionics 278 (2015) 32–37.
[28] Z. Lou, J. Peng, N. Dai, J. Qiao, Y. Yan, Z. Wang, J. Wang, K. Sun, High performance $La_3Ni_2O_7$ cathode prepared by a facile sol–gel method for intermediate temperature solid oxide fuel cells, Electrochemistry Communications 22 (2012) 97-100.
[29] Z. Lou, N. Dai, Z. Wang, Y. Dai , Y. Yan, J. Qiao, J. Peng, J. Wang, K. Sun, Preparation and electrochemical characterization of Ruddlesden–Popper oxide $La_4Ni_3O_{10}$ cathode for IT-SOFCs by sol–gel method, J Solid State Electrochem 17 (2013) 2703-2709.
[30] R.J. Woolley, S. J. Skinner, Novel $La_2NiO_{4+\delta}$ and $La_4Ni_3O_{10-\delta}$ composites for solid oxide fuel cell cathodes, Journal of Power Sources, 243 (2013) 790–795.
[31] G. Amow, J. Au, I. Davidson, Synthesis and characterization of $La_4Ni_{3-x}Co_xO_{10\pm\delta}$ ($0.0 \leq x \leq 3.0$, $\Delta x = 0.2$) for solid oxide fuel cell cathodes, Solid State Ionics 177 (2006) 1837-1841.
[32] A. Aguadero, J.A. Alonso, M.J. Martinez-Lope, M.T. Fernandez-Diaz, M.J. Escudero, L. Daza, In situ high temperature neutron powder diffraction study of oxygen-rich $La_2NiO_{4+\delta}$ in air: correlation with the electrical behavior, J. Mater. Chem. 16 (2006) 3402-3408.

[33] Z. Zhang, M. Greenblatt, J.B. Goodenough, Synthesis, structure, and properties of the layered perovskite $La_3Ni_2O_{7-\delta}$, Journal of Solid State Chemistry 108 (1994) 402-409.
[34] X.L. Weng, P. Boldrin, I. Abrahams, S.J. Skinner, J.A. Darr, Direct Syntheses of Mixed Ion and Electronic Conductors $La_4Ni_3O_{10}$ and $La_3Ni_2O_7$ from Nanosized coprecipitates, chemistry of materials 19 (2007) 4382-4384.
[35] C.D. Ling, D.N. Argyriou, G. Wu, J.J. Neumeier, Neutron Diffraction Study of $La_3Ni_2O_7$: structural relationships among n =1, 2, and 3 phases $La_{n+1}Ni_nO_{3n+1}$, J. Solid State Chem. 152 (2000) 517-525.
[36] Z. Zhang, M. Greenblatt, Synthesis, structure, and properties of $Ln_4Ni_3O_{10-\delta}$ (Ln = La, Pr, and Nd), J. Solid State Chem. 117 (1995) 236-246.
[37] L.J. Cote, A.S. Teja, A.P. Wilkinson, Z.J. Zhang, Continuous hydrothermal synthesis of $CoFe_2O_4$ nanoparticles, Fluid Phase Equilibr. 210 (2003) 307-317.
[38] J. Lee, A.S. Teja, Characteristics of lithium iron phosphate ($LiFePO_4$) particles synthesized in subcritical and supercritical water, J. Supercrit. Fluid. 35 (2005) 83-90.
[39] K.-T. Wu, H. Tellez, J. Druce, M. Burriel, T. Ishihara, J. A. Kilner, S. J Skinner, Surface composition of layered Ruddlesden-Popper $La_{n+1}Ni_nO_{3n+1}$ (n = 1, 2 and 3) epitaxial films, ECS Transactions 66 (2015) 89-93.
[40] N. Millot, B. Xin, C. Pighini, D. Aymes, Hydrothermal synthesis of nanostructured inorganic powders by a continuous process under supercritical conditions, J. Eur. Ceram. Soc. 25 (2005) 2013-2016.
[41] L.A. Bendersky, M. Greenblatt, R. Chen, Transmission electron microscopy study of Ruddlesden–Popper $Ca_{n+1}Mn_nO_{3n+1}$ n =2 and 3 compounds, J. Solid State Chem. 174 (2003) 418-423.
[42] J. Rodriguez-Carvajal, Recent advances in magnetic structure determination by neutron powder diffraction, Physica B 192 (1993) 55-69.
[43] P.D. Yang, D.Y. Zhao, D.I. Margolese, B.F. Chmelka, G. D. Stucky, Generalized syntheses of large-pore mesoporous metal oxides with semicrystalline frameworks, Nature 396 (1998) 152-155.
[44] J. Ding, J. Chen, Synthesis of Cu–Zn–Zr–Al–O catalysts via a citrate complex route modified by different solvents and their dehydrogenation/hydrogenation performance, RSC Adv. 5 (2015) 82822-82833.
[45] L. Rayleigh, On the equilibrium of liquid conducting masses charged with electricit, Philosophical Magazine Series 5 14(1882) 184-186.
[46] V. V. Poltavets, K. A. Lokshin, T. Egami, M. Greenblatt, The oxygen deficient Ruddlesden–Popper $La_3Ni_2O_{7-\delta}$ ($\delta = 0.65$) phase: Structure and properties, Materials Research Bulletin 41 (2006) 955-960.
[47] C. Fu, K. Sun, N. Zhang, X. Chen, D. Zhou, Electrochemical characteristics of LSCF–SDC composite cathode for intermediate temperature SOFC, Electrochim. Acta 52 (2007) 4589-4594.
[48] M.J. Escudero, A. Aguadero, J.A. Alonso, L. Daza, A kinetic study of oxygen reduction reaction on La_2NiO_4 cathodes by means of impedance spectroscopy, J. Electroanal. Chem. 611 (2007) 107-116.

[49] L. Mogni, N. Grunbaum, F. Prado, A. Caneiro, Oxygen Reduction Reaction on Ruddlesden–Popper Phases Studied by Impedance Spectroscopy, J. Electrochem. Soc. 158 (2011) B202-B207.
[50] S. Pang, X. Jiang, X. Li, Q. Wang, Z. Su, Characterization of Ba-deficient $PrBa_{1-x}Co_2O_{5+\delta}$ as cathode material for intermediate temperature solid oxide fuel cells, J. Power Sources 204 (2012) 53-59.
[51] N. Hildebrand, P. Nammensma, D.H.A. Blank, H.J.M. Bouwmeester, B.A. Boukamp, Influence of configuration and microstructure on performance of $La_2NiO_{4+\delta}$ intermediate-temperature solid oxide fuel cells cathodes, J. Power Sources 238 (2013) 442-453.
[52] S. Kim, S. Choi, A. Jun, J. Shin, G. Kim, Scale-Down and Sr-Doping Effects on $La_4Ni_3O_{10-\delta}$–YSZ Nanocomposite Cathodes for IT-SOFCs, Journal of The Electrochemical Society 161 (2014) F1468-F1473.
[53] Z. Lou, J. Qiao, Y. Yan, J. Peng, Z. Wang, T. Jiang, Synthesis and characterization of aluminum-doped perovskites as cathode materials for intermediate temperature solid oxide fuel cells, International Journal of Hydrogen Energy 37 (2012) 11345-11350.
[54] H. Gu, H. Chen, L. Gao, L. Guo, Electrochemical properties of $LaBaCo_2O_{5+\delta}$–$Sm_{0.2}Ce_{0.8}O_{1.9}$ composite cathodes for intermediate-temperature solid oxide fuel cells, Electrochimica Acta 54 (2009) 7094-7098.
[55] A. Montenegro-Hernández, A. Soldati, L. Mogni, H. Troiani, A. Schreiber, F. Soldera, A. Caneiro, Reactivity at the $Ln_2NiO_{4+\delta}$/electrolyte interface (Ln = La, Nd) studied by Electrochemical Impedance Spectroscopy and Transmission Electron Microscopy, Journal of Power Sources 265 (2014) 6–13.
[56] G. Amow, P.S. Whitfield, I.J. Davidson, R.P. Hammond, C.N. Munnings, S.J. Skinner, Structural and sintering characteristics of the $La_2Ni_{1-x}Co_xO_{4+\delta}$ series, Ceramics International 30 (2004) 1635–9.
[57] R. Sayers, J. Liu, B. Rustumji, S.J. Skinner, Novel K_2NiF_4-type materials for solid oxide fuel cells: compatibility with electrolytes in the intermediate temperature range, Fuel Cells 8 (2008) 338–43.

Supporting Information

XRD patterns of the screen-printed L3N2-CGO and L4N3-CGO composite films deposited on a CGO substrate after calcination in air at 1000 °C/1 h + 1050 °C /1 h.

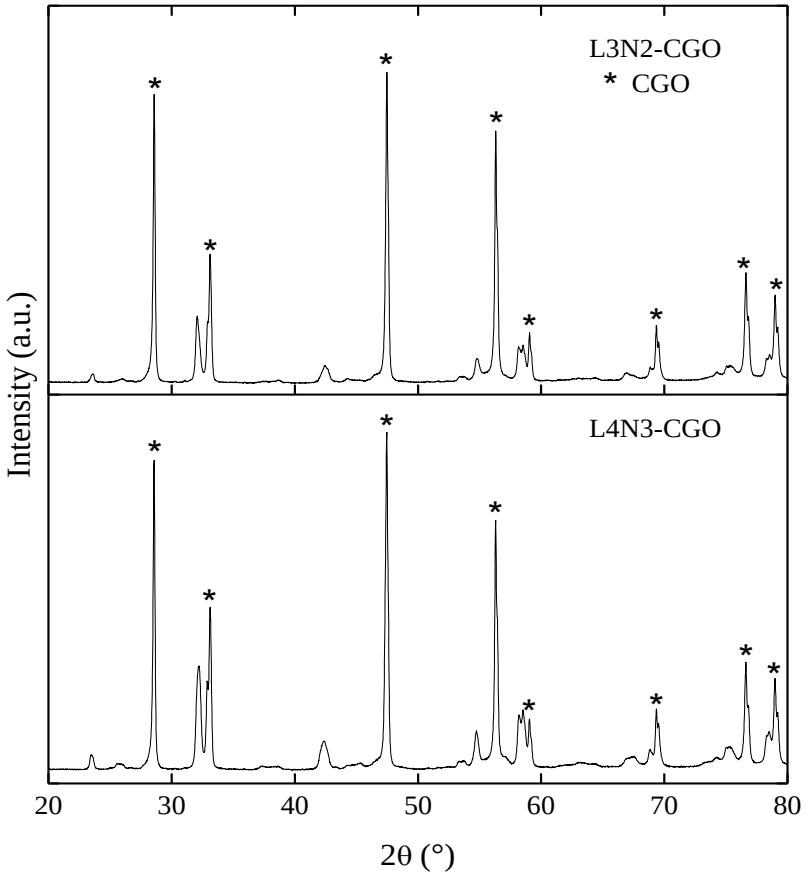

Fig. S1 XRD patterns of the screen-printed L3N2-CGO and L4N3-CGO composite films deposited on a CGO substrate after calcination in airat 1000 °C/1 h + 1050 °C /1 h (the remaining peaks correspond to the L3N2 and L4N3 phases).

Conclusions and perspectives

This PhD work was focused on the fabrication of new oxygen electrode materials on $Ce_{0.9}Gd_{0.1}O_{2-\delta}$ (CGO) electrolyte for IT-SOFC applications, with special emphasis on the optimization of the microstructure, architecture and composition of layered Ruddlesden-Popper (RP) type materials based on $La_{2-x}Pr_xNiO_{4+\delta}$, $0 \leq x \leq 2$ and $La_{n+1}Ni_nO_{3n+1}$ (n=2 and 3). CGO has been added to take advantage of its high ionic conductivity, particularly (i) in the $La_{n+1}Ni_nO_{3n+1}$ (n =2 and 3) electrodes forming composites and (ii) at the $Ln_2NiO_{4+\delta}$ (Ln = La, Pr) electrode/electrolyte interface, forming a dense interlayer.

Conclusions

The first objective of this work was to fabricate original porous coral-type $La_2NiO_{4+\delta}$ (LNO) films on CGO substrates by varying the ESD (electrostatic spray deposition) parameters: both the technical ones (nozzle-to substrate distance, the precursor solution flow rate and the substrate temperature) and the physico-chemical parameters of the precursor solution (surface tension, viscosity, boiling point and conductivity). Highly porous (84 ± 2 vol. %) $La_2NiO_{4+\delta}$ films were successfully and reproducibly deposited by ESD with the following optimized parameters: nozzle-to substrate distance, substrate temperature, precursor solution flow rate and deposition time of 50 mm, 350 °C, 1.5 mL h^{-1} and 3 h, respectively. A calcination step at only 950 °C for 6 h in air was sufficient for the crystallization of the films (20 μm thick) (in a pure orthorhombic structural type) with fine particle sizes (100-150 nm) and a good adhesion on CGO.

Different architectural designs based on ESD and SP (Screen-Printing) depositions were investigated by EIS (electrochemical impedance spectroscopy). The aim was to improve the electrochemical properties of the LNO cathode at moderate temperature, maintaining the percolation, the cathode/electrolyte interface adhesion and the contact between the cathode and the current collecting grid, to avoid current constriction issues. It can be noticed that the LNO thin and dense sub-layer (~100 nm) and the LNO « coral »-type layer were deposited by ESD in a single step. This thin dense contact has been proved to enhance the oxygen ion transfer to the electrolyte. When these LNO films deposited by ESD were topped by a flat SP porous LNO current collector film, a drastic reduction of the polarization resistance value, R_{pol}, from 1.26 to 0.08 Ω cm^2 at 700 °C, was obtained, which to the best of our knowledge is the lowest value reported in the literature so far for a pure $La_2NiO_{4+\delta}$ cathode. This substantially improved electrochemical performance is related to a decrease of both the ohmic and polarization resistances due to an improved electric contact between the cathode and the

current collector. Moreover, the $La_2NiO_{4+\delta}$ films are chemically stable and no reactivity has been observed between them and the CGO electrolyte after a heat treatment at 800 °C in air for 30 days.

The second objective was to fabricate and study the double-layered $La_{2-x}Pr_xNiO_{4+\delta}$ cathodes (with x = 0, 0.5, 1 and 2) on a CGO electrolyte with a view to take advantage of the complementary properties of the two extreme compositions, i.e. superior stability of $La_2NiO_{4+\delta}$ and higher electronic and ionic conductivity of $Pr_2NiO_{4+\delta}$. In other words the second objective was to improve the electrochemical properties of Pr doped LNO by enhancing its MIEC and transport properties despite its chemical instability. Original "3-D" coral $La_{2-x}Pr_xNiO_{4+\delta}$ (x = 0, 0.5, 1 and 2) films (~ 20 μm thick, porosity ~ 84 ± 2 vol. % and average particle size ~ 150 – 200 nm) were successfully prepared by ESD on CGO substrates. A solid solution with orthorhombic structure (*Fmmm* space group) was obtained in the entire range of compositions. All films were found to be oxygen over-stoichiometric with δ value equal to 0.16, 0.18, 0.22 and 0.24 for x = 0, 0.5, 1 and 2, respectively. As expected, the chemical stability was found to decrease with increasing Pr content. However, contrary to the very few literature results currently available, $La_{2-x}Pr_xNiO_{4+\delta}$ films were found stable in air at 700 °C for 30 days up to x = 1 ($LaPrNiO_{4+\delta}$) while x = 2 ($Pr_2NiO_{4+\delta}$) decomposes mainly into Pr_6O_{11} and NiO in the same conditions. A further thermal increase up to 800 °C for either 10 and 30 days led to the decomposition of $LaPrNiO_{4+\delta}$ into $(La, Pr)_4Ni_3O_{10-\delta}$, Pr_6O_{11} and NiO. $La_{2-x}Pr_xNiO_{4+\delta}$ films with x = 0 and 0.5 remained stable at 800 °C for 30 days under air, in good agreement with other literature reports.

The symmetrical electrochemical cells incorporating $La_{2-x}Pr_xNiO_{4+\delta}$ ($0 \leq x \leq 2$) electrodes on CGO have been characterized by EIS. The R_{pol} values were found to decrease from 1.26 to 0.95, 0.68 and 0.26 Ω cm^2 at 700 °C for ESD-single layer $La_{2-x}Pr_xNiO_{4+\delta}$ films by increasing the Pr content from x = 0 to 0.5, 1 and 2, respectively. Such decrease in R_{pol} values with increasing x could be attributed to the better MIEC transport properties due to Pr substitution. A further improved R_{pol} value was obtained for double layered $La_{2-x}Pr_xNiO_{4+\delta}$ cathodes (ESD + SP) down to 0.08, 0.067, 0.037 and 0.025 Ω cm^2 for x = 0, 0.5, 1 and 2 at 700 °C, respectively. These values are the lowest ones available in the literature for each composition to the best of our knowledge.

Finally, the $LaPrNiO_{4+\delta}$ phase was quite stable cell during long term operation in a symmetrical (after 500 h at 700 °C in OCP in addition to 500 h at 600 °C under -195 mA cm^{-2}

polarization). An anode supported single cell (Ni-3YSZ/Ni-8YSZ/8YSZ/CGO) with a $LaPrNiO_{4+\delta}$ double layer cathode produced a maximum power density of 438 and 323 $mWcm^{-2}$ at 700 °C and 650 °C, respectively. A degradation rate of 20 % was obtained after 408 h at 700 °C, a quite disappointing result since this $LaPrNiO_{4+\delta}$ cathode has shown promising electrochemical performance in symmetrical half cells. Post-mortem structural characterizations would be required to understand such degradation.

The third objective was to prepare and study the microstructural-dependent electrochemical properties of the higher order $La_4Ni_3O_{10-\delta}$ phase. Porous, continuous and crack-free $La_4Ni_3O_{10-\delta}$ cathodes were successfully deposited by ESD on CGO. Pure single phase $La_4Ni_3O_{10-\delta}$ films were obtained after calcination at 950 °C for 8 h in air, crystallizing in an orthorhombic symmetry. Various microstructures, such as isolated cauliflowers, connected round agglomerates and 3-D coral-type films, have been obtained by optimizing the ESD key parameters. Longer deposition times favored the preferential landing of the aerosol droplets and particle agglomeration. By increasing the substrate temperature and the nozzle to substrate distance, continuous and porous films could be obtained. The addition of 67 vol. % of water into pure ethanol resulted in films with a 3-D coral type microstructure with a continuous, dense thin layer adjacent to the electrolyte. It has been clearly shown that the electrochemical properties of these $La_4Ni_3O_{10-\delta}$ cathodes strongly depend upon the microstructure. Thanks to an improved percolation path and a better electrolyte/electrode contact the R_{pol} value at 700 °C decreased from 74.94 to 12.78 and then to 2.21 $\Omega\ cm^2$ by changing the microstructure from isolated cauliflowers to connected round agglomerates and then to the 3-D « coral »-type microstructure. Finally, thanks to an improved current collection, the lowest R_{pol} value obtained for the double layered cathode (3-D « coral »-type film by ESD topped by a screen-printed layer of same composition) was of 0.30 $\Omega\ cm^2$ at 700 °C.

The fourth objective was to explore the electrochemical properties of a novel architecture for the $Ln_2NiO_{4+\delta}$ (LnNO; Ln = La, Pr) cathodes further by replacing the thin LnNO dense sub-layer at electrode / electrolyte interface by a thicker (~ 3 μm) and porous composite layer (CGO-LnNO). Indeed the LnNO ESD deposited layer penetrates the porous CGO layer, which had been first deposited by SP directly on the CGO electrolyte. This led to the formation of a CGO/ LnNO composite.The presence of a composite sub-layer between the electrolyte and the double layer LnNO cathodes deposited via SP and ESD procedures, respectively, is a very innovative route to significantly improve the electrochemical

performance of $Ln_2NiO_{4+\delta}$. In this work, the symmetrical LaNO SP/ LaNO ESD/ (CGO + LaNO) composite/ CGO/ (CGO + LaNO) composite/ LaNO ESD/ LaNO SP cathode displayed polarization resistances as low as 0.16 Ω cm^2 at 600 °C (0.04 Ω cm^2 at 700 °C), whereas the symmetrical PrNO SP/ PrNO ESD/ (CGO + PrNO) composite/ CGO/ (CGO + PrNO) composite/ PrNO ESD/ PrNO SP electrodes displayed polarization resistances as low as 0.04 Ω cm^2 at 600 °C (0.02 Ω cm^2 at 700 °C). These values are among the best ones reported so far for SOFC cathodes. The lowest values, obtained for these composite cathodes, are due to the higher ionic conductivity of the composites, to a larger number of active points close to electrolyte, and to a larger contact area between CGO and LnNO, which facilitate the charge transfer from the cathode to the electrolyte. In addition, the R_{pol} values for both electrodes were found to be constant at 650 °C for 15 days, further proving their suitability to be used as IT-SOFC cathodes.

According to previously reported results, the overall electrical conductivity of $La_{n+1}Ni_nO_{3n+1}$ at 500-700 °C was found to increase systematically with *n*. This is the reason why $La_{n+1}Ni_nO_{3n+1}$ samples, with n = 2 and 3, ($La_3Ni_2O_{7+\delta}$, L3N2; $La_4Ni_3O_{10-\delta}$, L4N3) have been studied and CGO has been added with a view to take advantage of their complementary properties, i.e. high ionic conductivity of CGO and high electronic conductivity of L3N2 and L4N3, as the fifth and last objective of this thesis. Both L3N2 and L4N3 phases were prepared for the first time by a modified citrate–nitrate route using citric acid as the chelating agent and ethanol as the solvent. This modified route has proved to be an efficient and direct synthesis method. L3N2 was found to be slightly over stoichiometric (δ = 0.05) whereas L4N3 was slightly oxygen deficient (δ = 0.06). Dilatometric measurements revealed that the TECs of L3N2 (11.0×10^{-6} K^{-1}) and L4N3 (11.5×10^{-6} K^{-1}) match well that of CGO (12.2×10^{-6} K^{-1}). To evaluate these materials and their based composites as cathodes for IT-SOFCs, L3N2, L4N3, L3N2-CGO and L4N3-CGO oxide-based symmetrical cells were prepared and measured by EIS. L3N2 and L4N3 cathodes present typical R_{pol} values of 1.0 and 1.5 Ω cm^2 at 700 °C, respectively. An addition of CGO drastically reduces the R_{pol} value, especially in the case of the L3N2 matrix (from 1.0 to 0.03 Ω cm^2 at 700°C). In the case of L4N3, R_{pol} value was decreased only from 1.5 to 0.52 Ω cm^2 at 700 °C when CGO was added. Moreover, the L3N2-CGO composite cathode is chemically stable and no chemical reactivity between L3N2 and CGO has been observed after a heat treatment at 900 °C in air for 2 weeks. These preliminary results suggest that the L3N2-CGO composite prepared from the facile proposed method is a promising cathode material for IT-SOFCs. Hence this new modified

citrate–nitrate preparation method seems to be very versatile for the synthesis of higher order lanthanum nickelate based RP phases for IT-SOFC cathodes.

Table 1. Polarization resistance values (R_{pol}) of various cathodes with different architectures

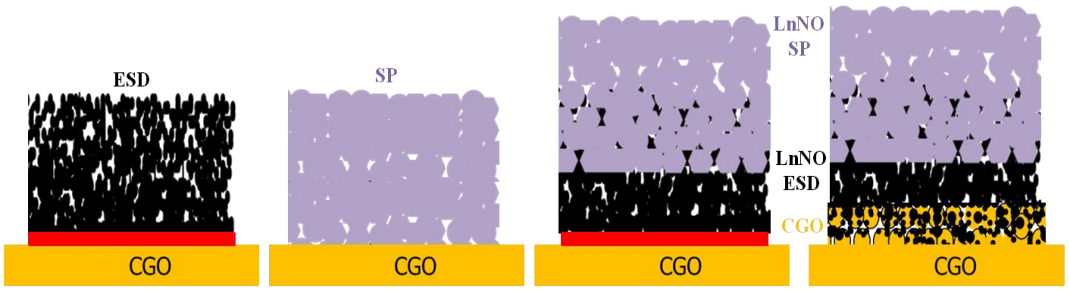

Electrode composition	Single layer (ESD)		Single layer (SP)		Double layer (ESD + SP)		Double layer (with LnNO-CGO sub-layer, Ln = La and Pr)	
	R_{pol} [Ω cm^2]	R_{pol} [Ω cm^2]	R_{pol} [Ω cm^2]	R_{pol} [Ω cm^2]	R_{pol} [Ω cm^2]	R_{pol} [Ω cm^2]	R_{pol} [Ω cm^2]	R_{pol} [Ω cm^2]
	600 °C	700 °C	600 °C	700 °C	600 °C	700 °C	600 °C	700 °C
$La_2NiO_{4+\delta}$	3.33	1.26	3.53	0.58	0.42	0.08	0.16	0.04
$La_{1.5}Pr_{0.5}NiO_{4+\delta}$	2.37	0.95	-----	-----	0.21	0.067	-----	-----
$LaPrNiO_{4+\delta}$	1.67	0.68	-----	-----	0.12	0.037	-----	-----
$Pr_2NiO_{4+\delta}$	0.83	0.26	-----	-----	0.08	0.025	0.04	0.02
$La_3Ni_2O_{7+\delta}$	-----	-----	3.59	1.00	-----	-----	-----	-----
$La_3Ni_2O_{7+\delta}$ / CGO	-----	-----	0.13	0.03	-----	-----	-----	-----
$La_4Ni_3O_{10-\delta}$	6.01	2.21	6.17	1.50	2.01	0.30	-----	-----
$La_4Ni_3O_{10-\delta}$ / CGO	-----	-----	2.67	0.53	-----	-----	-----	-----

The polarization resistance values (R_{pol}) of the various nickelate cathodes with different architectures, studied in this work, are summarized in **Table 1**. To the best of our knowledge, these R_{pol} values are the lowest available in the present literature for all the cathodes under study. As highlighted throughout this work, the cathode architecture is of great importance for obtaining a good electrochemical performance, as the gas/solid and solid/solid interfaces are crucial for the ORR to take place.

Perspectives

- The elementary processes associated with the oxygen reduction reaction (ORR) are numerous and strongly depend on the material intrinsic properties (transport, structure) and on the shaping (microstructure, electrolyte-electrode interface, design). **In order to further investigate the ORR mechanisms, an in-depth impedance spectroscopy study could be performed for the double-layered « coral »-type nickelate films by varying the oxygen partial pressure ($10^{-4} < pO_2 < 1$ atm).**
- In this work, we have reported the lowest cathode polarization resistance values (R_{pol}) for $Ln_2NiO_{4+\delta}$ (Ln = La, Pr) obtained so far by using the double-layer strategy in combination with a coral microstructure and adding a composite sub-layer. Indeed, the electrochemical performance of these films was simultaneously improved by the large surface area and affected by a proper oxygen transfer and current distribution. At the electrode/electrolyte interface, the creation of a CGO / $Ln_2NiO_{4+\delta}$ composite sub-layer was found to be very effective for improving the electrochemical performance. The **« coral »-type microstructure and double layered architecture with a composite sub-layer could be extended to the $La_{2-x}Pr_xNiO_{4+\delta}$** ($0 \leq x \leq 2$) **solid solution system,** since very low R_{pol} values and a good stability have been shown for $LaPrNiO_{4+\delta}$. This microstructure seems to be highly complex due to the heterogeneous porosity and architecture at different scales.
- The microstructure is crucial in determining the performance of a SOFC cathode. This oxygen electrode is particularly sensitive to microstructural changes, as more parameters such as porosity, surface area, particle size, percolation path and tortuosity play an intricate role on the oxygen reduction reaction mechanisms. A new tomography technique based on focused ion beam scanning electron microscopy (FIB-SEM) allows obtaining valuable three-dimensional electrode reconstructions. The 3D information obtained on electrode microstructures can feed an electrochemical analysis. A numerical tool can be used to obtain effective properties of the reconstructed microstructures. On top of the classical parameters such as porosity, surface area and percolation of the phases, the software allows flow properties and transport (electronic and ionic conductivities) to be computed. Thus, 3D reconstructed images will allow developing a direct link at a pertinent length scale between the microstructure and the performance in SOFC cathodes. All the microstructural

properties can be introduced in a physical model to compute the polarisation curves and impedance diagrams of electrode. The model will be adapted from a previous one already developed for a mixed ionic electronic perovskite conductor with oxygen under stoichiometry. **These simulations would also provide an interesting tool to propose optimized architectured microstructures.**

- A possible extension of this work could be to consider a cathode functional layer built by **large columns,** as a following conceivable morphology that could be obtained by electrostatic spray deposition after adjusting the process parameters. The space between columns would serve as gas channels distributing oxygen to the active zones. The electrochemical performance is also very dependent on the roughness of the electrode surface and, consequently, on the contact with the current collector. Since the surface of a columnar microstructure would be much flatter than the surface of the coral-one, a much better current collection is expected.
- Thanks to their flexibility and reversibility, Solid Oxide Cells (SOCs) can be alternatively operated in both fuel cell mode (SOFC) for energy production and in electrolysis mode (SOEC) for hydrogen production. Nevertheless, the industrial deployment of this technology is still hindered by key issues related to **durability** and **costs**. The aging of the electrode-electrolyte interface (in terms of reactivity and inter-diffusion of elements) is of great importance. Consequently it would be worth to conduct a fundamental study on the oxygen transfer at the cathode /electrolyte interface in operating conditions as a function of time and to study the degradation mechanisms for such kind of architectures prepared by ESD. Structural properties of the materials and strains at the electrode / electrolyte interface could be extracted using Raman spectroscopy and coupling it simultaneously with impedance spectroscopy to obtain electrochemical properties in a controlled atmosphere as a function of time.
- The I-V and P-V curves recorded on a larger scale anode supported cell integrating the double layer "coral"- type $LaPrNiO_{4+\delta}$ cathode were quite disappointing with respect to the promising electrochemical performance obtained using symmetrical half cells (objective 2). Indeed, this full cell produced a power density of only 438 mW cm^{-2} at 700 °C and exhibits a degradation rate of 20 % after 408 hours. To be competitive regarding the state of the art, we propose to use a thinner electrolyte such as ~1 μm (YSZ, 1 μm + CGO, 200 nm) instead of thick one (~ 10 μm). It would also be possible to use an anode supported half cell with a thinner electrolyte consisting of YSZ (200

nm) topped by CGO (1 μm). In such case, the series resistance corresponding to the electrolyte would be very small due to the higher conductivity of CGO compared to YSZ. In addition, durability tests in this new configuration could be undertaken and degradation mechanisms will be investigated.

Annexes

Annex A

Electrostatic spray deposition technique

Electrostatic spray deposition (ESD) is one of the most promising, innovative and efficient chemical deposition methods for fabricating functional ceramic films with a large array of different microstructures while presenting a strong adhesion to the substrate, some of which quite original, as shown in **Fig. 1** [1-9]. Dense electrolytes, ~10 nm to 1 µm thick [7, 10-13] as well as porous electrodes, ~ 100 nm to 50 µm thick, for solid oxide fuel cells, have been largely fabricated in LEPMI during the last years [5, 6, 8, 12-14].

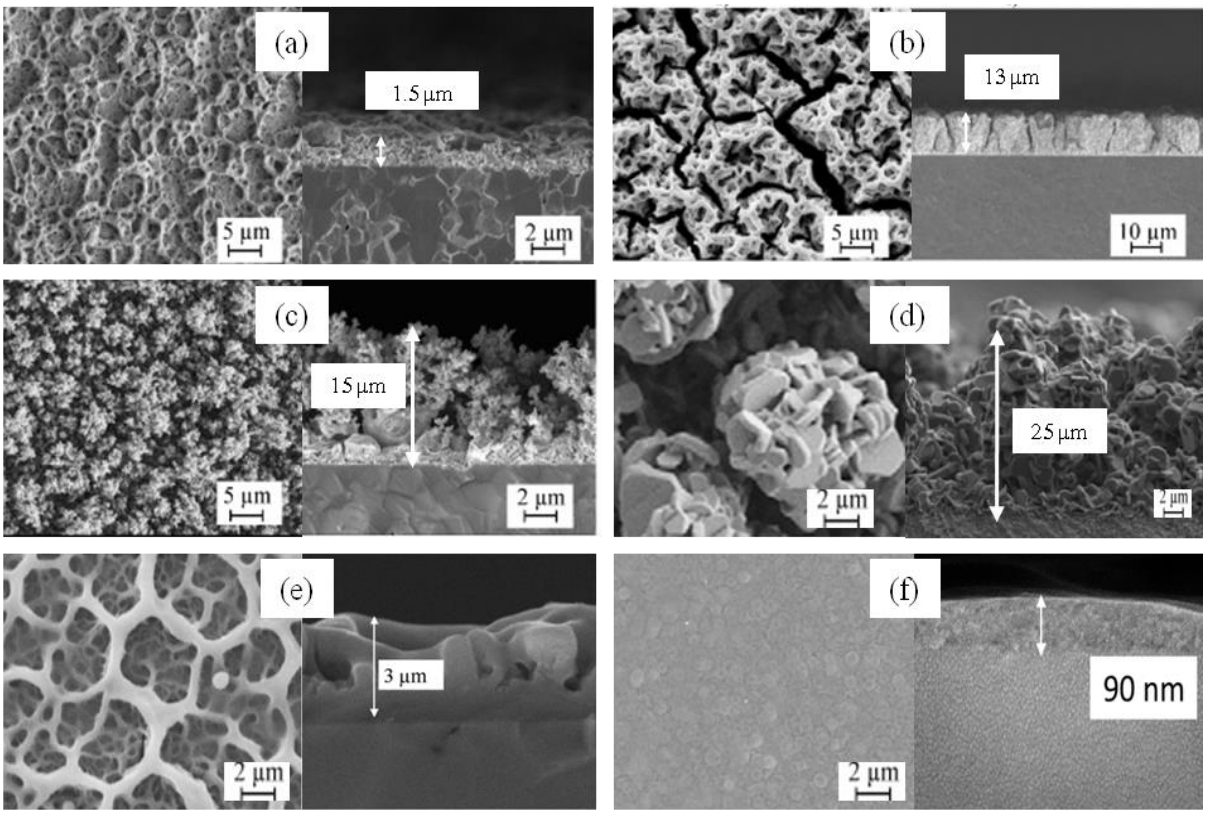

Fig. 1 SEM images of original microstructures of various materials: (a) dense $La_{0.6}Sr_{0.4}Co_{0.2}Fe_{0.8}O_{3-\delta}$ (LSCF), (b) columnar LSCF, (c) coral LSCF, (d) consisted of gypsum flower like $Ca_3Co_4O_{9+\delta}$ particles (d) coral CGO/ LSCF composite, (e) reticulated (La, Sr) $MnO_{3-\delta}$ (LSM), (f) dense CGO.

Moreover, this is a simple and low cost technique since it does not require vacuum chambers to function (**Fig. 2a**)**.** In this process liquid is forced to flow through a small metal nozzle which is subjected to an electric field due to which the liquid leaves the outlet of the nozzle in different forms or modes because of different electrohydrodynamic mechanisms. These modes include among others, the cone-jet mode (**Fig. 2b**).

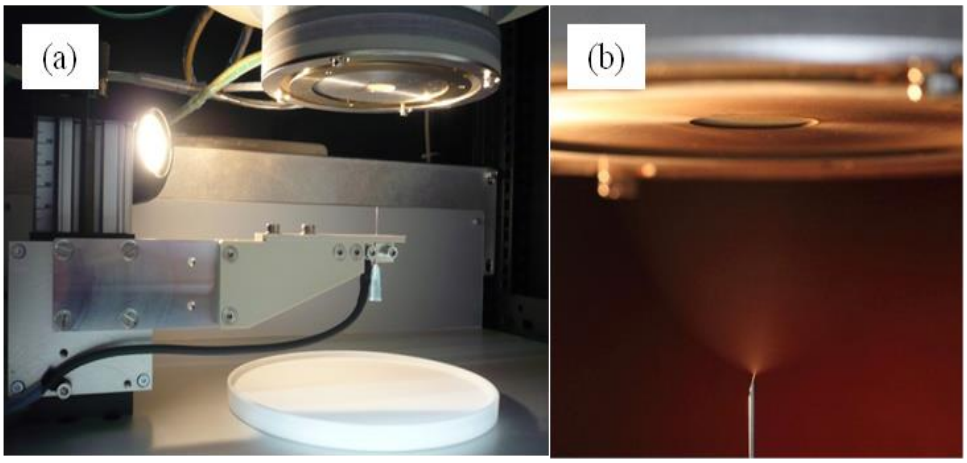

Fig. 2 ESD set up (a) and cone-jet mode (b)

Fig. 3 shows a schematic view of the ESD process which is consisted of a syringe pump, a syringe, a metal needle, a heating plate, a substrate holder and a high voltage power supplier. A syringe pump presses onto the syringe containing the precursor solution at a constant rate, then causing the solution to flow. A heating plate located in the substrate holder is surrounded by isolating material to provide the best thermal control of the substrate. One can adjust the distance between the nozzle and the substrate, the substrate temperature and the flow rate. A high-voltage supply (~ 10 kV) is connected to the metallic nozzle and is grounded on the substrate side.

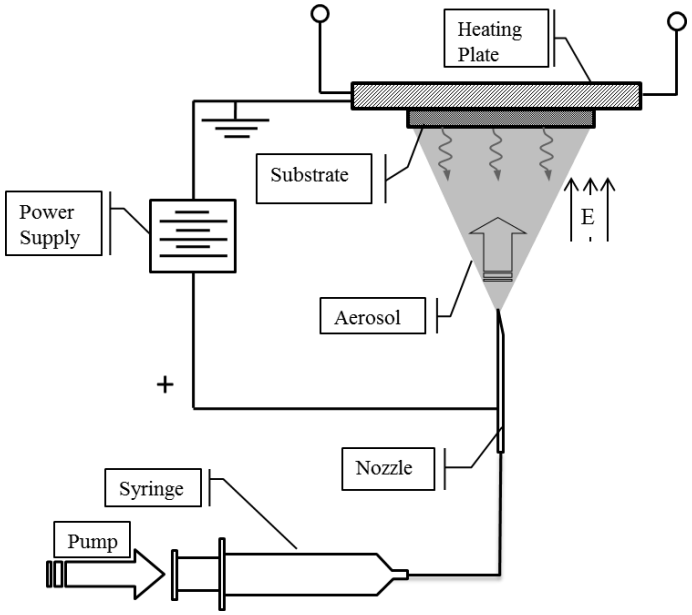

Fig. 3 Typical ESD setup [14].

Fig. 4 shows the schematic of Taylor jet cone and atomization during electrostatic spray deposition [8]. This is achieved when the electrostatic field applied between the positively charged needle and the grounded substrate polarizes the precursor solution on the needle tip and creates the so-called Taylor jet-cone. Atomization of the precursor solution is the first step of ESD process. This process can be divided in five successive steps, as shown in **Fig. 5**. Hydrodynamic instabilities break the surface tension of the cone which lead to the formation of charged droplets with micrometric sizes. Moreover, the self-repulsive force between the droplets avoids agglomeration and creates the aerosol. In the second step, the droplets are transported towards the substrate by the applied electrical field. During flight time, the size of droplets decreases due to the solvent evaporation, especially if the substrate is heated. Solvent losses depend upon the substrate temperature and the nozzle-to-substrate distance. The third step corresponds to the impact of droplets onto the substrate, while the fourth one is related to the spreading and drying of the droplets which impact onto the substrate and form the film. In the final step, the chemical reaction between the precursor salts occurs as the consequence of the substrate temperature which is usually chosen to cause complete solvent evaporation, and may even be enough high to decompose and promote partial (or complete) chemical reaction between the precursor salts.

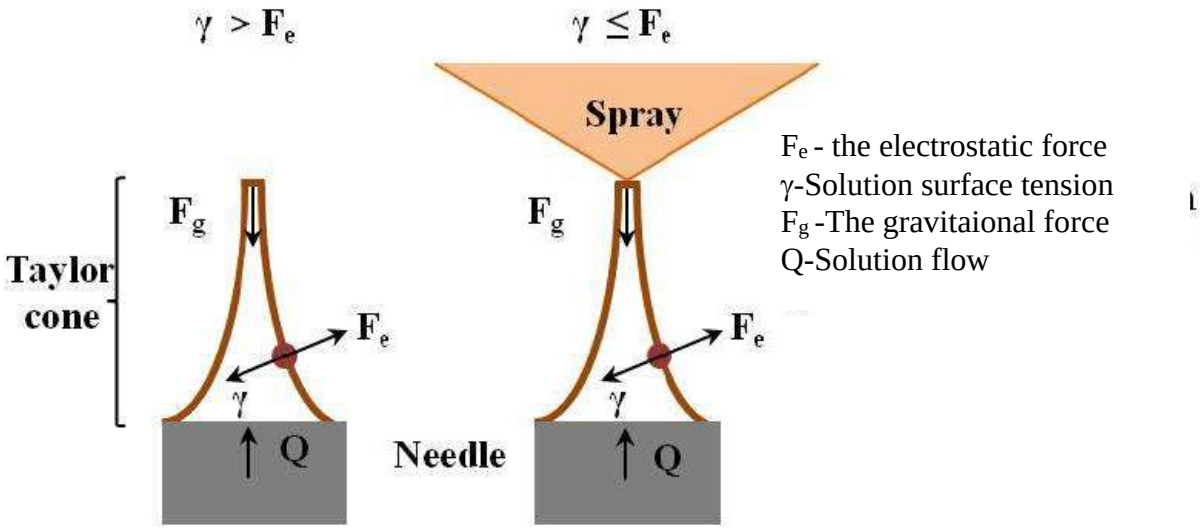

Fig. 4 Schematic of Taylor jet-cone and atomization during electrostatic spray deposition [8].

The microstructure of the deposited layer then results from a delicate compromise between the physicochemical properties of the precursor solution (boiling point, surface tension, viscosity, conductivity of the solution) and the deposition conditions (substrate temperature, nozzle to substrate distance, flow rate of the precursor solution, voltage,

deposition time). A large variety of very different microstructures with good homogeneity and reproducibility can be obtained by controlling some key process parameters. Such adjustments constitute one of the greatest advantages of ESD. In principle, the microstructure and thickness of the coating depends on the droplet size which can range from a few nanometers to approximately 100 μm [15]. According to literature, studies have been focused on the electro-hydrodynamic parameters that have an influence on the size of the droplets in the cone-jet. Gañan-Calvo et al. [16] presented an equation where the droplets size (d) is correlated to the solution density (ρ), vacuum permeability (ε_0) (equal to 8.85 x 10^{-12} $F.m^{-1}$), flow rate (Q), solution surface tension (γ) and solution electrical conductivity (σ), as the following:

$$d \sim \left(\frac{\rho \varepsilon_0 Q^a}{\gamma K} \right)^{1/6} \quad (1)$$

The correlation between deposition parameters and resulting microstructures was systematically studied and put into evidence in Marinha's PhD and Princivalle's PhD theses [5], dedicated to the preparation, microstructural and electrochemical characterization of $La_{0.6}Sr_{0.4}Co_{0.2}Fe_{0.8}O_{3-\delta}$ (LSCF) cathodes on gadolina-doped ceria (CGO) [10] and LSM, LSM/YSZ composite on YSZ, respectively [17, 18], .

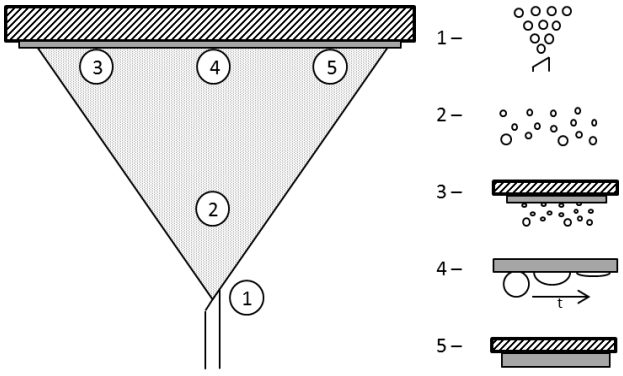

Fig. 5 ESD deposition successive steps: 1 - aerosol formation; 2 - droplet transport; 3 - droplet impact; 4 - spreading and drying; 5 - decomposition and reaction [11].

One of the greatest advantages of ESD is also an excellent control over the stoichiometry (cationic ratio) of the films. ESD has also the potential for up-scaling. In this work we have deposited nickelates films from 10 mm up to 40 mm in diameter. This process can be used to deposit much larger surfaces than obtained at the laboratorial scale.

References:

[1] R.K. Sharma, M. Burriel, E. Djurado, *J. Mater. Chem. A*, 3 (2015) 23833-23843.
[2] R.K. Sharma, M. Burriel, L. Dessemond, V. Martin, J.M. Bassat, E. Djurado, *J. Power Sources*, 316 (2016) 17-28.
[3] I. Taniguchi, R. C. Van Landschoot, J. Schoonman, *Solid State Ionics*, 156 (2003) 1 – 13.
[4] D. Marinha, C. Rossignol, E. Djurado, *Journal of Solid State Chemistry*, 182 (2009) 1742–1748.
[5] A. Princivalle, PhD Thesis, Grenoble INP, 2006.
[6] D. Marinha, PhD Thesis, Grenoble INP, 2010.
[7] G. Constantin, C. Rossignol, J.-P. Barnes, E. Djurado, *Solid State Ionics*, 235 (2013) 36–41.
[8] J. Sar, PhD Thesis, Grenoble INP, 2014.
[9] E. Djurado, A. Salaün, G. Mignardi, A. Rolle, M. Burriel, S. Daviero-Minaud, R.N. Vannier, *Solid State Ionics*, 286 (2016) 102–110.
[10] B.-H. Hwang, C.-L.Chang, C.-S.Hsu, C.-Y. Fu, *J. Phys. D. Appl. Phys.*, 40 (2007) 3448–3455.
[11] C. H. Chen, E. M. Kelder, M. J. G. Jak, J. Schoonman, *Solid State Ionics*, 86 (1996) 1301-1306.
[12] A. Princivalle, E. Djurado, *Solid State Ionics*, 179 (2008) 1921–1928.
[13] R. Neagu, D. Perednis, A.Princivalle, E. Djurado, *Solid State Ionics*, 177 (2006) 1981–1984.
[14] D. Marinha, L. Dessemond, E. Djurado, *Curr. Inorg. Chem.*, 3 (2013) 2–22.
[15] A. Jaworek, A. T. Sobczyk, *J. Electrostat.*, 66 (2008) 197–219.
[16] A. M. Gañan-Calvo, J. Davila, A. Barrero, *J. Aerosol Sci.*, 28 (1997) 249–275.
[17] A. Princivalle, E. Djurado, *Solid State Ionics*, 179 (2008) 1921-1928.
[18] A. Princivalle, D. Perednis, R. Neagu, E. Djurado, *Chemistry of Materials*, 17 (2005) 1220-1227.

Annex B

Scientific production

Peer-reviewed articles

1. **R. K. Sharma**, S.-K. Cheah, M. Burriel, L. Dessemond, J.-M. Bassat and E. Djurado, "Design of $La_{2-x}Pr_xNiO_{4+\delta}$ SOFC cathodes: a compromise between electrochemical performance and thermodynamic stability" *J. Mater. Chem. A* (DOI: 10.1039/c6ta08011a).
2. **R. K. Sharma**, M. Burriel, L. Dessemond, J.-M. Bassat and E. Djurado, "Design of interfaces in efficient $Ln_2NiO_{4+\delta}$ (Ln = La, Pr) cathode for SOFCs application" *J. Mater. Chem. A*, 2016, 4, 12451-12462
3. **R. K. Sharma**, M. Burriel, L. Dessemond, J.-M. Bassat and E. Djurado, "$La_{n+1}Ni_nO_{3n+1}$ (n = 2 and 3) phases and composites for solid oxide fuel cell cathodes: facile synthesis and electrochemical properties"*Journal of Power Sources*, 2016, 325, 337-345.
4. **R. K.Sharma,** M. Burriel, L. Dessemond, V. Martin, J.-M. Bassat and E. Djurado, "An Innovative Architectural Design to Enhance the Electrochemical Performance of $La_2NiO_{4+\delta}$ Cathodes for Solid Oxide Fuel Cell Applications" *Journal of Power Sources*, 2016, 316, 17-28.
5. **R. K. Sharma**, M. Burriel and E. Djurado, "$La_4Ni_3O_{10-\delta}$ as an efficient solid oxide fuel cell cathode: electrochemical properties versus microstructure" *J. Mater. Chem. A*, 2015, 3, 23833-23843.

Proceeding

1. **R. K. Sharma**, Ozden Celikbilek, M. Burriel, L. Dessemond, J.M. Bassat, E. Djurado, "Electrochemical performance and chemical stability of architecturally designed $La_{2-x}Pr_xNiO_{4+\delta}$ IT-SOFC cathodes" *ECS Transactions*, 2016, 72, 1-8.

Conferences (Oral presentations)

1. **R. K. Sharma**, M. Burriel, L. Dessemond, J.M. Bassat, E. Djurado, " Design and electrochemical properties of nickelate-based cathodes for solid oxide fuel cells: role of the interfaces" ECOSS -2016, Grenoble (France), August 28- Sept. 02, 2016.
2. **R. K. Sharma**, M. Burriel, L. Dessemond, J.M. Bassat, E. Djurado, "Architecturally designed $La_{2-x}PrxNiO4+\delta$ (x=0, 0.5, 1 and 2) IT-SOFC cathodes: a good compromise between electrochemical performance and chemical stability" GdRHySPàC -2015, Porticcio (France), October 14-16, 2015.
3. **R. K. Sharma**, M. Burriel, L. Dessemond, J.M. Bassat, E. Djurado, "$La_{n+1}Ni_nO_{3n+1}$ (n=1, 2 and 3) as IT-SOFC cathode materials: Screen Printing vs. Electrostatic Spray Deposition" Congress SCF -2015, Lille, 6-9th July, 2015.
4. **R. K. Sharma**, M. Burriel, L. Dessemond, J.M. Bassat, E. Djurado, "Microstructurally graded novel $La_2NiO_{4+\delta}$ cathode for IT-SOFC" SCF -2015, Lyon, 11th June, 2015.
5. **R. K. Sharma**, Vaibhav Vibhu, M. Burriel, L. Dessemond, J.M. Bassat, E. Djurado, "Electrochemical properties and stability of La_{2-x} $Pr_xNiO_{4+\delta}$ (x=0, 0.5, 1 and 2) films for IT-SOFC cathodes " FDFC -2015, Toulouse, February 3-5, 2015.

Conferences (Poster presentations)

1. **R. K. Sharma**, Ozden Celikbilek, M. Burriel, L. Dessemond, J.M. Bassat, E. Djurado, "Electrochemical performance and chemical stability of architecturally designed $La_{2-x}Pr_xNiO_{4+\delta}$ IT-SOFC cathodes"229th ECS Meeting, San Diego, CA, 29th May – 3rd June 2016.
2. **R. K. Sharma**, M. Burriel, L. Dessemond, J.M. Bassat, E. Djurado, "Novel Double-Layer $La_2NiO_{4+\delta}$ Cathodes: Screen Printing vs. Electrostatic Spray Deposition", SSI-2015, Colorado USA, 14-19th June, 2015.
3. **R. K. Sharma**, M. Burriel, L. Dessemond, J.M. Bassat, E. Djurado, "Architectural design of IT-SOFC Cathodes" JDD-2015, Grenoble, 29th June 2015.

Conception innovante de cathodes à base de nickelates de terres rares pour piles à combustible à oxyde électrolyte solide

Des oxydes appartenant à la famille structurale Ruddlesden-Popper (RP) sont des matériaux de cathode prometteurs des piles à combustible à oxyde électrolyte solide (SOFC) fonctionnant à température intermédiaire (~ 500-700 °C). L'objectif de cette thèse est l'élaboration de conducteurs ioniques et électroniques, mixtes (MIEC) tels que la solution solide, $La_{2-x}Pr_xNiO_{4+\delta}$, $0 \leq x \leq 2$, des phases RP de formule $La_{n+1}Ni_nO_{3n+1}$ (n= 2 and 3) et les composites associant les matériaux précédents à la cérine gadoliniée, $Ce_{0.9}Gd_{0.1}O_{2-\delta}$ (CGO). Une microstructure et une architecture innovantes de ces électrodes ont été obtenues avec succès en utilisant l'atomisation électrostatique (ESD) et la sérigraphie (SP). La structure, la composition, la non-stoechiométrie en oxygène et la microstructure de ces matériaux ont été caractérisées par diffraction des rayons X, par spectroscopie des rayons X à dispersion d'énergie, par analyse thermogravimétrique et par microscopie électronique à balayage. Les propriétés électrochimiques et la stabilité chimique de ces électrodes à oxygène sont discutées en fonction de leur architecture et de la composition en utilisant la spectroscopie d'impédance électrochimique (SIE) et la diffraction des rayons X, respectivement. Enfin, une cellule complète SOFC intégrant la cathode $LaPrNiO_{4+\delta}$ a été mesurée.

Mots Clés: Pile à combustible à oxyde électrolyte solide (SOFC), Conducteur mixte ionique et électronique (MIEC), Cathode, Nickelates, $Ce_{0.9}Gd_{0.1}O_{2-\delta}$ (CGO), Microstructure de type corail, Design architectural, Interfaces, Stabilité chimique, Atomisation électrostatique (ESD), Sérigraphie (SP), Spectroscopie d'impédance électrochimique (EIS).

Innovative design of rare earth nickelates as cathodes for solid oxide fuel cells

Layered Ruddlesden-Popper type (RP) oxides are promising cathodes for solid oxide fuel cells operating at intermediate temperature (~500 - 700 °C). This thesis is focused on the synthesis of mixed ionic-electronic conducting (MIEC) materials such as pure $La_{2-x}Pr_xNiO_{4+\delta}$, $0 \leq x \leq 2$, higher order $La_{n+1}Ni_nO_{3n+1}$ (n= 2 and 3) RP phases and composites adding $Ce_{0.9}Gd_{0.1}O_{2-\delta}$ (CGO) component. An innovative microstructure and architecture of these electrodes were successfully prepared using electrostatic spray deposition (ESD) and screen-printing (SP) processes. These materials were evaluated through structural, compositional, oxygen non-stoichiometry and microstructural characterizations using X-ray diffraction, energy-dispersive X-ray spectroscopy, thermogravimetric analysis and scanning electron microscopy. The electrochemical properties and chemical stability of these oxygen electrodes are discussed according to the architectural design and composition using electrochemical impedance spectroscopy (EIS) and X-ray diffraction, respectively. Finally, a single SOFC based on $LaPrNiO_{4+\delta}$ cathode has been measured.

Keywords: Solid Oxide Fuel cell (SOFC), Mixed Ionic and Electronic Conductor (MIEC), Cathode, Nickelates, $Ce_{0.9}Gd_{0.1}O_{2-\delta}$ (CGO), Coral-type microstructure, Architectural design, Interfaces, Chemical stability, Electrostatic Spray Deposition (ESD), Screen-Printing (SP), Electrochemical Impedance Spectroscopy (EIS).